The Challenges to predict and assess Flammability of Materials intended for use in Microgravity Environments - a case study of Polydimethylsiloxane (PDMS) membrane sheets.

Ulises Rojas-Alva

A thesis submitted **in partial fulfilment of the requirements for the degree of Doctor in Philosophy**

to

The University of Edinburgh

2021

Declaration

I declare that this thesis is composed by myself and is my own work. I declare that this work has not been submitted for any other degree or professional qualification.

Signed on April 30, 2021:

Ulises Rojas Alva

Abstract

Experimental work with different setups was carried out to study the flammability behaviour of polydimethylsiloxane (PDMS) membranes. The flammability was evaluated through thermal degradation analysis, ignition, flame growth, flame spread rates and extinction limits (near-limit phenomena). The experimental results were then compared with microgravity results from the Saffire II experiments that NASA carried out on board the Cygnus spacecraft. The environmental parameters used for the current study were forced flow, flow direction with respect to flame spread (opposed or concurrent), oxygen concentration, ambient pressure, normoxic condition (constant oxygen partial pressure).

The pyrolysis behaviour was evaluated by means of a thermogravimetric analysis in a standard TGA (ASTM E1131). A standard Cone calorimeter (ASTM E 1354) was used to assess the ignition behaviour under stagnant flow conditions where incident heat fluxes were required to derive fundamental properties. Then, for ignition, flame spread and near-limit behaviour under forced flows (concurrent and opposed) coupled with other environmental conditions (oxygen concentration, ambient pressure), three ad-hoc rigs were employed. The first rig was a customised flow tunnel where opposed and concurrent flame spread and near-limit phenomena were studied. The second rig was a modification of the FPA apparatus (ASTM E2058), where an inner flow reducer was custom-designed to improve and straighten the laminar forced flow. In both rigs, forced flows up to 150-200 cm/s could be attained. The third rig was a pressurised chamber, the TOPOFLAME (ZARM, Bremen), which was used to evaluate the effect of oxygen concentration and ambient pressure on the opposed flame spread, near-limit and the ignition behaviour. Lastly, it was also equally important to use a Scanning Electron Microscope (SEM) to quantify silica ash deposition (a PDMS by-product of pyrolysis and combustion) on post-burnt samples.

A complete theoretical evaluation of the flammability behaviour of PDMS was challenging as the literature does not offer reliable information or readily available fundamental properties. It was also found that the deposition of silica ash during any measurement pollutes any reading (such as a mass loss rate). Therefore, some fundamental properties were empirically determined and compared against literature values whenever possible. All the PDMS samples have a critical heat flux of about 30 kW/m^2, with small noticeable differences between sample thicknesses. The PDMS used in the current investigation behaves in a complex manner since silica is also formed via solid-phase. The TGA study and mass loss rate

measurements showed that the formation of silica in the solid-phase depends on the heating rate.

Under the effect of the forced flow and flow direction, the forced flow virtually affects the ignition delay times through cooling (pyrolysis) and mixing (increased flow time). The effect of flow direction, concerning the ignition location, affects the ignition delay times as a boundary layer is formed. Thus, the ignition coil for opposed flow (at the top of the sample) experiences a reduced flow, whereas the ignition coils face the forced flow in the concurrent case. The limiting flow condition for piloted ignition was found to be between 50 and 70 cm/s for opposed and concurrent forced flows, respectively. The linear dependency of ignition delay time on oxygen concentration and ambient pressure is via chemistry. For normoxic conditions, the ignition delay time behaves non-monotonically, and the regime change occurs at around 30% oxygen concentration and 0.7 bar ambient pressure. The mechanisms behind such change in behaviour are not well understood, but it is believed to be due silica-ash formation in the gas-phase and silica formation via the solid-phase.

The flame spread behaviour largely depends on the transport and deposition of silica-ash (SiO_2) and on the formation of silica in the solid-phase. Under opposed forced flows, if the chemistry is not changed (air under atmospheric pressure), the flame spread rate is independent of the forced flow, and silica-ash formation seems unimportant. Kinetics dominate extinction for high opposed forced flows, and the formation of silica in the solid-phase dominates near-limit as the sample increases in thickness. In the case of flame spread and near-limit, the SiO_2 ash deposition can be the dominant mechanism as it affects heat and mass transport significantly for the concurrent case. For high concurrent forced flows, enough silica ash is dispersed ahead of the flame front, and flame spread can reach a steady condition. There is a boundary condition at which concurrent traverses from extinction to steady flame spread.

As expected, flame spread rates were found to depend linearly on the oxygen concentration via chemistry. Flame lengths exhibited almost exponential dependency due to soot oxidation and increased fuel supply. For conditions where pressure was varied, it was found that two mechanisms control opposed flame spread. For relatively higher pressure, the flame spread was dominated by heat and mass diffusivity, whereas for lower pressures, radiative losses through the solid-phase dominated the flame until extinction occurred. Extinction at low pressure is believed to be due to heat losses and kinetics.

For normoxic conditions, the oxygen concentration dominated the flame spread more than the change in pressure. The change of regimes for flame lengths as a function of ambient pressure was found to occur near the normoxic limit coincidentally. That is, the largest flame length occurs at the normoxic limit. The flame spread rates were found to depend linearly on the gas-phase characteristic length (flame length) up to a limiting length (at around 20 mm); after that, flame spread rates were independent. Characteristic solid-phase lengths (pre-heat and pyrolysis) results were not conclusive, as the IR picked up the silica ash particles before the solid-phase.

Using a simplified extended theory (for opposed flame spread), the gas-phase kinetic parameters were empirically derived to evaluate the near-limit phenomena. The opposed flame spread was found to reach a kinetic regime for high forced flows where the effect of silica ash deposition was drastically reduced. Nonetheless, for low opposed forced flows, including in microgravity conditions, the silica formation through the solid-phase and silica-ash through the gas-phase dominated the heat and mass transfer. Pressure modelling for PDMS does not seem to reproduce the same behaviour as the one observed in microgravity, especially for near-limit conditions. In microgravity, for the sample thicknesses tested under 20 cm/s, it seems that the silica ash deposition is the dominant mechanism for flame extinction, but there should be a limiting case where under high forced flow, a steady flame spread might be viable.

A series of properties could be extrapolated from all the experimental results on the PDMS membranes and are presented in the following table. The results for the LOI vary according to the sample thickness, which agrees with the literature, due to the nature of the PDMS related to the thermal decomposition and formation of silica via solid-phase. Also, the pre-exponential factor found for the gas-phase varies on the sample thickness and should not be the case, but it is also a consequence of the thermal decomposition of this particular siloxane.

Method	Property		Value	Units
Thermocouple measurements	Flame temperature		1180	℃
Cone Calorimeter	Critical heat flux		30	kW/m^2
TGA (ASTM E1641-16)	Activation energy (solid-phase)		148	kJ/mol
	Pre-exponential factor (solid-phase)		$3.4 \cdot 10^7$	min^{-1}
Improved FPA	LOI	e = 0.125 mm	19.3	%
		e = 0.25 mm	20	
		e = 0.36 mm	20.8	
MLOC (empirical	Activation energy	e = 0.125 mm	224	kJ/mol

method)	(gas-phase)	e = 0.25 mm		
		e = 0.36 mm		
	Pre-exponential factor (gas-phase)	e = 0.125 mm	$2.59 \cdot 10^9$	$m^3/kg \cdot s$
		e = 0.25 mm	$2.19 \cdot 10^9$	
		e = 0.36 mm	$1.34 \cdot 10^9$	

A positive aspect shown by the PDMS membranes is their lower flammability results as they have higher LOI and higher critical heat flux. They’re less likely to ignite compared to other thermopolymers (such as PMMA, PP and others). The formation of silica via solid-phase and silica-ash via gas-phase, along with the transport and deposition on the unburnt fuel, can hinder self-sustained burning. Thus, such distinctive behaviour is desirable for a range of thermoplastic and polymers. Siloxanes, as coatings or silica as fillers on other materials, might help in reducing their flammability. However, it was observed that opposed flame extinction (kinetic regime) requires very high forced flows. The depressurisation strategy on spacecraft (fire-fighting) might not be ideal for an established diffusion flame over a PDMS or similar silicone material.

Overall, the current study found that the flammability criteria might fail to address the flammability behaviour of PDMS fundamentally. Such methods do not gather the effect of other environmental parameters, mainly affecting the silica ash deposition. Therefore, it is recommended that any future flammability assessment method for material selection should not be based solely on a criterion or a fundamental limit that depends on a limited environmental scenario. Instead, the flammability assessment of solid materials should be rated based on a robust array of methods based on normal gravity and microgravity along with fundamental properties inherent to the material that is being studied.

It is recommended to continue working on investigating the flammability behaviour of PDMS and other silicone-based membranes. The formation of silica or silica-ash via solid- and gas-phase, and the transport and deposition of the silica-ash need further understanding. Another important aspect is the effect of normoxic conditions on all aspects of flammability, and it is especially relevant on spacecraft. Experiments in microgravity should are encouraged to further expand the data, and thus a better understanding of microgravity can be attained. Given the PDMS's lower flammability, siloxanes and silica fillers or coatings should be explored and studied to evaluate reducing the fire risk of materials intended for spacecraft applications.

Lay Summary

Spacecraft fire safety is an important operational aspect of spacecraft, but also a fundamental aspect of how materials burnt in microgravity conditions. On spacecraft, the main fire safety strategy relies on selecting materials that are less flammable. There are methods and standards put in place that rate materials based on their performance to a prescribed energy. However, those methods are based in normal gravity environments and do not reflect how materials burnt in microgravity conditions. Therefore, there is a need to improve the current understanding of the fire behaviour of solid materials for spacecraft applications.

Polydimethylsiloxanes (PDMS) are silicone-based products used for many applications across several industries, including on spacecraft. A recent experiment in microgravity showed that PDMS membranes did not burn in microgravity. A series of experiments in normal-gravity conditions were conducted to elucidate the fire behaviour of PDMS in microgravity conditions.

It was found that the fire behaviour of PDMS is far more complex than anticipated. As the membranes are burning, silica-ash, a combustion by-product is generated. Silica-ash is transported and can deposit on the sample surface inhibiting further burning. In addition, as the PDMS burns, silica is left behind, and the amount of silica residue left depends on the intensity of the heat from the flame. All of these processes are affected in different ways by the environmental conditions found on spacecraft (oxygen concentration, forced flow and ambient pressure).

The PDMS was found to be less flammable than other common thermoplastics used in daily life (such as acrylic). The formation of silica-ash during the combustion process also helps to reduce flammability. Thus, PDMS and other silicone or siloxane materials could be safer in environmental conditions. Siloxanes, as coatings or fillers, could help in improving the thermal response and flammability behaviour on other materials intended for spacecraft applications.

Acknowledgements

Working on the PhD project has been very challenging indeed and I have doubted myself many times. When many things don’t make sense, either one gives up or one tries to look at the complexities from a different angle. One never knows what that might lead to, but it can certainly help to understand complex problems. Consequently, one learns and evolves. This is not just a work of one person alone. I have received the help from various people throughout the duration of the programme. First of all, I want to express my gratitude to my Supervisor, Prof Jomaas, who has allowed me to freely explore my thoughts and has supported me throughout. The best fuel is when other people believe in your capabilities, even when you don’t. Likewise, my friends and family have encouraged me along the way. My number one supporter is my boyfriend, who stoically has endured my low moods and has helped me greatly. I also want to thank the engineers from the Workshop at University of Edinburgh, who have made possible my designs. Specially, the fire lab manager, Michal, who has given me support in the laboratory. Another special gratitude to Prof Christian Eigenbrod, who allowed me to use their facilities at the German Space Agency in Bremen. Finally, it has been a great pleasure to work with other students whom I have learnt from and I have been able to exchange knowledge with. Particularly, a special thanks to Frederik, who offered an extraordinary support in very stressful situations during the pandemic.

Contents

Table of Figures

List of Tables

Nomenclature

a	Stretch flame rate	$\dot{q}''_{rs}$	Surface re-radiation
a_{abs}	Absorptivity	$\bar{\dot{q}}''_{s}$	Dimensionless neat heat flux at the solid surface
A_g	Gas-phase Pre-exponential factor	R	Gas universal constant
A_s	Solid-phase pre-exponential factor	r	Sample radius
C	Constant in Chapter 2.4.4.2	Ra	Rayleigh number
c_1	Constant in Fernandez-Pello	$R_{rad,e}$	Empirical Radiation number
c_2	Constant in Fernandez-Pello equation	Re	Reynolds number
c_{p}	Specific heat	S	Surface of cylinder
c_{SiO_2}	Specific heat of silica ash	T_f	Flame temperature
B_T	Mass transfer number	T_v	Vaporisation temperature of solid
Da	Damköhler number	T_∞	Ambient temperature
Da_e	Empirical Damköhler number	t_c	Characteristic time
E_g	Gas-phase Activation energy	t_{cond}	Conduction loss time
E_s	Solid-phase activation energy	$V_{f,o}$	Opposed flame spread rate
Fr	Froude number	$\bar{V}_{f,o}$	Dimensionless opposed flame spread rate
g	Gravity acceleration	$V_{f,th}$	Theoretical flame spread rate in the thermal regime
Gr	Grashof number	V^*	Dimensionless characteristic flame spread rate
ΔH_c	Heat of combustion	V_c	Concurrent flame spread rate
ΔH_p	Heat of pyrolysis	$\bar{V}_c$	Dimensionless concurrent flame spread rate
h_c	Convective heat transfer coefficient	V_{nb}	Characteristic buoyancy driven flow velocity
l	Characteristic length	V_r	Relative flow velocity
l_f	Flame length	V	Volume of cylinder
$\bar{l}_c$	Characteristic pre-heat length for concurrent flame spread	U_t	Thermophoretic velocity
$\bar{l}_o$	Characteristic pre-heat-length for opposed flame spread	x_c	Characteristic length
$\dot{m}''$	Mass loss rate	x_p	Pyrolysis length
Q	Heat loss term in Chapter 2.4.4.5	$Y_{O_2,\infty}$	Mass fraction of oxidizer
$\dot{q}''_e$	Incident heat flux	W	Sample width
$\dot{q}''_{fr}$	Radiative heat flux from the flame		

Greek Symbols

α_g	Gas-phase mass diffusivity	τ	Half-thickness of the solid-fuel
α_m	Thermophoretic parameter	τ_r	Residence time
β	Thermal expansion coefficient	τ_{ch}	Chemical time
ε	Surface Emissivity	τ_{SiO_2}	Half-thickness of the silica ash thickness layer
η_{EST}	Dimensionless flame spread rate in the thermal regime	υ	Dynamic viscosity
λ	Thermal conductivity	ϕ_o	Dimensionless parameter for opposed flame spread
μ	Kinematic viscosity	ϕ_c	Dimensionless parameters for concurrent flame spread
ρ_g	Gas-phase density	Φ	ratio of solid-heat conduction to the heat conduction through the gas-phase
ρ_s	Solid-phase density	χ	Radiative fraction parameters in Chapter 2.4.4.5
ρ_{SiO_2}	Density if silica ash	ω_g	Gas-phase chemical reaction rate
σ	Stefan-Boltzmann constant		

ACRONYMS

BASS	Burning and Suppression of Solids experiments in the MSG aboard ISS	SoFIE	Solid Fuel Ignition and Extinction
CNES	French National Centre of Space Studies	SSCE	Solid Concurrent Combustion Experiments
DAS	Diamond Air Services	TGA	Thermogravimetric analysis
DARTFire	Diffusive and Radiative Transport in Fire Experiment	TOPOFLAME	Combustion chamber at ZARM facilities
ESA	European Space Agency	ULOI	Upwards limiting oxygen concentration
EVA	Exploration Vehicular activities	WIF	Wire Insulation Flammability
JAXA	Japanese Space Agency	ZARM	Center of Applied Space Technology and Microgravity
JAMIC	Japan Microgravity Centre	ETFE	Ethylene
FIST	Forced-flow ignition and flame spread test	HDPE	High density polyethylene
FFFT	Forced Flow Flame Spread Test	LDPE	Low density polyethylene
FLARE	Flammability limits at Reduced-g Experiments	FEP	Fluorinated ethylene propylene
FPA	Flammability propagation	PC	Polycarbonates

	apparatus		
LIFT	Lateral Ignition Flammability test	PDMS	Polydimethylsiloxane
HASTIC	Hokkaido Aerospace Science and Technology Incubation Center	PE	Polyethylene
HNIRI	Hokkaido National Industrial Research Institute	PEEK	Polyether ether ketone
HRR	Heat release rate	PI	Polyimide
LOI	Limiting oxygen index	PMMA	Poly
NASA	National Aeronautics and Space Administration	POM	Polyoxymethylene
MGLAB	Microgravity Laboratory of Japan	PP	Polypropylene
MLOC	Minimum limiting oxygen concentration	PP/PG	Polypropylene glass fibre composite
MSG	Microgravity Science Glovebox	PPSE	Polyphenylsulfone
MOC	Maximum oxygen concentration	PS	Polystyrene
MWT	Microgravity Wind Tunnel	PTFE	Polytetrafluoroethylene
NMLC	National Microgravity Laboratory China	PVC	Polyvinyl chloride
RITSI	Radiative Ignition and Transition to Spread Phenomena	PUR	Polyurethane
PRIRODA	Shuttle-Mir Science Project	SIBAL	75% cotton – 25% glass fibre
Saffire	Spacecraft Fire Experiments	SH144YA	Silicone rubber
SCEM	Solid Combustion Experiments Module	SR-50	Silicone resin
SEM	Scanning Electron Microscope	Teflon	Modified ethyltetrafluoroethylene
SJ	Shi-Jian Satellite Programme		

1. Introduction

The development of human-crewed spacecraft missions requires ensuring astronauts' safety in various operational aspects. One clear integral operational aspect is fire safety on spacecraft [1]. As fire behaves differently on Earth than in microgravity, fire safety approaches on spacecraft differ from the measures and strategies used on Earth. One critical aspect is that evacuation is generally not an option on a manned spacecraft. Thus, the fire safety strategy for human-crewed spacecraft requires critical thinking and a fundamental understanding of combustion phenomena in microgravity to combat any fire developments. Such a programmatic need has spurred or pushed to conduct research on the combustion of solid matter in microgravity [2]. In addition, fire safety is important as an operational aspect for human space activities and exploration and as fundamental combustion research [1]. Therefore, a coupling of these aspects is required to study combustion research in microgravity. Furthermore, the new plans to travel beyond the Low Earth Orbit, to the Moon and Mars, have created a programmatic need to improve the understanding of the flammability behaviour of solid materials in microgravity, as well as in other gravity levels (Martian and Lunar). Thus, the current screening methods would benefit from being improved to provide a more scientific-based description of relevant materials [1].

Microgravity environments offer a unique opportunity to conduct fundamental research as the buoyancy effect is absent. This is of importance, as buoyancy can mask fundamental phenomena, and in the absence of gravity (or buoyancy), new phenomena arise. A clear example is shown in *Figure 1*, which shows a candle in normal gravity (left) and a photo of candle flame experiments conducted as part of the Space Shuttle Program aboard the MIR station (right) [3]. The candle in normal gravity is elongated (due to buoyancy), while the microgravity flame has a hemispherical shape. One can thus infer that the candle flame's heat and mass transfer mechanism are distinctively different between the normal-gravity and the microgravity environments. For the microgravity flame, the heat transfer from the flame can be thought to be larger as is it closer to the candle base. The mass transfer of fuel and oxidizer are also expected to be affected by the lack of buoyancy, as the candle flame in microgravity was tested in a quiescent environment. Thus, the mass transfer can be expected to be dominated by diffusion. Finally, the blue colour of the microgravity candle flame indicates that soot formation is very weak, which in turn makes the heat transfer quantitatively different from the microgravity flame. As such, fire, as represented by a flame, can be very different in microgravity, and it is vital to fundamentally understand combustion in microgravity to avoid or minimize any fire risk on Spacecrafts or other space infrastructure.

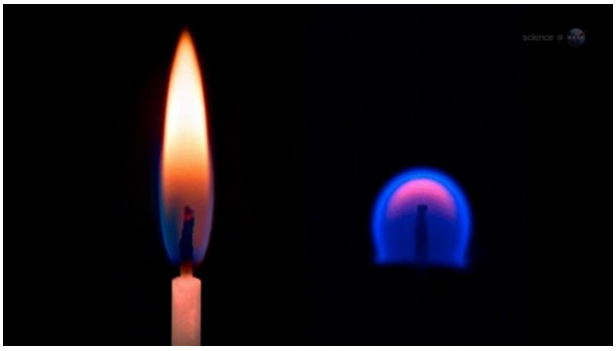

Figure 1 – Candle flame under Earth conditions (left) and under microgravity on a spacecraft (right). The picture of the candle flame in microgravity was captured during the Space Shuttle Program in the STS-50 (USML-1) mission in 1992. The pictures were taken from the NASA database [4].

Unfortunately, spacecraft have not been exempt from fire incidents in the past, see *Table 1*. The first fire incidents with casualties occurred in mock-up tests on Earth where the environmental conditions, pure or very high oxygen concentration, led to an extremely fast fire growth and development [5,6]. Subsequent spacecraft designs have reduced the amount of oxidiser in the spacecraft environment, such as those from the MIR and the ISS (21% oxygen concentration and sea-level atmospheric pressure). During operations of spacecraft in space, various near-fire incidents have been reported due to mostly electrical component overheating and electric short circuits (see *Table 1*). Perhaps, the most notorious fire incident occurred on the MIR space station [7]. Even with many precautions in place, there is always a risk of fire occurring on spacecraft.

Table 1 – Near-fire and fire incidents that have occurred on manned space missions or during preparations in normal gravity mock-up activities.

Gravity	Spacecraft		Date	Description	Fatalities	Ref.
Normal	Soviet Air Force		March 1961	Fire in altitude chamber, fire initiated by an alcohol-soaked cloth dropped on an electric hotplate.	1	[8]
	Apollo 1		January 1967	Fire during spacecraft test, an electrical fire lead to a rapid fire in a 100% oxygen cabin.	3	[5,6]
Microgravity	Space Shuttle	STS-6	April 1983	Fusing of overheated wires near a space-process unit.	None	[2]
		STS-28	August 1989	Electric short-circuit due to a cable strain and insulation failure	None	
		STS-35	December 1990	Failure of an overheated resistor	None	
		STS-50	July 1992	Blown electrical capacitor in a medical apparatus.	None	
	MIR		February 1997	Lithium perchlorate Canister on fire.	None	[7]

Complete elimination of the risk of fires on spacecraft is not feasible as it compromises spacecraft operability [2]. For example, paper sheets (cellulosic fuel) are flammable but are required for astronauts' daily tasks. Thus, there is a compromise between a minimum accepted risk (damage to components, but not to human life) and spacecraft operability [2,9]. Fire safety strategies on spacecraft rely on four aspects: namely prevention, detection, fighting and post-recovery [1]. Prevention involves the control of oxidiser levels, ignition and fuel. For the first, the oxygen concentration can be reduced, as happened in the first spacecraft designs, but it cannot be completely reduced, as a minimum concentration is required for life-support systems. Ignition and fuel control are done by designing standards and flammability tests for material selection. The active fire safety strategies are then based on operational emergency, quality control and suppression strategies [1]. NASA's fire safety strategy relies principally on fire prevention (material selection) [1,2,9].

One of the methods for screening materials is the NASA standard test 1 [10], the upwards ignition and flame growth. Materials are selected based on the response to pass/fail criterion (prescribed ignition energy and upwards flame travelling more than 15 cm). Upward flame spread is considered the most critical scenario. However, such an empirical procedure in normal-gravity entails serious concerns when its results are applied directly to microgravity environments. What is critical on Earth might not necessarily be in microgravity environments. Other methods have been proposed in the past to improve material selection [11,12]. Nonetheless, it is still unclear how their results directly translate to microgravity scenarios.

A significant amount of research on solid fuel combustion in microgravity has been carried out since the pioneering study led by Kimzey in 1966 [13–15], where the flammability behaviour of solid materials in parabolic flights and on the Skylab spacecraft was investigated for the first time. Subsequent studies have been conducted across various Earth-based microgravity platforms and spacecraft (Shuttle Programme and MIR) and on the International Space Station (ISS). These studies indicate that it is easier to ignite a solid in microgravity than in normal gravity, that radiation is very important in the flame spread of flames under very slow forced flows, the flammability of materials is extended in microgravity, and other surprising behaviour that has not been observed in normal gravity [9,16]. These results qualitatively showed the contrasting behaviour of solid flammability in microgravity.

Some of the experimental studies in microgravity have identified the flammability boundary limits as a function of environmental parameters, most commonly under oxygen concentration and forced flow [17–22]. Within this boundary map, self-sustained flame spread can take place and vice versa outside the boundary limit. It has been shown that there is a minimum oxygen concentration and forced flow, identified as a fundamental limit [23,24]. Such a fundamental limit has been shown to occur at lower oxygen concentrations in microgravity. Thus, identifying such a limit for any material can provide an improved screening method. Therefore, there is an ongoing effort to predict the fundamental limit and its discrepancy with normal gravity [12].

NASA along with an international topical team from other space agencies established the Saffire programme to address gaps not looked at before [25]. The main goal was to conduct large scale experiments in microgravity, as such experiments had not been done previously. Thus, the fire behaviour could be evaluated in a more realistic scenario.

As Polydimethylsiloxane (PDMS), a silicone-based product, has interesting properties that make it ideal for many applications on spacecraft, four PDMS membranes of various thicknesses were tested during the Saffire II flight [26]. The flame spread could not be self-sustained; such an outcome was not expected. It is unknown whether it was inherently an ignition of flame spread problem and its causes. It is suspected that this could relate to silica-ash (SiO_2) production, which occurs when a silicone, PDMS, burns, as its deposition on the sample is known to affect the heat and mass transfer process. However, it is not known how the transport and deposition of silica-ash affect the flammability behaviour of silicones on spacecraft. Given that none of the PDMS samples burnt during Saffire II, it is interesting to find out if this can imply that these materials can be deemed safe on spacecraft. In addition, the question arises whether or not the other proposed flammability assessment methods can effectively judge the fundamental behaviour of silicone materials.

In the current investigation, the key aspects, fundamental and technological, of the flammability behaviour of solid materials in microgravity have been reviewed in order to provide a holistic overview of the previous research conducted. This review of previous literature can help identify the critical aspects of flammability of solid materials needed to reduce the fire risks on spacecraft. In addition to that substantial review, PDMS was studied experimentally in normal-gravity conditions to understand its flammability behaviour (pilot ignition, flame spread and near-limit phenomena) in microgravity conditions. The silica-ash transport and deposition were evaluated as it affects heat and mass transfer. Two methods were used to evaluate the flame spread and near-limit behaviour of the PDMS. The first was a method based on the Limiting Oxygen Index approach [27,28], while the second method was pressure modelling. Finally, the experimental results were then compared to microgravity experiments as far as possible.

Figure 2 summarises the current investigation and provides an overview of each chapter. In Chapter 2, various topics defining the flammability of solid materials in microgravity are highlighted. These are ignition, smouldering, flame spread, and near-limit. The same chapter presents an overview of the experimental methodology to conduct microgravity experiments and the methodology to assess flammability. Also, this chapter provides more in-depth details and the burning behaviour of silicones. The chapter finishes with brief arguments and conjecture on the outcome of Saffire II tests (executed on the 10th of June 2017) with PDMS samples, which serves as motivation for the current study. Chapter 3 then presents the hypothesis and the objectives of the current study. Chapter 4 outlines the experimental procedures used to carry out the experimental study. In Chapter 5, the normal-gravity results are presented and discussed in connection with the microgravity results from Saffire II. This chapter is subdivided into sections dealing with silica-ash transport, ignitions, flame spread, and near-limit behaviour. Finally, Chapter 6 summarises the current investigation and provides conclusive comments.

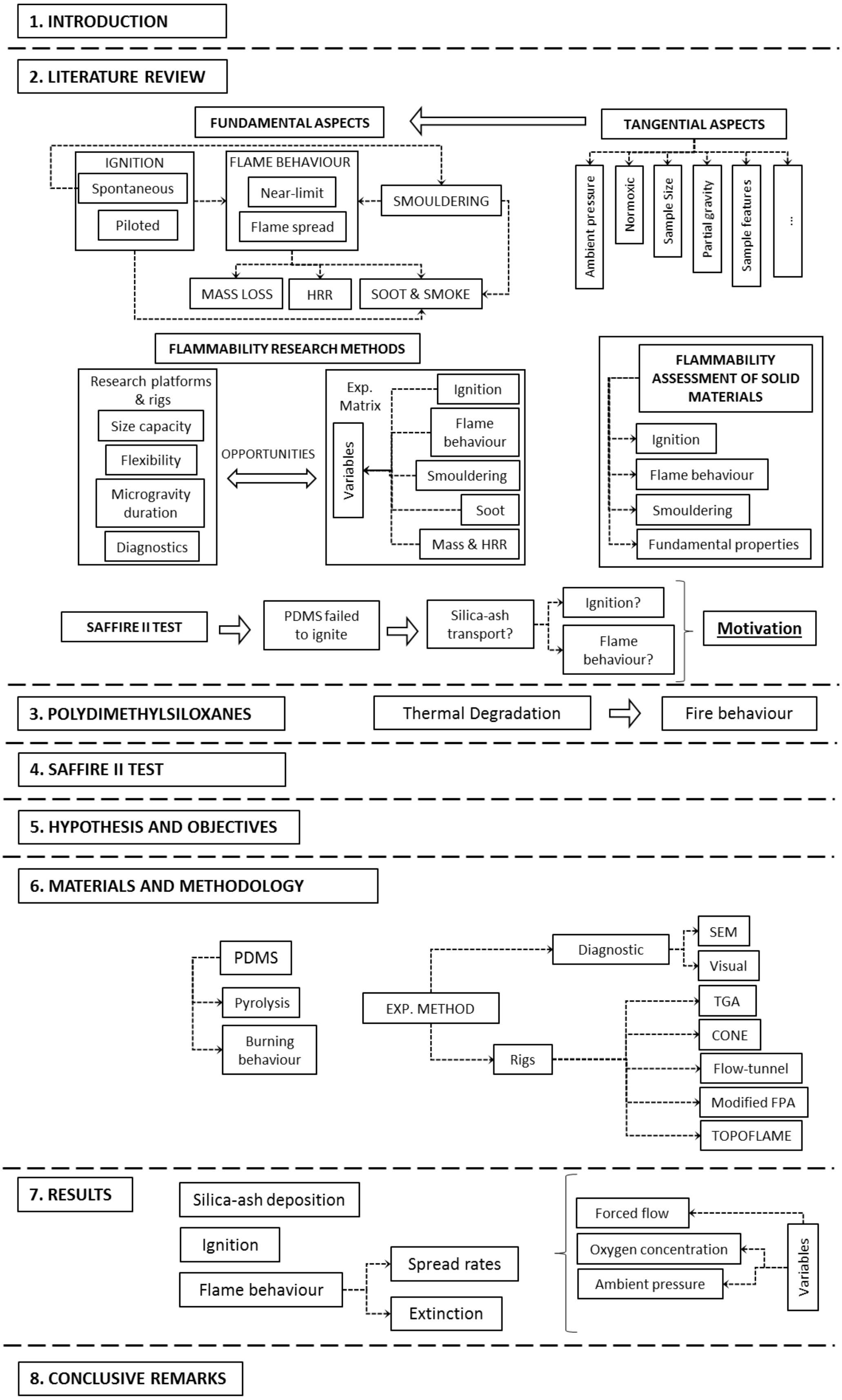

Figure 2 - Chart showing how the current investigation was structured.

2. Literature review

2.1. Fundamental aspects

The flammability behaviour of solid materials can be defined by ignition and flame spread, as well as by near-limit and smouldering phenomena. In addition, soot and species production characterise all these phenomena, and other parameters can be used to quantify the phenomena (e.g. burning rate, HHR or other properties), as shown in *Figure 3*.

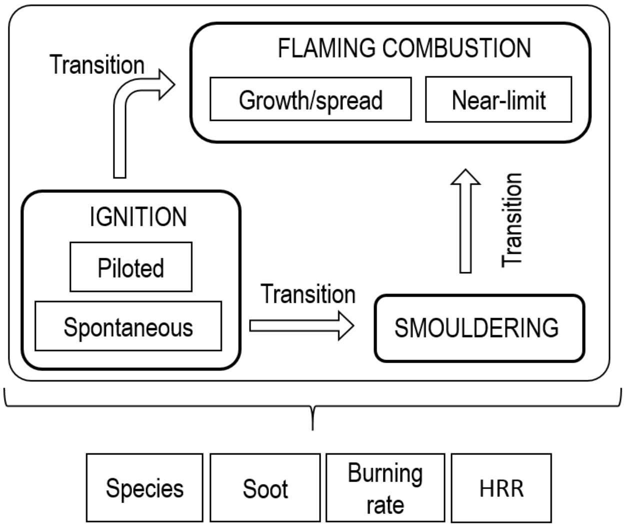

Figure 3 – Diagram showing the phenomena and concepts that define flammability.

Further sub-classification can be made within each main phenomenon depending on the environmental conditions. Ignition is often categorised as piloted or spontaneous. There are multiple ways to classify flame spread, but it is generally accepted that it is most appropriate to classify them according to the forced flow direction. If a flame travels against a parallel forced flow, it is considered opposed, and if the flame travels along with the forced flow, then this is considered concurrent flame spread. Flame spread occurring in a quiescent environment can inherently be considered as opposed [18]. There are other scenarios that do not fall within opposed/concurrent classification. One example is one-dimensional flames developing on a surface or a cylindrical sample. These are known as point-diffusion stagnant flames. Smouldering propagation can also be classified following the opposed-concurrent definition. Within these aforementioned categories, further classification can be established, but these are external parameters to the fundamental problem.

2.1.1. Ignition

The ease with which solid materials attain ignition has also been explored in microgravity conditions. In 1968, Neusting and co-workers [29] were the first to study ignition in microgravity, and they found that the time to ignition was affected by the gravity level**.** During drop tower tests, Kashiwagi and co-workers [30] observed that a low-speed forced flow did not have a significant effect on the time to ignition for a paper heated by radiation. However, in opposed flows, Roslon and co-workers [31] reported that the time to ignition (piloted) was reduced as the forced flow decreased for PMMA and polypropylene/glass fibre composite samples tested during parabolic flights.

In particular, Roslon and co-workers studied the effect of microgravity on the ignition delay time of two thermally thick fuels in parabolic flights [31]. They found that the ignition delay time in microgravity is strongly dependent on the convective heat transfer. Similar findings have been reported where ignition delay times are reduced in microgravity due to lower heating losses at the fuel surface and in an increase in mixing time [32–35]. However, ignition behaviour in microgravity is more complex, and the opposite behaviour has also been reported [36]**.**

2.1.2. Flame spread

The spread of diffusion flames is a complex phenomenon that has been widely studied, and there are various fundamental (theoretical) and numerical models for which this flame phenomenon was studied under various scenarios in normal gravity environments [37–56]. In microgravity environments, this flame spread phenomenon has also been explored theoretically and numerically [57–73]. It is well known that laminar flame spread in opposed flow is dominated by the leading edge, while the geometry and characteristics of the flame (i.e. flame length, temperature, thickness and attachment to the solid surface, and soot level) are the key parameters in concurrent flow.

For thermally thin fuels, three regimes that are functions of forced flow and oxygen level define the flame spread and flame stability in opposed flows [16,74]. In the thermal regime, the residence time is higher than the chemical time, $\tau_{res} > \tau_{chem}$. In this regime, the forced flow has little effect on the flame spread is considered to be constant and only affected by the sample thickness [75]. Thus, in this regime, the stability of the flame is dominated by the conduction from the gas-phase to the solid phase. However, if the forced flow is increased significantly, the residence time decreases and becomes significantly smaller than the chemical time, $\tau_{res} \leq \tau_{chem}$, corresponding to the kinetic regime, where finite rate kinetics play a significant role [76]. These two regimes can be found in both normal and microgravity environments.

If the forced flow is reduced and becomes too low ($\leq 0.2 m/s$), the residence time becomes much greater than the chemical time ($\tau_{res} \gg \tau_{chem}$). Thus, the radiative regime is approached, and the thermal losses through gas-phase radiation and solid-phase radiation greatly influence the flame spread. This regime can mostly be found in microgravity, where buoyant flows are absent. In normal gravity, the radiative regime has also been reported in one-dimensional flames (stagnation-point diffusion flame) [23]. As the forced flow is reduced, the radiative losses become greater until the flame extinguishes (quenching boundary limit). These regimes can be visualised in the microgravity experimental data in *Figure 4*.

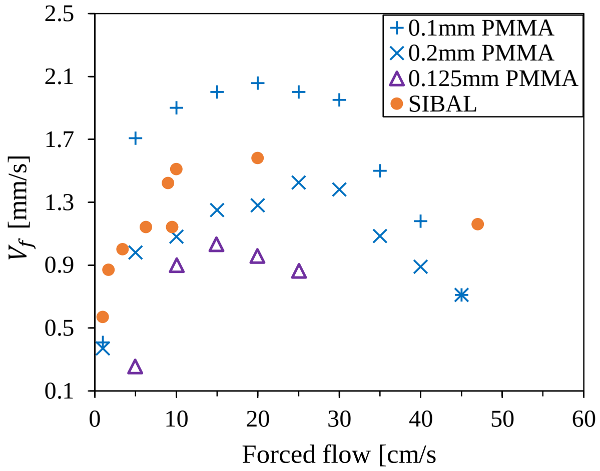

Figure 4 – Opposed flame spread rates as a function of the forced flows. The microgravity data points correspond to SIBAL fabric [77–79] and PMMA [80,81].

Analysis of flame spread in concurrent flow is more complicated than in opposed flow, because there are two length scales to consider (flame length and pyrolysis length). In general, less experimental work has been carried out with concurrent forced flows, because of the time limitations of the microgravity research platforms and the longer combustion time scales needed for the concurrent flame spread.

Flame spread results from various materials and environmental conditions are plotted as a function of a combined parameter in *Figure 5*. In normal gravity, upwards (or concurrent) flame spread tends to be acceleratory. On the contrary, in microgravity, the flame spread can be steady. Concurrent flame spread is dominated by the flame length, where convective heat transfer is dominant. The length scale is thus dependent on the forced flow [82]. As seen, the concurrent flame spread rate is linearly dependent on the forced flow.

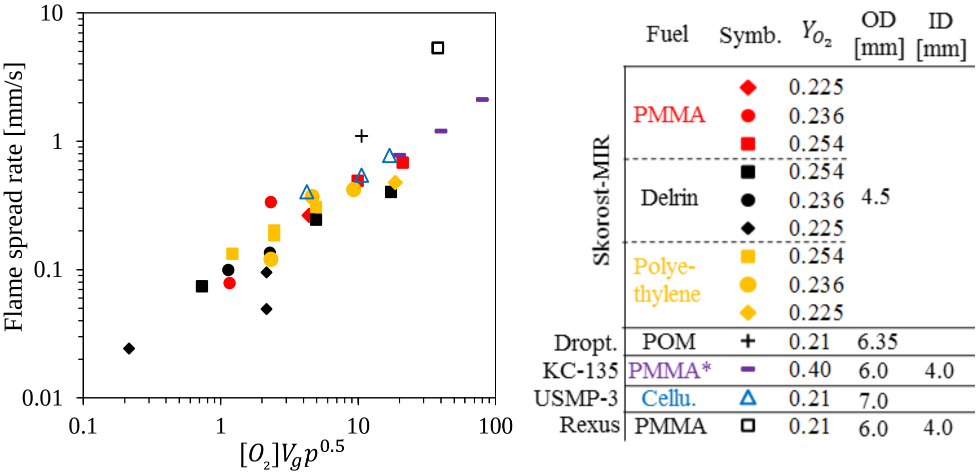

Figure 5 – Concurrent flame spread as a function of a combined parameters. The microgravity data are from various sources [83–88].

2.1.3. Near-limit phenomena

Two extinction boundary limits are defined in the kinetic and the radiative regimes of opposed flows as a function of the oxygen concentration and forced flow, namely the blow-off and the quenching (or radiative) limit. The blow-off extinction limit over thermally thin and thermally thick solid fuels in opposed flows was studied theoretically and experimentally in normal gravity by Fernandez-Pello and co-workers [18,45,51]. The Damköhler number (ratio of residence time and chemical time) was used to explain the blow-off branch. The quenching branch boundary was first found experimentally by Olson [17,18], and other researchers have also studied it [57,67,89–93]. Both branches shape the characteristic “U” shape flammability extinction boundaries, as shown in *Figure 6*. Also, the “U” shape has been found through stretch rate analysis of flame spread over cylindrical rods (PMMA) [82,94].

Extinction in the concurrent flame spread is more complex as the flame length is the dominant length scale. The mechanism leading to extinction in a concurrent flame is a combination of convective and radiative heat transfer from the leading edge to the trailing edge [95]. Also, the limiting condition of flame length is determinant as this can be affected by soot oxidation [20]. To find critical conditions leading to extinction, Torero has suggested estimating the Da and mass transfer number, B, along the flame length. However, there is still a knowledge gap related to microgravity's limiting length, and its prediction remains unresolved. Despite that, a few studies have shown that the flammability boundary limits for concurrent flame spread have a similar 'U' shape, shown in *Figure 6*.

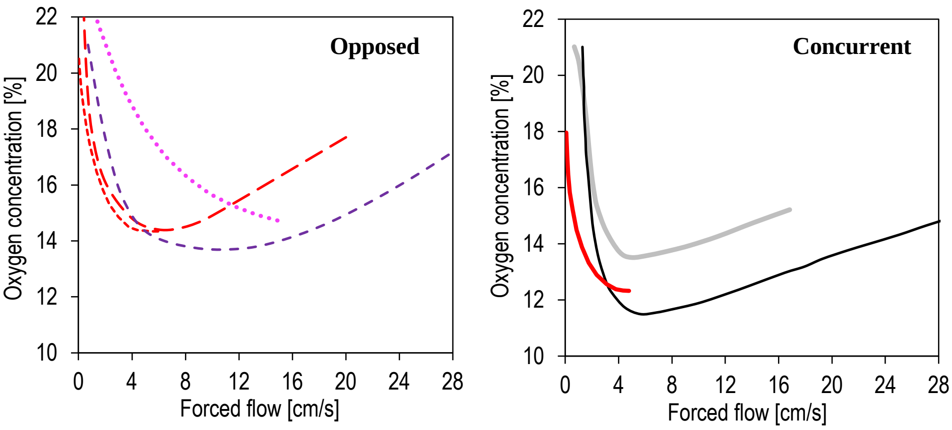

Figure 6 – Flammability boundary limits found experimentally and numerically for a cellulosic fuels as a function of the oxygen concentration and forced flow. The left pane represents the opposed case [17,18,96–99], whereas the concurrent case is plotted in the right pane [95,99].

In *Figure 6*, the extinction boundary (as a function of the forced flow and the oxygen concentration) shows a critical point (lowest condition to sustain flame spread). This point corresponds to a minimum oxygen concentration and critical forced flow that allows sustained flame spread. T'ien and his group [64,73,100,101]. Below the fundamental limit, there is no self-sustained flame spread. Thus, such a concept becomes interesting as it could be used as a threshold for flammability assessment as Fujita [12] (will be discussed in Chapter 2.4.3), but it depends on the environmental conditions and the characteristic behaviour specific materials.

2.2. External aspects that influence flammability in microgravity

2.2.1. Ambient pressure

The SSCE experiments over thin solids in a quiescent microgravity environment revealed that the flame spread rate increases with increasing pressure in microgravity. The characteristic optical depth of the flame explains the effect of pressure [90,91]. The optical depth is larger at lower pressures, where flames become cool and slower, while the optical depth decreases at high pressures. Consequently, high temperatures are achieved and thus faster flame spread. The pressure effect was also evaluated in the SSCE for flame spread over thick fuels, but no substantial difference was observed when the pressure was increased [57]. In parabolic flight experiments and numerical modelling, the pressure effect on flame behaviour as a function of the local acceleration resulted in two behaviours: Non-monotonic (U boundary shape) and linear behaviours were observed in the downwards and upwards configurations, respectively [101,102]. Olson and co-workers found that microgravity flame spread in concurrent and opposed flows over cellulosic fuels exhibited a dependency on the pressure but not on a polymeric fuel [103,104].

In work conducted in a FIST in normal gravity, the ignition delay time was found to suffer a decay with lower pressures due to a reduction in convective heat losses from the solid and critical mass flux [105,106]. Moreover, a “U” shape dependency of ignition delay time on the pressure in normal gravity was also found. The left branch (low pressure) was found to be controlled by gas-phase chemical kinetics, whereas the right branch was controlled by changes in convection heat losses and critical mass flux (high pressure) [107]. Osorio conducted experiments with fabrics in the FIST apparatus; he found that the reduced pressure effect on flame spreads over fabrics resulted in a lower flame spread rate. This behaviour is due to a decrease of heat flux from the flame to the solid surface since there is an increase in boundary layer thickness and an increase in flame standoff distance [108].

2.2.2. Normoxic

Decreasing the ambient pressure and simultaneously increasing the oxygen concentration (normoxic) for Exploration Vehicular Activities (EVA) resulted in increased flame spread opposed flows, and Olson thus pointed out the potential hazard of normoxic atmospheres [104,109]. In normal gravity, Osorio also suggested that flammability can be further extended in normoxic as the piloted ignition delay time was reduced [108,110]. However, results from microgravity experiments showed that the ignition delay time was not dependent on the partial pressure of oxygen [111].

2.2.3. Sample size

In normal gravity, the sample width affects upwards flame spread due to lateral oxygen entrainment and buoyancy; there are detailed analytical models to study the width effect [112,113]. It was predicted that for concurrent flows in microgravity, lateral air entrainment would be cancelled by gas expansion. Thus, sample width should not affect the flame behaviour [112]. This postulate proved wrong since recent large-scale experiments in microgravity (Saffire) have shown that the flame spread rate for the large samples [26,78] is lower than for the narrower samples tested during BASS-II [114,115].

Fujita suggests that the radiative effect of CO_2, soot and water affecting the heat balance at the fuel preheat zone can increase because more soot is produced in microgravity [12], especially for larger samples. However, this hypothesis cannot explain the results achieved in the large-scale Saffire tests [26,78,79], where the corresponding flame spread was much lower than for the larger samples with the same fabric fuel in the BASS experimental program. The fastest flame spread rates were achieved by an intermediate sample width (2.2 cm) under concurrent forced flows during BASS programme (competing mechanisms between side oxygen diffusion and cooling effect).

In addition, concerning the narrow samples, during BASS, the narrower samples further extended the flammability limits [114,115]. Similarly, in partial gravity experiments, the sample width affected the flame spread rate in upwards conditions [101]. The same behaviour has been reported through three-dimensional numerical modelling for thermally thin fuels [102,116,117], although Shih and T'ien [59] found a reverse behaviour in the numerical results. They reported that for the low flows close to quenching, oxygen side diffusion becomes dominant and narrower samples exhibit faster flame spread. Contrarily, for forced flows away from the quenching regime, wider samples presented faster flame spread. This reversal in behaviour can imply that the 3D model does not reproduce all the phenomena due to the simplifications made (gas-phase radiation and radiation from soot).

In opposed flows, microgravity experimental work conducted by Bhattacharjee et al. [118,119] showed that the sample width has little effect on flame spread over thermally thin fuels for a range of diluents (CO_2, N_2, and Ar). However, only with Helium was there an evident influence on the sample width due to lateral conductive heat loss. In the air, microgravity results in opposed flows, show the same flame spread rates for narrow and larger width samples over cotton/ fibreglass fabric [26,78]. These results also suggest that the sheer size of the sample fuel does not affect the flame spread for thermally thin fuels; it would only be distinctive if Helium is used as a diluent. However, contradictory behaviour was reported for thermally thick fuel in opposed flow [81,120].

As seen in the various experimental studies, the flame behaviour and flammability are also affected by the size of the sample (width). These results show the existence of critical sample width, and the current focus on an arbitrary dimension for sample selection testing might not lead to the worst-case scenario.

2.2.1. Confined spaces: Tunnel effect

As was observed during the space shuttle experiments, the tunnel rig can affect the flame spread results significantly [7]. The tunnel used was quite narrow, and the sample size was relatively small as the aim was to achieve a steady flame spread. Wang and co-workers [121] confirmed numerically and experimentally that the tunnel height has a significant impact on the flame spread in low-opposed flow due to acceleration in the thermal expansion of the gas-phase. A numerical study showed that flames over thermally thin fuels accelerated in confined spaces for low imposed flows compared to the unconfined case [116]. Shih and T’ien also conducted a numerical study where the narrow tunnel height was found to influence concurrent flame spread over thermally thin fuel by thermal expansion, flow channelling effect and radiative interaction [61].

In a three-dimensional numerical study, Shish and T'ien showed similar results, although the model did not take into account gas-phase radiation, and the kinetics were simplified [59]. They also studied the lateral heat loss and oxygen-side diffusion mechanisms from a three-dimensional flame to the adjacent tunnel wall. The influence of narrow tunnels or ducts on the solid material's flammability can translate into an increase in flammability, as demonstrated by the few experimental studies. Such an influence has a special significance in spacecraft since many materials are piled up such as in narrow ducts like the avionics bay.

2.2.2. Partial gravity

Only a few studies have been conducted addressing the effect of gravity level on the flame spread, including Lunar and Martian levels. Flame spread results with cellulosic fuels from two studies in parabolic flights [98,101,122] and in a centrifuge [123] for various oxygen concentrations and gravity levels can be seen in *Panel A* in *Figure 7*. The flame spread shows a non-monotonic behaviour for 21 and 18% oxygen concentrations at 101.3 KPa [98] and for 21% at 27 kPa [101,122] with maxima at an intermediate gravity level. For the high values of gravity level, the induced flow due to gravity level reduces the residence gas time at the expense of the chemical time (lower Da), which corresponds to the thermal and kinetic regimes. On the contrary, for the lower gravity level, surface radiation losses and oxygen transport contribute to reducing the flame temperature and hence the flame spread. This monotonic behaviour has also been found in microgravity results for opposed forced flows (BASS) [98,101,124–126]. At significantly reduced oxygen concentrations, less than 16%, the flame spread rate decreases nearly monotonically, where the oxygen transport seems to dominate over the radiative and kinetic regimes.

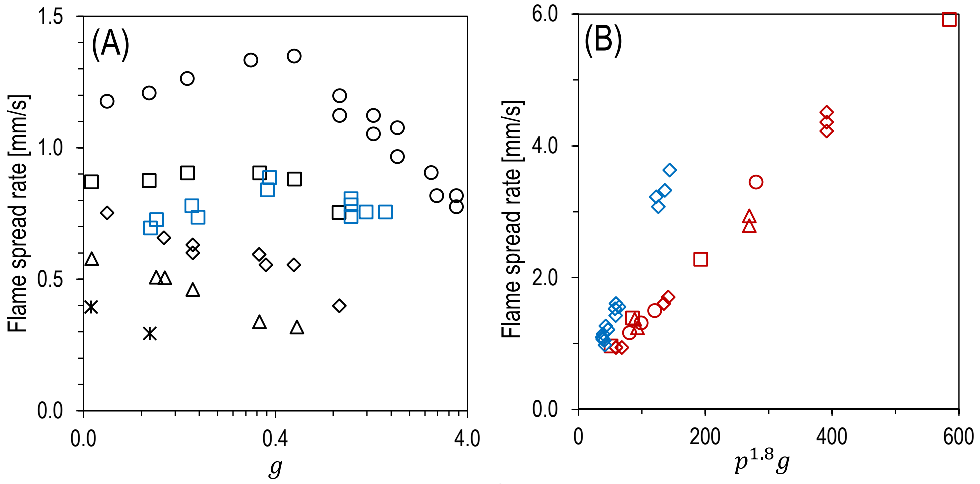

Downwards

Symb.	Y_{O_2}	P [kPa]	Width [cm]	Gravity level	[ref.]
○	0.21	101	7		[30,11]
□	0.18	101	7		[30]
◇	0.16				
△	0.15				
✱	0.14				
□	0.21	27	2		[151,61]

Upwards

Symb.	Y_{O_2}	P [kPa]	Width [cm]	Gravity level	[ref.
○	0.21	41	1	0.1-1	[61,151]
□		34			
◇		28			
△		22			
◇	0.21	28	2	0.1-0.4	[61, 151]

Figure 7 – Flame spread rate as a function of the gravity level (Pane A), and flame spread rate as a function of a combined gravity-pressure parameter (Pane B).

The results corresponding to the upwards flame spreads [101,102,122,127,128] are presented as a function of the combined effect of $p^n * g$, see Panels B and C in *Figure 7*. Based on pressure scaling/ Kleinhenz and co-workers found that a 1.8 pressure exponent resulted in a better fit of the data [127]. As predicted experimentally and with models, the flame length-scale increases with gravity or also with the forced flow, resulting in the dependency of flame spread on the gravity level [101]. Moreover, results and models for concurrent forced flow in microgravity show a similar behaviour [129,130].

The flammability boundary of cellulosic fuels as a function of the oxygen concentration and the gravity level in the downwards spread can be seen in *Panel A* in *Figure 8*. T'ien and co-workers reported the limits of a cellulosic fuel obtained experimentally through parabolic flights [131]; the minimum lower oxygen concentration seems to occur at around 0.08g, which corresponds to 7-8 cm/s buoyant flow. Sacksteder and T'ien [98] also reported experimental flammability boundary limits with Kimwipes, although only for the kinetic part. Both experimental boundaries are in contrast with the numerical flammability boundary found by Chen and Cheng [125], which has a much lower fundamental oxygen concentration. The treatment of the finite-rate kinetics and radiation through gas-phase and solid-phase seem to be behind the underestimation of the flammability limit [98].

Feier and co-workers [101] reported the flammability boundaries of cellulosic fuel in upwards, and downwards flame spread as a function of the pressure and gravity acceleration, see *panel B* in *Figure 8*. The downwards flammability exhibits a "U" shape similar to the boundary in forced flow, where the left and right branches correspond to radiative and kinetic effects, respectively. On the contrary, the upwards flammability shows lower flammability in line with results observed in concurrent flows. It is not clear whether the limit breaks down or continues for higher gravity levels due to a lack of experimental data.

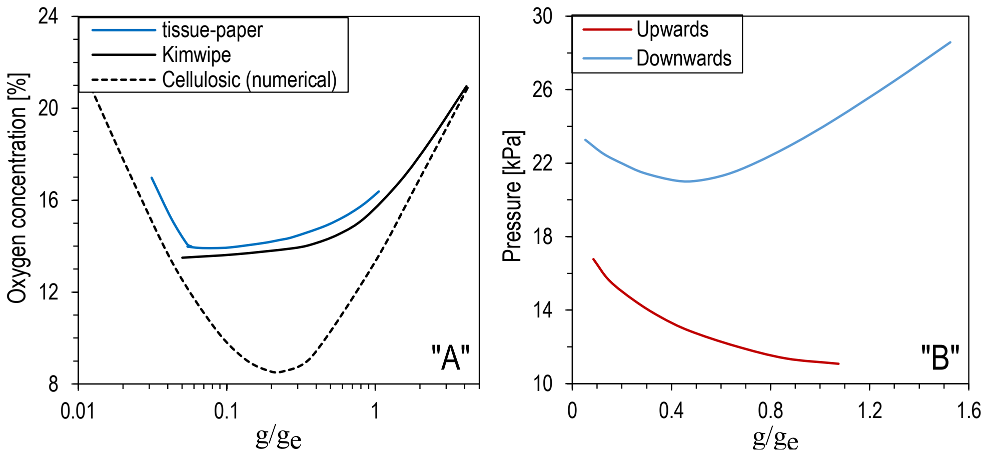

Figure 8 – Flammability limit boundaries as a function of the local acceleration level for thermally thin cellulosic fuel. Panel A depicts results in downwards buoyant flow. Panel B renders flammability limits with ambient pressure as a vertical axis [101].

2.2.3. Flow dynamics: flow boundary layer

Various rigorous analytical models (solved numerically) can predict the flame spread behaviour over thermally thin and thermally thick fuels, mostly in normal gravity [37,38,49,50]. The assumptions and simplification made in the analytical models to find a reasonable mathematical solution can limit the overall performance of such models or their application to a broad range of scenarios. One clear example is the justification of using a specific velocity profile (Oseen approximation) encountered by the leading edge of an opposed flame spread, as was done in the thermal-diffusive transfer model developed by De Ris [52], Frey and T'ien [53], and others [49,54]. In microgravity, the plug-flow has been used in theoretical models to study the opposed flame spread [67], thermally induced flows during ignition [132] and flame instabilities [133].

Numerical results have shown the importance of the flow boundary conditions for opposed flame spread in microgravity [134]. Wichman attempted to improve the plug-flow assumption and introduced a linear velocity profile in the heat transfer model, and this resulted in enhanced theoretical results for opposed flame spread [39,55,56]. Other authors used different models, such as boundary layer combustion models with fast kinetics, to characterise the velocity profile [44–47]. In microgravity environments, theoretical models also sought to improve the Oseen approximation [57,58].

The better characterisation of the velocity profile permitted to identify of the dependence of the entrance length (distance from the flame edge to the sample's upstream edge or identified as X_e) as reported by Fernandez-Pello [45]. Bhattacharjee and co-workers [43,68,69,135] also criticized the Oseen approximation, and they proposed an effective velocity profile inside the boundary layer in an improved thermal model (using a scaling approach). Their investigations predicted the effect of the velocity boundary layer (for that matter, also the entrance length) well quantitatively, and this was demonstrated through microgravity results in the kinetic regime [70,136,137].

The Oseen approximation was also used in theoretical models to describe flame spread under concurrent forced flows in normal gravity [40,41,49]. In order to study truly steady flame spread conditions, the effect of the entrance length in concurrent forced flow can be purposely eliminated [42]. A similar approach can be found for opposed flame spread [66]. Recent thermal models have improved the velocity profile substantially in microgravity, proving a more precise description of the flow field for flame spread investigations by T’ien and his group [59–62,71–73].

The effect of the entrance length (as a parameter) on the flame spread was investigated numerically for opposed and concurrent forced flows [63,64]. The worst-case scenario was found to occur with shorter entrance lengths as this influences the effective flow velocity encountered by the flame front. In the recent Saffire experiments, it was found that the effective flow (velocity boundary layer) influenced the concurrent flame spread over a Sibal fabric [36]. During burning, the fabric left an unburnt inert material that causes an entrance length to increase over time, and thus the effective flow profile. A three-dimensional numerical model confirmed the Saffire tests results and the effect of the boundary layer [79].

2.2.4. Instabilities

The fingering flamelet phenomenon is defined as a thermal-diffusion instability, and it was studied experimentally using a thin paper under opposed forced flow in normal gravity by Zik and Moses [138]. Olson [139] also defines the flamelets as instability near the quenching extinction boundary due to changes in oxygen diffusion and convective flow patterns. That is, an established two-dimensional flame breaks up into various three-dimensional flames. Olson and co-workers [96,140] studied the fingering flamelets over a thermally thin paper in the Narrow Channel Apparatus (NCA).

In microgravity, flamelets were observed over thin paper by Olson et al. [96], who established flammability maps drawing extinction and flamelet limits. It was found that the material flammability could be extended by the flamelet regime (lower forced flow and oxygen concentrations). In smouldering, finger-like phenomenon can also occur, and it was experimentally studied in microgravity [133,141–143]. Physical explanations point to the oxygen mass transport via gas-phase convection/diffusion [133]. However, Ronney [144] provides further physical explanations based on the estimation of the Lewis number. In a recent experiment with a thermally thick sample under opposed forced flow in microgravity [145], fingering flamelets were observed to transition from a two-dimensional established diffusion flame (in the radiative regime).

2.2.5. Surface features

Eigenbrod and co-workers conducted experiments in microgravity and found out that flame spread can be enhanced due to structures in the solid surface of a cylindrical sample [88]. An empirical model was presented to predict the flame behaviour, but the model requires further refinement. Over structured flat samples, the flame spread was reported to be faster along the groves than in the flat sections of the sample [26,77,146]. A recent experimental and numerical study with cardboard found a similar behaviour [147]. These results suggest that flame spread and flammability might be enhanced over structured surfaces, especially along the grooves, which merits further study.

2.3. Methodology to study flammability of solid materials in microgravity

Conducting solid combustion experiments in microgravity environments on Spacecraft is severely limited (financial, space and logistic constraints), but there are platforms on Earth where microgravity can be achieved. Each research platform has its constraints and capabilities. Consequently, choosing a platform depends on the flammability problem to be studied (ignition, flame spread, smouldering, soot, etc.), the environmental conditions and the diagnostics used for measurements.

All these aspects will be discussed in the following sections. First, the up-to-date available research platforms used for solid combustion research in microgravity are introduced and discussed according to their available time, microgravity levels and flexibility. The second section presents the spatial capacities of the combustion chambers used in various research platforms. The third section then provides an overview of the flammability phenomena that have been studied according to the microgravity research platform and type of material. Finally, the diagnostic systems used in the research platforms are reviewed in the last section.

2.3.1. Research platforms

To achieve true microgravity ($g/g_e = 10^{-6}$), one must be placed at a distance of 17 times the distance from the Moon to Earth (6545 km in total). Spacecraft and satellites are orbiting around Earth experience "apparent" microgravity, resulting from the Earth's gravity force and centrifugal force. It is in the same order as true microgravity [16]. Apparent microgravity can also be obtained in free fall. Reduced gravity levels such as those obtained in Spacecraft are not readily achievable on-ground facilities on Earth.

Apparent microgravity can be obtained in several ground-based platforms and Spacecraft, such as drop towers, parabolic flights, sounding rockets and spacecraft orbiting Earth, and microgravity combustion research has taken place in all of these. Various gravity levels can be achieved in the different platforms that have or are being used, see Figure 9. However, it must be noted that the gravity levels offered by the research platforms can vary and are not consistently reproducing the same levels as in spacecraft. A reduction in gravity or buoyancy translates into a reduction of convective heat losses from the gas-phase to the environment.

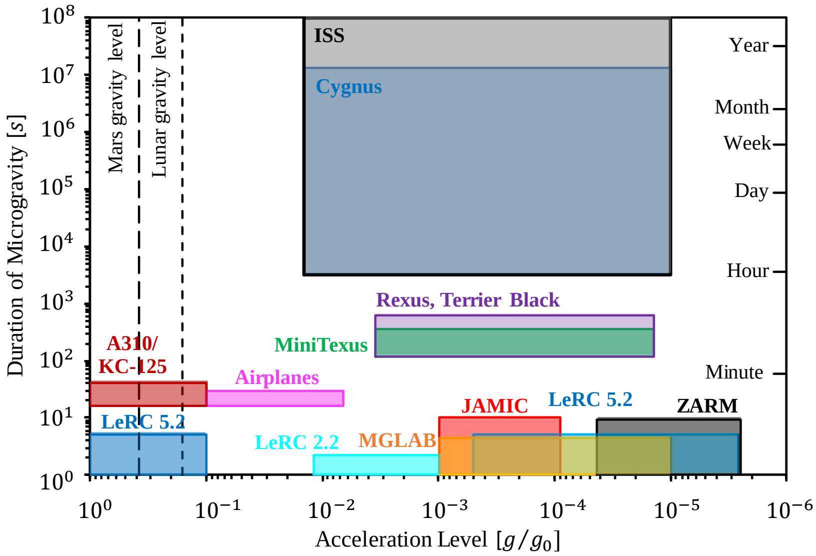

Figure 9 – Characteristic acceleration levels and duration in the microgravity of different platforms and microgravity laboratories. Adapted from [16,148]. *Not completely up-to-date for all platforms in use.*

As shown in Figure 9, the most frequently used platforms for microgravity combustion research are drop towers and parabolic flights. This is primarily due to their relative ease of operation and the relative low-budget associated with operations compared with other platforms. The number of publications with experiment studies taking place on spacecraft platforms is relatively moderate. Despite the logistic difficulties to research such a platform, the need for fundamental studies has driven experimental work on spacecraft. Sounding rockets and satellites are not as widely used because they entail operational difficulties and do not offer high productivity. Lastly, there is no strong appetite for centrifuge experiments with large gravity accelerations. The corresponding references to the platforms employed in solid combustion research in microgravity are listed in APPENDIX A.

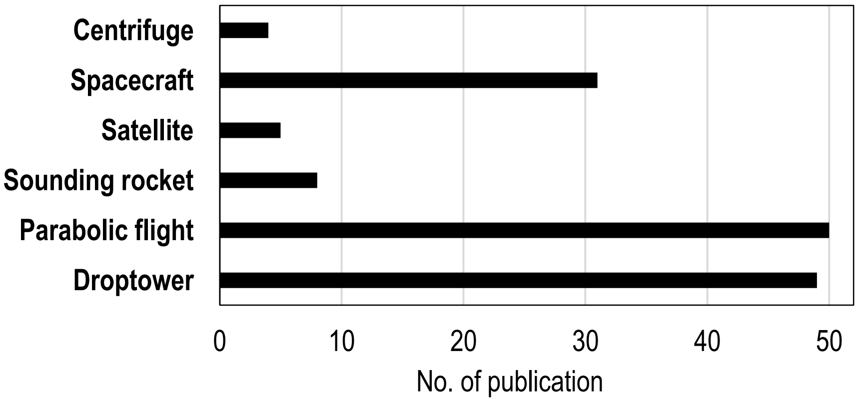

Figure 10 – Number of publications where the various research efforts from ground-based and spacecraft platforms were reported for solid combustion research from the 1960s. Experimental or experimental studies in combination with numerical investigations were counted.

2.3.1.1. Drop towers

In the late 1950s, Kumagai and Isoda [149] used a drop system for the first time to study liquid droplet combustion. As with the spacecraft development technology from the 1970s to the ISS assembly, a range of drop towers was established worldwide in the same period. These research capabilities have not developed further, with a couple of exceptions driven by the Chinese Space programme [121] and higher productivity requirements.

NASA was the first to build drop towers, and these two have been widely used since the early 1960s. In the 2.3-second drop tower (NASA Glenn Research Centre), the hardware and the rig are protected by a shield due to the aerodynamic drag. Initially, the experiment encountered a problem related to shock load (100g) when the hardware approached the bottom of the drop [9]. This issue was solved by an air-bag decelerator installed in the facility at the beginning of the 1990s when the drop tower suffered significant renovation [150]. In the 5.2-second drop tower, the undesired drag forces were removed by evacuating the drop in low pressure or vacuum (13 Pa). Due to a catapult system, it has recently been proposed to undergo an upgrading renovation that will extend the microgravity duration. Moreover, the maximum load of the hardware will also be increased along with a higher number of tests that will be performed daily.

In 1992 the drop tower in JAMIC (Japan Microgravity Centre) started operations [151], and further microgravity combustion research was implemented in Japan. The JAMIC drop tower offers 10 seconds of microgravity, the longest drop worldwide, and provides lower gravity levels since it uses a double capsule in the hardware. Other drop towers in Japan are the drop shaft or MGLAB (Microgravity Laboratory of Japan) in Gifu [137], a drop tower located at HNIRI (Hokkaido National Industrial Research Institute), the COSMOTORRE drop tower located at the University of Hokkaido, and the drop tower at HASTIC (Hokkaido Aerospace Science and Technology Incubation Center).

In Europe, the only drop tower used for combustion research is located in Bremen. It is commonly referred to as the ZARM (Center of Applied Space Technology and Microgravity) drop tower constructed between 1988 and 1990. The 110 m of free fall within a vacuum shaft (10 Pa) initially provided 4.65 seconds of microgravity. A catapult system was added later and allowed the drop tower to extend its microgravity duration to 9.3 s [152]. A second and smaller drop tower is being built at ZARM, which will offer a shorter microgravity time (2 s) but with a high yield of tests per day.

The drop tower at NMLC (National Microgravity Laboratory China) is also used in microgravity combustion research [153]; it can obtain 3.5 s of microgravity during 83 m of free fall. An additional drop system provides 2.3 s of microgravity [154].

Drop towers offer good microgravity acceleration levels that are very close to those characteristics in spacecraft. Besides, the maximum hardware load in the various drop towers ranges from 100 to 2100 kg, allowing the installation of effective diagnostic systems. The number of experiments that can be executed per month is 40 to 160, or potentially even higher, hence, allowing considerable parametric studies. In *Table 2*, the most important technical specifications for all drop towers are listed. The only drawback of this platform is the short microgravity duration that is, in most cases, insufficient to attain a steady problem (e.g. a steady flame). Thus the researcher is restricted to certain material and flammability phenomena.

Table 2 – Characteristics times and specifications for different drop towers used for microgravity combustion research.

Drop Tower	Duration [s]	Max hardware load [kg]	Tests per day
NASA Glenn Research Centre	2.2	125	8-12
Zero Gravity Research Facility*	5.2 (9.9)*	450 (2100)*	1-2
JAMIC	10	1000	3
MGLAB	4.5	400	6
HNIRI	1.2	100	-
HASTIC-COSMOTORRE	3	400	-
ZARM	9.3	100	3
ZARM 2nd tower§	2	-	50-60
NMLC	3.5	630	2-4
Drop system	2.3	-	-
****The 5.2 s drop tower is undergoing an upgrade and the microgravity duration will be extended.***			
§ A new drop tower is being built.			

2.3.1.2. Parabolic flights

Another widely used platform for microgravity combustion research is aeroplanes flying in parabolic (Keplerian) trajectories. This method can achieve longer microgravity times (15 to 40 s.) than those in drop towers, though with higher gravity levels ($5x10^{-2}$ to $75x10^{-2}$ g). Lunar (0.16 g) and Martian (0.38 g) gravity levels can also be achieved. Further reduced gravity levels can be achieved if the rig floats freely during the parabolic trajectories and the duration of microgravity is reduced for such experiments. One major challenge associated with parabolic flights is that g-jitter effect due to vibrations of the aircraft during the parabolic flights might influence the results [98].

NASA initially used a Learjet Model 25 aircraft (at Lewis Research Center) that could provide only six trajectories per flight. This aircraft was later replaced by a DC-9 model in 1995 [150], providing up to 40 trajectories per flight. The KC-135 turbojet (Lyndon B. Johnson Space Center) can supply the same amount of trajectories. In Europe, CNES (Centre National d'Etudes Spatiales) began using a Caravelle aircraft for microgravity research. It was replaced by an Airbus 300 until it in 2015 was replaced by an Airbus 310 model, which Novespace currently operates. The A310 flights typically provide 31 trajectories. In Japan, DAS (Diamond Air Service) operates the Mitsubishi MU-300 and Grumman Gulf Stream II aircraft for microgravity combustion research at the Parabolic Flight Center; both can provide 8 to 15 parabolic trajectories per flight. In Russia, a private company, Atlas Aerospace, offers parabolic flights aboard an Ilyushin II-76 airlifter at the Gagaring Research and Test Cosmonaut Training Center has a dedicated Ilyushin IL-76-MDK for microgravity research [1]. No research in solid combustion has been reported from the last two aircraft. The available parabolic flights are listed in *Table 3*.

Table 3 – The Currently operative companies that are offering commercial parabolic flights.

Company	Aircraft	Number of parabolas per flight
CNES (France)	Airbus310	31
DAS (Japan)	Mitsubishi MU-300	8
	Grumman Gulf Stream II	15
Atlas Aerospace (Russia)	Ilyushin IL-76	ND
	Ilyushin IL-76-MDK	ND

2.3.1.3. Sounding rockets

A sounding rocket can provide much longer microgravity times than the platforms presented previously, and microgravity can be for as long as 300 seconds. The experimental payload, 150-400 kg, must, however, withstand quite critical gravitational forces (10-40g) during take-off and landing [9]. The first sounding rocket used for microgravity combustion research was the MiniTexus 3 at the beginning of the 1990s [86,155]. Later on, MiniTexus 6 [20,156] and the larger sounding rocket version, Texus 38 [157], were also used. Both are part of the sounding rocket program run by the European Space Agency (ESA) and the German Space Agency (DLR). For the DARTFire testing programme (Diffusive and Radiative Transport in Fire Experiments), NASA used four Terrier-Black Brant sounding rockets [120,158–161]. A sounding rocket as part of REXUS European program was recently utilised for flame spread investigations of PMMA rods [88].

2.3.1.4. Satellites

Free flyers such as the non-crew Satellite can be used to conduct combustion research. This platform also offers an extended period of microgravity and adequate gravity levels. The Chinese Academy of Science has used a recoverable satellite "Shi-Jian" (SJ), to conduct various scientific experiments across a range of fundamental topics. The SJ-8 and SJ-10 were launched in 2006 and 2016 and hosted tests looking at ignition, smouldering and flame behaviour [162–164].

2.3.1.5. Spacecrafts and space stations

Spacecrafts can provide the most extended duration in microgravity conditions. Yet, experimentation in this type of platform is more challenging, primarily due to the substantial financial, technological and logistic constraints. Some of the missions of the space shuttle program (STS-USML) also hosted dedicated test programs and innovative hardware, such as SSCE (Solid Concurrent Combustion Experiments), RITSI (Radiative Ignition and Transition to Spread Phenomena), WIF

(Wire Insulation Flammability), FFFT (Forced Flow Flame Spread Test), candle experiments and smouldering tests [92,165–168].

The ISS currently has the Microgravity Science Glovebox (MSG), where various experimental programmes have taken place (BASS & GEL) [82,170,171]. Skylab was the first space station to host a laboratory for fire experiments [15]. A few experiments also took place in more extended permanent inhabited space stations, such as MIR, using the PRIRODA hardware [169].

In the near future, the ISS will offer many more opportunities since it will host new facilities for microgravity combustion research, such as MWT, SoFIE (Solid Fuel Ignition and Extinction) and SCEM (Solid Combustion Experiments Module). The ongoing Saffire (Spacecraft Fire Experiments) experimental series takes place in the ISS supply vehicle Cygnus after delivery of the payload [25].

2.3.1.6. Centrifuge

A centrifuge can be used to achieve higher gravity levels than Earth's, NASA used one for the first time for flammability studies [29]. The Japanese Space Agency (JAXA) has a centrifuge rotating arm which has also been used for flammability experiments [172]. It has been demonstrated that buoyancy effects at higher gravity levels than Earth's can provide useful data in order to correlate flame spread from microgravity to several gravity levels [123]. NASA has recently expanded its capabilities to produce Martian and Lunar gravity levels in their drop tower. A centrifuge (drop bus system) can be allocated inside the 5.18-second drop tower [173,174]. As a result, Lunar and Martian gravity levels can also be achieved in the drop tower and parabolic flights. However, the Lunar and Martian gravity time provided is short, and only specific phenomena with very short characteristic times can be studied.

2.3.2. Volumetric capacity

Different apparatus and combustion chambers have been utilised since the first microgravity combustion experiment on solid fuels. The platforms' capabilities can severely restrict the volumetric design of chambers of tunnel rigs where the combustion experiment takes place. Thus, the scientific objectives for any combustion project can also be limited.

Figure 11 depicts each microgravity research platform's characteristic times as a function of the sample size and volumetric capacity from various research projects conducted thus far. As seen in some of the drop towers, the volumetric capacity is large (NASA), but the specimen size still cannot be larger than 110 cm^2 due to the microgravity time restriction. In parabolic flights, rigs are restricted in size, and the sample size is also small. On other platforms (satellites, sounding rockets and other spacecraft), the volumetric capacity of the rigs is not improved, and the hosted samples are comparatively small, e.g. BASS (1 L). On the contrary, the Saffire rig tunnel has a much larger volumetric capacity. Given the longer microgravity times and the large volumetric capacity of the oxidiser, larger samples can be burnt. Similarly, the planned MWT can host mid-size specimens.

Another aspect to take into account is the productivity of each platform. Drop towers offer a high yield of experiments for parametric studies. Parabolic flights can also provide enhanced productivity. However, other platforms, especially spacecraft, do not provide such flexibility. Future rigs such as MWT, SoFIE and FLARE will offer much higher flexibility than previous rigs used on spacecraft. Thus, selecting a microgravity platform depends on the type of problem studied, the sample dimensions and the required environmental conditions. For example, flame spread over an infinitely thick slab, spontaneous ignition or smouldering through porous media should be studied using spacecraft platforms.

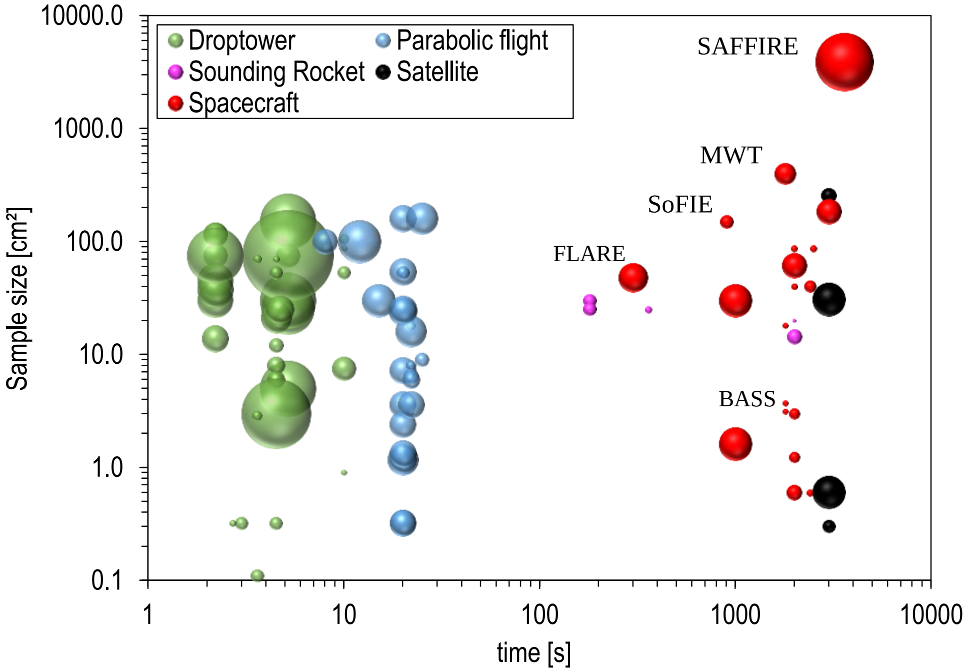

Figure 11 – Characteristic times and sample size in various experimental rigs and microgravity research platforms. The data point size depicts the tunnel rig volume of the experimental environment. The corresponding references for the graph depicted in Figure 11 can be found in APPENDIX A.

2.3.3. Phenomena and solid fuels tested

This section discusses which flammability phenomena have been studied in each microgravity research platform and which materials have been used. The goal is to identify which flammability phenomena can be studied in each platform. Following the definition provided in Chapter 1, the flammability behaviour of solid materials on spacecraft is defined by ignition, flame spread, near-limit and smouldering. For observation of those phenomena, it is often essential to quantify the soot production, burning rate and heat release rate.

Ignition can be divided into piloted and spontaneous. For the former, a small flame or ignition wires can act as the pilot; the latter is the predominant technique used in microgravity experiments. In the case of spontaneous ignition, it can be due to conduction through solid-phase from overheated wires (for wire jackets) or in a hot environment. Ignition due to intense radiative heating is also considered spontaneous ignition. For flame spread, three main scenarios studied in solid combustion are flame spread in quiescent conditions (no forced flow) and under forced flow – opposed or concurrent.

Figure 12 depicts the number of publications per flammability phenomena studied in microgravity. In some publications, more than one phenomenon was reported on various platforms. Therefore, some duplicities and the total number of publications per platform do not coincide with *Figure 10*. Across all microgravity research platforms, the most studied flammability problem is flame spread. In drop towers, most studies have been reported for flame spread under quiescent or opposed forced flows. The characteristic time to establish a steady flame in such conditions can be achieved by employing thermally-thin fuels. It is difficult to attain a steady-state for concurrent flame spread experiments in drop towers [16], unless an extremely thin fuel is used or one with very low density. A similar trend is observed in parabolic flights and satellites, where most flame spread studies focus on the opposed case or quiescent conditions. Steady concurrent flame spread can be achieved on spacecraft as longer microgravity times are provided.

Near-limit phenomena have mostly been studied in parabolic flights and primarily for opposed forced flows. Studying near-limit requires longer microgravity times and also a high yield of experiments. The flammability limits or extinction limits, more than being physical parameters, map the regions where flame spread cannot be sustained.

As seen in *Figure 12*, the extinction boundary limits of various materials have been reported in several publications. These extinction limits can be a function of the oxygen concentration, the forced flow, the pressure level, the gravity level and other parameters. They are essential since the drawing of both branches of the limits (quenching and blow off) can help to determine the critical conditions at which flame is viable, where both curves collide, and hence the flammability of the material associated with the environmental conditions can be ranked [12].

It is somewhat surprising that ignition has received less attention, given that NASA's prevention strategy relies on reducing the likelihood of ignition [1]. Most ignition studies have taken place in drop towers and parabolic flights, with only a very few on spacecraft platforms. This is due to the fact that ignition studies often require a rather substantial experimental matrix. It is also to be noted that spontaneous ignition has received little attention, and smouldering has only been briefly studied on spacecraft. The characteristic times for the latter are notoriously long (>1000 s) and can thus only be achieved on spacecraft. Spontaneous ignition leading to smouldering has not been reported.

Another phenomenon that has not received much attention is soot measurements, an essential aspect of the radiative transport phenomena for flame spread. Only very recently studies on soot formation over insulated wires have been conducted [175–179]. Burning rates are very challenging to measure using traditional gravimetric techniques in microgravity environments. The only visual diagnostic can be used to measure the mass loss of solid-materials. Thus, only a few studies have been reported on burning rates. Lastly, heat release rates have not been studied parametrically, and only a few studies have been reported. Parameters associated with gases concentrations, combustion and burning of the solid material have been reported in a few publications, as seen in *Figure 12*.

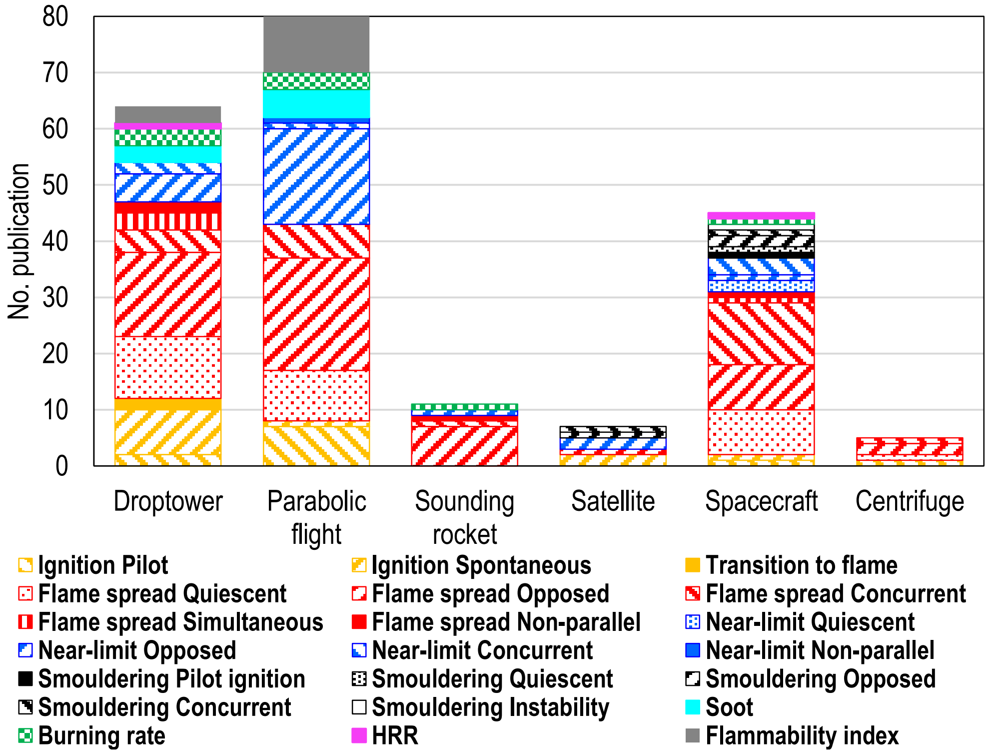

Figure 12 – Flammability phenomena studied in each microgravity research platform per number of publications. The studies selected to create this figure are experimental work and experimental accompanied by numerical studies. The corresponding references can be found in APPENDIX B, APPENDIX C, APPENDIX D, and APPENDIX E.

As seen in *Figure 13*, a range of materials has been tested in microgravity for solid combustion research so far. Among these materials, there are thermoplastics (PE, PP, PS, PVC, Nylon, etc.), some thermosetting plastic (polyester, PUR, silicone, neoprene and rubbers), organic polymers such as cellulosic materials (wipes and paper) and cotton fabrics, flame-resistant fabrics made of synthetic polymers (Nomex$^{®}$, Kevlar$^{®}$ and Conex$^{®}$), a few composites and other polymers. Many of the materials depicted in *Figure 13* are found in various applications on spacecraft. While testing them in microgravity provides direct information on their flammability behaviour, many materials have been investigated for fundamental studies. One example is a candle tested aboard Mir and STS [3,7], or wax on Skylab [180]. For fundamental studies, the most widely used solid fuels are cellulosic fuels and thermoplastics (Polymethyl-methacrylate and polyethylenes).

Cellulosic charring fuels are mostly used in drop towers, where steady phenomena can be achieved (opposed flame spread) or where characteristic ignition times are easily achieved. Using an extremely thin cellulosic fuel for concurrent flame spread would allow for achieving steady conditions [180]. Alternatively, if one wants to evaluate the flame spread over an infinitely thick fuel, then polyphenolic or a PUR foam slab would be ideal [181,182]. PMMA, as a thin and thick flat sample (Biot number definition in thermal behaviour) and as rods and spheres, is by far the most tested fuel as it has stable properties and does not char. As seen in *Figure 13*, researchers preferably use PMMA to study the flame spread and near-limit across several platforms, especially in parabolic flights and other platforms with longer microgravity times (ideal for thermally-thick samples).

Notably, spheres of PMMA, and other thermoplastics (PE and PS) have been used intrinsically to study the burning rate [183,184]. A few studies also report that the burning rate and heat release rates have been measured or empirically determined. Electrical wire insulation is another type of material tested for ignition and flame spread, mainly in parabolic flights. The wire jackets tested are polyethylene, thermoplastics compounds with ethylene and other polymers. Only a few studies focusing on soot have only been reported with PMMA and LDPE wire jackets as solid materials [175–177,185]. For smouldering studies, foams (PUR) fuels have been selected, given their porous properties [186].

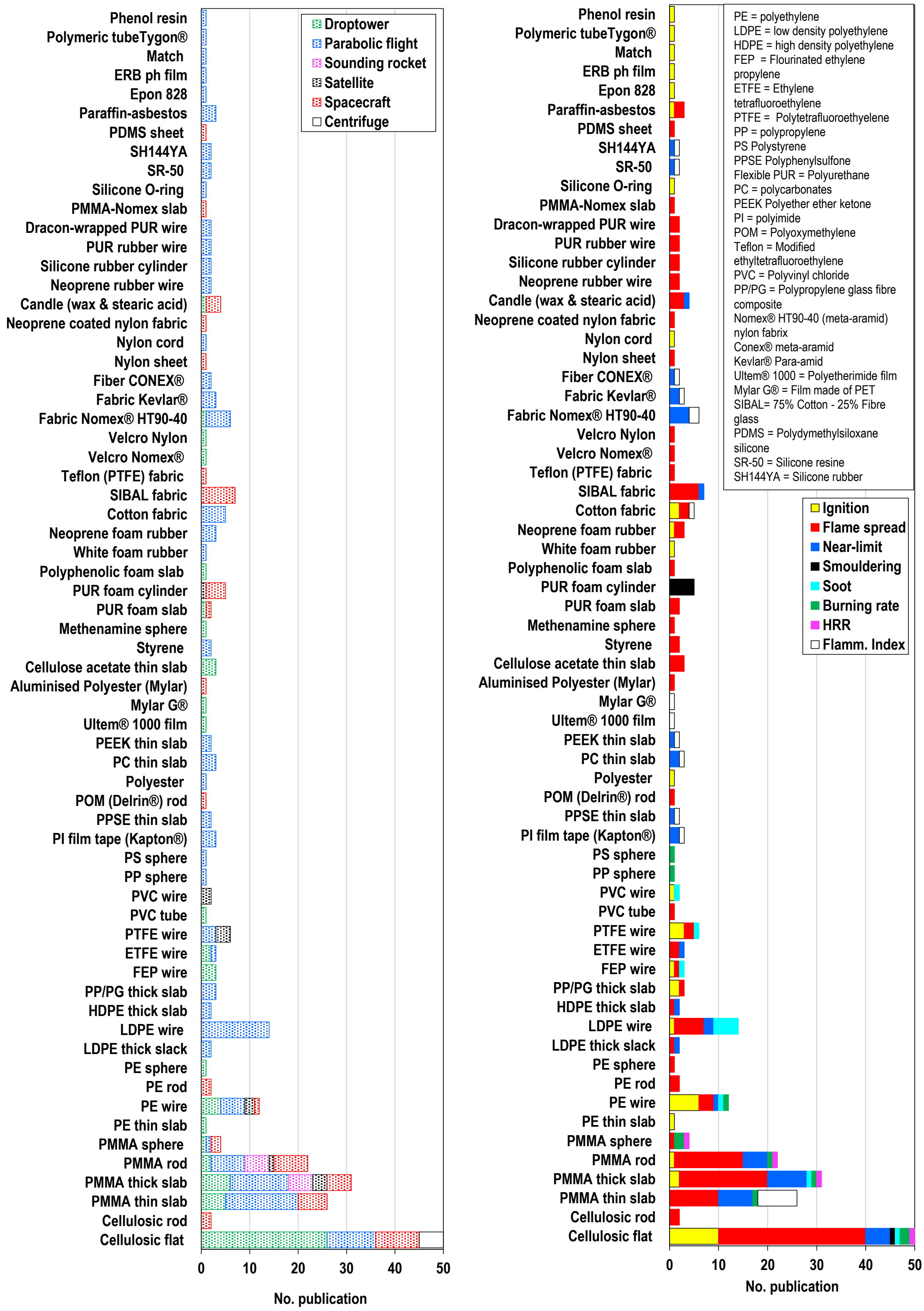

Figure 13 – Materials studied in previous solid combustion investigations in microgravity per number of publications. On the left, the number of publications per material is segregated further into the research platform where the material type was tested. On the right, the segregation is done per

the flammability phenomena studied. The corresponding references can be found in APPENDIX B, APPENDIX C, APPENDIX D, and APPENDIX E.

As seen previously, the database of materials tested in microgravity is somewhat extensive, and new materials have been recently added. However, not all materials used on spacecraft have been tested yet in microgravity [187]. Extending the database is in line with NASA's decadal review recommendations [1], where it was encouraged to test more complex materials (composites and new materials).

2.3.4. Diagnostic systems

Conducting experimental research often requires dedicated diagnostic systems to measure the parameters of interest. Using a specific diagnostic system or measuring tool depends on the objective of each fundamental study. In microgravity combustion research, each research platform's limitation can affect the choice of diagnostic procedures. The interest in ignition, flame behaviour and smouldering relies on obtaining the gas-phase and solid-phase temperatures and visual recordings of the phenomena. Notably, for flame behaviour studies, it is crucial to quantify and characterise the flame geometry, the velocity profile around the flame and the soot distribution (for sooty flames). In the case of soot, sophisticated diagnostics are employed to provide the soot distribution and morphology. For measurements of the mass loss rate, as it is impossible to perform gravimetric measurements in microgravity, other methods (visual) to track the regression rate have to be used.

2.3.4.1. Temperature measurements

For temperature measurements, the most straightforward technique is using thermocouples. Gas-phase and solid-phase temperatures are needed to estimate the heat balance and assess the flame's behaviour over the solid fuel in different environmental and thermal conditions. The discrete use of thermocouples is an easy way to obtain accurate gas-phase temperature. These have been used in several experimental programs across all research platforms, see APPENDIX C. Nonetheless, solid-phase temperature measurements can be affected by the gas-phase because the solid surface retracts [130]. Moreover, there is a lack of accuracy in precisely determining the temperature gradient, which adds inaccuracies to estimating the heat back from the flame at the fuel surface [188]. Consequently, other diagnostic systems to measure or qualitatively analyse the temperature and temperature changes in the gas-phase and solid-phase have been used. These methods are holographic interferometry [28,137,189–192], rainbow Schlieren [98] and infrared cameras (IR) [88,101,156,157,189,193–195]. For IR cameras, a bandwidth from 3.8 to 4.28 μm to filter the radiation from the gas-phase is required to provide the solid-phase temperatures. These techniques allow quantifying the characteristic solid-phase lengths (pre-heat length and pyrolysis length) and the gas-phase lengths. Other diagnostic techniques can provide accurate temperature fields within the diffusion flame based on the soot characterisation and quantification, these methods will be discussed later.

2.3.4.2. Visual measurements

Characterising ignition occurrence, flame geometry (flame length, standoff distance), and how it evolves to determine the flame spread rate can also be obtained through the most common visual diagnostic, video and photographic cameras and more sophisticated cameras. Compared to the first photographic cameras used in the first microgravity experiment 70 years ago, the current cameras offer a substantially better characterisation. The 16 mm motion camera used in the first microgravity research in the Skylab could not detect the dim-blue flame characteristic microgravity environments (diffusion-radiative regime), so that had to be directly observed by the operators [15]. Research conducted during the 70s to 90s in drop towers and parabolic flights used colour cameras with 100 to 400 fps, considered high-speed at the time [14,17,97,196–200]. From the 90s onwards, the introduction of cameras with CCD (Charged Couple Device) sensors has become dominant in the research conducted nowadays across all microgravity research platforms (See APPENDIX B and APPENDIX C). This technology has enabled the video cameras to obtain sharper images for each frame obtained to the detriment of the more considerable amount of frames obtained.

2.3.4.3. Flow-field

The measurement of flow-field velocities in microgravity combustion research can be challenging given each research platform's constraints. A pulse-smoke wire technique was used during drop tower experiments [18]. Other systems that have been used are Particle-Image Velocimetry (PIV) [201,202] and Laser Doppler velocimetry (LDV) [156]. Both systems have been used in only a few experiments owing to the difficulties of seeding the flow. A less complex option is using a hot wire anemometer.

2.3.4.4. Soot quantification

The quantification of soot can be done by providing global properties (characteristic residence time, luminous flame length, smoke point) of a jet diffusion flame. Detailed spatial quantification of soot can be used to extrapolate soot temperatures and temperature gradients within the flame. Most of the diagnostics for soot studies, whether complex or modest, have focused mostly on gaseous-jet diffusion flames, as will be discussed in the following, as it can be very useful for diffusion flame problems arising from condensed-matter, as well.

Sunderland, Urban and co-workers [203,204] employed simple video cameras or CCD cameras to reveal the global properties of diffusion flames in microgravity experiments. Fujita [205] used a conventional video camera to qualitatively discuss the soot formation on microgravity diffusion flames established over a paper sheet and butane gas jet diffusion flame. However, other complex techniques are needed to provide spatial quantification of soot formation.

Light extinction (or laser attenuation) is a widely used technique to quantify aerosol particles by using the Beer-Lambert law [206]. The principle behind the method relies on the scattering of light through saturated media; the beam light is absorbed, reflected and transmitted through the body of particles (in this case, soot in diffusion flames). The ratio of absorbed light to incident light defines the extinction factor (If transmitting is the dominant phenomenon). This non-intrusive technique can be used to determine soot volume fraction within the flame, and it allows for evaluating soot formation. The volume fraction is a useful property in sooty flames because it affects the amount of radiative heat transfer [207]. The first techniques were based on point-by-point analysis of the soot field (highly time-consuming), while an improved method based on optical tomographic reconstruction was developed by Greenberg and Ku [207] to describe a spatial (two-dimensions) soot volume fraction. This full-field laser-light extinction technique was used to quantify the soot volume fraction of axisymmetric laminar gas-jet diffusion flames [208–211]. Recently, the technique was used to study the soot generated during the transition from ignition to flaming over wire jackets in microgravity [212,213].

These methods did not account for the luminosity changes under the effect of forced flows, which can affect soot oxidation, and they were thus not ideal for describing such a flame type [185]. Fuentes et al. [185] used a two-dimensional extinction method based on Bouguer's law [214] for estimating the extinction factor in a boundary-layer established diffusion (non-axisymmetric) flame over a solid fuel. In their method, the light beam emitter is a green LEDs. This scattered light passes through the flame, and then it is received by a monochrome CCD camera with a filter for soot bandwidth. To estimate soot concentration from their method is not straightforward as flames are three-dimensional; corrections are required [185]. Later, Legros et al. [215] corrected the diffusion flame's three-dimensional effect by using chemiluminescence with a tri-CCD camera and a line-of-sight light attenuation technique. In their work, they tracked the soot and chemiluminescence with three cameras with the corresponding bandwidth filters (one for soot and the other for chemiluminescence). This method allows measurements from multiple directions (opposite to extinction measurements). Thus, corrected local soot concentrations are obtained, and soot volume fractions can be estimated. Fuentes used the same method to study the soot trajectory [216]. With the appropriate filter, intensified UV cameras can also be used to track the chemiluminescence and soot, as it was used in the past for flames over solid fuels [120].

Fuentes et al. [217] used chemiluminescence measurement along with laser-induced incandescence to provide the soot volume fractions. In the laser-induced incandescence (LII) method, a laser sheet is emitted and passes through the flame; this laser energy excites the soot particles (intrusive). Then, an intensified charge couple device (ICCD) camera with a filter collects the images. For chemiluminescence measurements, another ICCD camera with its corresponding filter is needed. This method has some complications associated with the laser affecting the soot particle's radiative heat for soot temperature extrapolations [218]. Another technique with non-intrusive laser levels is the Modulated Absorption/Emission (S-MAE) technique, which can provide soot volume fraction and soot temperature measurements [219]. Guibaud and co-workers [218] extended the S-MAE technique with improved optics settings (LEDs with broadband tools) to create the broadband absorption/emission (B-MAE) technique, which requires less space than S-MAE and can fit the spatial constraints of parabolic flights [218]. The B-MAE technique implements Tomographic Three Colour Spectrometry, where a tri-digital CCD camera collects the red, green and blue intensities emitted by the soot (has three spectral bands to discriminate those colours). Thus, spatial (2D) measurements of volume soot fraction and soot temperature can be estimated with the corresponding numerical post-processing tools, as they did on opposed flame spread over PE insulated wires in microgravity [175,177–179].

Another simpler and more affordable technique is the Colour-ratio pyrometry, which can track soot formation and temperature changes within the flame. Ma et al. [220] used that technique on gaseous co-flow flames in the Microgravity Science Glovebox (MSG) on the ISS. Similarly, the RGB pyrometry technique with affordable digital cameras has been used to obtain the flame's spatial temperature measurements [154,221]. Such a technique is less complex and can fit in very restrictive platforms, though the accuracy of the measurements can be compromised.

2.3.4.5. Soot morphology

Soot morphology provides qualitative information on soot formation, which can be used to compare normal and microgravity environments. For soot morphology (particle diameter) and soot distribution (size distribution), thermophoretic soot sampling and transmission electron microscopy are commonly used techniques. Soot samples are collected and processed in transmission electron microscopy (TEM) or Scanning Electron Microscope (SEM) and image analysis post-processing. This technique has been used on gaseous diffusion flames in microgravity [211,215,222] and on diffusion flames established on solid fuels [205,212]. The laser-induced incandescence (LII) method can also be used for soot morphology studies [218].

2.3.4.6. Smouldering propagation velocities

For smouldering, techniques to measure in-depth reaction changes over time are needed to track the smoulder propagation front and derive the smoulder propagation rates. It is possible to monitor the propagation front with a discrete thermocouple embedded in the sample. Another technique used during smouldering tests aboard the Space Shuttle [223,224] was ultrasound imaging. Permeability histories were obtained with an ultrasound imaging system. This technology benefits from the change of structure on open-cell foam undergoing smouldering. Both the unburnt foam and the char layer left behind the smoulder propagation front have different permeability, thus contrasting attenuation to ultrasound. For smouldering instabilities over a thermally-thin fuel, a visual diagnostic would suffice, such as the one used to study finger-like smouldering [133].

2.3.4.7. Mass loss rate and HRR

During burning in microgravity, mass loss rate measurements are difficult to accomplish with gravimetric techniques that are the norm in normal gravity. Visual diagnostics can be used to track the condensed-phase regression during experimental work in microgravity with easy geometries. Droplet combustion of solid spheres benefits from the D^2-law to provide the condensed fuel's burning rates, as it was done in microgravity tests [154,183,184]. A few studies have tried to provide the mass loss with visual diagnostics in other studies with more complex geometries, flat plates or wire jackets. Citerne and co-workers [225] retrieved the burning wire jacket's mass burning rate with CCD camera and a backlighting technique. Such a method requires the sample to be thin and uniform throughout the process. If the instantaneous flame spread rates are known, a simple mass balance can then be used to estimate the mass burning rates [226]. By the same principle, average burning rates can be estimated for the problem's total duration [180,227].

If the HRR's burning rates from solid droplet combustion experiments and the material properties are known, then the HRR can be estimated [184]. For oxygen calorimeter analysis to be used, it is required to measure the concentration of O_2, CO and CO_2 during burning. Two diagnostic systems are installed aboard the International Space Station within the MSG (Microgravity Science Glovebox), the Compound Specific Analyser-Combustion Products (CSA-CP) and the Carbon Dioxide Monitor (CDM). The first can monitor the O_2 and CO concentrations, and the second can track the CO_2 concentrations. Thanks to these diagnostics, combustions parameters can be estimated, such as oxygen depletion, gas concentration changes, CO/CO_2 ratio, heat release rate and the global equivalence ratio [82,228].

2.3.4.8. Gases

A multispectral intensified UV video camera with a six-filter internal wheel hosting bandwidths in the spectrum that corresponds to each combustion gas, (CO_2, CO, MMA vapour and H_2O) was used by Olson et al. [158,229] during the DARTFire testing programme. There were also other filters for soot and chemiluminescence. This ad-hoc technology allowed to use only one camera to measure gases species distribution over a sample during combustion in such a contained space (sounding rocket).

2.4. Flammability assessment

This section discusses the current standards, proposed standards, and other methodology that aim to assess the flammability in microgravity scenarios. The focus is solely on flammability behaviour, as discussed in earlier sections. First, each standard or method is introduced and briefly discussed in lieu of the flammability behaviour (ignition, flame spread, near-limit, smouldering, mass loss rate and HRR). Although toxicity (species production) is also an important aspect of flammability, it is not considered herein.

2.4.1. The current standards for flammability

The evaluation, testing, and selection of materials to avoid unsafe conditions (flammability, emission of gases and fluid compatibility) are currently established using the NASA-STD-6001B standard tests [230]. Three tests are important to discuss herein, as they are related to the flammability of solid materials for use in spacecraft habitable areas, see *Table 4*. The tests are conducted on representative samples in the worst-case scenario and environment where the samples are intended to be used. All tests are conducted in normal gravity environments and have been standardised (see the corresponding standard for each test in *Table 4*).

Table 4 – Required and supplemental tests for the flammability evaluation of solid materials used in habitable flight compartments and other areas.

Test no.	Requirement	Title	Standard	Material or test type	Sample Size* [cm]	Min. Number
1	Required	Upward flame propagation	ISO 14624-1:2003 Part 1	Solid	30 x 6.4 x e	5
				Thin films	30 x 7.5 x e	
				Coating	30 x 6.4 x e	
				Foam	30 x 6.4 x e	

4		Electrical wire insulation flammability	ISO 14624-2:2003 Part 2	Test A	30	5
				Test B	30	
				Wire bundle	43	
2	Supple-mental	Heat and visible smoke release rates	ASTM E1354	Solid	10 x 10 x e	18
				Coating		
				Foam		

**"e" stands for the sample thickness.*

In both Test 1 and Test 4, the purpose is to determine if a material will self-extinguish when exposed to a standard ignition source and that it will not cause ignition of nearby materials by falling debris. In Test 1, the vertically oriented sample is ignited at the bottom edge with the aim to facilitate upward flame spread. In Test 4, the sample is a wire jacket mounted at a 15-degree angle from the vertical. Materials are intended to be subjected to the worst-case scenario that represents the environment that the material would encounter on spacecraft. The environmental conditions considered are the oxygen concentration and the ambient pressure (high oxygen concentration prevails) for both tests. Some contrasting differences are established for each test. Test 1 is performed in quiescent conditions (no forced flow), and different thicknesses are tested. Test 4 can be conducted in a quiescent environment (Test A) or under the effect of a forced flow at 25% oxygen concentration at ambient pressure (Test B), and the wire sample can be overloaded. Additionally, another scenario contemplates the grouping of up to six wires that can be subjected to the same procedures in Test A and Test B. The acceptance criteria for both tests are defined by the burnt length (no more than 15 cm of damage) and ignition of a secondary material (underlying paper) by burning debris. This burnt length criterion was raised from applying to three samples in the standard from 1998 to the five samples required in the latest version (2011). Finally, the latest version of the standard introduces the maximum oxygen concentration (MOC) definition, at which at least five specimens pass the acceptance criteria. This concept is applied when the maximum oxygen concentration at which the sample would encounter is not known.

Test 2 provides supplemental information and is not compulsory (current standard). In the previous version of the standard (1998), Test 2 was required when the sample did not pass Test 1. The standardised rig used is a cone calorimeter in an enclosed chamber (where the oxygen concentration can be regulated) with Oxygen Consumption Calorimetry and a mass loss. The specimens are subjected to three various incident heat fluxes and air or an oxygen-enriched environment (representative of anticipated conditions on spacecraft). Test 2 provides the effective heat of combustion, the time to ignition, heat release rate (HRR), smoke obscuration, extinction coefficient and total heat released. There are no criteria in this test, but the flammability information can be used in a risk assessment.

The inconsistent criteria of Test 1 and Test 4 have been subjected to criticism because the test results do not provide an understanding of the fundamental principles behind the relevant flammability phenomena [12,129,130,231–233]. The sample's width can have significant effects on the upwards flame spread due to lateral oxygen diffusion [234]. Also, the scenarios considered in both tests might, in fact, be the worst case in normal gravity, but that is not necessarily the case in microgravity, which means that the test outcome can be misleading. In microgravity, other phenomena and conditions can represent more critical scenarios, as seen in Chapter 2. For example, the effect of enclosures or oxygen diffusion and the side cooling effect on the sample width can further extend the flammability of materials. Experimental work has shown that opposed flame could occur in a creeping fashion in conditions where concurrent does not happen [103]. The behaviour of flamelets and oscillatory flames can also extend the flammability region. Test 2 suffers a similar conceptual misunderstanding, and the mass loss rate and HRR are measured in normal gravity conditions and might not represent microgravity environments.

2.4.2. Improved NASA standard

As seen, Test 1 and Test 4 only provide pass-fail results that cannot be used to establish quantitative comparisons in microgravity. To overcome the drawback of Tests 1 and 4, NASA introduced two concepts that quantify the extinction limit for upwards flame spread (PD ISO/TS 16697:2012). They are the Maximum Oxygen Concentration (MOC) and the Upwards Limiting Oxygen Index (ULOI) [10]. Both indexes are based on cumulative probability and are presented in *Figure 14*. MOC is defined as the level of oxygen concentration where at least five samples pass the burning criteria and where at least one sample did not pass in an environment containing 1% more oxygen by volume. ULOI is the oxygen concentration at which half of the tested samples fail the criteria for Test 1 or Test 4.

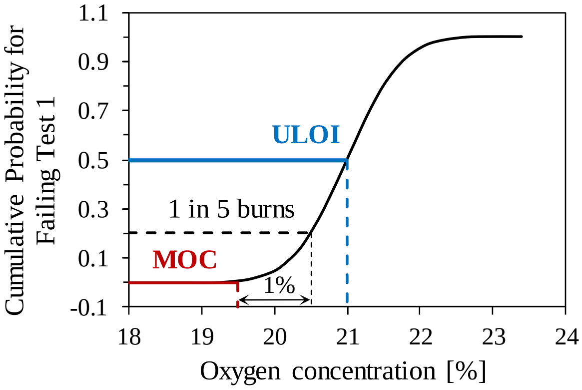

Figure 14 – Definition of the parameters MOC and ULOI based on the cumulative probability of failing burning criteria for Test 1. The data is from microgravity tests by Olson and Ferkul [173].

These indexes have also been applied to other environmental (ambient pressure and normoxic conditions) and experimental conditions [187,235,236]. These new concepts are linked to the flammability limits, as explained in Chapter 2.1.3, which can indeed provide a better flammability assessment of materials. However, establishing quantitative comparisons against microgravity results would require a large amount of data. If the difference is found, it can define the safety factor to be applied to normal gravity results [173]. A few studies have attempted to estimate both MOC and ULOI under microgravity and partial gravity environments obtained in drop towers [173,174,237]. However, steady flame spread under concurrent forced flows (or upwards) is difficult to achieve in drop towers or even in parabolic flights. Thus, obtaining quantitative data in microgravity proves very challenging. Even in the hypothetic case that intensive labour testing is feasible, flammability's scaling laws would not be adequately addressed, casting doubts on any safety factor concept. In addition, the upward (or concurrent) flame spread is not necessarily the worst-case scenario a material would encounter in space.

2.4.3. Limiting Oxygen Index (LOI)

Another proposed fuel selection methodology is extending the Limiting Oxygen Index (LOI) [238,239] to microgravity scenarios, which is currently under scrutiny to prove its applicability [12]. The LOI is the minimum oxygen concentration for the self-sustained downward flame spread over a solid material (a vertical sample is ignited on top). It is similar to the MOC concept as it seeks to define the extinction limit but for opposed flame spread. Fujita [12] argued that such a method presents advantages compared to Test 1 and test 4. The reproducibility in the LOI is higher because it relies on a steady downwards flame spread. The difficulty that the LOI method presents is finding the difference between the oxygen-limiting value from normal to microgravity environments (ΔO_2) is far from trivial because it requires experimental results in both normal gravity and microgravity. Furthermore, as discussed in Chapter 2.1.3, for most materials tested, there are two extinction branches for high forced flow (blow-off branch) and for very-low forced flows (quenching branch). The kinetic branch can be achieved under normal-gravity scenarios. However, low forced flow is required for the radiative branch and can only be found in microgravity.

There is a minimum oxygen concentration or limiting oxygen concentration in normal gravity for a range of forced flows and oxygen concentrations (LOC). Beyond this LOC point, there is no sustained flame spread. In microgravity, flows slower than the induced buoyant can exist, and the extension of the flammability would translate into a lower concentration; this is called the minimum limiting oxygen concentration (MLOC). Both concepts are depicted in *Figure 15.* This minimum oxygen concentration in microgravity corresponds to a critical forced flow velocity, and flame spread will still be possible under these critical conditions. The critical velocity concept has been further investigated by Bhattacharjee et al. [80,193]. Experimental and theoretical work led by Kashiwagi, Maruta and co-workers [27,28,195,240–244] has been able to identify the discrepancy (ΔO_2), between LOC and MLOC, for various polymeric materials (polymeric and fabrics). Their theoretical approach aims to find the MLOC without being required to perform microgravity experiments. Thus far, not all the materials tested have been shown to fall into the LOI method, which indicates that such a method cannot be applied universally.

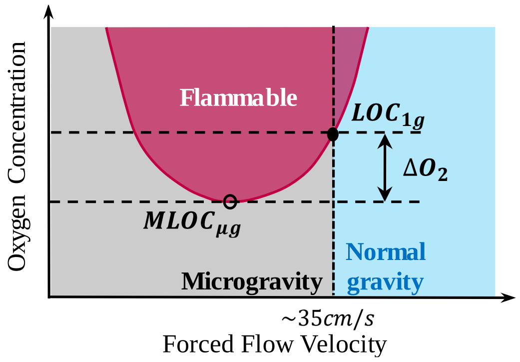

Figure 15 – Flammability map based on the oxygen concentration versus forced flow. The concepts of LOC and MLOC are depicted, and they correspond to the normal and microgravity regions, respectively.

The new flammability assessment methodology based on the opposed flame spread, the LOI-MLOC method, has prompted promising results. Nonetheless, a few experimental and numerical studies with a cellulosic thermally-thin fuel have shown that the flammability boundary is extended under concurrent forced flows [17,18,64,95,101]. That is, the MLOC for concurrent forced corresponds to an even lower oxygen concentration compared to opposed forced flows. As discussed in Chapter 2.1.2, the leading mechanisms for concurrent flames occur along the flame length. The near-limit is defined by the extinction at the trailing edge of the flame length. Predicting concurrent flame lengths and, consequently, flame spread rates and extinction limits are still not possible. Also, the method does not consider the three-dimensional (sample width) effects. The sample width affects the heat transfer mechanism and the extinction boundaries [60,101,114,245]. Likewise, other tangential aspects have also been shown to alter the extinction limits, see Chapter 2.2. Thus, the proposed LOI-MLOC method might not represent the worst-case scenario for the flammability assessment of materials.

2.4.4. Other methods

Other alternative standardised and non-standardised methods have been proposed to aid in the flammability assessment. Most of these methods have not been extensively validated with microgravity data and require more information to be implemented.

2.4.4.1. Modified Test 1

Ohlemiller and Villa [11] carried out a quantitative comparison of the upward Test 1 and the Cone Calorimeter (Test 2) to establish a trend. They suggested a modified version of Test 1 where the sample is exposed to an incident heat flux. A critical heat flux that enables flame to spread upwards could then be estimated. If evaluated under worst-case scenario environmental conditions, such a property could provide supplemental information for material classification. The procedure is affected by buoyancy and thus requires experimental work in microgravity to establish comparisons.

2.4.4.2. LIFT

The standardised LIFT (Lateral Ignition Flammability Test) apparatus (ASTM-E-1321) is used in normal gravity, where the sample is exposed to an incident heat flux. Empirical properties based on the fundamental properties can be extrapolated; these properties provide information on ignition and flame spread behaviour [246]. For ignition, the critical heat flux and the ignition temperature are the inherent properties of the materials. The flame spread rate is estimated based on the external incident heat flux, and conditions for flame extinction (minimum critical heat flux and surface temperature) can therefore also be determined empirically. This method was proposed for ranking spacecraft materials based on their properties [246,247]. The LIFT procedure is carried out for opposed flame spread; thus, buoyancy dominates heat and mass transport.

2.4.4.3. FIST

Based on the LIFT apparatus's principles, a new rig was developed to improve the similarity with the ambient conditions in spacecraft (forced flow, oxygen concentration and ambient pressure). The Forced-Flow Ignition and Flame Spread Test (FIST) apparatus was developed by Cordova et al. [248]. The FIST allows the study of ignition and flame spread as a function of an incident heat flux and characteristic spacecraft conditions. Fundamental properties of materials can be then derived as a function of those parameters. In addition, the apparatus enables the assessment of the ignitability and flammability of solid fuels based on results for flame spread and ignition delay times through the use of a theoretical model [249].

Experimental studies and simplified models on the FIST apparatus have explored parameters coupled with the production of gas or the pyrolysate mass flux at the onset of piloted ignition. For example, it was found that a minimum fuel gasification rate is required for piloted ignition delay [250]. The critical pyrolysate rate at piloted ignition and the critical heat flux were found to be linearly dependent on the forced flow, including low forced flows encountered on spacecraft [31,251]. The critical pyrolysate rate was also evaluated at the flashpoint and fire point (solid material properties) [252]. Piloted ignition has also been assessed under the characteristic space exploration atmospheres (oxygen concentration, pressure and normoxic) [105–107,110], and flame spread studies have even been conducted in parabolic flights [65,253,254].

The critical parameters (ignition and flame spread) of materials might be directly estimated based on the material's properties and environmental conditions, which can translate to microgravity environments. These critical parameters rely on the properties of fuel and environmental conditions rather than just on empirical estimates [31]. Based on these estimated critical properties, it was proposed that the FIST methodology could be used to grade the flammability behaviour of materials for spacecraft applications [249].

This methodology has not been implemented because further validation, specifically for flame spread, is needed, and this requires longer microgravity times not offered by ground-based platforms. The advantages of the FIST apparatus over previous methods are significant because it offers high accuracy control of the thermal and fluid thermal boundary conditions under various environmental conditions in a systematic fashion. The proposed SoFIE and MWT rigs intended for the ISS have the same principles as the FIST, which means that validation of old data can be expected in the foreseeable future.

2.4.4.4. Dimensionless scaling

2.4.4.4.1. Opposed flame spread

Torero presented an approach for opposed flame spread based on a simple heat transfer model where the key parameters were non-dimensionalised [129,130]. The dimensionless opposed flame spread rate was defined as:

$$\bar{V}_{f,o} = V_{f,o}/V^{*} = \bar{l}_o(\dot{\bar{q}}_s'')^2 = \phi_o \quad \text{(Equation 1)}$$

As seen, the opposed flame spread, V, is non-dimensionalised by the characteristic velocity $V^{*}= x_c/t_c$. The characteristic length ($x_c= \lambda/h_T$) is the ratio of thermal conductivity to total heat transfer coefficient and the characteristic time t_c is established by the ratio $k\rho c/h_T$. The dimensionless opposed flame spread rate $\bar{V}_o$ is established as a function of the dimensionless characteristic pre-heat length ($\bar{l}_o$) and the dimensionless neat heat flux at the solid surface, $\dot{\bar{q}}_s''$. The pre-heat length is non-dimensionalised by a characteristic length (x_c), and the neat hut flux by a characteristic heat flux $\dot{q}_c''= h_T(T_{ig} - T_\infty)/a$. The neat heat flux encompasses the heat flux from the flame, the external incident heat flux, and the heat losses. Since it is opposed flame spread, the heat exchange occurs via conduction from the gas-phase to the solid-phase at the leading edge. The global parameter, ϕ_o, includes the dimensionless pre-heat length and the neat heat flux. The characteristic length can vary and depend on environmental conditions and material properties. Thus, ϕ_o can be challenging to evaluate unless the sample is brought to thermal equilibrium by imposing an incident flux.

Torero demonstrated that two dimensionless parameters control flame spread for a wide range of fuels in the opposed flame spread (LIFT) protocol, namely $\bar{l}_o$ and ϕ_o. The global parameter was found to be constant in normal gravity conditions. However, in microgravity, due to the reduction of convective motion and increase in radiation losses, the parameter ϕ_o is different. Also, away from steady conditions, particularly at low forced flows, ϕ_o will vary as the forced flow is further reduced with increasing heat losses through the pre-heat length, and extinction will therefore occur (due to radiation losses). This approach is simplistic in the treatment of flame spread, yet it can provide a ranking system based on the global parameter. The inconvenience is determining those parameters empirically in microgravity and whether the parameter can be scaled as a gravity level function. Another drawback of the method is its omission of kinetics.

2.4.4.4.2. Concurrent flame spread

Torero similarly presented the concurrent flame spread [129,130], where the dimensionless concurrent flame spread rate is:

$\bar{V}_c = V_c/V^* = \bar{l}_c(\dot{\bar{q}}_s'')^2 = \phi_c$ (Equation 2)

The main difference with the opposed case is that the heat transfer occurs along the flame length, and this serves to define the characteristic length scale as $\bar{l}_c = (l_f - x_p)/x_c$. Thus, the neat heat flux includes convective heat, surface re-radiation and radiation from the flame. Under certain forced flow situations in normal gravity, Torero assumes that the convective heat flux is the only component to consider as it dominates the heat transfer. Torero showed that the convective heat flux to the surface could be obtained as a function of the mass transfer number based on fast kinetics. Then, the characteristic length scale can be assumed to be a function of a constant and the pyrolysis length, $\bar{l}_c = C\bar{x}_p$. The constant, C, is a function of the mass transfer number. Based on normal-gravity experimental data, Torero found the above relation to be valid for laminar flows ranging from 70 to 140 cm/s as the ratio of characteristic length to pyrolysis length (l_c^*/x_p) remains constant. On the contrary, for microgravity environments, the assumptions made for normal gravity are no longer valid because the microgravity data shows a linear ratio of l_c^*/x_p from low flows up to approximately 40 cm/s. The characterisation of concurrent flames in microgravity is more complex, and Torero proposed another analysis approach, which will be briefly introduced in the following.

2.4.4.5. Modified Mass Transfer and critical Damköhler number

Torero et al. [48,232,233] used a second analysis based on Emmons' work [232] to describe the mechanism in the concurrent flame further spread ahead of the flame leading edge (entire flame length). Emmons used a bi-dimensional reactive boundary layer flame established over a flat plate for his theory. The mass transfer number can describe the flame, and the only convective heat transfer is assumed through the mass transfer number. In microgravity environments, radiation through the solid-phase and gas-phase becomes important, see Chapter 2.1.2. Hence, Torero et al. [48] incorporated a corrective parameter, χ, to account for the radiative heat losses from the flame to the environment (function of the flame's emissivity). The modified mass transfer number is defined as

$$B_T = \left[(1-\chi)\left(\Delta H_c Y_{o_2,\infty}\right) - c_\mathrm{p}(T_v - T_\infty)\right] / \left(\Delta H_p + Q\right) \quad \text{(Equation 3)}$$

In the heat loss term, Q, surface re-radiation, conduction and radiative heat from the flame are incorporated. In-depth conduction and radiation absorption can be incorporated if the material is infinitely thermally thick. The radiative corrective parameter, χ, can be derived empirically by matching the stand-off distance as demonstrated by Torero et al. [48] and

Rangwala [233] microgravity data. Using the B_T to predict flame length over solid materials yielded overly conservative results as Emmons' theory is based on infinitely fast chemistry. Thus, flame spread under concurrent forced flows cannot be predicted well.

The mass transfer number cannot predict extinction due to the assumptions made. Thus, Torero et al. used the Damköhler number (flow time to chemical time ratio) to explain the flame's extinction mechanism. They defined the Damköhler number:

$$Da = \frac{\tau_r}{\tau_{ch}} = \frac{\rho_g A T_f e^{-E/RT_f}}{V_g^2/\alpha_g} \text{ (Equation 4)}$$

Based on data from experiments carried out in microgravity, Torero et al. [255] showed that Da along the flame length is reversely influenced by the forced. That is, close to the trailing edge, Da increases with decreasing forced flow, while the opposite was observed at the leading edge. Thus, a critical Da for the trailing edge can be defined (experimentally) and it can help to determine the flame length.

The critical Damköhler number and the modified mass transfer number can be used to assess the flammability of fuels in concurrent flows quantitatively. The mass transfer number can also serve to predict the burning rate [233]. The modified transfer number is the main material property that depends on forced flow, oxygen concentration, and distance to the leading edge. Deriving its value is impractical as it requires quantitative experiments in microgravity. Instead, Torero et al. [232] suggested using other versions of the mass transfer number: the adiabatic mass transfer number, leading-edge mass transfer number and the critical mass transfer number. The last two, as well as the critical Da, can be derived based upwards flame spread experiments. More quantitative experimental data is needed to further validate this approach that can confirm the normal-gravity results could be translated to microgravity scenarios. The applicability of this approach is restricted to situations that follow the boundary-layer theory, and where the assumptions made hold.

Torero's approach attempts to describe the flame properties and extinction conditions in concurrent flows for a range of scenarios in microgravity environments. Nonetheless, further validation is required, preferably employing other fuel types and breaking up the transitional regime from 40 to 70 cm/s. Therefore, experiments of this nature would be of great value in combination with the detailed numerical solutions that are needed for a proper evaluation of the critical Da and the modified mass transfer number.

2.4.4.6. Pressure modelling

The idea of pressure modelling emerged from the need to provide a powerful predicting method that is able to forecast full-scale fire behaviour based on small-scale laboratory experiments. Various researchers have used the technique in the past [256–258] and demonstrated that for different fires scenarios on small-scale, the product of pressure-squared times length-cubed (p^2l^3) remains constant for a range of pressures. A large-scale fire can therefore be modelled by that relation. De Ris demonstrated that the method could model steady-state burning, solid-phase and mass transfer, flame spread and other transient phenomena [258]. The Froude number, $Fr = (\Delta\rho/\rho)(gl/V^2)$, and the Reynolds number, $Re = \rho Vl/\mu$, must be preserved to model the dynamic mechanics of a fire. Thus, the Grashof number, $Gr = (\Delta\rho/\rho)(gl^3\rho^2/\mu^2) = Fr\,Re^2$ is the controlling non-dimensional parameter for buoyant related problems [258]. The method assumes that dynamic viscosity and flame temperature changes ($\Delta\rho/\rho$) are independent of pressure.

This method allows to modelling flame spread and other phenomena in reduced gravity since $\rho^2{\sim}p^2$ and thus gp^2 should be preserved in the Gr number. Kleinhenz and co-workers [127] found that upwards flame spread over a thin fuel in partial gravity (Lunar and Martian) can be reproduced in normal-gravity with the $gp^{1.8}$ correlation. Thomsen et al. [259,260] found that concurrent flames over solid fuels in a 30 kPa and under 20 cm/s forced flow resembled those reported in microgravity experiments [79]. They found a scaling relation for the flame spread rates, from normal gravity to microgravity, as a function of a mixed convective flow, which only assumes convective heat transfer. Thomsen et al. [261] then used the same approach for opposed flame spread over a cylindrical fuel, but the scaling relation did not yield sound qualitative results. Pressure modelling was also found to correlate well with the flame spread over wires in microgravity, though only away from the radiation regime [262]. Another potential application of pressure modelling is smouldering, which has been explored experimentally and numerically [263,264]. However, there is no microgravity experimental data to validate the approach to smouldering.

As kinetics and radiation are disregarded, this scaling technique is predominantly applicable to flammability phenomena where convection is dominant. Thus, the method might not be suitable for flammability extinction regions, where kinetics and radiation are relevant or where radiation is dominant (low forced flows). Also, it is not ascertained how a sufficiently low pressure for mimicking microgravity affects the chemistry of flames and at which point the method's assumptions no longer hold.

2.4.4.7. Rayleigh analogy

This methodology is based on the sub-critical Rayleigh number analogy, $Ra = g\beta\Delta T l^3/\alpha v = Gr\,Pr$, where convection driven by buoyancy can be suppressed for values lower than a critical number [249]. For example, buoyancy-forced flows can be eliminated in narrow channels. Several experimental studies have taken place to establish comparisons between the Narrow Channel Apparatus (NCA) and microgravity for a range of phenomena such as flame spread and near-limit under opposed and concurrent forced flows for rods thermally-thin samples and thermally-thick fuels [84,145,265–267]. The NCA results agree qualitatively with the microgravity flammability phenomena but with quantitative discrepancies.

Another flammability emergent phenomenon also seemed explored in the NCA is flamelets observed in flaming combustion in microgravity [96,140]. The NCA matches the microgravity data qualitatively via gas-phase (oxygen transport, diffusivity and thermal expansion) [96]. Though, in another study in NCA [268], the flamelet spread behaviour was explained best by an effective Lewis number (thermal diffusivity to mass diffusivity) where the heat losses to the NCA walls were incorporated via the thermal diffusivity (gas-phase). A similar phenomenon, fingering instabilities in flaming combustion and smouldering, has been explored in NCA. However, it is not clear which mechanisms in microgravity are effectively reproduced in the NCA. Olson and co-workers claim that smouldering instabilities in microgravity are dominated via the gas-phase convection-diffusion (oxygen transport and losses) [133], whereas NCA studies have shown that a modified effective Lewis number (diffusive-thermal mechanism) explains the instabilities behaviour [138,269–271]. Others have attempted to correlate the spontaneous ignition in NCA at low pressure with microgravity results [272].

The channel gap affects the heat transfer of the flame and flamelet [273], affecting fingering instabilities (heat losses to the wall). Also, the incoming flow field does affect the heat losses and kinetics [274]. For flame spread, it is not clear how accurate the NCA can reproduce the radiative heat losses. As seen, this method requires further refinement.

2.4.4.8. Stagnant-point diffusion flame

A stagnation-point diffusion flame is a one-dimensional type of flame. It has been used to study various aspects of solid combustion due to easier analytical and numerical solutions. The radiative and blow-off extinction limits can be characterised by stretched flames [23,100]. These flames are quantified by the stretch rate, which is the velocity gradient near the stagnation-point diffusion flame.

In buoyant conditions, the stretch flame rate is $a_b = ((T_f - T_\infty)g/T_f r)^{1/2}$, where r represents the sample's radius (spherical or cylindrical). Under purely forced flows, the stretch rate for a cylinder $a_f = (3/2)(V_g/r)$. A mixed stretch rate is thus $a_m = (a_b^2 + a_f^2)^{1/2}$. Equivalent gravity levels (partial gravity and microgravity) can be attained from the buoyant stretch rate. T'ien [275] suggested that the fundamental limit or the MLOC (LOI method) could be attained with stretch flames and translated to microgravity.

Low stretch environments can also occur in spacecraft when forced flows pass over flammable solid fuels [247]. Also, two-dimensional diffusion flames can be translated into stretch rates [276]. As a function of the oxidiser level and stretch rates, the blow-off extinction boundaries found in microgravity experiments with concurrent flame spread over cylinders were found to collapse with normal gravity data [82,277]. The normal gravity data collapsed if it was shifted to account for buoyancy. Extending the blow-off limit to the vertical axis provides a minimum oxygen limit. This limit could serve as an overly conservative flammability criterion. Similar scaling behaviour with experiments in low-pressure environments was reported by Marcum et al. [278]. They proposed that the blow-off limit as a function of ambient pressure should be used as the threshold flammability criterion for normoxic environments.

A normal gravity low-stretch diffusion flame can also be attained if cylindrical samples of different large radii are imposed to forced flow from below, as reported in [279–281]. These studies investigated the extinction limits, flame structure, and regression rates as a function of the stretch rates. An incident flux is added from below to study piloted ignition and regression rates [281–283]. Another phenomenon observed in this arrangement is flamelets near the quenching regime [281]. Most of the phenomena observed still require validation with microgravity results.

2.4.4.9. BRE, the Burning Rate Emulator.

The Burning Rate Emulator, BRE, apparatus is a gaseous fuel burner (sintered metal) that can emulate the burning of condensed matter (solids and liquids). The principle rests on matching four fundamental properties of condensed fuel, namely the heat of combustion, heat of gasification, vaporisation temperature and smoke point [284]. Ignition and extinction mechanisms have been explored in the BRE apparatus [285]. Recent interest has focused on applying the same technique in microgravity environments [284,286], with the potential to find a direct translation of the burning behaviour in normal gravity. If confirmed, the BRE technique could be used as an affordable method reinforcing NASA Test 2. However, BRE microgravity experiments in drop towers and on ISS have shown that the steady-state is difficult to achieve because the stagnant flames are dominated by radiative extinction and instabilities [284,286,287].

2.5. Overview

There are many relevant aspects behind the study of solid materials' combustion in microgravity and fire safety on Spacecraft. The fundamental aspects of microgravity are, in essence, the same as those in normal gravity; however, the complication arises since the controlling mechanisms for many phenomena in microgravity remain unknown. Thus, it is still not possible to predict all phenomena behind solid combustion in microgravity. Quantitative microgravity data, very necessary, can be obtained through experimental work (aided by numerical and theoretical studies) and available technology. In the following, the main findings for every chapter, and corresponding subchapters, are summarised:

- Fundamental aspects (ignition): microgravity affects ignition via convective heat transfer and increases mixing time.
- Fundamental aspects (flame spread): The leading edge dominates the opposition flame spread. At very low forced flow, heat losses and reduced

oxygen transport become dominant, leading to the extinction of the opposed flame. The flame length and the flame characteristics dominate the concurrent flame spread. The definition of flame length is dependent on soot oxidation.

- Fundamental aspects (near-limit): In opposed flames, two extinction boundaries are defined on the leading mechanisms are kinetics and radiative losses. Kinetic regime can be defined by the Damköhler (flow time vs chemical time) number, whereas an arbitrary radiative number defines the radiative regime. Both limits form a “U” shape, depending on environmental and other parameters, and can lead to identifying a critical point (fundamental limit). Near-limit in a concurrent flame is more complex due to radiative and convective heat transfer (flame length interaction). The flammability limits are extended for the concurrent case.
- Fundamental aspects (smouldering):
- Heat transfer and kinetics might affect external parameters (pressure) and ignition. Flame is affected via heat transfer (flame optical thickness), and possibly kinetics at very low pressure. Extinction limits also show the “U” boundary when ambient pressure is one of the parameters for opposed flame spread. However, the limit is linear for the concurrent flame case.
- External parameters (Normoxic): The oxygen effect might be greater than ambient pressure. However, the results are not conclusive.
- External parameters (sample size): Combined effect of side oxygen diffusion and side convective heat losses. Either mechanism can be dominant depending on other external variables. Thus, flammability can be extended for narrower samples.
- External parameters (confined spaces): the flammability can be extended due to thermal expansion (gas-phase), flow channelling effect and radiative heat transfer.
- External parameters (gravity level): the induced buoyant flow has similar effects as forced flows. The fundamental limit for opposed flame might occur between 0.1g and 0.4g, whereas for concurrent, the worst-case scenario is in normal gravity (length scale increases with increasing gravity).

- Instabilities: the flame instabilities occur near extinction and are dominated by oxygen diffusion and convective flows. The instabilities can extend the flammability limit. For smouldering instabilities, the dominant mechanism is mass diffusivity/thermal diffusivity.
- Boundary layer: The entrance length can affect the effective flow seen by the flame leading edge and thus can contribute to an increase in flammability.
- Discrete position of samples:
- Surface features: Surface features Grooves could enhance flammability.

Concerning the technical aspects, a range of research platforms offers different levels of gravity, time lengths, sample lengths and volumetric capacity, test productivity (number of tests that can be performed per day), and capabilities. Also, the diagnostic systems, whether complex or simple, are essential to quantify and characterise the diverse phenomena emerging in microgravity conditions. Thus, for any investigation, the choice of research platform and technology heavily depends on the phenomena to be studied.

Concerning fuel selection for spacecraft applications, there is a range of methods aiming to assess the flammability of materials for spacecraft microgravity environments. The focus of each method varies according to the flammability phenomenon to be assessed or properties to be quantified, as seen in *Table 5*. Some methods are based on threshold criteria or provide estimations of the phenomena. On the other hand, methods such as Test 2 or the BRE aim is to provide fundamental properties. In the latter, these properties can help classify materials that can be evaluated based on risk analysis. While earlier methods are intrinsically empirically-based (such as ULOI), recently proposed methods look at the fundamental phenomena from simplified theoretical analyses and have established scaling laws between normal and microgravity. For the latter, the LOI-MLOC is based on a simplified model but accounts for the dominant near-limit phenomena (radiation and kinetics) or the piloted ignition behaviour evaluated in the FIST apparatus. Another method is the modified mass transfer number and the critical Damköhler number, which can be used to estimate the limiting flame length and the concurrent flame spread. Most of the methods proposed are still in their infancy or require quantitative data to be validated. Yet, it is a significant improvement compared to the pass/fail criterion established early by NASA in Test 1 and Test 4.

Table 5 – Existing and proposed methods for flammability assessment of materials in microgravity. The "X" marks which phenomena or parameters these methods aim to or can assess.

Standard or Assessment method	Ignition	Flame spread		Near-limit		Smouldering	Flamelets & instabilities	Burning rate	HRR	Flammability properties
		Opposed	Concurrent	Opposed	Concurrent					
Test 1 & 4			🟧 X							
Test 2	🟧 X							🟧 X	🟧 X	🟧 X
MOC & ULOI					🟧 X					
LOI-MLOC				🟩 X						
Modified Test 1			🟧 X							🟧 X
LIFT	🟧 X	🟧 X								🟧 X
FIST	🟩 X	🟧 X								🟧 X
Dimensionless scaling		🟧 X	🟩 X							
B_t & Da					🟧 X			🟧 X		🟧 X
Pressure modelling		🟧 X	🟩 X			🟧 X				
Rayleigh analogy (NCA)	🟧 X	🟧 X	🟧 X	🟧 X	🟧 X		🟧 X			
Stagnant-point diffusion flame	🟧 X			🟩 X*				🟧 X		
BRE								🟧 X		🟧 X

Colour legend		
	🟧	Not validated to microgravity or no scaling law to microgravity.
	🟩	Partly validated, reasonable scaling laws (few materials or experimental conditions).

*The stagnant-point diffusion flame is a 1D problem and it does not classify as opposed or concurrent.

The advantages and limitation of each flammability assessment method are listed in *Table 6*. As seen, the advantages of each method make them very attractive, especially if the method is feasible to apply in normal gravity conditions. Material selection for so long has trumped the fundamental understanding. Standard methods should be feasible and easy to apply since there is a need to provide cost-saving methods, but it should not jeopardise spacecraft fire safety. It has been the case for material selection where pass/criteria are uncomplicated. However, the main preoccupation is which level of hazard can we tolerate. Most of the proposed methods have a range of applicability depending on the material type and environmental conditions, which should be accounted for and defined clearly. As no method can be applied universally, it might be more robust to set several flammability assessment methods in place.

Table 6 – Summary table on the limitations and advantages for each flammability assessment method. Blue (left columns) are the advantages, and red columns (right) represent the disadvantages.

<table>
<tr><th colspan="2">Test 1&4</th></tr>
<tr><td>It is easy to execute, feasible, empirical, Simple cut-off criteria</td><td>It is not representative of microgravity environments, or worst case scenario.
It does not address fundamental behaviour</td></tr>
<tr><th colspan="2">Test 2</th></tr>
<tr><td>It provides some fundamental properties and is useful to rank materials and allows classification.</td><td>It is not necessarily the same properties in microgravity.</td></tr>
<tr><th colspan="2">MOC & ULOI</th></tr>
<tr><td>It uses stricter criteria based on environmental scenarios and probability.</td><td>It relies on every environmental conditions, requires large quantitative comparisons.</td></tr>
<tr><th colspan="2">LOI-MLOC</th></tr>
<tr><td>It uses a fundamental concept (fundamental limit). Feasible to obtain empirically.</td><td>It is only applicable for opposed flames, not addressing other environmental conditions or critical scenarios. It might not be applicable for all solid fuels.</td></tr>
<tr><th colspan="2">Modified Test 1 & LIFT</th></tr>
<tr><td>It aims to determine a fundamental property for flame spread empirically.</td><td>It requires quantitative comparisons in microgravity to establish scaling comparisons. It is restricted to few environmental scenarios</td></tr>
<tr><th colspan="2">FIST</th></tr>
</table>

Fundamental properties for ignition and flame spread can be determined empirically and theoretically. It allows more environmental conditions. Properties can be used to classify materials	It requires quantitative comparisons in microgravity to establish scaling laws. It does not address all critical scenarios.
Dimensionless scaling	
It empirically determines global properties that could be used to classify materials. It is simple.	Requires quantitative comparisons in microgravity to establish scaling laws. It does not address all critical scenarios.
B_t & Da	
It determines critical fundamental properties that can predict flame lengths. It is complex since it requires numerical tools.	Requires quantitative comparisons in microgravity to establish scaling laws. It does not address all critical scenarios.
Pressure modelling	
It is feasible to conduct in normal gravity.	It is not clear the effect of kinetics at very low pressures. The range of applicability is limited.
Rayleigh analogy (NCA)	
It is also feasible in normal gravity. It addresses other phenomena not looked at in previous methods.	It requires quantitative comparisons with microgravity data.
Stagnant-point diffusion flame	
It can provide a fundamental limit and it is feasible in normal gravity.	Requires quantitative comparisons in microgravity to establish scaling laws. It cannot be applied to all materials.
BRE	
Provides fundamental properties, and it is feasible to conduct in normal gravity.	It is not known the scope limit on which materials it could be applied. It requires further validation.

The NASA standard enforced the idea of testing any sample under the worst-case scenario that the material encounters on spacecraft. The definition of a worst-case scenario seems to be circumstantial and subjective to human decisions. As seen in the previous chapters, concurrent flame spread (or equivalently upwards flame spread) might not be the worst scenario depending on the environmental conditions. Flame or smouldering instabilities have occurred at unexpected low oxygen concentrations and forced flow, extending the extinction boundaries. Therefore, it is of interest to establish if these phenomena should be considered the most-critical scenarios on spacecraft or if worst-case considerations also should include the probability of occurrence. For example, most of the fire incidents reported on spacecraft were due to overheating of wires (spontaneous ignition), which could be used to argue that they are most important to study. In addition, there are still microgravity flammability phenomena on solid materials not well understood (smouldering or spontaneous ignition). New environmental scenarios (normoxic, partial gravity) and other constraints arise on the horizon (extended missions far beyond Earth). These need to be addressed by the flammability assessment methods.

3. Review on Polydimethylsiloxanes

This chapter is centred around the flammability and burning behaviour of silicone-based materials in general and the behaviour of PDMS in particular, as this is a silicone-based product. The discussion starts with the general combustion behaviour of silicone, how they pyrolyze, their chemistry, and some reported properties found in the literature for silicones. As for PDMS, being a manufactured material for very specific applications, properties are scarce in the literature. It is of great importance to know beforehand how silicone behaves. Such a goal can help in understanding the reasons behind the results obtained on-board the spacecraft Cygnus (Saffire II tests).

3.1. The thermal degradation behaviour

Silicones are inert, synthetic compounds found across a range of products such as oils, grease and resins [288], and as other silicone-based products such as flame-retardant materials [289]. Silicones are widely used in a range of industries ranging from food, construction engineering, electrical, transportation, textiles, aerospace and cosmetic industries due to their unique properties [290–293]. Due to the thermal properties, mainly thermal stability, resistance to the spread of fires, and low burning rates, low heat release rate, silicones are also used as flame retardants [294]. Their fire retardancy is mainly attributed to the formation of silica ash, SiO_2, during thermal decomposition and diffusion flaming combustion [291,295]. The ash deposits on the unburnt fuel decrease the heat flux from the flame to the condensed or liquid silicone. The amount of silica ash formation and ash deposition will depend highly on the specific silicone, oxygen level in the environment and other factors [292,296].

However, silicones are far from being considered the perfect non-flammable material as they can also burn and combust. A silicone vent cap was ignited and burnt by flamelets during the Swissair Flight 111 in 1998. As a consequence, a greater airflow was allowed into the narrow channel leading to a systematic failure of the cockpit commands, and the plane crashed into the Atlantic ocean, killing 229 passengers [297]. Also, it is difficult to evaluate the utility of these materials based on existing fire tests since the flammability properties of any particular polymer, in this case, the silicones, are not only inherent to the polymer itself. Instead, their flammability behaviour is dependent on the test method used [289]. In addition, as discussed in Chapter 2, environmental conditions can also affect the flammability and burning behaviour of solid materials. Thus, it is important to understand how silicones react to thermal exposure and how they burn, which requires an overview of the thermal decomposition and burning behaviour.

The most dominant polymer in the silicone industry is polydimethylsiloxane, or PDMS, an inorganic polymer formed with a backbone structure of repeating siloxanes [291,298]. The basic chemical equation for polydimethylsiloxane is $(CH_3)_3SiO[(CH_3)_2SiO]_xSi(CH_3)_3$, which is a distribution of trimethylsiloxy end-blocked species. In the previous chemical formula, ‘x’ represents the average degree of polymerisation. Thus, it can form different types of structures (liner, cyclic and others). The commercially available PDMS are often designated by their viscosity in centistokes [291]. PDMS have properties of special interest, such as thermal stability, low-temperature performance, minimal temperature effect, high permeability of gases, and hydrophobic and physiological inertness [299].

Depending on the chain length (or molecular weight), silicones can range from liquids (0.65 to 20 cS) to rubber or membranes (from 20 to 60 000 cS). Silicone membranes such as PDMS have long chains with higher molecular weights [291]. There are many studies on thermal decomposition in non-oxidative and oxidative environments, mainly for curation processes [300]. However, there is scarce and reliable information on high molecular weight silicones such as the one specific PDMS membrane in this current investigation [301].

The thermal degradation studies of silicones, though mainly focused on the curation processes, can be helpful to understand the pyrolysis phenomenon of PDMS. The products forming during the thermal degradation of PDMS are determined by the heating conditions and the nature of the gaseous environment [302]. During thermal decomposition in non-oxidative environments, the depolymerisation products of high viscosity polymers (PDMS) are mainly cyclic dimethylsiloxanes and minor lineal siloxanes, namely trimer (D3) and upwards (Hexamethylcyclotrisiloxane, octamethylcyclotetrasiloxane, dodecamethylcyclohexasiloxane, decamethylcyclopentasiloxane) [291,301,303–305]**.** In oxidative environments, the thermal degradation of a specific PDMS (end blocked with trimethylsiloxy-groups $(CH_3)_3SI$- containing vinyl-methyl-siloxane unit) resulted in two stages at heating rates of 1 °C/min & 50 °C/min [306]. In both, it was found that the major degradation products are a similar mixture of oligomers as those produced in non-oxidative environments, along with CO_2 and H_2O. These oligomers, once they leave the PDMS, can also oxidase, especially, at under high heating rates (>100 °C /min), and silica ash is formed due to oxidation [306]**.** The onset of oxidation for PDMS in oxidative environments is found to be approximately 240 °C. Thus, during pyrolysis of polydimethylsiloxanes, the volatilisation of molecules results from the thermally induced degradation via siloxane rearrangement [307].

3.2. The burning behaviour of silicones

Lipowitz studied the diffusion flaming behaviour of fluid polydimethylsiloxanes ranging from low viscosity to high viscosity (or short chain to long-chain) in pool fires [295,308]. The model proposed by Lipowitz for pool burning of high molecular weight PDMS is shown in *Figure 16*. Such a model, though meant for liquid polydimethylsiloxane, can also be applicable to the PDMS membranes. The PDMS pool decomposes into cyclic oligomers, as previously discussed, and these polymers form other compounds along with the oxidiser. Once the new polymer compounds enter the reaction zone (the diffusion flames), they react further with the oxidizer, and the final products are CO_2, H_2O and SiO_2. The silica ash is believed to be in the amorphous form [289]. According to Lipowitz [308], the formation of amorphous silica ash occurs during gas-phase combustion because the fast cooling of the melted material prevents crystallisation.

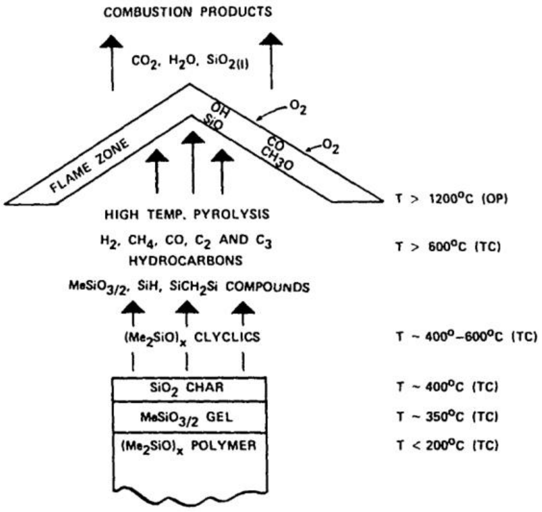

Figure 16 - A model for pool burning of low volatility PDMS ($(M_2SiO)_x$ polymer (high molecular weight) with high boiling points (>250 °C) [295,308].

The amorphous silica ash randomly falls onto the pool, where it forms a char layer on top of a methylsiloxane gel layer (forms due to oxidation at the surface in liquid PDMS). Such a gel layer is not likely to appear on the PDMS membrane. The amorphous silica ash layer protects the obtaining heat fluxes from the flame and effectively reduces volatiles' diffusion into the exothermic reaction [289]. The formation of silica ash is strongly dependent on the molecular weight of the PDMS [295,305]**.** Thus, for PDMS membranes, it is expected that they will produce amorphous silica ash. The stoichiometry for the complete combustion of PDMS is [291]:

$$(CH_3)_3Si - O[-Si(CH_3)_2 - O]_n - Si(CH_3)_3 + (12 + 4n)O_2 \\ \rightarrow (2 + 2n)SiO_2 + (6 + 2n)CO_2 + (9 + 3n)H_2$$

The white silica emits at a short wavelength, bringing the flames to short wavelengths [308]. Consequently, the flame temperatures are reported to be lower than those from adiabatic estimations [309]. In experimental studies, it is reported that the heat flux coming from the flame to the unburnt fuels is low (26 kW/m^2) [290,292]. Such a peculiarity is significantly different from other diffusion flames of organic materials. Likewise, the falling silica ash particles onto the fuel make measuring several fundamental properties very challenging. As the density of amorphous silica is only 2.2 g/cm^3 [310], measurements in standardised equipment should be treated with precaution. During thermogravimetric analysis in oxidative environments, the silica ash randomly falls onto the weighing scale and can influence the mass loss data and the final results. Good et al. [311] reported that after correcting the weight of the silica ash, the corrected heat of combustion was 6% higher.

Some properties of PDMS and a range of similar composites are listed in *Table 7*. It can be seen that many of the properties listed vary depending on the molecular weight of the PDMS. In addition, the kinetic properties can also vary according to the publication of origin. There is clear heterogeneity in the silicone industry, with variability in the physical and thermochemical properties reported. Silicones are treated with other chemical components for many applications to improve their properties for specific purposes. For instance, polymer flammability can be attained by adding silica and silicate in the condense phase (fillers) [288,312]. There is scarce reliable information on high molecular weight silicones [301]. This consequently might make it more difficult to investigate the flammability behaviour of silicones.

Table 7 – List of kinetic and thermochemistry properties of various polydimethylsiloxanes.

PDMS type	**Activation energy** [kcal/mol]		Ref.
	Non-oxidative	In oxygen	
PDMS and composites	42±3	30±2	[301]
Me$_3$SiO end-blocked PDMS			[313]
Silanol terminated PDMS	40		[304]
Vinyl terminated PDMS	46		[304]
PDMS end-blocked with trimethylsiloxy-groups (CH$_3$)$_3$SI- containing vinyl-methyl-siloxan	26.76		[306]
Methylhydrogen PDMS and Vinyl terminated PDMS	25		[293]
PDMS >50 cS	43		[291]
Catalyst free PDMS	80.8		[291]

PDMS type	**Heats** [MJ/Kg]		Ref.
	Of combustion	**Of gasification**	
> 10 CS	26.8	3-3.6	[290,299]
>50 CS	24.6	1.2-1.3	[291,314]
	19.53 (net)		[315]

50 cs	28.03		[316]
From oxygen consumption	18.78		[289]
Stoichiometry	24.8 (net)		[291]
PDMS type	**Property**	**Value**	Ref.
PDMS (1000-12500 cS)	Density [g/cm^3]	0.97	[299,317]
PDMS (100-60000 cS)	Thermal expansion coefficient α [1/K]	9.6 x 10^{-4}	[299]
PDMS (2-1000 cS) at 298 K	Specific heat C_p [kJ/kg K]	1.35-1.51	[299]
		1.05	[317]
PDMS (1000-60000 cS) at 50 ˚C	Thermal conductivity [W/mK]	0.1591	[299]
		0.2	[317]
PDMS membrane	Ignition temperature [K]	673	[317]
PDMS (100 cS)	Autoignition temperature [K]	>763	[299]

In the literature, the flammability threshold results from standardised methods, such as those discussed in Chapter 2.4, are reported, and these are also inconsistent. For example, in tests with liquid PDMS in cups, Lipowitz found that the LOI decreased as the cup diameter increased LOI [295]**.** Various flammability thresholds and indexes results from standardised methods for PDMS are presented in *Figure 17*. As seen in the plotted data, the LOI and MOC results for PDMS seem to be linearly dependent on the sample thickness. However, such a dependency seems to weaken the ULOI results. A similar material, silicone rubber (Polysiloxane), also presented in *Figure 17*, appears to behave differently. This may be attributed to the fact that it was tested in different ambient conditions. From these results, it seems that the methodology used to test the polydimethylsiloxanes can affect the results. The deposition and accumulation of silica ash on the unburnt layer might not aid the burning, which also depends on the sample disposition and how the sample is tested [312]. LOI is useful in indexing materials, which is relevant for polymers, and is a way to judge how flammable material is. However, the LOI data does not correlate with real-life scenarios and do not correlate with the flammability concepts either (ignition, flame spread and heat release rate) [318,319].

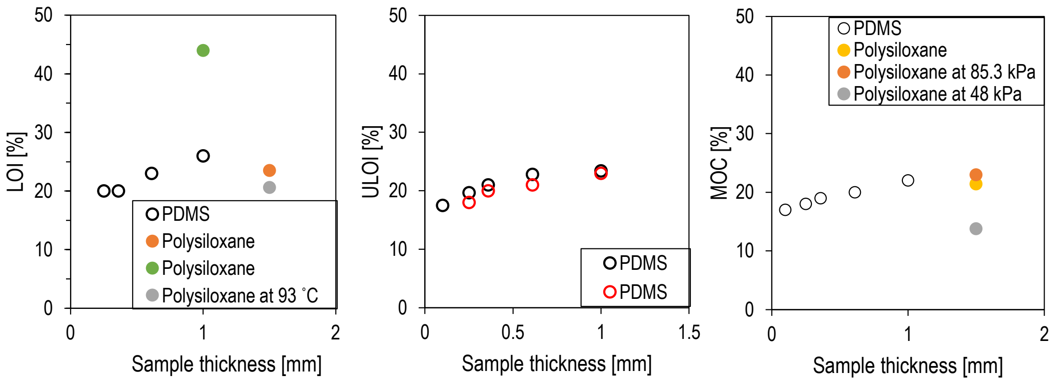

Figure 17 – Various flammability indexes for PDMS and silicone rubber (Polysiloxane) as a function of the sample thickness and some environmental parameters. In most cases, the test conditions were in 101 kPa and at ambient temperature. The flammability index are results collected from literature [187,235,236,244,317,318]. *LOI stand for limiting oxygen index (normal downwards flame spread), ULOI is the upwards limiting oxygen index), and MOC is the maximum oxygen concentration.*

During the SKYLAB flammability testing, silicone O-rings were used. These had 2.59 mm diameter and were threaded over steel of a ceramic mandrel (not reported the dimensions) [13,14]. The microgravity flame spread results along with the corresponding normal gravity results are presented in *Figure 18*. As seen, the microgravity environment has a clear effect on the flammability of the silicone rubber. For the tests aboard the SKYLAB, no forced flow was applied, and flame spread was likely dependent on diffusive forces. There was no further information on the microgravity results, and it is thus difficult to hypothesise a plausible explanation for the contrasting behaviour.

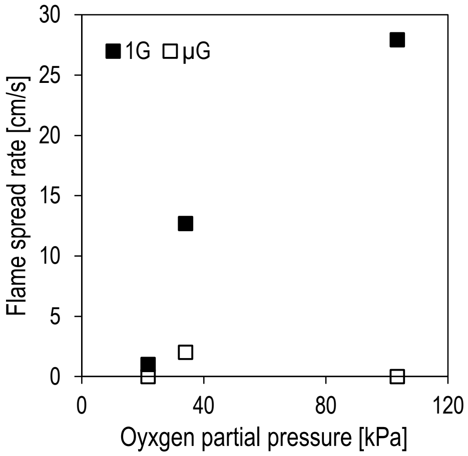

Figure 18 – Flame spread results as a function of the oxygen partial pressure for a silicone O-ring tested aboard the SKYLAB spacecraft [13,14].

4. The Saffire II tests outcome

As shown in the previous sections, most of the samples tested in microgravity research platforms have been restricted to small dimensions due to the limitations of each platform. Also, because of the absence of data on realistic samples, it is very challenging to validate proposed flammability assessment methods. Thus, the Saffire testing programme was established to fill that gap, and much larger samples in more realistic scenarios are being tested in that programme [25].

The Saffire II tests were conducted in orbit aboard the unmanned Cygnus spacecraft before re-entry into Earth's atmosphere. Nine samples of dimensions 30 cm x 5 cm were allocated inside the 6.6 l combustion chamber. Among these were four PDMS samples, which were placed at the end of the sample holder card, as shown in *Figure 19*. The first three PDMS samples had thicknesses 0.27, 0.61, and 1.03 mm and based on ground experiments, these samples were expected to ignite, possibly ignite and not ignite, respectively. These samples were ignited at the bottom with respect to the 20 cm/s forced flow as the concurrent flame spread was the goal. The last PDMS sample had 0.36 mm thickness and was meant to develop an opposed flame spread against a 20 cm/s forced flow. For all tests, the oxygen concentration was 22.1% at 100 kPa. To achieve ignition, a hot Ni-Cr wire (29-gage Kanthal®, 0.286 mm diameter, 3.85 A) was attached to the sample edge (in a sinusoidal shape), and it was energised for 9.2 s at 80 W, which provided 736 J uniformly. The energy provided for ignition is the same as prescribed in the NASA 6001 Test 1. Two video cameras were used to record the experiments.

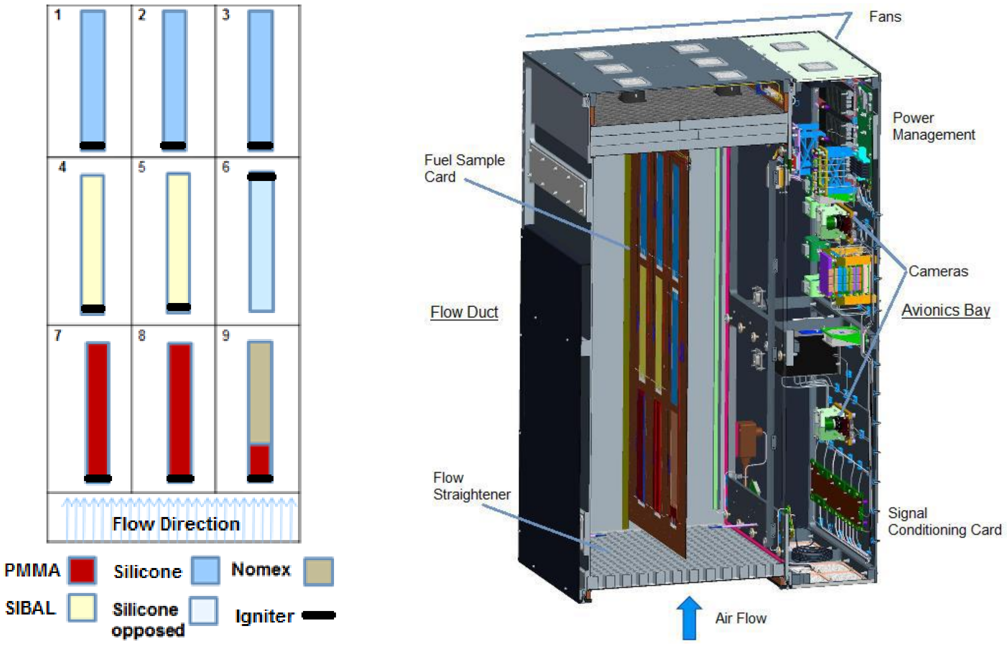

Figure 19 – Left, schematic showing the place where the PDMS and other samples were allocated for the Saffire II tests. On the right, a rendering of the sample holder card inside the chamber. Image obtained from Niehaus et al. [317].

As seen in *Figure 19*, the sample cardholder occupied the entire width of the chamber. As such, the incoming forced flow could have created a boundary layer over the cardholder. The distance from the top edge of the sample card holder to the samples igniter (where the flame starts) is 72 cm; the incoming forced flow of 20 cm/s encounters the sample card and creates a boundary layer. Knowing that air's kinematic viscosity at 20 °C is $1.516 * 10^{-5}$ m^2/s, the laminar boundary layer thickness is then 3.7 cm. Thus, the forced flow over the PDMS samples (at the ignition location) is lower than 20 cm/s.

The Saffire II tests with the PDMS sample resulted in no flame propagation, which was not expected [317]. Images taken after the ignition period for all samples can be seen in *Figure 20*. From the images, it is clear that the ignition wire damaged the sample thermally. It seems that ignition was achieved as flames emerged after the wires were energised for some time. Nonetheless, it is not clear whether the problem is, in principle, ignition or flame spread or during the transition from ignition to flame.

Two main observations can be made based on the images taken during the Saffire II experiments. First, the area around the ignition coil is much brighter than the rest of the unburnt sample. These areas clearly might indicate an accumulation of silica-ash that has a white colour and thus reflects more light. It is not clear if the ash produced was due to thermal degradation (pyrolysis) or flaming combustion. Second, the videos revealed that a white-smoke plume was travelling along the forced flow direction. This white smoke is presumably agglomerates of silica-ash (SiO_2) being transported by the convective forces.

	Thickness	Event	Video frame
Concurrent	0.25 mm	Coil energising (2s)	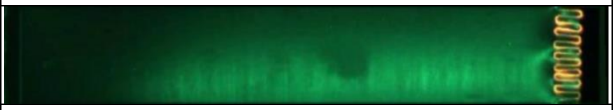
		Ignition and flames (11s)	
		Extinction (43s)	
		Post burnt (52s)	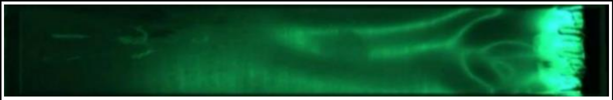
	0.61 mm	Coil energising (0s)	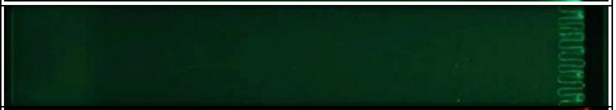
		Ignition and flames (0.26s)	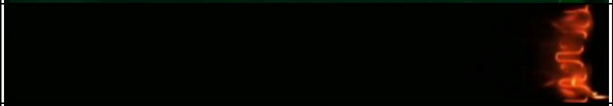
		Extinction (0.48s)	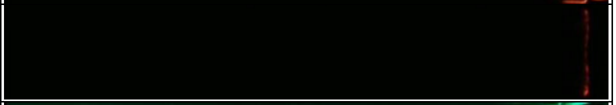
		Post-burnt (78 s)	
	1.02 mm	Coil energising (3s)	
		Ignition and flames (40s)	
		Extinction (68s)	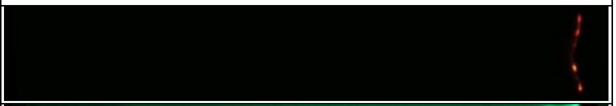
		Extinction (82s)	
Opposed	0.36 mm	Coil energising (12s)	

		Ignition and flames (46s)	
		Extinction (66s)	
		Post-burnt (84s)	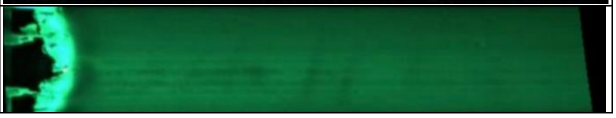

Figure 20 – Frames taken from video recordings of PDMS tests during Saffire II. Each samples had dimensions of 50 mm x 300 mm. The frames are taken during three key events: energising of ignitor, ignition of sample and diffusion flames, and extinction. In all experiments, the forced flow direction is from right to left. The flame spread is concurrent and opposed to the forced flow in the corresponding experiments.

The corresponding burnt lengths, listed in *Table 8*, measured from the Saffire II videos, are minimal and comply with the NASA Test 1 criterion. A priori, one might easily conclude that the PDMS membranes are safe materials to be used in spacecraft applications. These results, however, do not strengthen the current flammability criteria for material selection. Still, the fundamental mechanisms behind PDMS fire behaviour are unknown, and such behaviour might be different in other environmental conditions. Therefore, it is essential to conduct a fundamental study on the behaviour of PDMS membranes.

Table 8 – Burnt length results from an anticipation study conducted by Niehaus et al. [317] and from Saffire II [26].

Spread direction	PDMS membrane thickness [mm]	Burnt length [cm]	
		1g [317]	Saffire II [26]
Upwards/concurrent	0.25	27.5	0.0
	0.61	7.6	0.0
	1.00	0.0	0.0
Downwards/opposed	0.36	30	1.5

5. Hypothesis and objectives

As seen in the previous Chapter, there is a need to understand the leading mechanism behind the flammability behaviour of the polydimethylsiloxanes in normal gravity. Such a study will also support the understanding of microgravity environments. Thus, the main question relevant in the current investigation are:

- What are the dominant mechanisms in the flammability behaviour on PDMS membranes and similar materials?
- What is the effect of microgravity on the flammability behaviour of PDMS membranes?
- Are the Saffire II results with PDMS inherent to an ignition problem or to a flame spread problem?
- What is the simultaneous effect of the silica-ash deposition on the heat and mass transfer for ignition and flame spread behaviour?

It is hypothesised that the formation and deposition of silica-ash significantly affect the flammability behaviour of PDMS membranes, and it could have led to the non-propagation of flames during Saffire II. Despite such results, valuable lessons can be learnt from the information obtained from the videos. These videos offer interesting information on the ignition, flame spread and near-limit behaviour that could be explained with complementary experiments in other microgravity ground-based platforms or normal-gravity data. Hence, the current investigation was motivated to elucidate the flammability behaviour of PDMS in microgravity conditions through a series of normal-gravity experiments.

Thus, a series of experiments were designed to obtain normal-gravity data on four key aspects: silica-ash transport and deposition, piloted ignition, flame spread and near-limit behaviour. The data produced in normal gravity can be compared with the information from Saffire II, and phenomenological comparisons and predictions could be established. The proposed flammability methods, the LOI-MLOC and the pressure modelling were used along with other experimental methods. In addition, the results are expected to cast some light on various aspects discussed in previous chapters.

6. Materials and methodology

5.1. Experimental methodology

The materials tested in this study were polydimethylsiloxane membranes manufactured by SSP (Specialty Silicone Products Inc). The commercial name is Polydimethyl Silicone membrane with the commercial code SSP-M823. These silicone membranes are used in various applications owing to their permeability properties – they are permeable to gases but are impermeable to liquids. The membrane thicknesses employed in the current investigation were 0.125 mm, 0.152 mm, 0.2 mm, 0.25 mm, 0.36 mm and 0.61 mm. These membranes are the same that were tested during the Saffire II testing programme aboard the Cygnus spacecraft. The properties provided by the manufacturer are listed in *Table 9*. The manufacturer did not provide the physical and thermochemical properties. Consequently, the properties from other studies for similar materials will be used in the analysis of the experiments (see *Table 8* in Chapter 3.1). For the PDMS used for the current investigation, it is suspected that the PDMS has added silica filler to strengthen its properties [312].

Table 9 – Physical properties of PDMS membranes from SSP.

Material Property	Value	Units	Reference
Tensile Elongation	1300	psi	Data sheet brochure from manufacturer [320]
Elongation (400 min)	570	%	
Specific Gravity	1.12 – 1.16	-	
Operating Temperature Range	-70 – 200	°C	

In addition, a clear, thin 0.125 mm PMMA film was tested in two of the experimental rigs to validate the experimental rigs' design and the theoretical approaches used for the PDMS samples. The PMMA membrane is commercially known as Acryplen HBS006 and is manufactured by Mitsubishi Chemical Corporation. The properties of this PMMA can be found in *Table 10.*

Table 10 – Physical properties of PMMA.

Material Property	Value	Units	Reference
Density	1.14	g/cm^3	Brochure from manufacturer
Vaporisation temperature	670	K	[321]
Thermal conductivity	$5.1 \cdot 10^{-5}$	W/mmK	
Specific heat at room temperature	1465	J/kgK	
Flame temperature	2640	K	
Pre-exponential factor in the gas-phase	$1.0 \cdot 10^{9}$	m^3/kgs	[45]
Activation energy in the gas-phase	$1.5 \cdot 10^{5}$	J/mol	

The PDMS membranes and the PMMA film were tested in a series of experimental ad-hoc rigs and more standardised testing equipment. *Figure 21* depicts a chart showing the rigs, standard methods and measuring techniques employed to study the flammability behaviour of PDMS experimentally. The Saffire test is also included for comparison as the current results will be compared against those obtained during Saffire II. The main ad-hoc rigs used are the flow tunnel, the modified FPA and the TOPOFLAME chamber. In each particular rig, the goal was to study the effect of various environmental parameters (forced flow intensity, oxygen concentration and ambient pressure) on the ignition, flame spread and near-limit phenomena. During the Saffire II test, the effect of forced flow on the flame spread in microgravity was the quantitative goal. From these microgravity tests, the ignition behaviour could also be extracted to be compared with the normal-gravity experiments.

Three standard testing methods were used: cone calorimeter, thermogravimetric analysis (TGA), and scanning electron microscope (SEM). The cone was used to evaluate the piloted ignition behaviour of the PDMS samples under stagnant flow conditions. In addition, essential information could be obtained from the cone method (critical heat flux, heat of combustion, etc.). The kinetic properties for the thermal decomposition of the PDMS under oxidative and in nitrogen environments were obtained from the thermogravimetric analysis (TGA) test.

The SEM was utilised to quantify the silica ash, SiO_2, and deposition on the post-burnt (in extinction conditions) samples. The gravimetric weight loss measurements were done with weighing scales wherever it was feasible (only in the TOPOFLAME combustion chamber). Videos were recorded for characterisation and tracking of the flame. Infrared cameras were used to quantify the characteristic solid-phase lengths. The gas-phase and solid-phase temperatures were recorded by employing thermocouples.

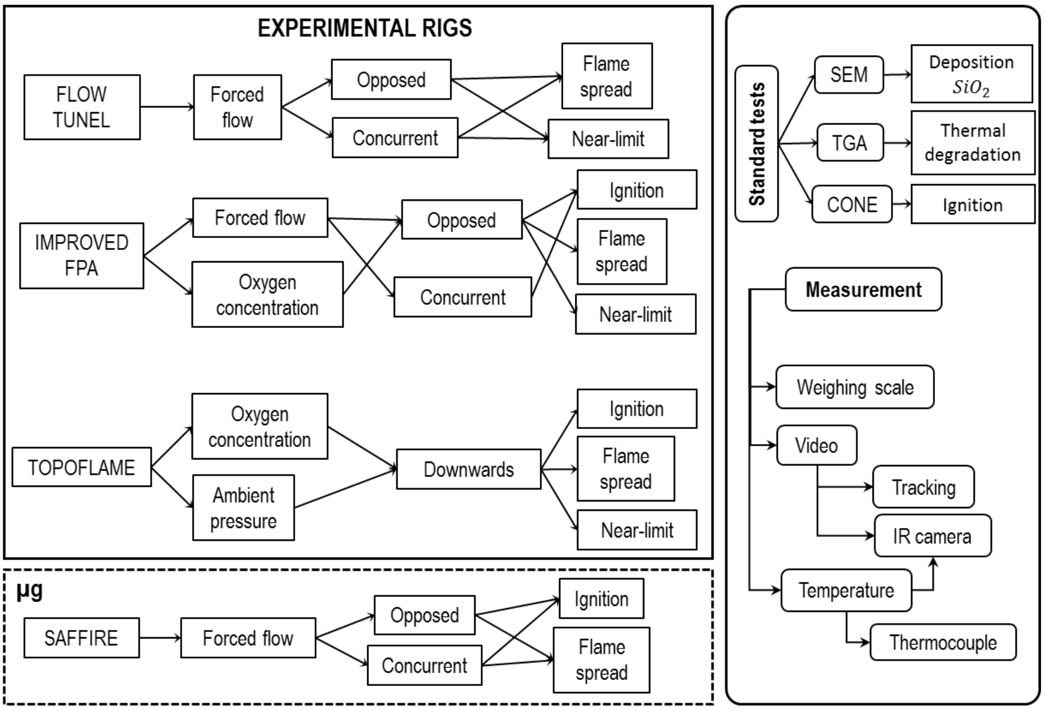

Figure 21 – Overview of the experimental rigs, standard tests and measurement techniques used for the current investigation. The Saffire II experiments were not carried out in this study, but data and information from the experiments is used.

The rate of opposed flame spread is defined by the flame tip, or flame base, location as a function of time. The opposed flame spread was observed to be steady in most experiments with a few exceptions (in near-limit conditions). As the flame tip and flame base position were tracked, the characteristic flame length could be extracted. In the case of concurrent flame spread, this was very unsteady and different from the opposed case. There was a fuel burnout in the opposed flame, whereas the flame length seemed to grow over time in the concurrent case. Thus, for concurrent flame spread, the rate is the flame's advancement over time, and it was measured whenever the flame showed steady behaviour. The near-limit is defined when the flame spread is no longer sustained, and since there were various sample sizes, the extinction was defined as when the flame did not spread more than half of the total sample length. Similarly to the Saffire II experiments, the sample dimensions were the same in the flow tunnel and TOPOFLAME (5 cm x 30 cm). However, in the improved FPA, the combustion chamber was much smaller, and the sample was much smaller than in the previous rigs, namely 10 cm x 5 cm.

The flame spread was studied under opposed and concurrent forced flows in the flow tunnel. In the improved FPA, only opposed flame spread was studied. In the TOPOFLAME combustion chamber, no forced flow was imposed on the flame spread. The sample was ignited in the top edge, and the established travelled downwards. The effect of forced flow on the piloted ignition was studied in the improved FPA. The heating coils used as the pilot were placed at the top of the sample to allow opposed flame spread and at the bottom of the sample to allow concurrent flame spread. Consequently, in this rig, the piloted ignition was evaluated under opposed and concurrent forced flows. However, the problem is fundamentally the same. In the TOPOFLAME, the effect of the ambient conditions on the piloted ignition was also evaluated. The rigs and the experimental method will be described in more detail in the following. Note that the measurement details for each of these rigs are separated into a subchapter on diagnostics (See Subchapter 5.1.5).

5.1.1. Flow tunnel

A customised rig was designed and constructed to study the flame spread behaviour (including the near-limit or extinction phenomenon) for two flow configurations (opposed and concurrent). The flow tunnel consists of three sections, the lower- and middle-part act as a flow straightener where the flow is mixed and passed through a honeycomb mesh and as the transition area to the test section, as shown in *Figure 22*. A fan was located at the bottom of the rig, just before the honeycomb. The top part, where the sample holder is located, has inner dimensions of 250 mm x 250 mm. Thus, it is ensured that the tunnel allows the flame to expand and diffuse thermally. There are two transparent PMMA panels in the top part of the tunnel, the frontal PMMA panel allows to take videos of the flame spread. The side PMMA panel is permitted to inspect the flame thickness.

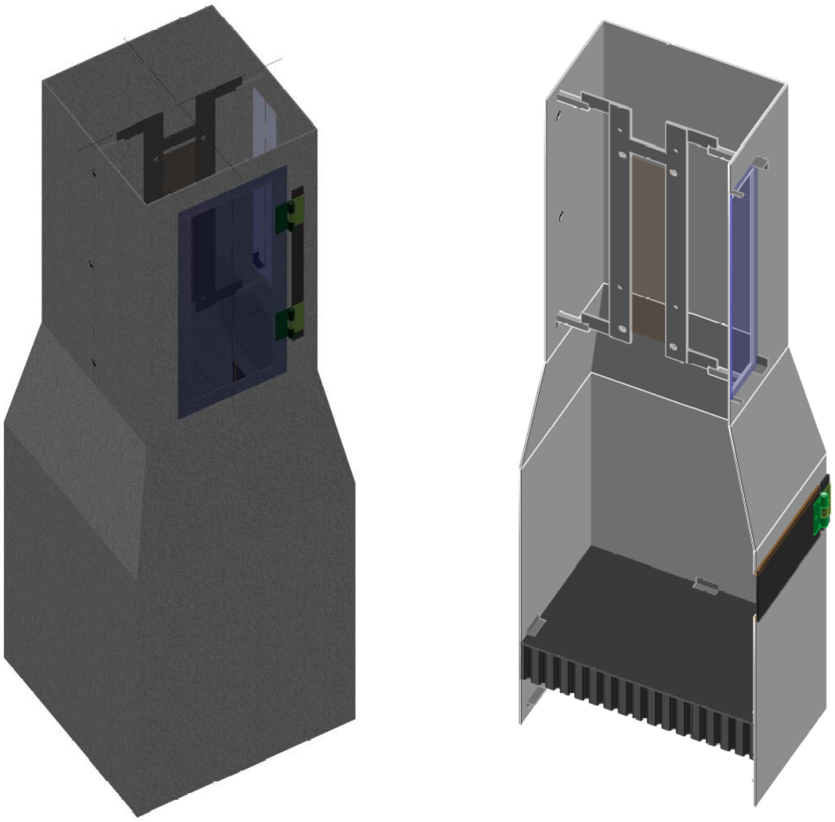

Figure 22 – Rendering of the flow tunnel rig used for the experimental work. The entire rig can be seen on the left with the sample holder placed inside. A vertical section allows the sample holder to see the position inside the tunnel on the right. The total height of the tunnel is 1 metre. The inner size of the top part and of the bottom part are 0.25 m x 0.25 m and 0.35 m x 0.36 m, respectively.

Figure 23 shows the three sample holders that were designed for the flow tunnel. The sample holders for the flat samples consist of two aluminium profiles where the sample is placed in the middle. The sample holders can accommodate samples dimensions of 30 cm x 5 cm and 30 cm x 10 cm. In addition, a third sample holder can host insulated wires. For the current investigation, only the 30 cm x 5 cm sample holders were employed. Notice that those are the same dimensions for the samples used in the Saffire II test, and they are the same dimensions prescribed in NASA STD-6001 Test 1.

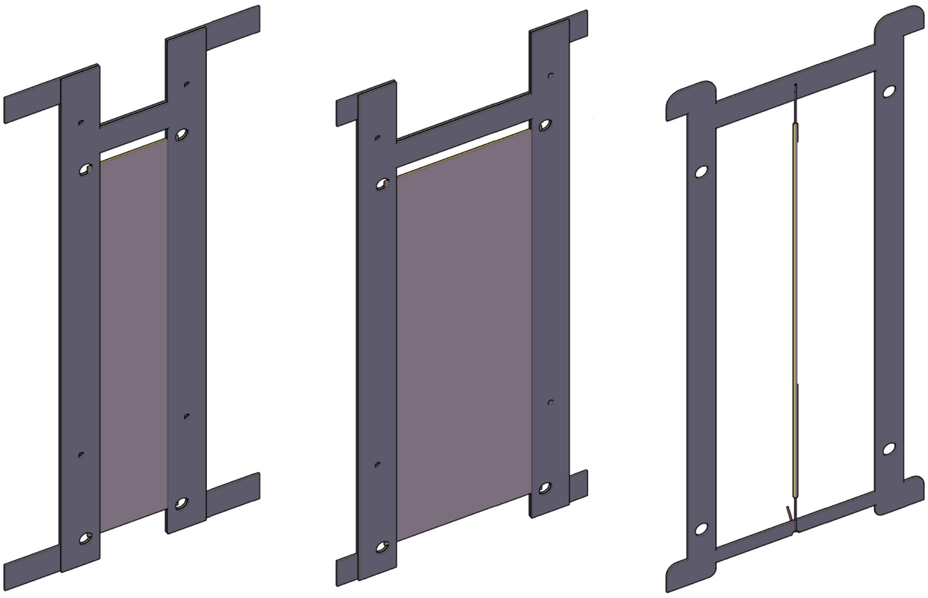

Figure 23 – Rendering of three sample holders that can be allocated in the tunnel rig apparatus. From left to right, the sample holder for a flat 5 cm x 30 cm sample, for a 10 cm x 30 cm sample, and for a 30 cm insulated wire sample.

The velocity flow profile was measured with a hot wire anemometer (CTV 210-R) at the bottom, middle, and top of the sample's position inside the flow tunnel. The flow measurements are shown in *Figure 24,* and it is seen that the flow is laminar up to 60-70 cm/s (Re number is 4000). After that, the force flow starts to become turbulent. Laminar and turbulent flows were considered to be used for the experimental matrix as it was not clear where the extinction limit would occur for the PDMS samples. For the PMMA films, the extinction limit was expected to occur after 50-60 cm/s.

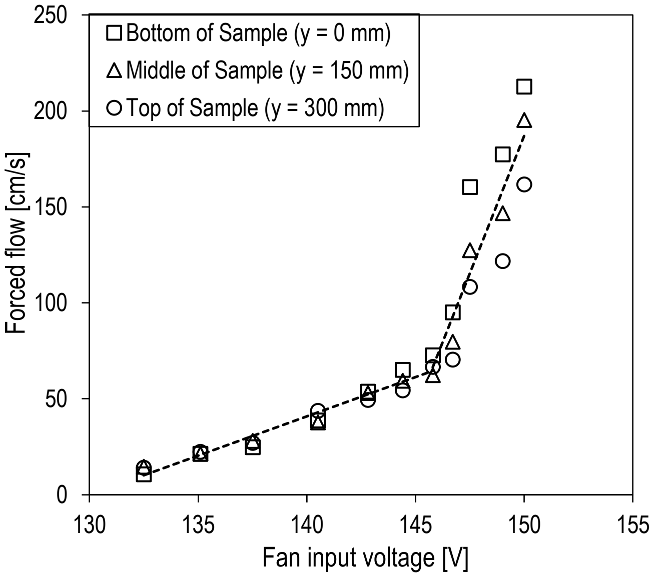

Figure 24 – Flow velocity measurement inside the flow tunnel rig. The measurements were done where the sample is placed.

Two ignition systems were used depending on the laminar flow or turbulent flows. For laminar flows, a 23-gauge AWG Nickel-Chromium resistant wire was used and was energised for up to 10 seconds at 10 A; thus, the energy provided for ignition was 754 J. The wires were coiled (8 mm diameter) and threaded through 7 holes closely spaced across the sample width, as shown in *Figure 25*. Under a very high forced flow, ignition could not be attained easily using heating coils. Thus, a flame torch was used to attain ignition. The ignition method was applied to the top part of the sample to allow flames to travel downstream (opposed flame spread). When the ignition was applied to the bottom, the flame traveled upwards (concurrent). The same procedure was employed in the other two experimental set-ups. In addition, the coil system was used as a pilot to study ignition behaviour under various parameters.

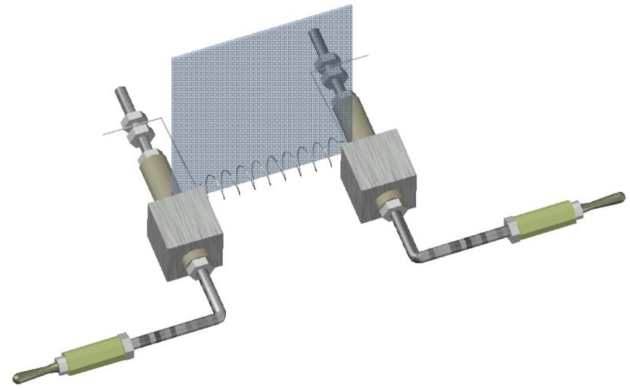

Figure 25 – Rendering of the ignition system used to achieve flame spread under laminar flows. The same system was used to study ignition in the other rigs. The width of the sample is 5 cm.

5.1.2. Modified Fire Propagation Apparatus (FPA)

The Fire Propagation Apparatus (FPA) was designed by FM Global and has since been standardised (ASTM E2058). The apparatus serves to determine critical heat flux, heat release rates, effective heat of combustion and other thermal and fire indexes. The main features of the FPA are the infrared heaters (allowing imposed heat fluxes of up to 100 kW/m^2), mass loss measurements, ignition pilot tube, gas sampling analysis (O_2, CO_2 and CO) and air supply inside the chamber (forced flow). The FPA is located in the fire lab at the University of Edinburgh, and it allows to study ignition as a function of the forced flow and incident heat flux. However, the FPA rig had some shortcomings with respect to the goals of the current investigation. First, the flow inside the FPA combustion chamber was not even across the section. Second, there were no sample holders that allowed studying the flame spread on flat samples parallel to the forced flows. Third, the maximum forced flow measured with a hot wire anemometer was 60 cm/s, and higher flows were required to achieve near-limit conditions. Last, the chamber's supply of flow could not provide oxygen concentrations higher than 21%. Therefore, several improvements were required to be implemented in the FPA to fulfil the current investigation's goal.

Improving the flow inside the combustion chamber and achieving higher forced flow was done by inserting a duct reducer, see *Figure 26*. The flow reducer transitions from a 155 mm diameter (the FPA combustion chamber) to a 90 mm diameter. The duct reducer was placed inside the FPA combustion chamber, see *Figure 27*. Thus, the forced flow could be much higher at the duct reducer outlet. Glass beds (3 mm in diameter) were placed on top of a wire mesh at the bottom of the duct reducer. In the top part of the duct reducer, a 15 mm thick honeycomb was placed to straighten the flow. The detailed measurements of the flow will be discussed later.

The duct reducer has three small tubes that serve to allocate the wires for the ignition system. Two small female brackets were welded to the top of the duct reducer. Thus, the sample holder could be placed easily as matching male brackets (see *Figure 26*. The sample holder was designed to host a 10 cm x 5 cm sample of various thicknesses. The ignition system could be placed on top or the bottom of the sample. Thus, flammability (ignition, flame spread, and near-limit) could be studied under opposed or concurrent forced flows.

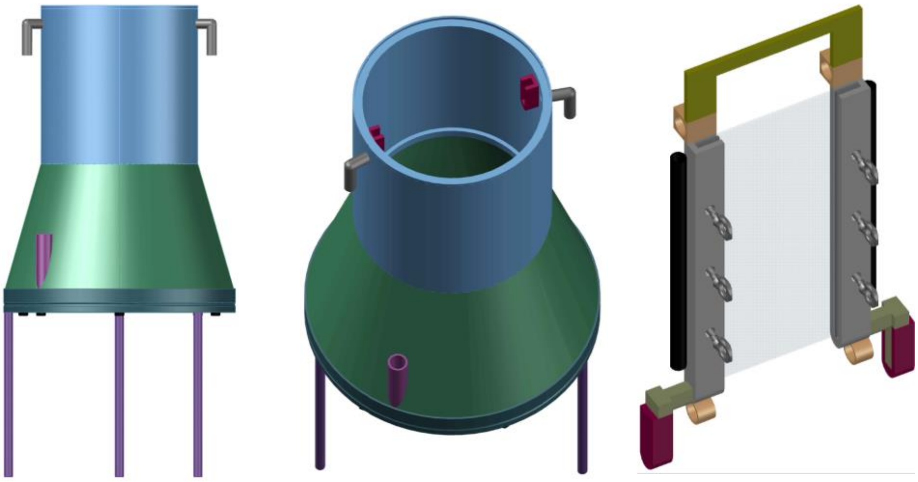

Figure 26 – Rendering of the duct reducer used to improve the flow inside the FPA combustion chamber and of the sample holder. From left to right: a side view of the reducer, a 3D view from above of the duct reducer, and a 3D view of the sample holder. The inner diameter of the top part is 0.09 m, the total

height of the duct reducer is 0.3 m. The sample dimensions are 100 mm x 50 mm.

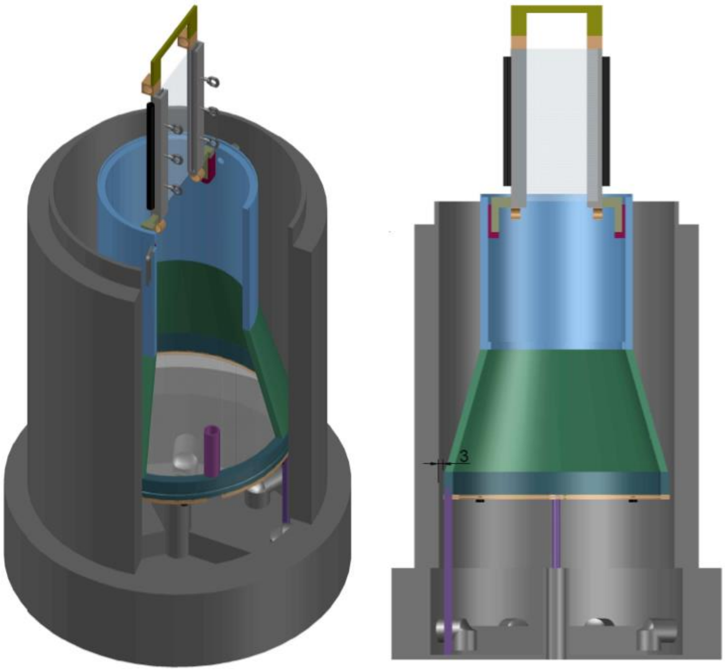

Figure 27 – Rendering of the duct reducer inserted in the FPA chamber along with the sample holder. On the left, a 3D view of a sectioned improved FPA rig. On the right is a vertical section of the improved rig. The inner diameter of the rig is 0.154 m.

The reduction of the oxygen concentration (lower than 21%) on the incoming flow into the chamber was easily achievable as it is part of the in-built design of the FPA system. Nitrogen can be mixed with air before reaching the combustion chamber, allowing for oxygen concentrations between 14 and 21%. However, providing incoming flows with higher oxygen concentrations required installing a mass flow controller Omega FMA-2610A-V2. The mass flow controller could then provide oxygen from a cylinder (40% oxygen content). The 40% oxygen pipeline was joined with the incoming airflow line. The lines were combined as far as possible from the FPA combustion chamber to ensure good mixing of the air and the oxygen. Thus, any oxygen concentration of up to 40% could be obtained. The oxygen probes measured the oxygen concentration in the combustion chamber's outlet, ensuring that the target concentration was achieved. Finally, providing the appropriate oxygen concentration and forced flow at the same time was also challenging. The incoming pressure was relatively high for a specific oxygen concentration and did not allow to obtain low forced flows (<60 cm/s). The excess flow had to be removed to allow for small forced flows at the desired oxygen concentration.

A hot-wire anemometer (CTV 210-R) was used to characterise the flow profile seen by the sample at the bottom edge. The flow measurements that were taken axially (along the sample width) are depicted in *Figure 28*. It is seen that the flow profile remains even for a series of forced flow intensities. The average flow velocity measurements at the bottom of the sample are plotted against the incoming volumetric flow, see *Figure 29*. The measurements show that the flow in the improved FPA is laminar and can reach higher values.

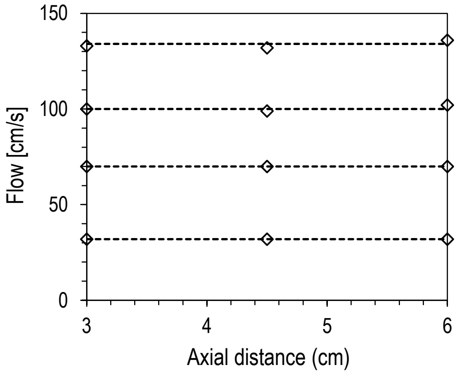

Figure 28 – Discrete flow measurements at axial distances with respect to the bottom of the sample.

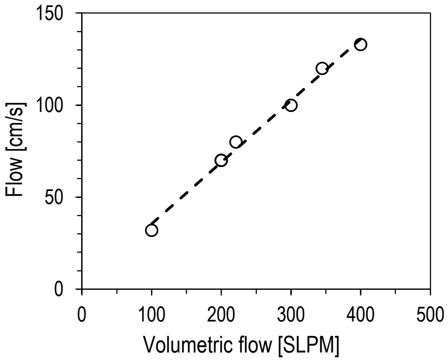

Figure 29 – Average flow measurements at the sample's bottom edge as a function of the volumetric inlet flow provided by the mass flow controllers.

Lastly, for each series of tests done with the incident heat flux as a parameter, a calibration of the heat flux received by the sample was required. A heat flux gauge was used to measure the heat flux vertically whenever it was possible. The heat flux was estimated based on the view factor from Hamilton and Morgan [322]. In *Figure 30*, both the heat flux measurements and predictions are plotted as a function of the energy provided to the heat lamps.

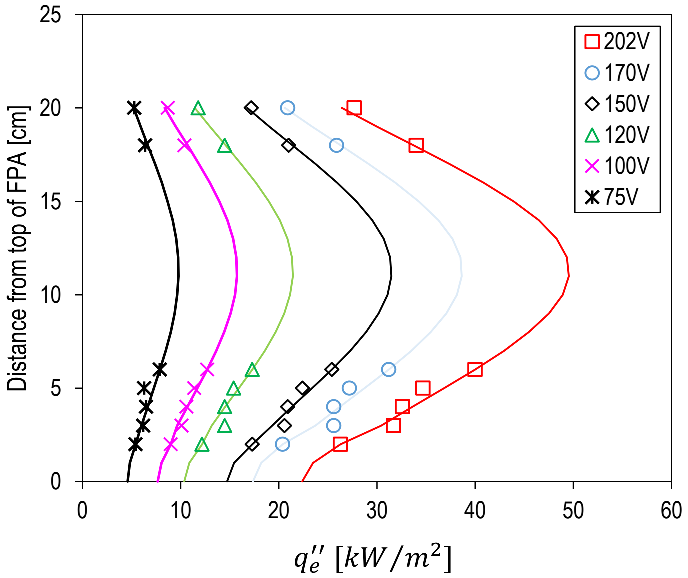

Figure 30 – Measured and estimated heat flux that a vertical sample experiences in the FPA (measurements for one side what the sample experience).

5.1.3. TOPOFLAME chamber

Figure 31 shows a photograph of the TOPOFLAME rig, which is a 1000 L customised combustion chamber located in the ZARM facilities in Bremen. Two environmental conditions can be controlled inside the chamber: oxygen concentration and ambient pressure. The ambient pressure can vary from vacuum to 5 bar, and the oxygen concentration from 0 to 40%. For the experimental matrix, two sample thicknesses were selected, 0.125 mm and 0.25 mm, and these were tested for two sets of experimental conditions. For the first set, both samples were tested under normoxic conditions. Thus, the effect of a normoxic environment on two sample thicknesses could be evaluated. The 0.125 mm sample was tested in a wider variety of oxygen concentrations and ambient pressures for the second set. The later set's goal was to investigate the dependency of normoxic conditions on the downwards flame spread. In addition, the extinction conditions were also sought by extending the originally planned experiments. The diagnostic systems will be discussed later in Subchapter 5.1.5.

Figure 31 – The assembled TOPOFLAME rig before a test takes place, the inner volumetric capacity of the chamber is 1000 L. The total height of the chamber is 2.6 m.

5.1.4. Other standard tests

5.1.4.1. Cone calorimeter

The cone calorimeter is a known standardised method (ASTM E 1354, ASTM D 5485) used to study the flammability behaviour through piloted ignition and burning. The cone was used to evaluate the ignition behaviour of various thicknesses of PDMS membranes under stagnant flow conditions. Besides, the critical heat flux of the PDMS could be derived from the results. During the experiments, it was observed that the PDMS sample would expand and thus get closer to the ignition pilot device, which could affect the results. Therefore, a mesh was tightly placed on top of the sample to avoid this.

5.1.4.2. SEM

In the tests where the samples were not fully consumed, small samples of the unburnt fuel were taken to be analysed in a scanning electron microscope (SEM) JEOL JSM-6010 PLUS/LN. The SEM is capable of magnifying in the order of 10μm to 500μm. For the concurrent experiments, the samples were taken at the point of extinguishment and intervals of 20 mm up to 80 mm for the downward spread experiments.

For the opposed experiments, samples were taken from the extinguishment edge. Then, the cross-sections of the samples were placed inside the SEM chamber. The images provided by SEM were then processed in order to quantify the silica ash thickness.

5.1.4.3. TGA

TGA or Thermogravimetric analysis (ASTM E1641-16) was used to extract the solid-phase kinetic properties of the PDMS membrane used in the current investigation. The procedure followed is presented in detail in the corresponding standard, which uses the Ozawa, Flynn and Wall method. Four samples were subjected to heating rates of 2.5 K/min, 5 K/min, 7.5 K/min and 10 K/min, respectively. The kinetic properties obtained are the solid-phase activation energy and pre-exponential factor. Based on these properties, the pyrolysis rates for the PDMS sample could also be estimated, which can be used for assessing the ignition behaviour. The temperature gradients and the mass loss profiles were also compared with similar materials.

5.1.5. Diagnostic systems

In the tunnel rig and FPA, the ignition and flame spread were recorded with a Canon Camera. The videos were subsequently analysed by a MATLAB binary code where the flame leading edge was tracked as a function of time. Thus, the flame spread rate could be estimated. In the case where the heating lamps were used in the FPA, the code was modified to look at the RGB colours to track the burnout leading edge position in the bright background.

K-type thermocouples with 0.5 mm diameter were placed discretely across the sample to measure the gas-phase (flame) and solid-phase temperatures in a rig that followed the NASA-STD test 1 procedure. In addition, for the solid-phase pre-heat and pyrolysis areas and characteristic lengths, a FLIR A655sc Infrared camera IR camera was used. The IR camera covers a temperature range from 300 °C to 2000 °C, and the spectral range is between 7.0 and 14.0 μm and was set to operate at a frame rate of 30 Hz. The emissivity used will be discussed in Chapter 7 – Results.

The diagnostic systems used in the TOPOFLAME chamber can be seen in *Figure 32*. Three cameras were used for visual observations and measurements: A Canon EOS 7000 was placed outside, and its goal was to obtain side view pictures of the flames. The other two cameras were placed inside the chamber, a VIS camera and an IR camera (8.33 f/s). A mass balance was used to monitor each test's mass loss and mass-loss rate. The ignition consisted of a 29 AWG Kanthal wire coiled to the top of the sample. The energy released to the different models was 80 J, equivalent to 8 s of 10W.

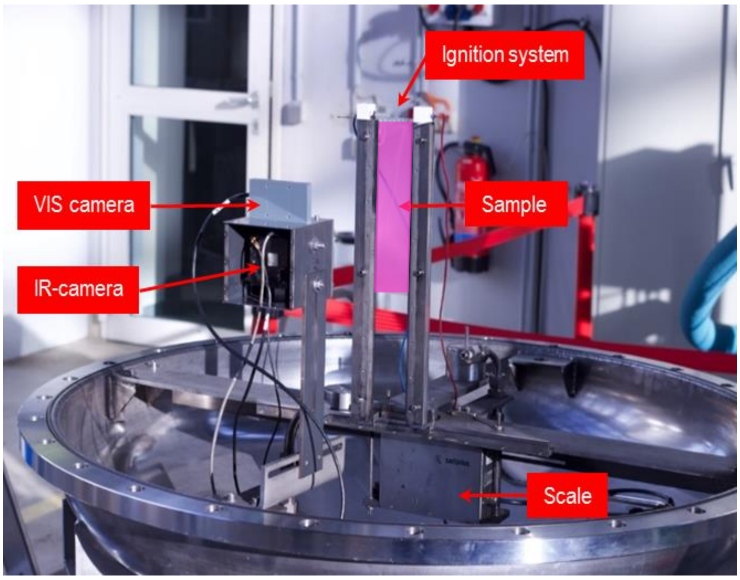

Figure 32 - The internal structure and the diagnostic systems in the TOPOFLAME combustion chamber. The sample (shaded in pink) is 50 x 200 mm in dimensions.

7. Results

In the second part, the experimental framework to study the flammability behaviour of PDMS membranes is laid out. An extended simplified theory and experimental methods are employed to derive some of the fundamental properties of silicones and analyse them. The same flammability concepts used in Chapter 2 will be studied, namely ignition, flame spread and near-limit. Lastly, the results will be presented and discussed accordingly.

7.1. Validation

Both rigs purposely designed and modified for the current investigation – the flow tunnel and improved FPA – were required to undergo a validation review. It was important to ascertain the control of two parameters in both experimental apparatuses, namely the forced flow in both rigs and the amount of oxidiser in the improved FPA.

Opposed flame spread is studied since it allows to attain steady conditions, contrarily to the concurrent case. Thus, the flame spread was first studied under the thermal regime where flames were established over the PMMA sample under opposed forced flow (ambient air at atmospheric pressure). Also, using identical solid fuels, the blow-off limits for opposed flame spread were studied following an established theoretical approach. Comparisons were established with literature where the same fuel was used.

To begin, it was examined whether both rigs provided the even forced flow required to attain the thermal regime. As discussed in Chapter 2.1.2, the thermal regime for opposed flame spread is characterised by the flame spread rate independence from the oncoming forced flow. This is true for a range of forced flows where the conduction of heat from the gas-phase to the solid-phase at the leading edge dominates the spread phenomenon [323]. Based on the thin-sheet problem, de Ris [52] derived an expression for the opposed flame spread on thermally-thin fuels

$$V_{f,o} = \sqrt{2}\frac{\lambda}{\rho_s c_p \tau}\left(\frac{T_f - T_v}{T_v - T_\infty}\right) \qquad \text{Equation 5}$$

Notice that the equation only portrays heat conduction from the gas-phase to bring the solid-phase to its vaporisation temperature. This formula does not hold when kinetics start to get noticeable (increasing forced flows or reduced oxygen concentration). The kinetic effects will be discussed later on in the second part of the validation. Using de Ris' theoretical expression with the properties of the fuel found in the literature, the flame spread rates were estimated in the air under atmospheric conditions. The results of this are presented in *Figure 33*. In the same illustration, the flame spread result conducted in both rigs and the data point from other investigations [323] is also plotted. As expected, the current data from both rigs aligns with the theoretical predictions for flows up to 60 cm/s. For flows higher than 60 cm/s, the flame spread rates decrease with increasing forced flow. This behaviour is characterised by kinetics, and Equation 5 cannot be applied.

The data from Takahashi et al. [28,119,192], only one point coincides with the current data. In the experimental work conducted by Takahashi et al. [28,119,192], the sample width tested was either 1 cm or 2 cm. As a consequence, their flame spread was three-dimensional in nature and was affected either by side oxygen supply or cooling effects, see Chapter 2.2. In contrast, the sample used herein was 5 cm in width and was therefore affected by those concerns. These results confirm that the forced flow provided by both rigs met the initial goal and yielded relevant results.

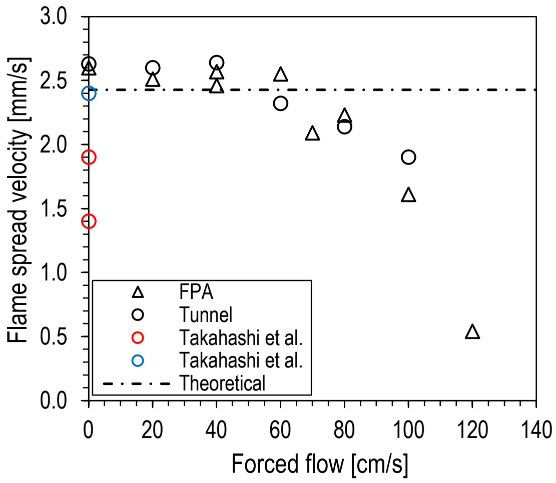

Figure 33 – Estimation and experimental flame spread rates for the 0.125 PMMA sample as a function of the opposed forced flow. The data is from the current study and literature [28,119,192].

For the second part of the validation, in the improved FPA, the goal was to provide a reasonably accurate oxygen concentration. A theoretical approach was used to evaluate the kinetic extinction regime for the PMMA and derive fundamental properties required to predict kinetics. The theoretical approach used is thus introduced in the following.

Bhattacharjee and co-workers demonstrated the limitation of the assumptions established in de Ris' expression for opposed flames spread [43,54], which are mainly related to hydrodynamics and kinetics. Thus, they derived a semi-empirical expression based on an extended simplified theoretical analysis for both cases of thermally-thin and thermally-thick samples. Their theoretical model, labelled as the Extended Simplified Theory (EST), predicted the flame structure and the flame spread rate over thermally thin and thick fuels in the thermal regime. Using the same theoretical method (EST), Takahashi, Bhattacharjee and co-workers [137,324,325] implemented the effect of radiation and derived close-up analytical flame spread formulae. They assumed surface re-radiation to be dominant in their solution and disregarded gas-phase radiation. The EST equations showed qualitative agreement with the microgravity experimental results demonstrating the validity of the approach. Takahashi et al. [195,240,241] included kinetic effects in the EST formula through the Damköhler number and were able to predict the extinction limits in microgravity and normal-gravity, and they were also able to estimate the MLOC (See the flammability method in Chapter 2.4.3. In the EST, the flame spread rate for thermally-thin fuels in the thermal regime is:

$$V_{f,th} = \frac{\lambda_g}{\rho_s c_s \tau_s}\left(\frac{T_f - T_v}{T_v - T_\infty}\right) \qquad \text{Equation 6}$$

The flame spread expression is similar to de Ris expression. The surface re-radiation, which is only available in microgravity environments, is represented by a non-dimensional radiation number.

$$R_{rad,e} = \frac{\in(1-a_{abs})\sigma\left(T_v^4 - T_\infty^4\right)}{\rho_g c_g V_r (T_v - T_\infty)}$$ Equation 7

The effect of chemistry is evaluated through the Damköhler number, which is flow time to chemical time ratio.

$$Da_e = \frac{\alpha_g}{V_r^2} \rho_g Y_O A_g \, exp\left(-E_g / R \, T_f\right)$$ Equation 8

The relative forced flow (V_r) is the combined effect of the forced flow and flame spread rate ($V_g + V_f$). Then, the experimental flame spread in the thermal can become dimensionless:

$$\eta_{EST} = V_f / V_{f,th}$$ Equation 9

Coupling all the regimes in the opposed flame spread provides the following non-dimensional equation:

$$R_{rad,e} + \eta + (1/Da_e) = 1$$ Equation 10

At extinction conditions, this expression ($R_{rad,e} + (1/Da_e)$) approaches unity, and the dimensionless flame spread rate no longer holds, leading to extinction. Thus, Equation 10 is semi-empirical, but it still allows to examine of the extinction conditions in the radiative and kinetic regimes. The approach is simple in nature due to its assumptions. From all the properties required to estimate the extinction limit, the emissivity is often assumed to be unity for simplicity. In reality, the emissivity values depend on the emitting material's temperature and on the spectral range [326]. Another two values required in the set of equations are the gas-phase activation energy, E_g, and pre-exponential factor, A_g. These parameters can only be found in literature for well studied materials, such as PMMA. Equation 10 can also be used to extrapolate the gas-phase kinetic properties if the flame spread rates near extinction are known. The manipulation should be done carefully as it is not expected that all materials will follow the assumptions used to establish the EST.

The extinction results for the PMMA that took place in the FPA are plotted in *Figure 34*. The results show that the kinetic extinction limit was attained in the modified FPA apparatus. The extinction limit increases monotonically with increasing oxygen concentration and forced flow. Such behaviour is expected as, according to Equation 8, an increase in the oxidiser level also increases the flame temperature. The lowest oxygen concentration value, or LOI value, is 17.9 %, which is in line with values (17% & 17.3%) reported elsewhere [195,240,289]. The largest discrepancy with the values reported by Takahashi and co-workers [195,240] might be due to the main differences in experimental design. First, their sample width dimension was 2 cm as compared to the 5 cm wide samples used in the current investigation. Second, their rig was placed inside a Glovebox where it was possible to perform tests in quiescent conditions (buoyancy driven flame) at a desired oxygen concentration. Taking the flame spread results values near the kinetic extinction curve, the empirical values of the gas-phase kinetic properties were extrapolated, see *Figure 35*. As seen the values for the gas-phase activation energy and pre-exponential factor are independent from the forced flow as it was expected. The values obtained are $1.0 \cdot 10^9$ m^3/kgs and $1.5 \cdot 10^5$ J/mol for the pre-exponential factor and activation energy, respectively. Similar values for PMMA were reported by Fernandez-Pello et al. [45].

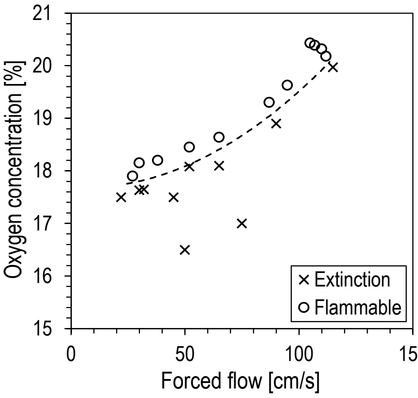

Figure 34 – Experimental normal-gravity extinction limits on for a 0.125 mm PMMA sample as a function of the forced flow and oxygen concentration.

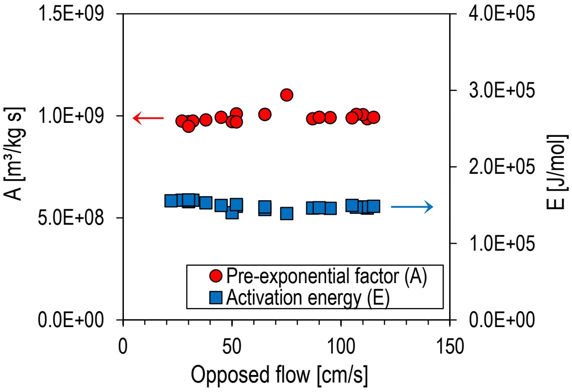

Figure 35 – Empirical gas-phase activation energy and pre-exponential factor for a 0.125 mm PMMA sample tested in near limit conditions in the modified FPA chamber.

Finally, the extinction limits were estimated based on the properties of the PMMA sample and on the properties extrapolated. The current results for the predicted extinction limits and data from literature are presented in Figure 36.

The current results deviate almost 1% in oxygen concentration compared to the literature results [195,240–242]. This difference is understandable by the two arguments provided above. Despite those discrepancies, the oxygen concentration and forced flows provided by the improved FPA can be deemed acceptable to study the flame spread and near-limit phenomena.

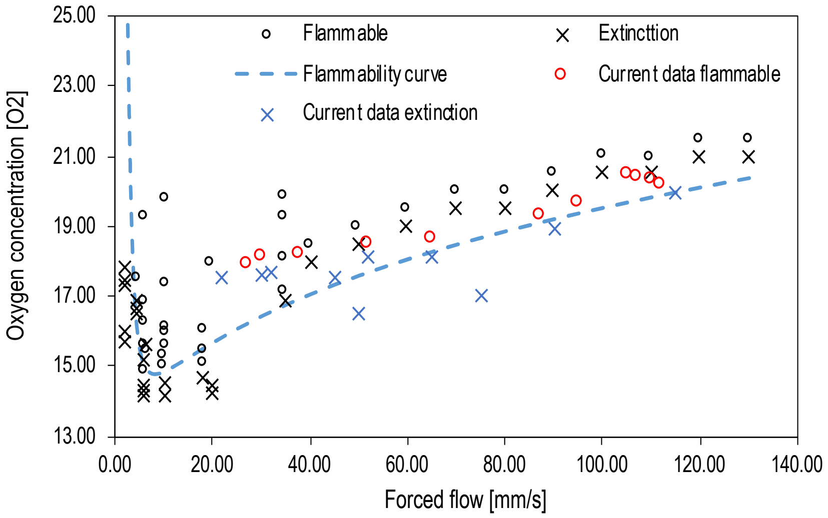

Figure 36 – Predicted extinction boundaries for a 0.125 PMMA sample as function forced flow and oxygen concentration for the current data and data from other studies [195,240–242].

7.2. Solid-phase and gas-phase temperature

The gas-phase and solid-phase temperatures can serve to establish the heat balance needed to analyse the flame spread. The gas-phase temperature readings obtained in the flow tunnel from the various thermocouples as a function of time can be seen in *Figure 37*. Each line represents the thermocouples placed discretely along with the sample which was intended to measure the solid-surface and gas-phase temperatures. As seen in *Figure 37*, the pyrolysis temperature was not measured, and the gas-phase measurements were not even. The silicone samples warped and expanded during burning, which can explain the disparity in the temperature recordings. Despite the difficulties, the maximum temperature measured was 1137 °C, which is slightly lower than the temperature values reported for measurements with thermocouples and optical pyrometry, 1200-1300 °C [308]. Again, the warping and deformation of the sample could have shifted the position of the thermocouples with respect to their measuring target, and this can explain the lower recorded temperatures. However, these recorded gas-phase temperatures are well below the adiabatic estimated flame temperature, 2134 °C (See *Figure 38*). The silica particles or ash produced during the exothermic reaction might contribute to a flame's low emissivity will deter radiative heat, and lead to lower measured temperatures [308].

The IR camera was used to track the solid-phase temperatures during various initial tests. An image taken from a video is depicted in *Figure 39*. As seen, the pyrolysis temperature recorded fluctuates between 670 K and 730 K (about 396.9 °C and 456.9 °C), approximately. In other experimental studies and thermogravimetric analysis [289], pyrolysis temperatures for silicones were reported to be 717 K, which matches the IR recording. However, in *Figure 39*, temperatures higher than the pyrolysis temperature are also observed. This can be explained by the fact that the IR camera relies on the emissivity of the recorded objects to provide the temperature. To be more precise, the corresponding software used to estimate the temperature based on the raw videos requires the emissivity values of the sample, and the PDMS and the silica-ash, produced during the exothermic reaction, have different emissivity values.

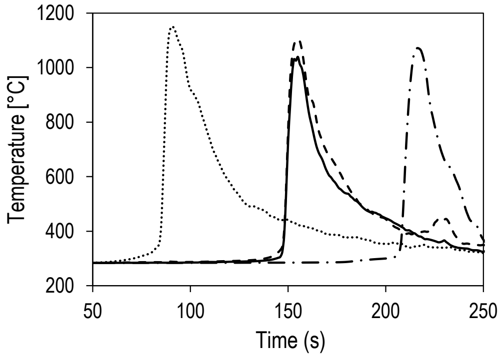

Figure 37 – Flame temperature readings were taken for downwards flame spread.

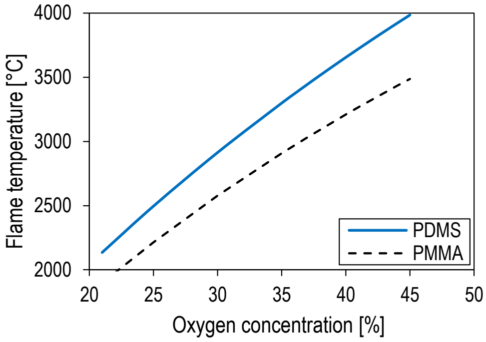

Figure 38 – Estimated adiabatic flame temperatures for PDMS and PMMA. For PDMS, the chain length is assumed to be n = 1000.

The emissivity of SiO_2 at high temperatures ranges from 0.45 to 0.9 [327] for the wavelength range of the IR. For the PDMS, there is no emissivity information in the literature, but similar materials, such as silicone rubber or glass, have variable emissivity values depending on the temperature and thickness [328–330]. Furthermore, the emissivity of the gas-phase products also varies with the wavelength [302], and, as such, the IR camera sees an overlapping of gas-phase particles, unburnt PDMS and silica ash residues forming on the PDMS ahead of the pyrolysis zone. Thus, as the silica ash lays on top of the unburnt silicone as the flame travels upwards, it is extremely challenging to discern the pyrolysis and pre-heat lengths with an IR camera. In addition, any silica-ash that forms in the combustion zone would create a shadow effect, and the IR might see the solid-phase lying in the background. Thus, the pre-heat length has only been measured for the opposed flame spread where silica-ash might be less detrimental (will be discussed in Chapter 7.5.4.).

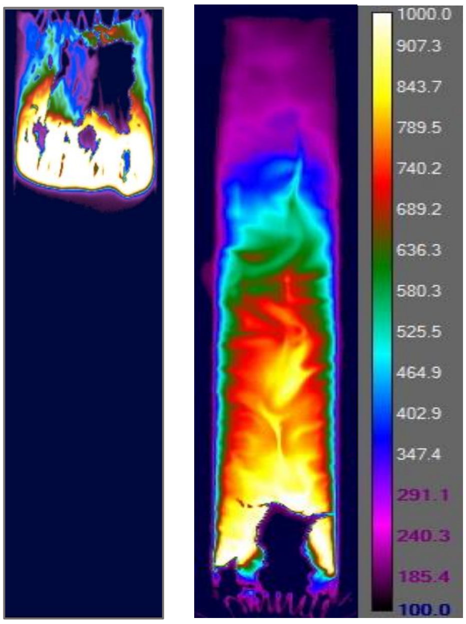

Figure 39 – Solid-phase temperatures captured by the IR camera of a 0.125 mm PDMS sample during an opposed (left) and concurrent (right) flame spread experiments. The sample dimensions were 300 x 50 mm in both experiments.

7.3. Silica-ash deposition and burnt lengths

Images of post-burnt samples where the silica-ash is visible can be seen in *Table 11*. The images correspond to selected concurrent experiments with and without forced flow. The images show the extent of the deposited white silica-ash being driven by either buoyancy or forced flow. The deposition observed during the opposed experiments will be discussed later (see Chapter 7.3.2).

Table 11 – Snapshots from concurrent representative experiments. The post-burnt images show the coverage of the silica-ash residue left. The dimensions for each samples were 300 x 50 mm.

		Sample thickness			
		0.125 mm	0.25 mm	0.36 mm	0.61 mm
Forced flow	0 cm/s		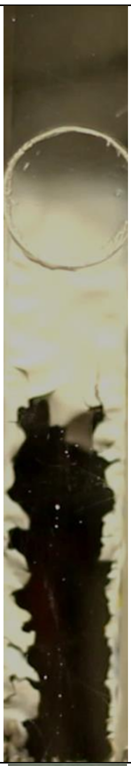	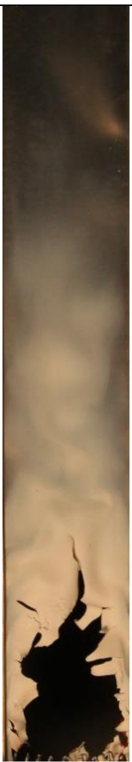	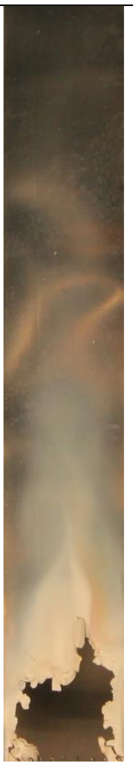
	50 cm/s				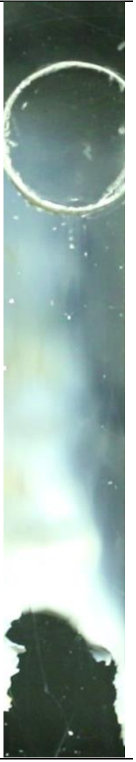

This Chapter first presents the burnt length results for various PDMS samples for flame spread in opposed and concurrent forced flows. The burnt length criterion is shown to be a weak concept for this particular material. The second part deals with the transport and deposition of silica-ash, thus establishing comparisons with soot production and flammability in microgravity environments.

7.3.1. Burnt lengths and NASA Test 1 criterion

In this section, one of the pass/fail criteria – the burnt length – in the NASA Test 1 is evaluated as a function of the sample thickness and the direction of the flame spread with respect to the forced flow. That is, both conventional upward (concurrent) and downward (or opposed) flame spread are evaluated. In addition, the variation of the forced flow velocity acts as a third variable.

The PDMS sample in Saffire II tests did not attain self-sustained flames, and the respective burnt lengths were therefore minute. In contrast, the equivalent normal gravity burnt length results (obtained from the experimental study that was undertaken to prepare the experimental matrix for Saffire II) were significantly longer (See *Table 8* in Chapter 4). These results might intuitively indicate that PDMS is not flammable in microgravity conditions and that the 15 cm burnt length criterion established in Test 1 could thus be deemed acceptable. However, these results in microgravity do not indicate the fundamental behaviour of silicone membranes and other silicone-based materials. The following results from the current study can partly anticipate the effect of environmental conditions on the burning behaviour of silicones.

The burnt length results as a function of forced flow, sample thickness and flame spread directly from the current study are plotted in *Figure 40*. It is very clear that the forced flow affected the burnt length for both opposed and concurrent flame spread. The burnt length can increase or decrease for upward or concurrent flame spread as the forced flow increases. On the contrary, for opposed flame spread, the burnt length decreased in length for high forced flows for most of the experiments conducted. The burnt length also shows dependencies on the sample thickness.

In the upward case, the results require a more detailed explanation of the mechanisms behind the non-monotonic effect of the forced flow on the burnt length. The kinetic effects start to dominate the opposed flame spread for very high forced flows; thus, the burnt length is affected negatively. In both scenarios, the deposition of silica ash, the combustion by-product of siloxanes, can help establish phenomenological arguments for both flame spread modes, as discussed in the following subchapter.

These burnt length results thus provide quantitative information in advance on how the burnt length criterion can be very subjective to scenarios beyond those included in NASA Test 1. More specifically, opposed flame spread and the effect of forced flow are not considered, although the current results indicate that they should be. Also, it can be inferred that the worst-case scenario occurs for downward flame spread, where most of the samples did not pass the burnt length criterion of less than 15 cm spread. Furthermore, it then becomes important to understand the detailed burning behaviour of silicone and siloxanes.

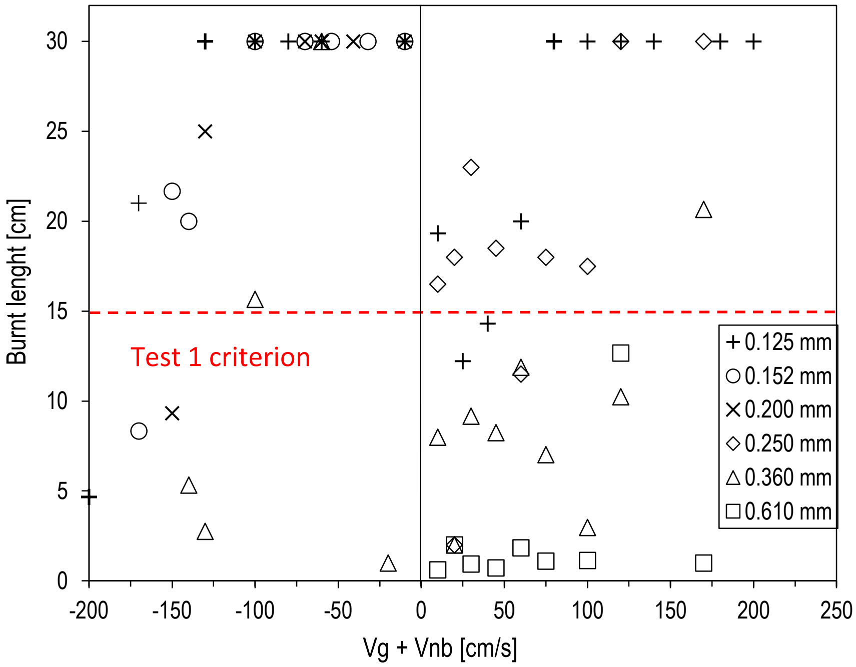

Figure 40 – Burnt lengths results for various sample thicknesses as a function of the mixed flow velocity. The negative values on the x-axis represent opposed flows, and the positive axis represents concurrent flows. The sample

had equal dimensions to those required for the NASA-STD-6001 Test 1 and the threshold limit of 15 cm is therefore included. The results were obtained from the tunnel flow rig.

7.3.2. Silica ash deposition

As discussed in Chapter 3, the amorphous silica ash (SiO_2) is a by-product that forms during thermal degradation and during the gas-phase near the combustion field. In the FPA experiments where ignition under forced flow was not viable (See Chapter 4.4.3), the area around the hot wire did not show any significant silica ash residue. It is plausible that the amount of ash produced during pyrolysis is not significant. On the contrary, during flaming, silica ash production is significant. In the experiment work from Lipowitz [308], the deposition of the silica ash in the pool fire experiments was attributed to buoyancy. That is, the particulate formed in the combustion zone had left that field, cooled down and fell back onto the silicon pool fire. However, buoyancy might not be the determinant force in the silica ash deposition in other particular scenarios.

SEM images of the post-burnt samples collected after extinction occurred in the upwards and downwards flame spread experiments are depicted in *Figure 41*. The left figure shows a very thick SiO_2 layer in the order of half-thickness of the PDMS sample. By contrast, the silica residue left in the opposed case is much thinner. In both cases, only one side of the sample had a silica-ash layer, as the other side was removed due to mechanical manipulation during SEM measurements. It is clear that the silica-ash deposition is very significant and more detrimental for the upward flame spread case. The mechanisms behind the silica-ash deposition on the unburnt fuel ahead of a travelling diffusion flame might differ from the case of silicone pool fires studied by Lipowitz [295,308]. Also, in the Saffire II, it was observed that silica-ash was formed on the sample near the ignition coil (See Chapter 4). Thus, buoyancy is not the dominant force on silica-ash deposition.

There appear to be no studies on the transport and deposition of silica-ash emerging for diffusion flame spread in normal gravity. As pointed out in

Chapter 3, most studies looking at the fire behaviour of silicones and polysiloxanes focus on silica ash's overall behaviour or effect on burning parameters. Thus, predictions in microgravity can only be attempted or speculated. Soot deposition is a relatively similar problem that could potentially help establish comparisons.

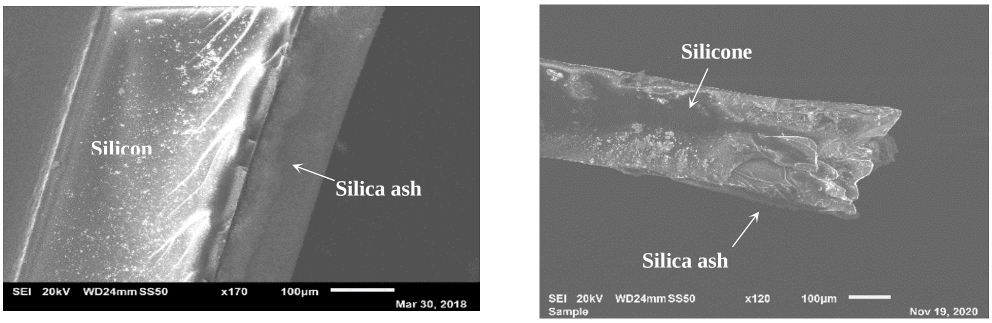

Figure 41 – SEM image of cross section samples from Flow Tunnel experiments under concurrent forced flow (left image) and opposed forced flow (right image).

The dominant mechanisms of soot formation in microgravity are defined by residence time and oxidation [331]. In the case of silica-ash, formation occurs during the gas-phase, and there is no information on the leading mechanisms. As neither soot nor silica-ash has a crystalline structure, both can agglomerate to form larger structures. In pyrogenic processes, where silica-ash is formed in a similar fashion as in a diffusion flame on PDMS, the primary silica-ash particles form tightly-bound aggregates that form larger conglomerates [332]. In addition, the primary particle size diameter for soot and silica-ash are in the same order of magnitude, see *Table 12*. Thus, the thermophoresis process attributed to soot deposition can be used to describe silica-ash transport and deposition.

Table 12 – Particulate size length for Soot and Silica-ash.

Type	Mean primary particle size diameter [nm]		Problem	Reference
	µg	1g		
Soot		46	Liquid diffusion flames (toluene, benzene, n-heptane, diethyl ketone)	[333]

	70	30	Flame forming on fluorinated ethylene propylene wire jacket under	[212]
	330	150	Pyrolysis of ethyltetrafluoroethylene wire insulation	[334]
SiO_2		<100	Amorphous silica ash	[332]

Thermophoresis is a relevant topic within particle deposition, and it refers to the transport of small particles in a temperature gradient (towards the colder region). Thermophoresis forces have been demonstrated to dominate soot deposition on cold walls from gaseous diffusion flames [331,335,336]. Thus, considering thermophoresis is essential to estimate the behaviour of soot deposition on the walls. The velocity induced by thermophoresis, or thermophoretic drift velocity, can be estimated based on the particle size and the temperature gradient. The thermophoretic deposition is characterised by the thermophoretic velocity. For particles less than 10,000 nm in diameter, the Waldman expression [331] to estimate the thermophoretic velocity is

$$U_t = \frac{3v}{1(1+(\pi/8)\alpha_m)}\frac{\nabla T}{T} \qquad \text{Equation 11}$$

The estimated and measured thermophoretic velocity for soot particles in microgravity conditions has been reported to be of the order of 0.1 to 1 cm/s [331,333,336].

A reduction in gravity has shown to result in an increased mean size of soot particles by two-fold compared to normal gravity [212,334]. Likewise, the agglomerate sizes have been reported to increase three-fold, which is attributed to thermophoretic forces and long residence times in microgravity [212,337]. The thermophoretic velocity increases with smaller soot particles sizes [333]. For soot deposition, estimated thermophoretic velocities in microgravity were reported to be more than three times larger than estimates based in normal-gravity semi-empirical relation [338].

There is a proportional dependency of the thermophoretic velocity of soot particles on the temperature gradient in microgravity [333]. In open-structure aggregates, the thermophoretic forces are dependent on the primary particle size. However, if the morphology of the aggregates is different (closely bound), then these behave like large particles [333]. Silica-ash agglomerates produced in pyrogenic processes can achieve sizes up to 600 nm and have open-fractal morphology [339]. Thus, silica-ash aggregates might behave akin to soot aggregates in microgravity.

Other relevant environmental parameters affecting soot deposition for an established diffusion under a boundary layer are oxygen concentration and the forced flow velocity. With increasing oxygen concentration, the soot volume fraction increases, and so does the deposition of soot [335]. Under the effect of forced flows, soot deposition is dominated by a combined simultaneous effect of thermophoretic and convective forces [336,340].

As seen, the thermophoretic forces dominate the deposition of soot in normal gravity and microgravity scenarios. Silica-ash particles and agglomerates share-alike features with soot. Thus, soot behaviour will be used to discuss the behaviour of silica-ash in the following. The silica-ash deposition as a function of the forced flow, oxygen concentration and ambient pressure.

7.3.2.1. Silica-ash deposition in experiments with forced flow

Quantification of the deposited silica-ash was only done for samples where the flame self-extinguished either due to the ash affecting the heat and mass transport (concurrent flame spread) or at blow-off extinction conditions (opposed flame spread). The silica-ash deposition was quantified by measuring the thickness at the point of extinguishment and at various distances (x_{ext}) downstream from that point. In the case of opposed flame spread, measurements were only done at the point of extinguishment. For concurrent flame spread, it was possible to provide profiles of the silica-ash thickness for distances downwards from the point of extinguishment. If thermophoretic forces are taken into account, the highest temperature would occur at the trailing edge of the flame.

The profiles of silica-ash thickness for a 0.36 mm PDMS sample are plotted in *Figure 42*. In the left panel, the silica-ash thickness is at a maximum at the point of extinguishment; then, the thickness decreases in an exponential manner downstream from there. The deposition process is transient, but as the flame travels upwards, the largest accumulation of ash will occur where the temperature gradient and the flame temperature are highest. According to Equation 11, the thermophoretic velocities are greatest, where the temperature gradient is largest. An estimate of the thermophoretic velocity that uses the maximum temperature from Chapter 7.2 and the temperature gradient yields a thermophoretic velocity of 1.5 cm/s.

By imposing concurrent forced flow, the ash profiles diminish in thickness. The left panel of *Figure 42* shows that all the ash thickness profiles have a similar negative exponential behaviour. In fact, all have a similar exponent in their fitting function. The right panel in *Figure 42* shows the ash thickness as a function of the forced flow. It can be seen the direct effect of imposing a convective force on the concurrent flame spread. The convective force produces a larger momentum compared to the momentum created by the thermophoretic forces. Thus, part of the silica-ash is transported away without depositing on the downstream unburnt fuel.

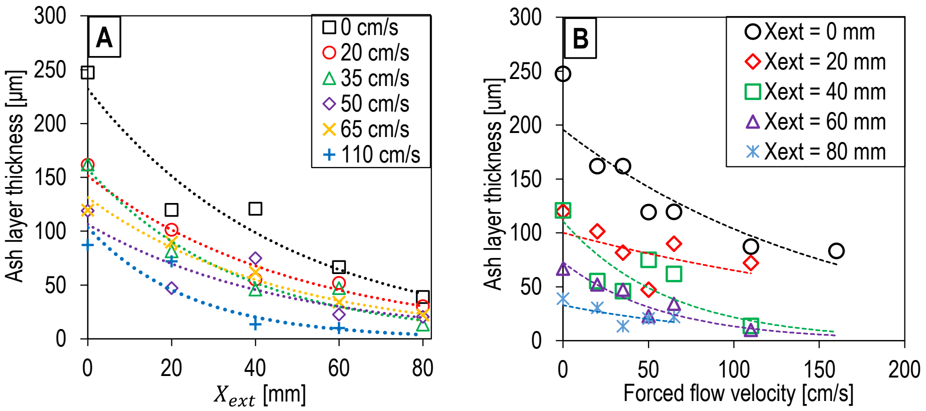

Figure 42 – Silica ash thickness as a function of the concurrent forced flow velocity at various distances from the point of extinguishment for a 0.36 mm thick PDMS sample, as measured using SEM. The samples were obtained from the Tunnel flow rig. In the left panel (A), the silica-ash thickness is plotted for various distances downwards from the point of extinguishment (X_{ext}*) as a function of the forced flow. The right panel (B)*

depicts the silica-ash thickness as a function of the forced flow velocity for various distances from the point of extinguishment (X_{ext}).

The normalised silica-ash thickness is plotted as a function of the forced flow for various PDMA sample thicknesses in *Figure 43*. The ash thickness normalisation was done against the half-thickness of the corresponding PDMS sample. Thus, a dimensionless thickness of unity means that the measured silica-ash was half the thickness of the corresponding sample. There are some discrepancies in the data points in *Figure 43*, as some silica-ash thicknesses increase with increasing forced flow velocity. During the flame spread experiments, the PDMS sample deformed and warped quite noticeably. Regardless of those points, the profiles in *Figure 43* indicate that the convective forces dominate the silica-ash deposition.

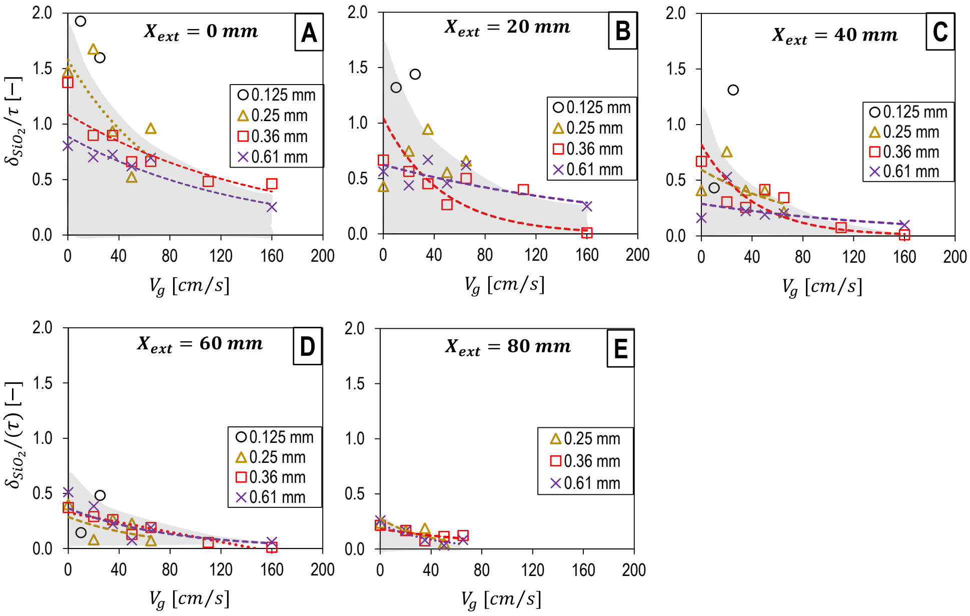

Figure 43 - Normalised silica-ash deposition as a function of the forced concurrent flows at various distances from the point extinguishment (X_{ext}) for various PDMS thicknesses. These results were obtained from samples tested in the Tunnel Flow rig. Panel (A) represents the data measured at the extinction point ($X_{ext} = 0$ mm). Panel (B) represents the data at 20 mm from the point of extinguishment ($X_{ext} = 20$ mm). Panel (C) represents the data at 40 mm from the point of extinguishment

($X_{ext} = 40\,mm$). Panel (D) represents the data at 60 mm from the point of extinguishment ($X_{ext} = 60\,mm$). Finally, Panel (E) represents the data at 60 mm from the point of extinguishment ($X_{ext} = 60\,mm$).

With increasing sample thickness, the results in *Figure 43* do not show a significant increase in silica formation and eventually more deposition (increase in thickness). That is, the silica-ash thickness accumulated is proportionally smaller as the sample thickness increases. Although the precise mechanisms in the formation of silica-ash are not known, unlike soot formation, stoichiometric considerations could be used to explain such behaviour. If the oxidiser concentration remains the same (air), the number of moles of SiO_2 per mole of fuels remains invariable with respect to the stoichiometric ratio [308]. Only if the local supply of oxidiser is restricted to the combustion zone will the production of silica-ash be affected. It seems that with increasing thickness, there is not enough oxidiser to match the vaporised mass at the combustion zone. The problem can then be considered fuel-rich. The oxidiser level would have to increase significantly near the combustion zone in order to yield more silica-ash.

For opposed forced flows, the silica-ash residues measured are much thinner compared to the concurrent measurements, as shown in *Figure 44*. The silica-ash thickness at the point of extinguishment is almost 30 times thinner in the opposed case as compared to the concurrent case. These results are from flame spread extinction under the kinetic regime. The results in *Figure 44* indicate that the forced dependency on silica-ash deposition is strong for the thick sample but weak for the thinner samples. At the leading edge, gas-expansion is the leading mechanism controlling soot motion, and thermophoretic velocities are absent [336]. Thus, only very small quantities of silica-ash deposit on the sample burnout tip.

For opposed flow, the thickest sample (0.36 mm) had the largest silica-ash thickness, as shown in *Figure 44*. The formation of silica-ash in the combustion zone is noticeable since the order of magnitude of the silica-ash thickness is much smaller than in the concurrent case. The opposed flame spread is a steady problem that takes place in the thermal regime. The presence of the silica-ash in the gas-phase might affect the heat transfer from the flame to the solid-phase. This is a contrasting behaviour as compared to concurrent flame spread, which is transient.

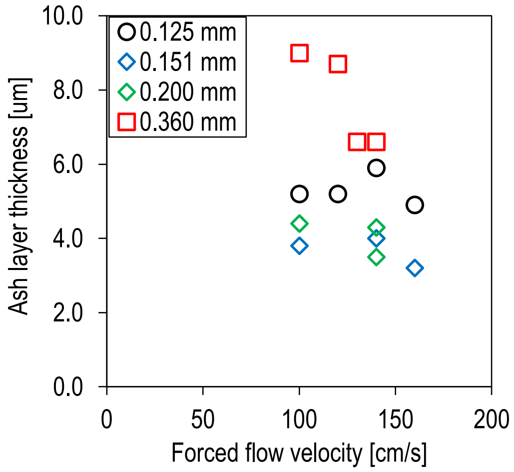

Figure 44 – Silica ash thickness as a function of the opposed, forced flow velocity at the point of extinguishment for various PDMS membranes.

7.3.2.2. Silica-ash deposition for various oxygen concentrations and ambient pressures

As mentioned, the effect of the oxygen concentration and ambient pressure on the formation of silica-ash is not known or has not been reported in the literature. Also, the oxygen concertation in the ambient can affect the formation of silica-ash [292]. In addition, silica-ash was only reported to occur in oxidative environments in thermal degradation studies [290,295,341]. *Figure 45* (right panel) shows that the silica-ash thickness increases linearly for increasing oxygen concentration at a fixed, ambient pressure. From the model of the stoichiometry of complete combustion, even with increasing oxygen concentration, the formation of silica-ash might be restricted to the formation of the products H_2O and CO_2 simultaneously.

The effect of ambient pressure on the silica-ash deposition is also plotted in *Figure 45* (right panel). It is not clear how the formation of silica-ash is affected by sub-atmospheric pressures. Reduced pressure affects soot formation, and the soot volume fraction does not resemble microgravity soot formation [342]. In contrast, thermophoretic velocities increase with a reduction in pressure, which is similar to the microgravity effect [343]. The results in *Figure 45* show that the silica-ash formation has a weaker dependency on pressure than on oxygen concentration. Only at very low pressures, there is a significant increase in silica-ash thickness.

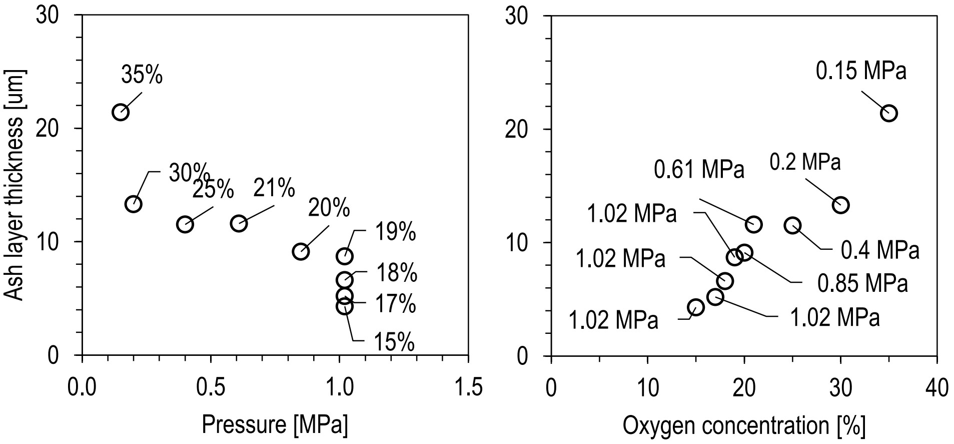

Figure 45 – Silica-ash deposition at the point of extinguishment for a 0.125 mm PDMS as a function of the ambient pressure (left) and oxygen concentration (right). The experiments were performed in the TOPOFLAME.

These results in normal gravity along with thermophoretic forces being larger in microgravity, strongly indicate that the deposition of silica-ash might have been much greater during the Saffire II experiment. Images from Saffire II show floating silica-ash agglomerates and cumulated ash near the ignition zone. Thus, in part, the flame spread did not succeed as a larger layer of silica-ash reduced the heat transfer from the flame to the solid and restricted the mass diffusion from the pyrolyzing solid.

7.4. Ignition behaviour

In this section, the ignition behaviour of PDMS is discussed for a range of scenarios. First, the thermal degradation is discussed to characterise the formation of silica-ash. Then, the time to ignition is evaluated in stagnant and forced flow environments. In the latter, the forced flows, oxygen concentration and ambient pressure are the main variables.

4.4.1. Thermal degradation behaviour

The mass loss and DTG curves obtained from the TGA apparatus are plotted in *Figure 46*. As seen, two or three stages of degradation occur at very low heating rates (2.5 °C/min and 5 °C/min). It is not clear if it is due to impurities in the sample or what are the governing mechanisms in the depolymerisation of PDMS (kinetic consideration and molecular structure or bond energy breakage). A plausible explanation for the multiple-step degradation is solid-phase oxidation [302,344]. At this heating rate, the solid-phase oxidises to form silica – the same silica ash that forms in the gas-phase. Details on the depolymerisation are beyond the scope of the current investigation. By contrast, at higher heating rates, only one stage of thermal degradation occurs. The degradation products are siloxanes, as seen in Chapter 3, along with CO_2 and H_2O in all reaction steps.

Regardless of the small steps in thermal degradation, the large stage of degradation occurs 646 °C at a heating rate of 2.5 °C/min. As the heating rate is increased, the temperature for the degradation stage increases consistently. Likewise, the residue left decreases with increasing heating rate, as seen in *Figure 46*. The residue left is a combination of condensed-phase silica-ash along with ash formed in the gas-phase falling on the weighing scale. Camino et al. [306] reported very small residue left for high heating rates (> 50 °C/min). They suggest that high heating rates decrease the oxidation of the solid-phase while increasing the degradation reaction. Thus, more siloxane from the solid-phase can depolymerise.

Silica-ash can occur elsewhere than in the combustion zone of a diffusion flame. These results clearly indicate that the formation of silica ash occurs both in the gas-phase and the solid-phase. The heating rate is the key factor in the formation and proportion of silica via solid- or gas-phase. Thereby, both modes of silica formation should be considered during ignition and flame spread behaviour.

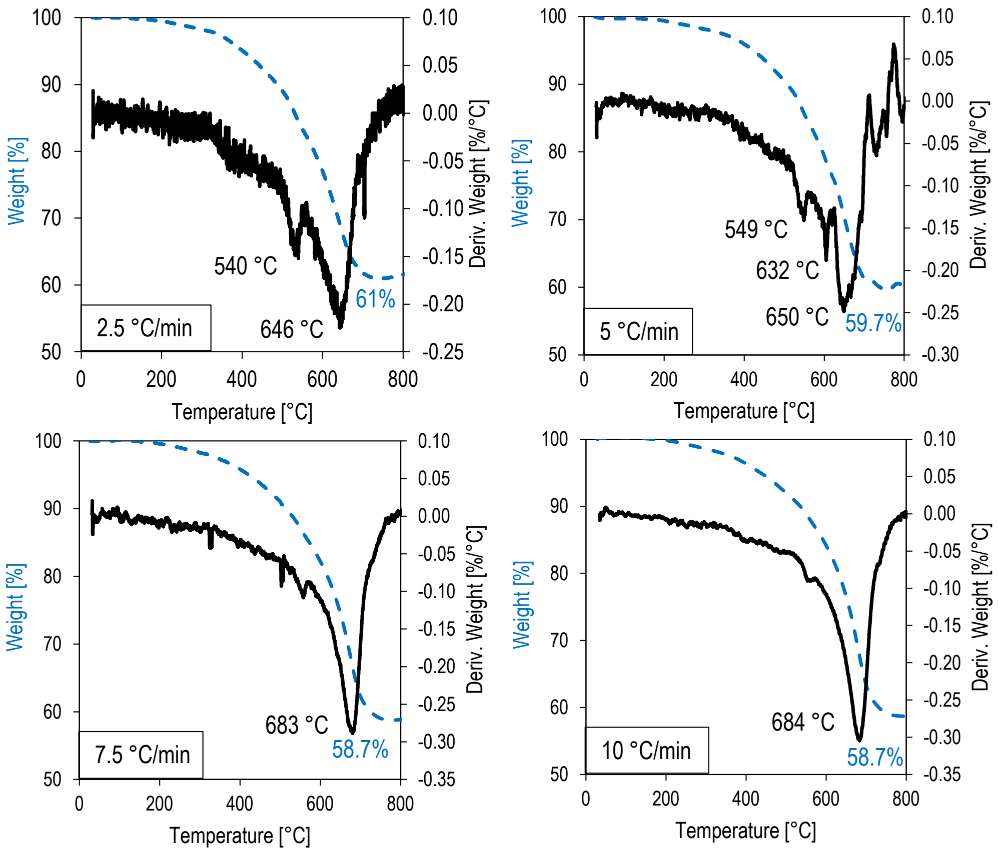

Figure 46 – TG and DTG curves of PDMS in air at various heating rates.

The thermogravimetric results were used to calculate the kinetic properties of the PDMS. The Ozawa/Flynn/Wall method was used to derive the properties (ASTM E1641-16). The prescription recommended in the standard was followed as the four mass loss curves from *Figure 46* were employed. The activation energy and pre-exponential factor derived were 148 kJ/mole and $3.4 \cdot 10^7$ min^{-1}. The values are in the same order of magnitude as those reported for PDMS of high molecular weight [301]. These properties correspond to the solid-phase and can be used to estimate mass flux through the Arrhenius expression.

4.4.2. Ignition behaviour for stagnant conditions (Cone Calorimeter)

Images from an ignition test under the Cone can be seen in *Figure 47*. It is clear that the sample achieves pyrolysis (second image from the left), and subsequently, ignition is attained. In the last image, it can be seen that the sample turns white, indicating the formation of silica in the solid-phase and possibly in the gas-phase (during thermal degradation).

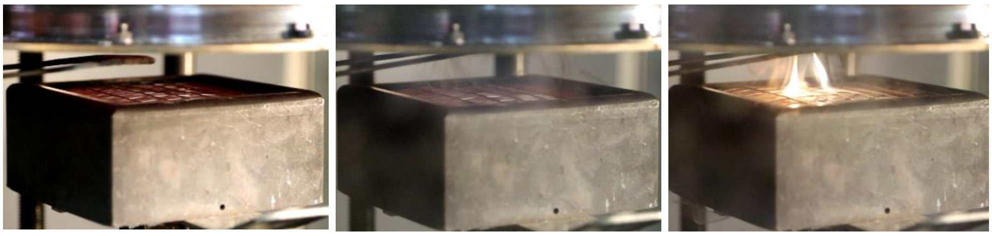

Figure 47 – Sequence of images showing a test with a 0.25 mm PDMS sample under the Cone Calorimeter at 35 kW/m2. From left to right: time zero where the sample was just exposed to the incident heat flux, the second image shows pyrolysates emerging from the samples, and the last image shows the first flames appearing.

The piloted ignition results obtained in the cone calorimeter are shown in *Figure 48*, along with literature results for a thermally-thin propylene (PP) sample [345] for comparison. As seen, the ignition delay time has negligible or almost no dependency on the sample thickness. The fitting curve for the PDMS samples behaves in an asymptotic fashion, which is surprisingly far from the linear behaviour expected for a thermally-thin fuel. By comparison, the ignition delay time curve for the polypropylene sample exhibits a linear dependency as a function of the imposed heat flux. The general assumption is that ignition can be synthesised to consider pyrolysis only and this is dominated by conduction.

For the cone conditions, one side is exposed to radiant heat and with the other side is insulated, the ignition is restricted to pyrolysis only. The ignition delay time is composed of pyrolysis time, mixing time and chemical time. Only the pyrolysis component is discussed here and is expressed as:

$t_{ig} = \rho c \tau \frac{(T_{ig}-T_0)^2}{\dot{q}_r''}$. (Equation 12)

If the results for the PP sample in *Figure 48* extended are extended by a linear curve to intersect with the axis, then the critical heat flux ($\dot{q}_{cr}''$) can be extrapolated. The $\dot{q}_{cr}''$ for PP is estimated to be 12 kW/m^2. For the PDMS samples, extending the exponential curve leads to a critical heat flux of 30 kW/m^2, which is almost three times larger than critical heat fluxes for common thermo-plastics [289]. During the experiments with an incident heat flux near the critical value, the PDMS sample was whitened before ignition. Those visual observations indicate that silica might have formed in the solid-phase during the initial heating process.

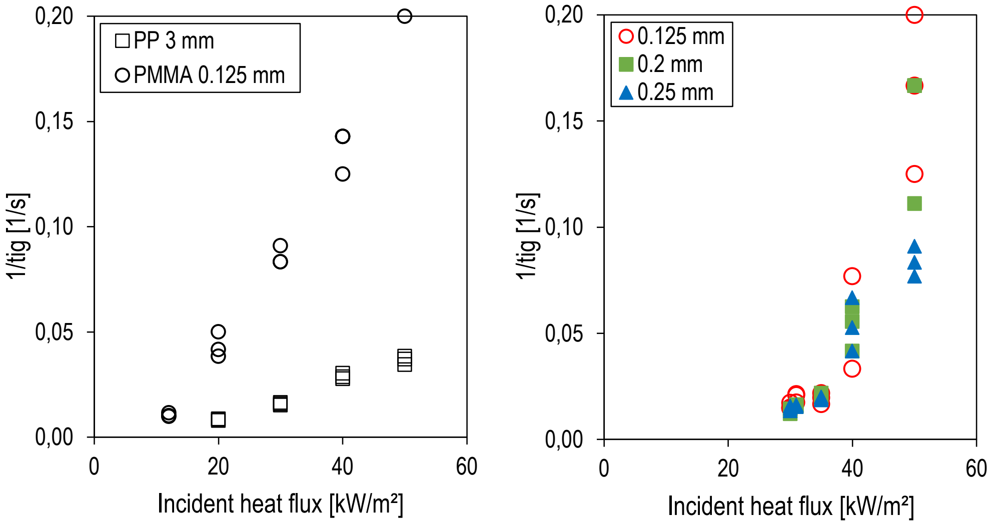

Figure 48 – Time to ignition results for various PDMS samples. The experimental results were obtained from the Cone Calorimeter (right pane. For comparison, results from PP and PMMA are displayed on the left pane. The polypropylene (PP) results are from the literature [345].

The heating of the PDMS sample at the surface is transient, and it depends on the absorptivity and the intensity of the irradiated heat. The heating rate is determinant in the formation of silica in the solid-phase. For low heating rates, more silica is formed in the solid-phase. This was also corroborated in the previous Chapter. Silica has a lower thermal conductivity ````and higher reflectivity and stabilises the sample further. The consequences on the thermal exchange and mass transfer are further reduced. At low incident heat fluxes, the ignition behaviour portrays the simultaneous thermal behaviour of the PDMS along with silica forming in the solid-phase. Thus, the PDMS behaves like a composite material for low incident heat fluxes or under low heating rates.

Silica-ash forming during the gas-phase could have also been deposited on the sample surface. In the stagnant condition provided in the Cone apparatus, the deposition of the ash particles is dominated by buoyancy. However, the silica-ash deposition did not have a large impact as the silica-ash measured was insignificant. It is expected that the material will behave more like a truly thermally-thin material for higher incident heat fluxes. In the previous section, it was shown that at high heating rates, most of the PDMS depolymerises, thus leaving little change to the formation of silica in the solid-phase. As seen, the pyrolysis behaviour of the PDMS is rather complex and behaves differently according to the heating rate the sample is exposed to. At low heating rates, the pyrolysis is dominated by the formation of silica in the solid-phase, whereas at a high heating rate, the material behaves as a thermally-thin material.

Based on the critical heat flux value found for the PDMS samples, the ignition temperature (T_{ig}) can be estimated. Delichatsios [346] used a one-dimensional heat balance model including surface re-radiation to derive the ignition temperature as $T_{ig} = (\dot{q}''_{cr}/\sigma)^{0.25}$. In Delichatsios' model, the emissivity is assumed as unity, and with that value, the ignition temperature for PDMS is 573 °C. However, it should be noted that the emissivity of PDMS and silica is lower and varies with temperature, and with decreasing emissivity, the computed value increases. In the literature, the only reference value found was 444 °C, as provided by Grand and Wilkie [289]. The latter value from literature is in the same range as for other thermo-plastics.

4.4.3. Ignition behaviour in forced flow

In order to compare the time to ignition for the results obtained during the Saffire II tests and the current results, similar energy was provided. In the Saffire II tests, the 29 AWG Kanthal wire provided 80 J/s. The current tests were performed with a 22 AWG wire providing 76 J/s. Thus, the heating provided in both cases was similar, which allows establishing comparisons. The main difference between both ignition systems was the installation of the wire. A sinusoidal shape was used for the Saffire II experiments, whereas a coil was used for the current investigation. In the sinusoidal shape, further displacement of the Kanthal wire was observed. This might lead to some errors in the comparisons of the ignition delay times.

Another consideration to raise is the role of convective heat losses in the ignition procedure. That is, the ignition coil loses energy due to the incoming forced flow. The coiled igniter can be idealised as a cylinder of a fixed volume with the coil diameter being 8 mm and 50 mm in length. As this is energised, it reaches almost 900 °C heating of the nearby air. As a forced flow is imposed on the coil, convective heat energy is lost and can be estimated as $h_c(T_w - T_\infty)$. In addition, the hot air around the idealised cylinders would also be affected by an incoming forced flow. As a result, the time needed for the conduction loss is $t_c = \rho V c_p / h_c S = r^2/2\alpha$ [347]. The volume of the idealised cylinder is V, the surface is S. In that characteristic time, the thermal diffusivity is a function of the temperature.

In the current experimental rig, the improved FPA, the forced flow is laminar with a low Reynolds (Re) number. Assuming a boundary layer over a flat plate, the convective heat transfer coefficient for forced flows is $h_c = Re^{1/2} Pr^{1/3}$ [348]. Here, Re is the Reynolds number, and Pr is the Prandtl number. The Reynolds number is a function of the forced flow. As the forced flow increases, the temperature of the idealised cylinder and heating coils decreases. Also, the Prandtl number is also affected by the forced flow as the thermal conductivity of air decreases with temperature. Thus, it is expected that as the forced flow increases, the energy provided by the coil decreases accordingly.

The results for the ignition delay times are plotted in *Figure 49*. As seen, the ignition delay exhibits a linear increase up to certain forced flow velocities in both cases. Thereafter, the ignition delay time seems to behave asymptotically. The linear dependency on the ignition delay time can be explained by the fact that the mixing time is inversely proportional to the forced flow velocity. The same behaviour has been reported elsewhere for another thermally-thin fuel [167]. It should be mentioned that the cooling effect of the forced flow might affect the pyrolysis as well. As for the asymptotic behaviour, it is suspected that the cooling effect on the ignition wire is far too great, and the heating rate to the PDMS goes down, allowing the formation of silica in the solid-phase. This is again corroborated by the whitening of the sample near the ignition wire at extinction conditions.

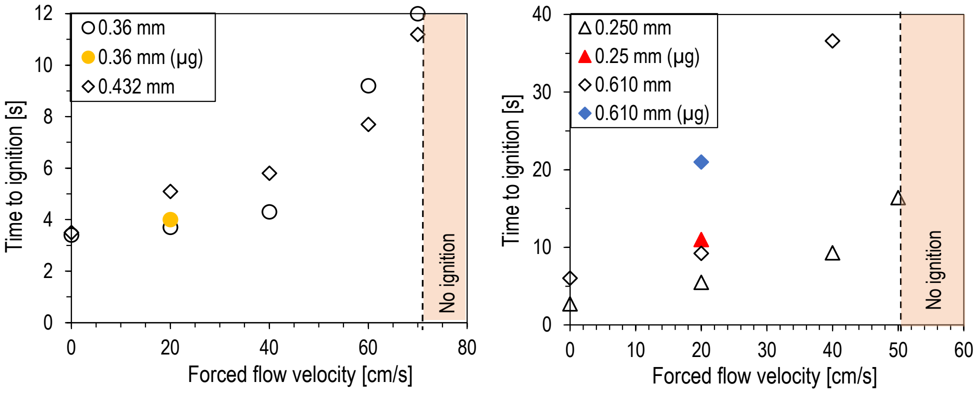

Figure 49 – Time to ignition for various PDMS samples under opposed (left panel) and concurrent (right panel) forced flows in normal gravity and microgravity environments. The results were obtained in the Tunnel Flow rig.

Notice that extinction regions differ between opposed and concurrent forced flows, as shown in *Figure 49*. The ignition delay time is fundamentally the same under both conditions. The flow encountered during the ignition at the bottom of the sample (for concurrent) and at the top of the sample (for opposed) is not the same. In the concurrent flow case, the flow is the actual one seen by the sample edge, whereas in the opposed flow case, a boundary layer would be created, and the top of the sample will thus experience a reduced forced flow where the ignition wire heats the sample.

The differences with microgravity data might also arise from a combined effect of energy and flow dynamics. The effective flow seen by the PDMS sample in the Saffire experiment was lower due to the boundary layer established. Despite these differences, the microgravity results are in the same order of magnitude. Thus, it is clear that the PDMS samples tested during Saffire II ignited successfully. The failure to attain a steady flame was more related to the transition from ignition to flaming or the flaming process.

4.4.4. Effect of oxygen concentration and ambient pressure

The effect of oxygen concentration on the ignition delay times can be seen in *Figure 50* (left panel). The ignition delay times decrease following a linear dependency on oxygen concentration. Hsieh and Buch [314] obtained similar dependencies on the oxygen concentration for similar silicone elastomers. They suggested that an increased oxygen concentration aids the depolymerisation of the silicones. Such linear dependencies have also been reported for other thermally-thin and thick polymeric fuels for varying oxygen concentrations [110,111,189]. In numerical auto-ignition investigations, the dependency was found to be exponential [32,349] and polynomic [350].

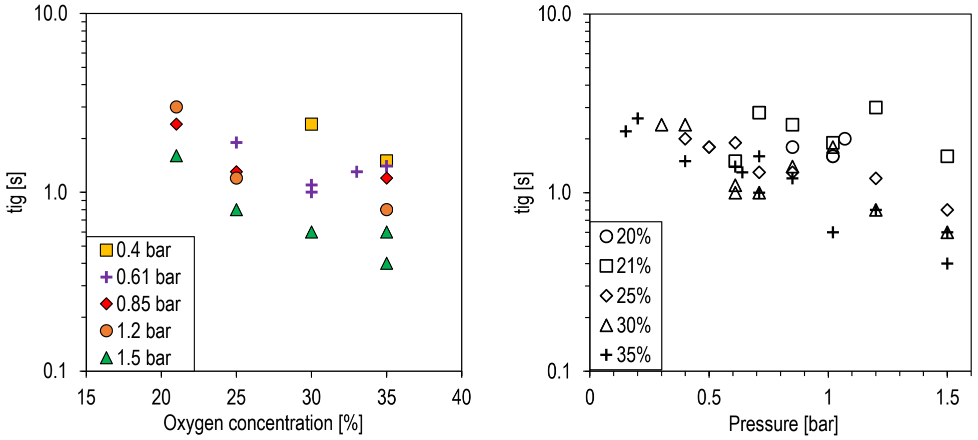

Figure 50 – Ignition delay time for a 0.125 mm PDMS sample as a function of two environmental parameters, the oxygen concentration (left panel) and ambient pressure (right panel). The experiments were carried out in the TOPOFLAME.

The ignition delay time also decreases linearly on increasing ambient pressure, see *Figure 50* (right panel). Other studies have reported the same behaviour for thermally-thin cellulosic sheets [111,189] and for thermally-thick samples at low pressures [107]. However, Fereres et al. [35,106] and McAllister et al. [107] reported that the ignition delay time decreased as the ambient pressure decreased for thermally-thick solid. In their work, they revealed that the convective heat losses are reduced with decreasing pressure dominating the heat losses (reduced at lower pressures) and transport.

In previous studies, the effect of both environmental parameters has been shown to affect the convective heat losses and mass transport quantitatively and to depend on the thermal behaviour of the sample. The PDMS used in the current study behaves differently, as has been shown previously, and thus the findings from other studies might not necessarily be the same. Therefore, it is important to look at the effects of both environmental parameters on convective heat losses, chemical time, formation of siloxanes and silica-ash in the gas-phase, silica formation in the solid-phase, and the pyrolysate rate.

The convective heat transfer coefficient in buoyant conditions, $h_c = (GrPr)^{1/4}$, is proportional to the square root of pressure (through the Grashof number). Thus, reducing pressure decreases the convective heat losses and increases the heating rate at the fuel surface (being heated by conduction and convection by the coil). However, this effect seems to have little or no influence on the PDMS samples, as seen in *Figure 50*. It is not clear how reduced pressure affects the formation of silica-ash during depolymerisation. Thomas and Kendrick [301] reported higher activation energy for depolymerisation in vacuum conditions when compared to a thermo-oxidative environment. With respect to the transport of the ash, a reduction in pressure decreases the buoyant forces and more silica- might accumulate on the surface, as was shown to occur with the silica-ash produced during the exothermic reaction (see Chapter 3).

Increasing the oxygen concentration might increase the depolymerisation (pyrolysis rate), as this has been observed for other polymeric fuels [107]. This behaviour is noticeable in *Figure 50*. Oxygen variations can affect the formation of silica-ash and impact the formation of silica in the solid-phase. For the latter, it might be more plausible if the heating rate from the ignition is too slow. The coil reaches around 900 °C in less than one second, providing a very fast heating rate and might be positively affected by the reduction in convective heat losses as the pressure is reduced.

An increase in oxygen increases the gas-phase chemical reactions according to the following expression; $\omega_g = A_g \rho_g Y_{O_2} \rho_f Y_f e^{(-E_g/RT_g)}$ [323]. Or conversely, the chemical time in the gas-phase, $\tau_{ch} = (\rho c_p T)/(E/RT)\Delta h_c A e^{-E/RT}$ [347], is reduced. It is clear that the effect of oxygen on the reaction rates, or chemical time, dominates the ignition delay time for the PDMS as a function of the oxygen concentration, see *Figure 50* (left panel). The effect of pressure on the chemical and reaction rates happens via gas-phase densities and reduction of mass pyrolysates. Then, chemistry dominates the ignition delay times for pressure as a variable, see *Figure 50* (right panel).

Fereres et al. [35] suggested that an ambient pressure of 0.55 bar resembles microgravity through a convective transport mechanism. Wang et al. [272] reported that microgravity auto-ignition time could be attained at a sub-atmospheric pressure. However, the ignition delay results presented herein are most likely dominated by chemistry. Thus, convective heat losses might only be relevant for thermally-thick fuels or for other scenarios where ignition delay times are much larger than for thermally-thin fuels. As such, pressure modelling might not be applicable to piloted ignition of thermally-thin fuels.

The ignition delay time for normoxic conditions, i.e. where the oxygen partial pressure is kept constant, is plotted in *Figure 51*. An inverse "U" phenomenon is observed for both the PDMS thickness and the change in the non-monotonic behaviour occurs for a combination of 0.7 bars and 30% oxygen concentration. It is a surprising behaviour, as chemistry dominates ignition delay times when changing pressure and oxygen concentration only. Previous studies in normoxic conditions with pilot and auto-ignition on thermally thin materials have shown no dependencies [111,351]. However, McAllister et al. [110] showed that for a thermally-thick fuel, the ignition delay times exhibited an almost linear dependence on the normoxic environment. In these studies, chemistry dominated for thermally-thin fuels, whereas convective transport dominated for thermally-thick fuels.

It is difficult to hypothesise the forces behind the behaviour observed in *Figure 51*. The only notorious difference with previous studies is regarding the PDMS and the formation and transport of silica. From *Figure 51*, it is seen that ignition occurs more readily at 0.7 bar and 30% oxygen concentration for the 0.125 mm sample than in normal atmospheric conditions. The same behaviour is observed for two data sets of 0.61 bar and 30% oxygen concentration. This change of regimes coincidently also occurs for flame lengths (will be discussed later in Chapter 7.5.4), and it is thus strongly suggesting that such changes might occur in the gas-phase. It is less plausible that this was a mistake due to the experimental procedure. Determining the forces behind such non-monotonic behaviours will require further attention in future studies.

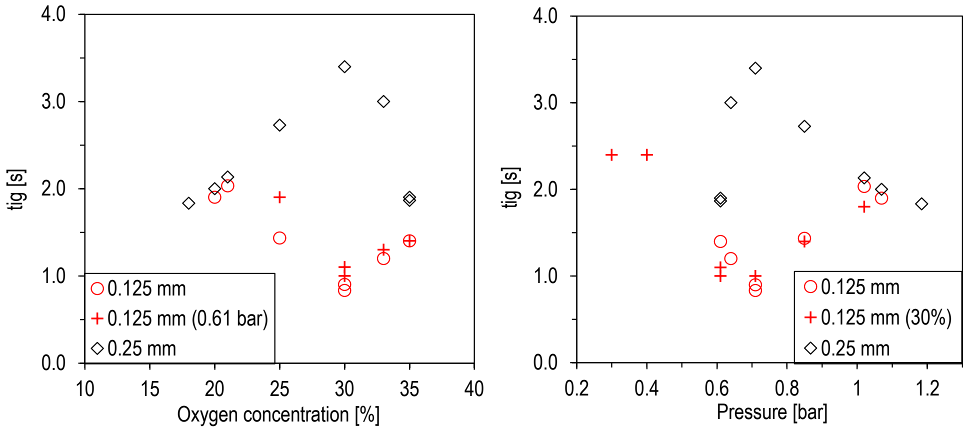

Figure 51 – Ignition delay time in normoxic conditions for two PDMS samples as a function of the oxygen concentration (left) and ambient pressure (right). Data from 0.61 bar and 30% is also plotted for comparison. The experiments were conducted in the TOPOFLAME.

7.5. Flame spread behaviour

The previous section discussed the possible mechanisms affecting thermal degradation and ignition. Those findings will be useful for a deeper understanding of the flame behaviour results presented in the following. The Saffire II results for the PDMS sample are presented first as these will be compared against the normal-gravity results. The flame spread behaviour, which involves flame spread rates and near-limit, are presented as a function of forced flows, oxygen concentration and ambient pressures. In addition, two methods for flammability assessment are employed.

7.5.1. Overview of results from Saffire II

In the Saffire II experiments with PDMS samples, no self-sustained flame spread was achieved during the tests. As discussed, all samples achieved ignition, but they did not transition from ignition to self-sustained flame spread. The most likely mechanism leading to extinction is the deposition of silica-ash. The transport and deposition of silica-ash, SiO_2, strongly depends on the convective and thermophoretic forces. The latter is especially stronger in microgravity, and consequently, the deposition of silica-ash is larger in microgravity, as discussed in Chapter 7.3. The excessive accumulation of ash has consequences on the heat and mass transfer during flame spread.

From the videos recorded in the Saffire II experiments, it is possible to analyse the flame development during the energisation of the heating coils. The energy provided by the coil in each test is the same, and thus, the same energy. The energy provided by the heating coils was 80 J/s or equivalently 80 W. Knowing that the ignition coil covered 1.3 cm breadth of the 5 cm sample width, the computed heat applied to the edge of the sample was 12.3 W/cm^2 or 123 kW/m^2. The same heat was applied to all the PDMS samples, and the convective losses due to the forced flow were identical for each test as the forced flow velocity was the same (20 cm/s). Warping or displacement of the coil might have reduced the heat applied to the edge when the wire was energised. Thus, the development of the flame's leading edge could only be analysed during the energisation of the coils.

The position of the flame's leading and the position of the coil are plotted as a function of time for all samples in *Figure 52*. Note that the two thinner samples experienced flame spread in ground experiments carried out as part of the preparation for the flight experiments [317]. As seen, the coil suffered displacement at some point in the first test (0.25 mm thick sample). Despite that, the flame's leading edge for that sample exhibited a linear increase over time. For the 0.61 mm and 1.02 mm thick samples, the displacement of the coil was minimal, and these samples thus received the same heat. As seen in *Figure 52*, the flame's leading edge exhibit steady behaviour. However, for the 0.36 mm thick sample, which was tested in opposed flow, the displacement of the coil was significant enough to influence the ignition and flame spread.

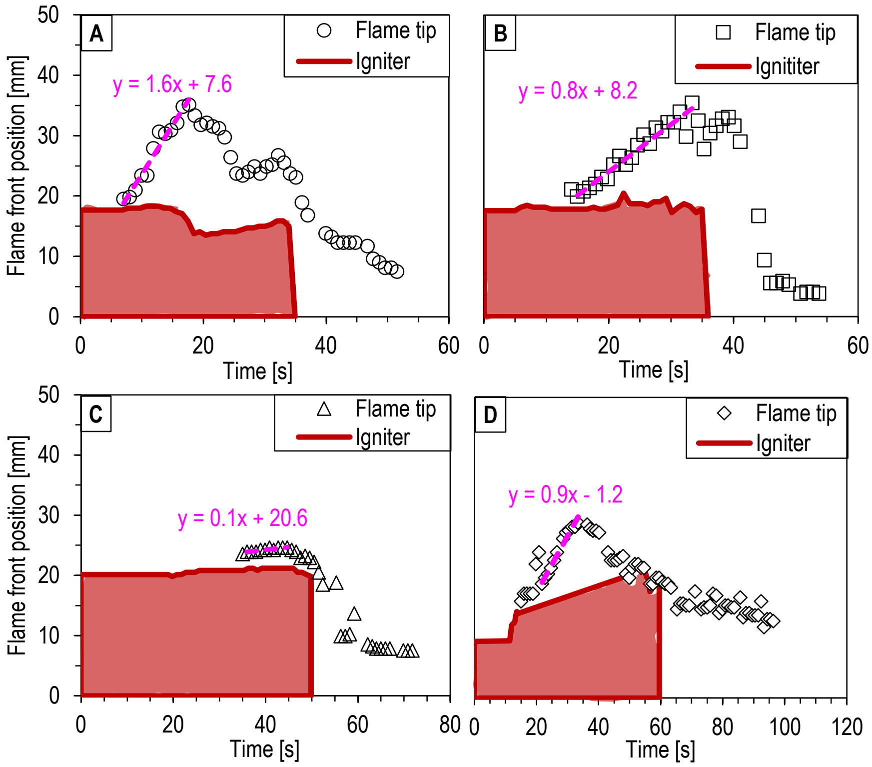

Figure 52 – Flame's leading edge position along with the igniter position for the four PDMS samples tested during the Saffire II tests. A: 0.25 mm (Concurrent), B: 0.61 mm (concurrent), C: 1.02 mm (concurrent), D: 0.36 mm (opposed).

Despite the large energy initially received by all the samples in the Saffire II tests, it is plausible that the deposition of silica-ash was quite substantial, and no flame spread could travel beyond the initially ignited area without further assistance. Also, the formation of silica in the solid-phase and the radiative heat losses in the gas-phase (due to microgravity) might have played a role in the failure to achieve flame spread in these tests. Based on the slope of the flame tip curves, the displacement rates of the flame's leading-edge were extracted and are plotted as a function of the corresponding sample thickness in *Figure 53*. As expected, the displacement rate under concurrent forced flow exhibits a linear dependency on the sample thickness. However, beyond the energisation of the heating coils, flames are not viable and can then be deemed an extinction phenomenon.

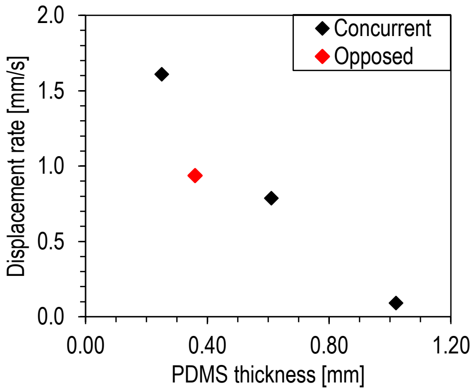

Figure 53 – Displacement rate of the flame's leading edge as a function of the PDMS sample thickness in the Saffire II experiments.

7.5.2. Forced flow effect on opposed and concurrent flame behaviour

Snapshots taken from the videos of the experiments in normal gravity and microgravity are compared in *Table 13*. Ignition is attained as diffusion flames emerge from both sets of experiments. In the microgravity case, flames were only visible when the heating oil was energised. Once ignitors were off, the flame in microgravity could not self-sustained itself. O the contrary, in the normal gravity experiments, flames could be established and travelled beyond the igniter's area.

Table 13 – Comparison of flame spread occurring on PDMS samples of various thicknesses in similar scenarios in microgravity and normal gravity environments. The first snapshot was taken when ignition occurred, the other snapshots were taken in 10-second intervals thereafter. Note: the length of the sample was cut to accommodate all samples in the table, the width of the samples is 5.

Flow direction	CONCURRENT				OPPOSED	
Sample thickness	0.25mm		0.36mm		0.36mm	
Gravity / Time	µg (4s)	1g (24s)	µg (18s)	1g (20s)	µg (14s)	1g (42s)
Ignition				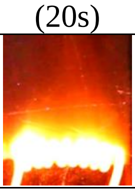		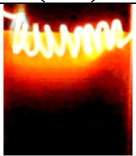
10s	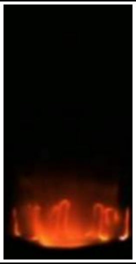	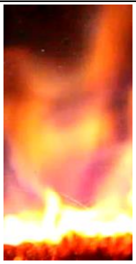	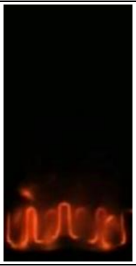			
20s	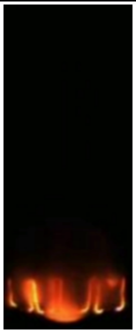					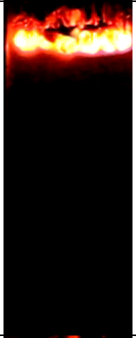
30s	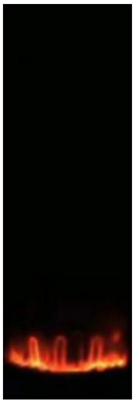		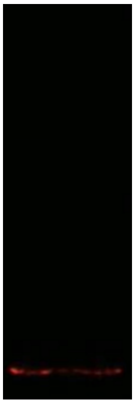			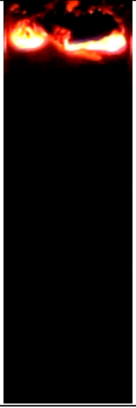

The results obtained in the flow tunnel for flame spread under opposed and concurrent forced flows are presented in the following. In addition to changing the forced flow, the sample thickness was varied. The results from Saffire II are also included in the corresponding plots (extinction limits) for normal-gravity data to enable comparisons.

Under buoyant conditions, a characteristic relative velocity is generated for a diffusion flame, and it depends on the thermal characteristic of the gas-phase (temperature changes). Bhattacharjee et al. [352] proposed an expression to compute the characteristic buoyancy-driven flow as $V_{nb} = [(\alpha_g g(T_g - T_\infty))/T_\infty]^{1/3}$. Thus, the forced flows affecting the flame spread can be corrected by adding the characteristic buoyant flow. In the following, the data will be presented as a function of the corrected forced flow.

The flame spread rates as a function of the opposed forced flows for various PDMS samples is plotted in *Figure 54*. The flame spread rate decreases with increasing sample thickness, as expected according to the de Ris expression for the flame spread [52]. For all the samples thicknesses, the flame spread rates exhibit a very small linear dependency as the forced flow increases. This behaviour is not very consistent with other observations for thermally-thin fuels [323]. In the work of Fernandez-Pello et al. [323], the flame spread rate over a cellulosic fuel decreased slightly with increasing forced flow at 21% oxygen concentration. On the contrary, they reported the opposite for thermally-thick fuels for high oxygen concentrations (>30%). For a thermally-thick material, increasing the forced flow increases the flame attachment, and in turn, the solid-phase receives larger heat flux from the flame. However, in the case of the thermally-thin PDMS, in-depth losses (or solid-heat up) should be negligible. The results plotted in *Figure 54* were obtained in the flow tunnel, where the forced flow started to transition to a turbulent flow at 70-80 cm/s. It is known that flame radiation can become prominent under turbulent flows.

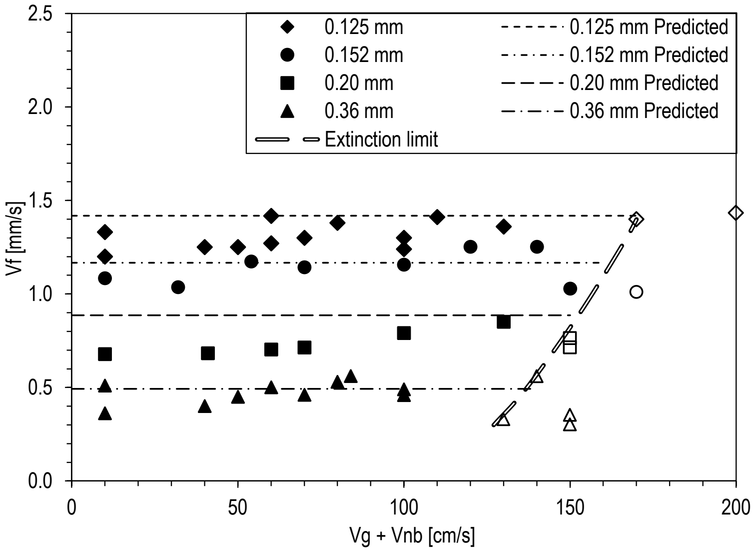

Figure 54 – Measured and predicted opposed flame spread rates for various PDMS thicknesses as a function of the mixed opposed forced flows (buoyant and forced). The data corresponds to the normal (flow tunnel rig). The closed symbols represent propagation conditions, and the filled symbols represent extinction conditions. The extinction limit defines the propagation zone (left) and the extinction zone (right).

Figure 54 also shows the extinction limit for high forced flow velocities. For extinction conditions where the kinetic effects are important, Fernandez-Pello [323] proposed that $V_f = V_g^2/\tau_{chem}$. The expression is very similar to the Damköhler number, which is the ratio of the flow time to the chemical time. If the thermal diffusivity is considered unity, then $V_f \alpha\ Da$. For the conditions of the experiments, the chemistry is not changed since the oxygen concentration remains the same, but the flow time is inversely proportional to the forced flow ($\tau_{flow} = \alpha_g/V_r^2$). Thus, for large forced flow velocities, the Da is reduced via the flow time, and extinction will occur for the opposed flames established over the PDMS samples.

The extinction limit decreases with flow and sample thickness, as seen in *Figure 54*. Such behaviour cannot be explained by the Damköhler number alone as it only reflects gas-phase chemistry. Intuitively, increasing the sample thickness increases the energy required to pyrolyse the fuel, which is relevant for flame spread over a material affected by silica-ash deposition and silica formation via solid-phase. T'ien, Endo and co-workers [353,354] evaluated the quenching limit of thermally-thick fuels by evaluating the ratio of solid-heat conduction to the heat conduction through the gas-phase, $\Phi = [\lambda_s(\partial T_s/\partial n)_s]/[\lambda_g(\partial T_g/\partial n)_s]$. In that expression, the heating via the temperature gradient is with respect to the normal of the sample surface (∂n) since the sample was spherical. They demonstrated that near-limit phenomena (quenching) are also dependent on in-depth heating. For the PDMS, the particularity in its behaviour during flame spread is the formation of silica in the solid-phase. As the sample increases in thickness, the formation of solid-phase silica might increase, and it could affect the heat transfer through the solid-phase. Such a hypothesis most likely explains the behaviour seen in *Figure 54*.

It is noticeable that kinetic extinction conditions for PDMS samples occur at high forced flows. By comparison, for a 0.125 mm PMMA film, kinetics become noticeable at 60 cm/s (or roughly 70 cm/s for mixed flow). The gas-phase activation energy for PMMA is 150 kJ/mol, and it is most likely many times higher for the PDMS (it will be confirmed later). This implies that a diffusion flame established over PDMS or other siloxane products is much harder to blow-off. This characteristic behaviour might have some implications related to the depressurisation approach to tackling a fire on spacecraft (fire-fighting measures). An established flame over a PDMS sample might not be extinguished during depressurisation.

In *Figure 54*, the theoretical predictions are also plotted. These did not foresee extinction conditions and were plotted to cover the thermal regime only (before kinetic extinction). The predictions slightly overestimate the experimental normal-gravity results, but they can still be deemed acceptable. Heat conduction from the gas-phase to the solid-phase is dominant for this opposed flame spread over the PDMS samples. Radiation from the gas-phase and surface re-radiation seemed not to be relevant. The choice of the theoretical prediction and input parameters was required to evaluate and deserves some discussion. Two expressions were considered for computing flame spread. The first is the de Ris expression, $V_f = \sqrt{2}\frac{\lambda}{\rho_s c_p \tau}\left(\frac{T_f - T_v}{T_v - T_\infty}\right)$. The second expression, $V_f = \frac{\lambda}{\rho_s c_p \tau}\left(\frac{T_f - T_v}{T_v - T_\infty}\right)$, is based on the an extended simplified theory (EST) developed by Bhattacharjee, Takahashi and co-workers [28,242,325]. Both equations are fundamentally the same; the only difference is the value of the constant in the expression by de Ris.

In addition, different values for the flame temperature pyrolysis temperature were evaluated. For the flame temperature, the adiabatic case and the measured flame temperature were used. A reference value from the literature [317] and the computed value from Chapter 7.2 were considered for the pyrolysis temperature. The computed results for the flame spread rates are listed in *Table 14*. Comparing both theoretical expressions, the expression by de Ris provides higher values, which is to be expected given the value of the constant ($\sqrt{2}$) in the expression. The adiabatic flame temperature yields overly conservative spread rates for a fixed value of the pyrolysis temperature. It was discussed earlier that adiabatic flame temperatures are a few hundred degrees over the measured values. In the case of the pyrolysis temperature, the computed value obtained in Chapter 3 provides lower spread rate values. Again, the pyrolysis behaviour of PDMS depends on the heating condition. The estimated spread rates closer to the experimental values are from the reference pyrolysis temperature and the measured flame temperature from all the computed scenarios.

Table 14 – Flame spread rate predictions based on different values of the flame temperature and pyrolysis temperature. The $T_{p,ref}$ *is the pyrolysis temperature reported by Niehaus* [317], $T_{p,comp}$ *is the pyrolysis computed in Chapter 4.4.2,* $T_{f,adv}$ *is the calculated adiabatic flame temperature and* $T_{f,m}$ *is the maximum measured flame temperature by thermocouples.*

Theory			de Ris [75]				EST [28,242,325]			
PDMS thickness [mm]			0.125	0.152	0.2	0.36	0.125	0.152	0.2	0.36
Parameter	$T_{p,ref} = 444°C$	$T_{f,adv} = 2134°C$	4.87	4.01	3.05	1.69	3.45	2.83	2.15	1.20
		$T_{f,m} = 1114°C$	2.01	1.65	1.25	0.70	1.42	1.17	0.89	0.49
	$T_{p,comp} = 573°C$	$T_{f,adv} = 2134°C$	3.06	2.52	1.91	1.06	2.17	1.78	1.35	0.75
		$T_{f,m} = 1114°C$	1.52	1.25	0.95	0.53	0.75	0.62	0.47	0.26

The flame spread rates as a function of the concurrent forced flows for various PDMS samples are plotted in *Figure 55*. The results for this mode of flame spread are, in principle, more complex than the previously discussed opposed flame spread cases. The transport and deposition of silica-ash on the sample ahead of the combustion zone determines the heat and mass transfer processes. As discussed in Chapter 7.3.2, the transport and deposition of the SiO_2 ash is dominated by two forces – thermophoresis and convection. It was seen that for increasing forced flows, convective forces dominate. Thus, the silica-ash deposition decreases with increasing forced flows. A modified expression for the concurrent flame spread over a thermally-thin material developed by Fernandez-Pello [323] will be used to establish phenomenological discussions. The modified expression is the following:

$$V_f = l_h \left[\frac{[(\rho_{SiO_2} c_{SiO_2} \tau_{SiO_2}) + (\rho_s c_s \tau)](T_p - T_o)}{(c_1 k_g \rho_p V_g/x)^{1/2}(T_f - T_p) + \dot{q}''_{fr} + \dot{q}''_e - \dot{q}''_{rs}} - \frac{c_2 x}{V_g} t_{chem} \right]^{-1}$$

Notice that the effect of silica-ash is incorporated in the heat transfer rate needed to raise the sample temperature to its pyrolysis temperature. Thus, the silica-ash affects the transfer of heat from the flame via convection $(c_1 k_g \rho_p V_g/x)^{1/2}$, flame radiation $\dot{q}''_{fr}$ or any externally applied heat $\dot{q}''_e$.

Moreover, surface re-radiation $\dot{q}''_{rs}$ is also affected by any deposited silica-ash. Another effect of the ash is its deterrent mechanism on the diffusion of pyrolysates and oxidisers at the fuel surface. This reduced diffusivity effect can be accounted for via the chemical part in the above equation. In Fernandez-Pello's definition of the Damköhler number ($Da = \frac{A_g \Delta H_R \rho_g E_g Y_{o,\infty} Y_{Fs}}{c_p R T_f^2 Y_g / x} e^{-E/RT_f}$), the reduction of diffusivity reduces the mas fraction of species locally Y_{Fs}, and the mass fraction of oxidiser $Y_{o,\infty}$.

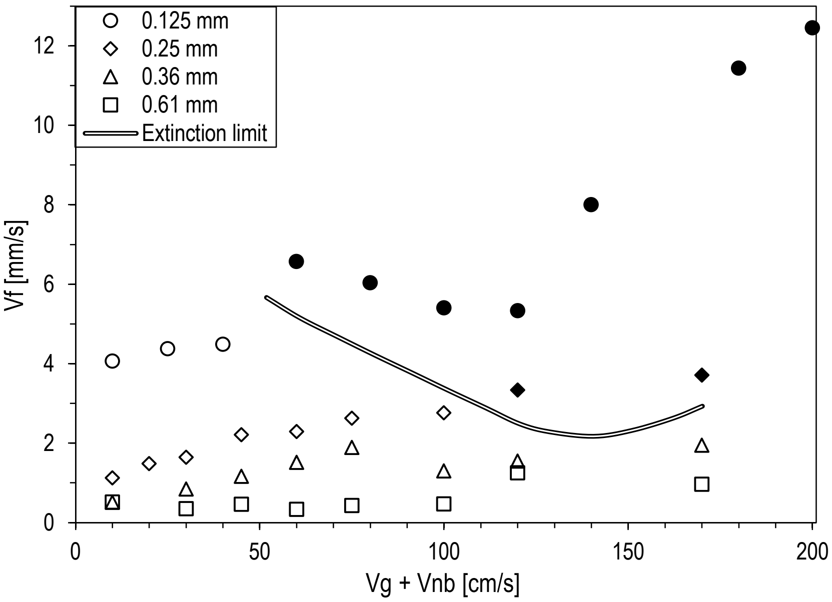

Figure 55 – Flame spread rates for various PDMS samples as a function of the mixed concurrent forced flows (buoyant and forced). The data plotted corresponds to normal-gravity (flow tunnel rig). The open and closed symbols represent extinction and propagation conditions. The extinction region lies below the extinction boundary, and above the curve lies the propagation region.

As seen in *Figure 55*, the flame spread rate at low laminar forced flows is considered a "near-limit" condition as the flame did not propagate over the entire sample length. Despite that, the flame spread rate for most of the samples exhibits a linear dependency as a function of the laminar forced flow. In Chapter 7.3.2, it was shown that silica-ash deposition was nearly exponential with respect to distance and laminar forced flows.

As the forced flow is increased further, the near-limit behaviour due to excessive silica ash deposition is left behind, and flame spread is practically propagating steadily over the entire sample. For these high forced flows, the deposition of silica ash on the fuel is reduced drastically. As such, the deposition is becoming insignificant, and the flame spread is dominated entirely by the heat and mass transfer along the characteristic flame length. It is worth mentioning observations of the behaviour exhibited by the thinnest sample (0.125 mm). Under propagation conditions, the 0125 mm thick samples showed a non-monotonic behaviour as the forced flow increased. This behaviour might be associated with the radiative nature of turbulence in the flow.

The extinction limits in *Figure 56* is thus dominated by the transport and deposition silica-ash and the sample thickness (via silica formation in the solid-phase). Another way of visualising the extinction boundaries can be seen in Figure 56, where the boundaries are plotted as a function of the forced flow and sample thickness. As seen, the contrasting near-limit behaviour for the flame spread between opposed and concurrent flame spread is due to various dominant forces. The opposed flame spread extinction map shows that flames are predominantly viable for extensive forced flows. Extinction occurs via kinetics for a specific sample under increasing forced flows (moving leftwards in the map). However, for increasing sample thickness (moving upwards in the map), extinction occurs due to insufficient energy to counteract the energy loss to break through the formation of silica in the solid-phase. The dominant mechanisms for near-limit under concurrent forced flows are directly dependent on the transport and deposition of silica-ash and the sample thickness (via thermal penetration).

The microgravity data points from Saffire II are also plotted in *Figure 56*. For the concurrent case, the microgravity data lies within the extinction flammability region obtained in normal-gravity scenarios. This suggests that concurrent flame spread over a PDMS sample is largely dominated by silica-ash transport and deposition in microgravity as well. However, when comparing the opposed case, the single data point obtained in microgravity disagrees with the normal-gravity flammable region. This might also suggest that silica-ash transport dominates opposed flame spread in microgravity, but it is not clear to which extent. From *Figure 56*, it is clear that the most critical scenario would be for flame travelling under opposed forced flows over a very thermally-thin sample. If this flammability map was available before designing Saffire II tests, it would have been obvious which PDMS thicknesses and conditions would have been most appropriate for the flight experiments.

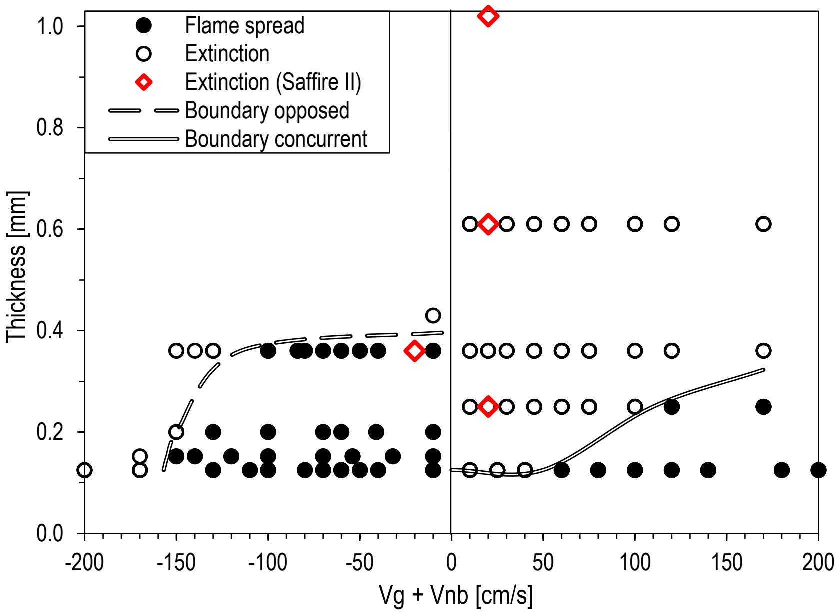

Figure 56 – Extinction boundary limits for PDMS membranes for a range of mixed flow velocities and sample thicknesses. The negative and positive axes represent opposed and concurrent forced flows, respectively. The data corresponds to normal (flow tunnel rig) and microgravity (Saffire II). The closed and open symbols represent propagation and extinction conditions, respectively.

7.5.3. Prediction of the extinction boundaries

Figure 57, *Figure 58* and *Figure 59* show the data points where flammability conditions are met and where extinction occurs. The flammability boundaries between those regions are drawn and are shown for all three sample thicknesses. As seen, the extinction limits differ quantitatively between sample thicknesses. For each PDMS sample thickness, there is a minimum condition (fundamental limit), i.e. a flammability limit. This fundamental point is identified with the LOI method, as explained in Chapter 2.4.3. Thus, the LOI for the 0.125 mm, 0.25 mm and 0.36 mm thick samples are 19.3%, 20% and 20.8%, respectively. These results are in agreement with values reported in the literature for similar materials (siloxanes and silicones) [187,235,236,244,317,318]. The change in LOI as a function of the sample thickness might be due to the silica formation in the solid-phase.

The extinction limits seen for all the sample thickness can be explained by kinetics or by using the Damköhler number, $Da = (\alpha_g / V_r^2)\, \rho_g Y_O A_g \, exp\left(-E_g / R\, T_f\right)$. When the oxygen concentration is reduced, the chemical time increases. As the forced flow increases, there is a reduction in the residence time, which is inversely proportional to the forced flow velocity. Thus, either reducing the oxygen concentration or increasing the forced flow will reduce Da below a critical value, and extinction will occur. The extinction data point obtained in the Saffire II experiment is plotted in *Figure 58*. It was discussed earlier that silica-ash transport and deposition dominate the extinction behaviour in microgravity.

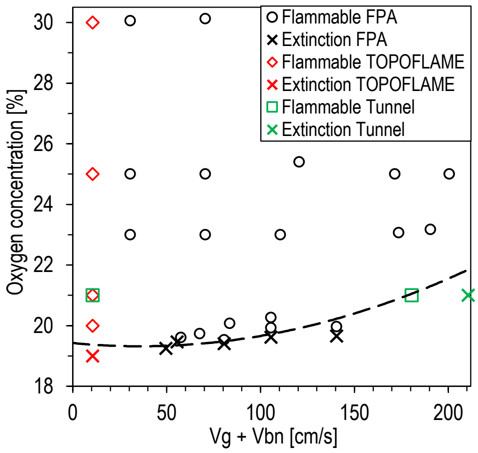

Figure 57 – Experimental flammability limit for a 0.125 mm thick PDMS sample for a range of opposed mixed flow velocities and oxygen concentrations.

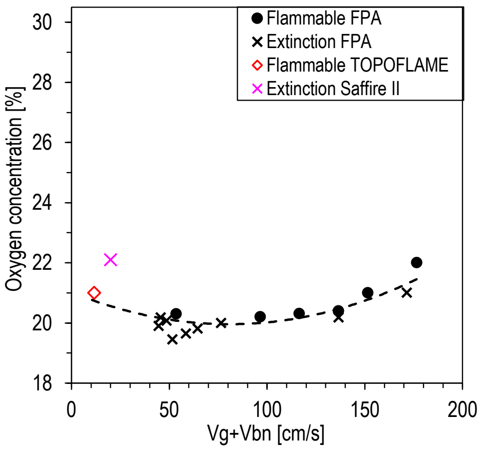

Figure 58 – Experimental flammability limit for a 0.25 mm thick PDMS sample for a range of opposed mixed flow velocities and oxygen concentrations.

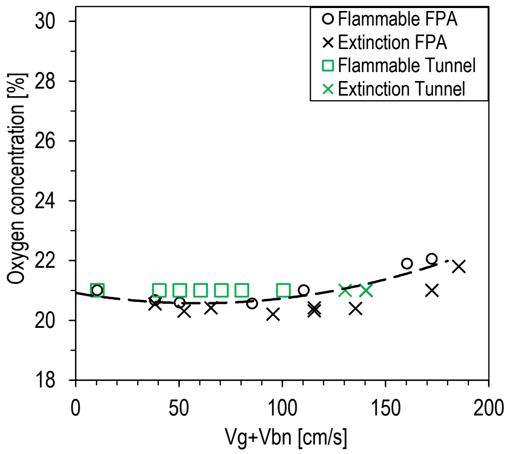

Figure 59 – Experimental flammability limit for a 0.36 mm thick PDMS sample for a range of opposed forced flow velocities and oxygen concentrations.

The LOI-MLOC method is utilised to predict the flammability limits for the PDMS samples. The goal of the method is to empirically determine the quenching and blow-off flammability limits of a material to determine the lowest fundamental point, the MLOC (in terms of oxygen concentration and forced flow), that allows flame spread to occur. The LOI-MLOC method is first used to derive two important parameters that describe the kinetic extinction behaviour, these are the gas-phase activation energy and pre-exponential factor. These properties are not readily available in the literature, and values for the most studied materials have been reported (PMMA and cellulosic fuels) [49,73].

One of the advantages of the LOI-MLOC method is that it can be used to empirically derive relevant properties, which can be used later to predict the flammability limits. It is worth mentioning that the method was simplified based on various assumptions (see Chapter 2.4.3). Other numerical and experimental studies have shown that radiation via the gas-phase is also important [66,355]. Also, another simplification taken is matching the gas-phase length and the solid-phase lengths. In addition, at the far limit of each extinction branch, only one mechanism is accounted for. That is, for quenching, only radiative losses are assumed, and for blow-off, only kinetics is included.

The formulae for the determination have already been introduced in Chapter 2.4.3 and Chapter 7.1. The properties used for the model are those of the PDMS listed in *Table 7*. As for the pyrolysis temperature, 444 °C was chosen as it was demonstrated to be the only value close to the predictions from the flame spread analysis. Lastly, for the flame temperature, the adiabatic flame temperature was selected since it is what the model requires. This will have anticipated consequences as it was discussed where the adiabatic flame temperature vastly overestimated the computed flame spread rates.

For the derivation of the gas-phase pre-exponential factor and activation energy, the idea of the model is to determine the kinetic flammability boundary empirically. For the kinetic regime, the expression $\eta + (1/Da_e)$ should be unity at the extinction boundary. The flame spread values near the extinction limit for each sample thickness, as seen previously, were obtained, and the equation was fitted to those values. The values of the pre-exponential factor and activation energy are iteratively obtained until the deviation from the mean is the smallest.

The empirical gas-phase pre-exponential factor and activation energy derived from three PDMS thicknesses are plotted in *Figure 60* (left panel). The empirical activation energy derived from all the PDMS samples collapsed to a very close averaged value for each sample thickness. Some scatter is obvious and was expected as the accuracy of the modified FPA rig in delivering a set oxygen concentration was 0.1%. The activation energy is greater than the one reported for PMMA; as discussed earlier, this is why extinction conditions for PDMS occur at twice over the flow as those of a thermally thin PMMA. This makes diffusion flame established over PDMS much harder to blow off during a depressurisation event.

The average values for the derived pre-exponential factor seen in *Figure 60* (right panel) differ as it decreases with increasing sample thickness. The difference in values is because the formation of silica via solid-phase is not accounted for in the model. Instead, these effects are artificially translated to the pre-exponential factors. This drawback of the LOI-MLOC method is purely based on kinetics and radiation-diffusion. Thus, several sample thicknesses of the same material require to be tested.

Another disadvantage of the LOI-MLOC method, already discussed in Chapter 2.4.3, is the three-dimensional effect. For small samples (in width), side diffusion and side losses can yield different results. The samples are wide enough in the current investigation, and the flame is purely two-dimensional. There is a critical sample width where the lowest MLOC is found [245,356]. The LOI-MLOC method does not account for three-dimensional features, but it artificially translates those effects into the derivation of the gas-phase activation energy and pre-exponential factor.

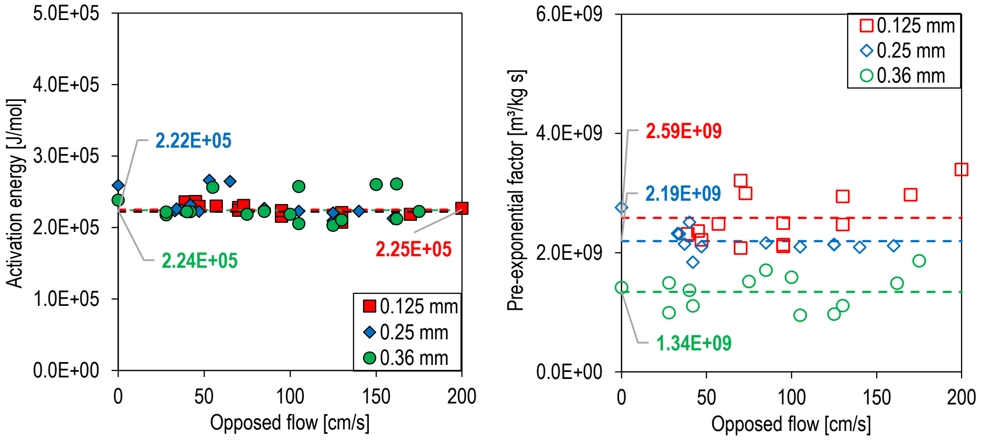

Figure 60 – Empirically determined gas-phase activation energy and pre-exponential factor for 0.125 mm, 0.25 mm and 0.36 mm PDMS thick samples, respectively. The horizontal lines represent the average values for each sample thickness. The experiments were carried out in the FPA.

Once the gas-phase kinetic properties were derived, these were used to compute the flammability boundaries for all the PDMS sample thicknesses. For extinction conditions, the following expression should be satisfied: $R_{rad,e} + \eta + (1/Da_e) = 1$. The predicted flammability boundaries for the 0.125 mm, the 0.25 mm, and the 0.36 mm thick PDMS samples are plotted in *Figure 61*, *Figure 62* and *Figure 63*, respectively. As seen, only the kinetic regime and results for high forced flows compare quantitatively with the experimental data.

On the contrary, the radiative regime seems to fit the experimental data for the 0.125 mm thick samples. However, it is just a coincidence, as those data points were obtained in normal-gravity, where radiation is not relevant. For the other samples, the radiative branch is extended with increasing thickness. The corresponding MLOC values found by the predicted flammability boundaries are extended with increasing sample thickness. This antagonistic behaviour indicates the assumption breakdown for increasing PDMS sample thicknesses. In addition, only one reference data point from microgravity is not reflected either by the predicted radiative regime. The microgravity extinction point due to silica-ash transport and deposition affects the heat and mass transfer at the leading edge. Corrections should be made for the flame temperature and to account for in-depth heat losses and the formation of the silica via the solid-phase.

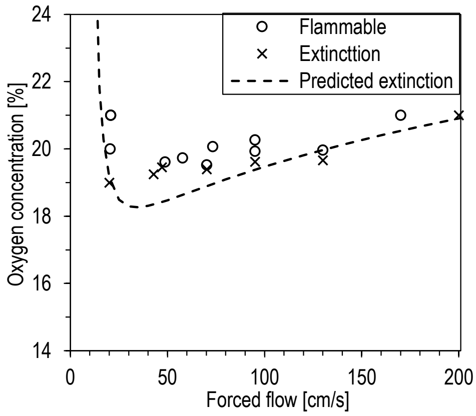

Figure 61 – Predicted extinction boundary for different oxygen concentrations and opposed forced flow velocities for a 0.125 mm thick PDMS sample. Experiments were carried out in the FPA.

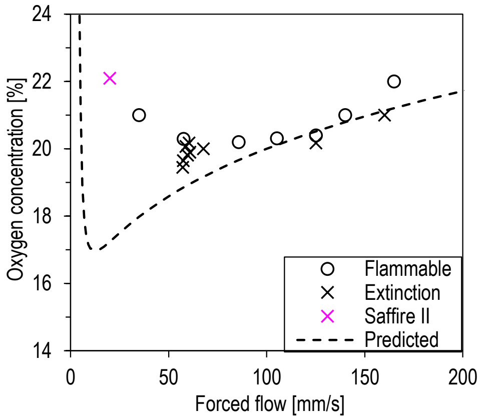

Figure 62 – Predicted extinction boundary for different oxygen concentrations and opposed forced flow velocities for a 0.25 mm thick PDMS sample. The experiments were carried out in the FPA.

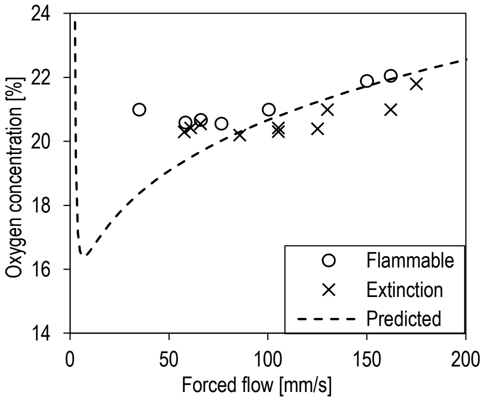

Figure 63 – Predicted extinction boundary for different oxygen concentrations and opposed forced flow velocities for a 0.36 mm thick PDMS sample. The experiments were carried out in the FPA.

7.5.4. Effect of oxygen concentration and ambient pressure

Images of the flames established over a 0.125 mm PDMS sample as a function of the environmental conditions can be seen in *Table 15*. The flame shape increases in size for any fixed ambient pressure when the oxygen concentration is increased. However, the same behaviour is not seen for increasing ambient pressure (at fixed oxygen concentrations). Thus, it is visually clear the strong effect of oxygen concentration over ambient pressure.

Table 15 – Snapshots of established flames over a 0.125 mm PDMS sample under various environmental conditions. The top row indicates the oxygen concentration, and the left column represents the ambient pressure. The length of the sample is cropped, but the width of the flame is 50 mm on a real scale. Results were obtained in the TOPOFLAME rig.

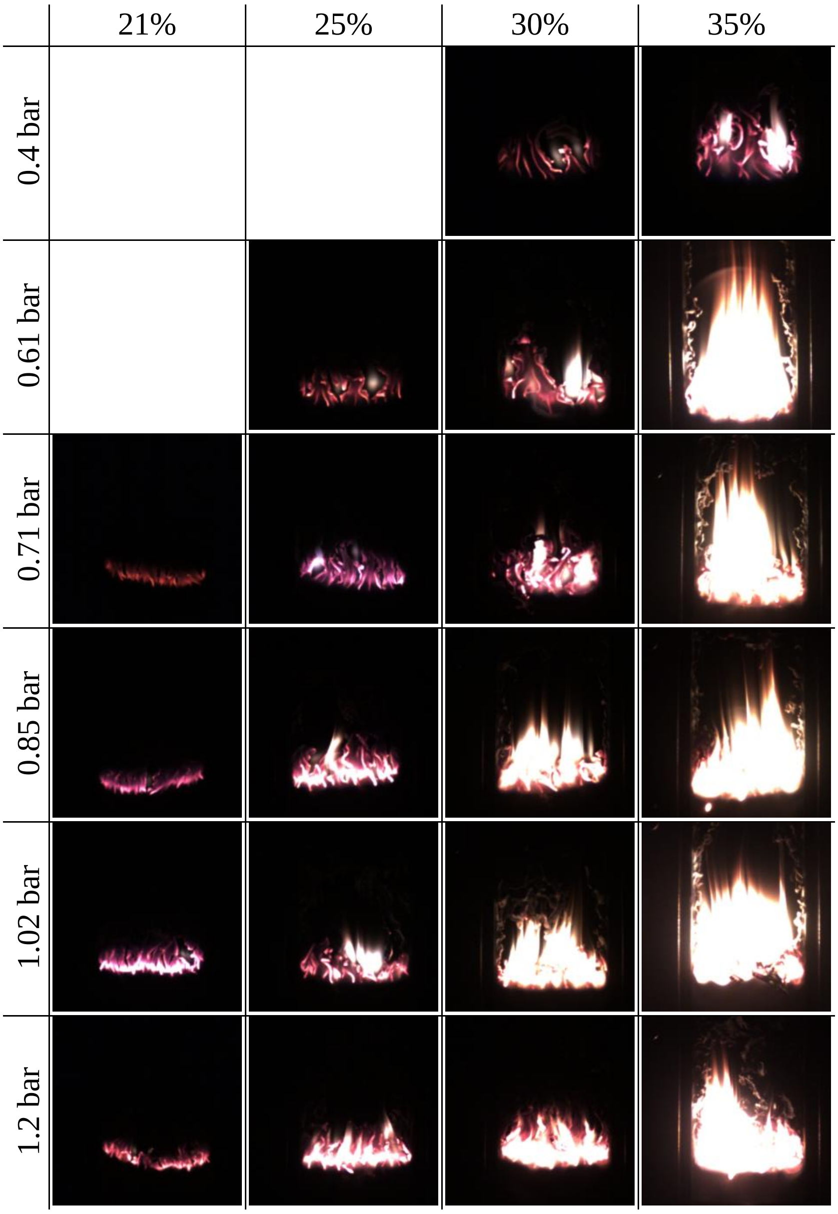

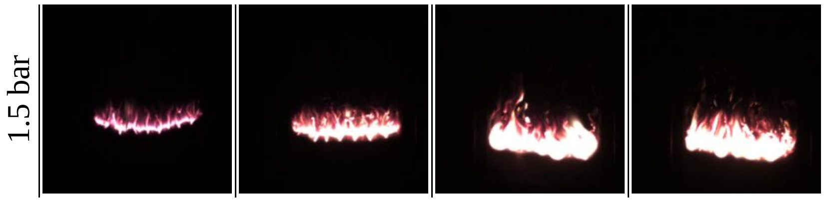

The flame spread rate and flame lengths as a function of the oxygen concentration are plotted in *Figure 63*. The flame spread rates under different fixed ambient pressures exhibit a linear dependency on the oxygen concentration. As the oxygen concentration is increased, the flame temperature increases due to chemistry [52,357]. In turn, the heat from the solid-phase to the gas-phase increases. Then the increase in flame temperature, and increase in gas-phase properties, is directly proportional to the flame spread rate, as confirmed by $V_f = \frac{k_g \rho_g c_p (T_f - T_p)}{\rho_s c_s \tau (T_p - T_o)}$. In addition, a reduction of the flame temperature translates into a decreased in the induced buoyant velocity.

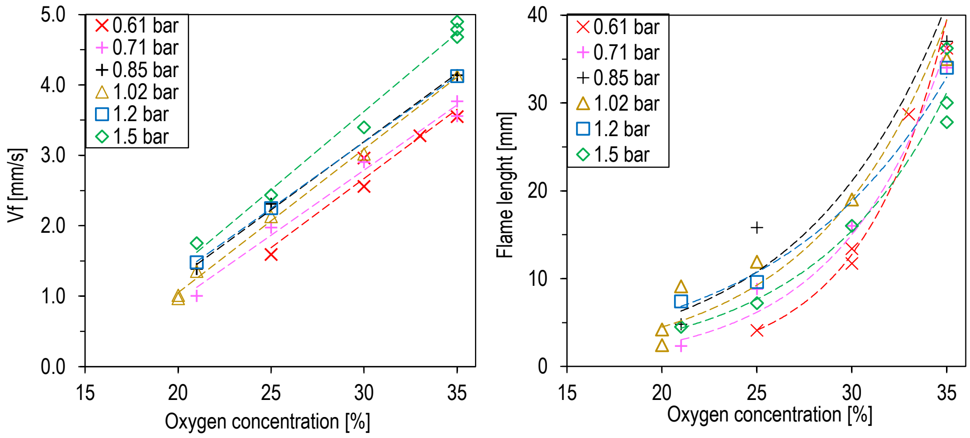

Figure 64 – Opposed flame spread rate (left panel) and flame length (right panel) as a function of the oxygen concentration for a range of ambient pressures for a 0.125 mm thick PDMS sample. The experiments were carried out in the TOPOFLAME.

The dependency of flame length on the oxygen concentration is exponential for all data sets, *Figure 63*. Bhattacharjee et al. [118] derived an expression for the flame length in the thermal regime

$L_f \sim 0.0345[(T_f - T_v)/((T_p - T_\infty)y_{O_2})]^2 L_g$. For all the pressures tested, it is assumed that the thermal regime will hold, away from extinction. In the former equation, the flame length directly proportional to the square of the oxygen concentration and flame temperature. Thus, it coincides with the current results. The effect of the oxidiser on the flame length relies on two aspects, the supply of fuel and the local supply of oxidiser. Increase in oxygen results in increasing flame temperature and soot oxidation [358], which increases the heat feedback (radiation) and elongates the flame. Under buoyant conditions, the buoyant induced flows do not affect the supply of an oxidiser, and thus flame lengths will be mainly dependent on the oxygen concentration.

The flame spread rates and the flame lengths are plotted as a function of the ambient pressure in *Figure 65*. The pressure shows to affect the flame spread and flame length differently as two apparent regimes emerged. As the pressure is reduced, the flame spread rates decrease linearly with decreasing ambient pressure for any fixed oxygen concentration. This dependency is shown to be weak compared to the oxygen concentration dependency. If the ambient pressure is reduced further, the flame spread rate decreases in an asymptotic manner, reaching a limiting vertical value. Such behaviour has been reported previously with different materials [53,359–362].

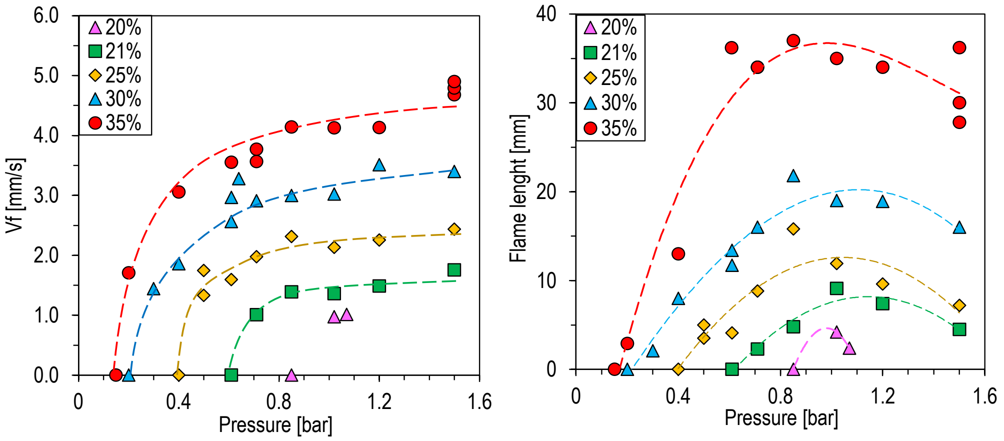

Figure 65 – Opposed flame length as a function of the ambient pressure for a range of oxygen concentrations for a 0.125 mm thick PDMS sample. The experiments were carried out in the TOPOFLAME.

As pressure is reduced, the incident heat flux from the flame is reduced. The heat from the gas-phase to the solid-phase is reduced proportionally as the flame thickness is increased with decreasing pressure [53]. The flame spread has a weak dependence on the pressure but is heat transfer controlled [360]. For the non-linear and asymptotic behaviour, the gas-phase diffusion is inversely proportional to the pressure ($\alpha \sim 1/P$). In contrast, the reaction time increases with decreasing pressure. Thus, Da becomes small and flame spread rate is controlled via kinetics for the asymptotic regime. It has been hypothesized that at very low pressure, there is a combination effect of radiative losses (via solid-phase) along with a decrease in kinetics [363]. Bhattacharjee et al. [363] have shown that a radiative parameter is proportional to $(1/p^2 g)^{2/3}$ and the Damköhler number is proportional to $(p/g)^{2/3}$.

The flame length dependency on ambient pressure exhibits a non-monotonic behaviour, as seen in *Figure 65* (right panel). Increasing pressure increases the flame length for a fixed oxygen concentration until it reaches a peak. Thereafter, the flame length decreases with increasing pressure. Similar results have been reported in the literature for the left regime in the flame length concerning the pressure increase [364,365]. As flame height is defined by the supply of fuel and oxygen entrainment in the combustion zone, these would also be affected by changes in ambient pressure. Increasing pressure while fixing oxygen concentration affects the local supply of oxidiser since the induced buoyant velocity is proportional to pressure. At the same time, an increase in pressure increases the flame temperature, providing more heat feedback to increase the fuel supply rate [360,361]. For the results presented in (right panel), it is clear that the leading mechanism is fuel supply via thermal transfer as the flame length increases with increasing pressure.

For the second regime, where flame lengths decrease with increasing pressure. Increasing pressure leads to an excess of fuel which will be burnt in the flame region. The flame height or length is determined by the ratio of the heat of gasification to the stoichiometric oxygen-fuel mass ratio [366]. For increased pressure, there is an excess of fuel supply (infinitely large Da). Then, the dominant force is the oxidiser supply since the induced buoyant velocities increase with increasing ambient pressure. Thus, the local oxidiser supply increases the stoichiometric oxygen-fuel mass ratio, and in turn, the flame length decreases, as suggested. Another mechanism that might aid in the local oxygen supply is pressure-induced turbulences. The flame length at high pressures exhibited a flickering behaviour that was not observed at lower pressures. Ban et al. [367] also reported flame height (gaseous diffusion flame) decreasing with increasing pressure. They attributed it to the shift from a laminar regime towards a turbulent regime.

The flame spread rates for normoxic conditions as a function of the oxygen concentration and ambient pressure are plotted in *Figure 66*. A combined effect of reducing ambient pressure while increasing the oxygen concentration has mainly consequences via heat transfer. As seen previously, increasing oxygen results in higher flame temperatures. On the contrary, reducing pressure enlarges the flame (thick optical flame) and reduces the heat transfer from the flame to the solid at the leading edge. The results seen in *Figure 66* indicate that heat transfer via chemical reaction has a larger effect on the flame spread rates, at least away from extinction conditions. Also, the flame spread rate is proportional to the sample thickness, as expected. Thus, normoxic conditions do not offer an improved flammability scenario for PDMS. Similar results have been reported for cellulosic fuels [103].

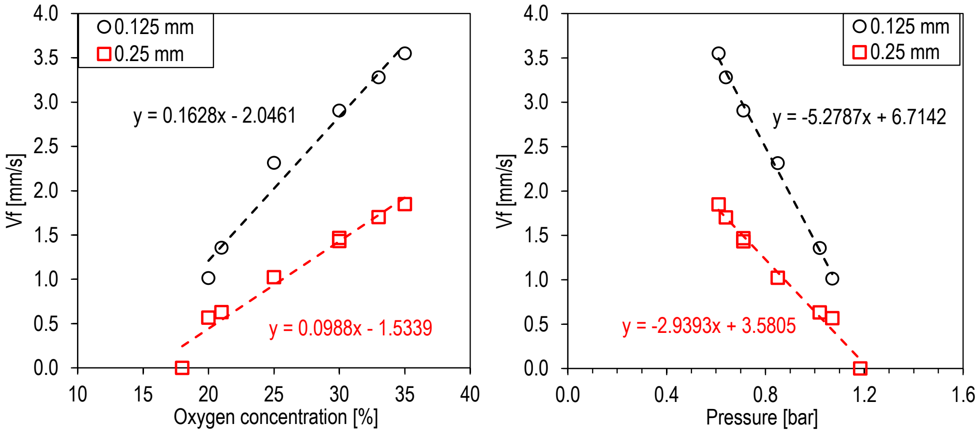

Figure 66 – Opposed flame spread rates as a function of the normoxic condition for two PDMS samples (thicknesses of 0.125 mm and 0.25 mm). The experiments were carried out in the TOPOFLAME.

The corresponding flame length results in a normoxic environment exhibited similar behaviour, as seen in *Figure 67*. Again, from a combined effect of oxygen concentration and ambient pressure, the former seems to help in providing a large fuel supply and large flames. Thus, oxygen supply dominates the flame lengths under normoxic conditions. The flame length is nearly the same for both sample thicknesses. This indicates that there is no substantial increase of fuel supply from a 0.125 mm to a 0.25 mm thick PDMS sample. It appears that oxygen supply dominates the flame lengths independently of sample thickness, at least in the current investigation.

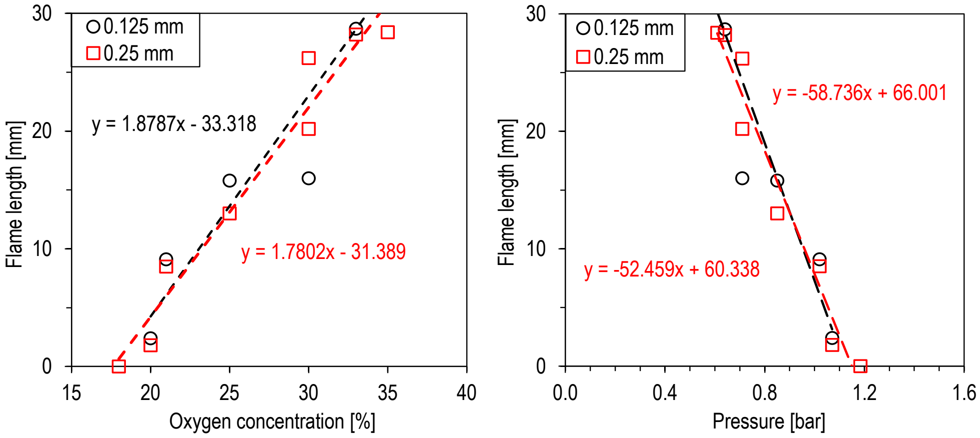

Figure 67 – Opposed flame lengths as a function of the normoxic condition for two PDMS samples (thicknesses of 0.125 mm and 0.25 mm). The experiments were carried out in the FPA.

The flame length results are plotted against the oxygen partial pressure in *Figure 68*. As seen in the left panel, the maximum flame length occurs at reduced pressures for normoxic conditions to be kept (vertical line). That is, between 0.61 bar and 0.71 bar, the normoxic flames are the longest. In the right panel of *Figure 68*, two regimes in flame length are observed as a function of the oxygen partial pressure. The same mechanism behind both regimes described earlier applies in *Figure 68*. It is interesting is the change of regimes that occur at the actual normoxic condition. Thus, normoxic conditions help flame spread and provide the best conditions for the longest flame lengths in buoyant scenarios.

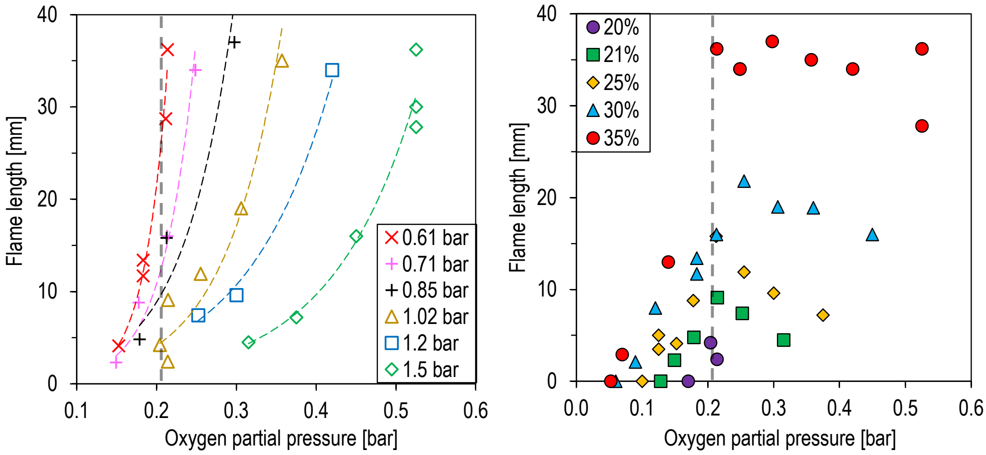

Figure 68 – Opposed flame length as a function of the Oxygen partial pressure (Opp). The vertical line indicates the normoxic condition. The experiments were carried out in the TOPOFLAME.

The opposed flame spread velocities results are plotted as a function of the flame lengths for a range of environmental conditions in *Figure 69*. As seen, the flame spread rate exhibits a similar dependency for flame lengths as a function of the oxygen concentration and ambient pressure. It is noticeable that the dependencies reach an asymptotic behaviour for the longest flame lengths only for the 0.125 mm thick PDMS sample. This behaviour is a reflection of the two regimes shown earlier, where the ambient pressure is a determinant parameter that defines the change of regimes.

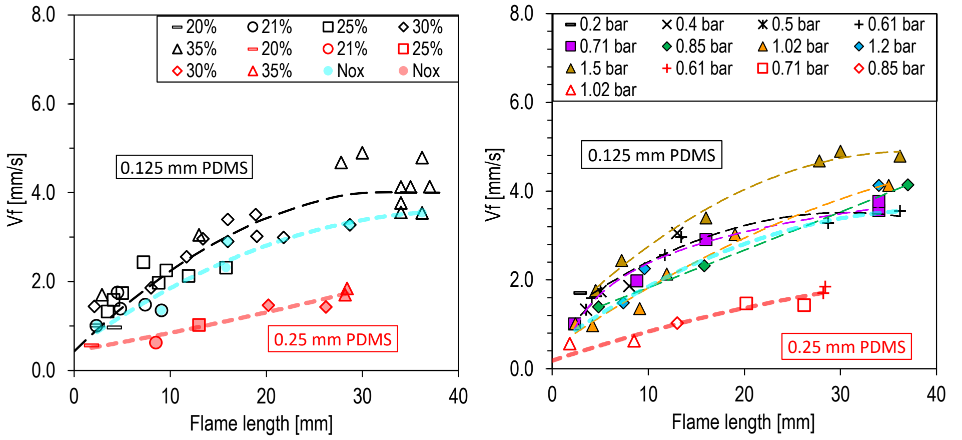

Figure 69 – Opposed flame spread rates plotted against of the corresponding flame length for a range of environmental conditions (oxygen concentration, ambient pressure and normoxic condition). The experiments were carried out in the TOPOFLAME.

Figure 70 shows the boundary limits as a function of the oxygen concentration, ambient pressure and oxygen partial pressure. These extinction limits resemble the radiative branch found in microgravity. A similar extinction boundary has been found in normal-gravity with other materials [108,360]. Previous studies have suggested that the extinction limits at low pressure are dominated by kinetics. This is related to molecular diffusion inversely proportional to the ambient pressure [360] and that the reaction order decreases with decreasing pressure [278]. Thus, the flow time is short, and the chemical time is very small, yielding a smaller Damköhler number. Also, as the pressure is reduced, the heat losses increase and can also contribute to extinction [368]. A recent numerical study suggested that there is an interaction between kinetics and heat losses at low pressure [363]. Thus, the extinction conditions at low pressure might be a combination of a reduction in heat losses through the solid-phase and gas-phase and a combination of slower chemical reaction rates.

The normoxic curve and the hyperoxic limit are also plotted in *Figure 70*. Between those limits, the PDMS still encounters favourable flammability conditions. This zone corresponds to the earlier flame spread and flame length results, which were enhanced in normoxic conditions. Thus, this particular PDMS is still flammable in normal gravity scenarios. It is not clear how different these limits would be in microgravity conditions. It seems that the transport and deposition of silica-ash is not determinant for the 0.125 mm thick PDMS sample. However, in microgravity, the opposite was demonstrated. The silica-ash measurement at the extinction condition showed a very small increase with decreasing pressure. Only for the lowest pressure was there a significant increase in deposited ash. Thus, a reduction in pressure might not help in the silica-ash deposition.

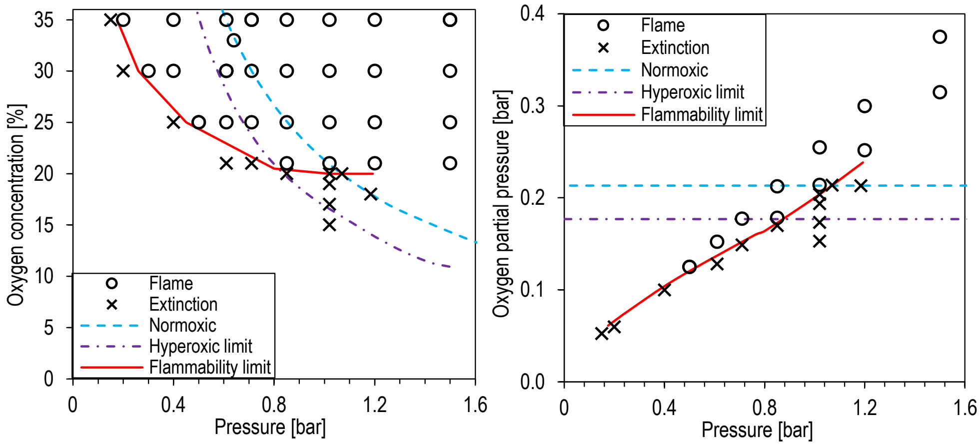

Figure 70 – Flammability limits for a range of ambient pressures and oxygen concentrations (left panel). The right panel shows the flammability limit for a range of ambient pressures and Oxygen partial pressures (Opp) (right panel). The normoxic curve and the hyperoxic limit are also shown. The data are for opposed flame spread over a 0.125 mm thick PDMS sample. The experiments were carried out in the TOPOFLAME.

The mass loss rate data acquired during the experiment performed in the TOPOFLAME can be seen in *Figure 71*. The scattering of the data is evident and is a consequence of the formation of silica in the solid-phase. As flame travels downwards, the left solid-phase silica falls down due to the action of gravity. Consequently, the measurements taken by the weighing scale are a combination of the mass loss due to exothermic reaction (flaming combustion) and the falling debris comprised of the silica (mostly this). The mass loss rate can also be defined by the flame spread rate under steady conditions, $\dot{m}'' = \rho_s V_f 2\tau W$, thus the maximum computed mass loss rate is 0.03 g/s. Thus, it is clear that the mass loss data seen in *Figure 71* was largely corrupted by the falling rate of the silica debris.

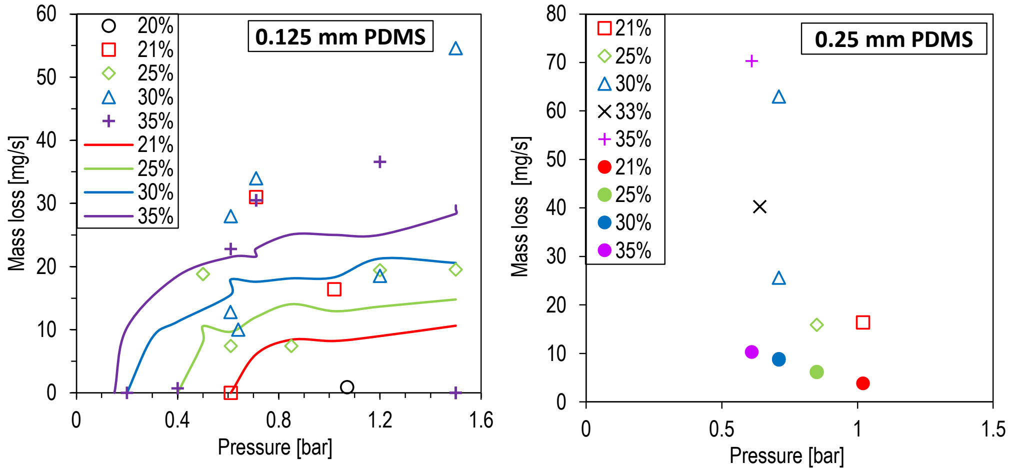

Figure 71 – Gravimetric mass loss as a function of the ambient pressure for a range of oxygen concentrations for opposed flame spread over two PDMS samples. The left panel shows data for the 0.125 mm thick samples, for which oxygen concentration and ambient pressure were evaluated separately. In the right panel, the mass loss data for the 0.25 mm thick samples at normoxic conditions is shown. Predictions based on the experimental flame spread rates are also plotted. The results were obtained in the TOPOFLAME

In *Figure 71*, the largest mass loss rate appears to be from the highest oxygen concentration. Conversely, the lowest mass loss rates were for the lowest oxygen concentration and lowest ambient pressure. These latter experimental values match better the computed mass loss. From IR video analysis, it was observed that the left silica formed a fragile structure in some of the experiments with good measurements. Thus, the mass loss was a true measurement of mass loss. Both environmental parameters affect the formation of depolymerisation and formation of silica in the solid-phase. Such behaviour can be directly linked to the formation of silica via the solid-phase

For high oxygen concentrations, the flame temperature is increased via chemistry. Thus, higher heating rates at the leading edge are attained, and the depolymerisation process will leave less silica. This silica is fragile and will fall down immediately as the flame travels downwards. Pressure also decreases the flame temperature, as seen previously. Thus, for increasing pressure, the heating rate at the leading edge is increased proportionally, and less silica is left behind, which is weaker and falls more readily.

On the contrary, for sub-atmospheric pressures, the heat losses via solid-phase and gas-phase are much greater and will reduce the heating rate drastically at the leading edge. Fewer siloxanes pyrolysate and more silica are left behind, which forms stronger structures. These results are corroborated by the thermogravimetric analysis presented earlier and confirm the complexity of the PDMS material.

The measured pre-heat and pyrolysis length are plotted in *Figure 72*. The data show significant scatter, especially for the pyrolysis lengths. These results showed that it was very challenging to measure the solid-phase characteristic lengths with the PDMS pyrolysis temperature as a basis. First of all, the PDMS and silica emissivity are different and are a function of temperature. Previously, it was shown that the heating rate at the leading edge and the solid-phase temperature distribution are affected by environmental conditions. In turn, the formation of silica in the solid-phase and via gas-phase will be also influenced. Also, as silica-ash forms in the gas-phase, it is likely that the IR camera would first see these particulates (shadowing effect).

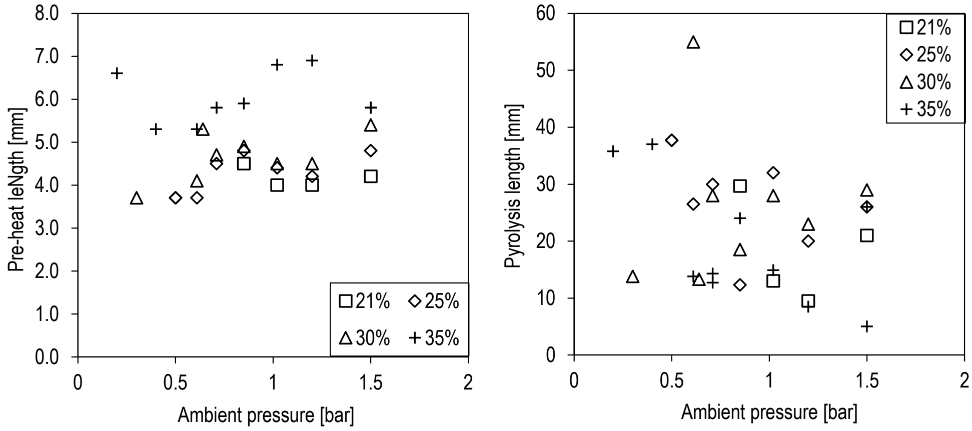

Figure 72 – Pre-heat lengths (left panel) and pyrolysis lengths (right panel) as a function of the ambient pressure for a range of oxygen concentrations. The case is an opposed flame spread over a 0.125 mm PDMS sample. The results were obtained in the TOPOFLAME.

Another problem observed during the experiments is that the sample bends at the flame trailing edge. Thus, the camera does not see a perpendicular plane of the flame front at the leading edge. It was expected that the pre-heat length would increase in size for sub-atmospheric pressure. However, the pre-heat length showed non-monotonic behaviour as a function of the ambient pressure and also as the oxygen concentration was varied.

8. Conclusions

Fire safety on spacecraft goes hand in hand with fundamental studies on the combustion of solid materials in microgravity. Fire safety prerequisites on spacecraft have created a need to understand the flammability behaviour of solid materials in microgravity environments such as those encountered on spacecraft. As seen in the literature review Chapter, predicting the flammability behaviour of solid materials (ignition, flame spread and near-limit) in microgravity environments is currently not very feasible. Some simplified methods and numerical approaches can partly predict certain flammability phenomena. However, those methods require quantitative microgravity data in order to be validated. Conducting experiments in microgravity environments has many constraints, and obtaining quantitative information faces many limitations.

Assessing the flammability of solid materials has relied for a long time on a series of tests based on normal-gravity data. Thus, these standard tests do not represent conditions encountered by spacecraft materials. The established criteria for flammability behaviour were based on the worst-case scenario. The NASA Test 1 (Upwards Flame Propagation) burnt length criterion is a clear example. It was seen that there might be other worst-case or critical scenarios on spacecraft that are not covered by the current assessment standards. Various methods based on fundamental behaviour have been proposed in the quest to improve the flammability assessment of solid materials in microgravity. These methods are a substantial qualitative improvement with respect to the current standards. Nonetheless, these methods still require quantitative microgravity data to prove their validity and their application range. One of the methods, the LOI-MLOC is based on the fundamental flammability behaviour of materials. The method empirically predicts the flammability boundary limits that can be used to rank materials. Pressure modelling is another method that has been proposed to study various flammability phenomena.

Silicones are widely used across several industries and spacecraft due to their stable thermal behaviour and are considered flame-retardant material. During thermal degradation of silicone under oxidative environments, and more during diffusion flaming, white silica ash (SiO_2), is formed and can deposit on the unburnt fuel. Thus, the silica ash forms a protective layer that influences the heat and mass transfer (through diffusion). Silicone samples (Polydimethylsiloxane) membranes were tested during the Saffire II testing programme on the Cygnus spacecraft. None of the samples achieved a self-sustained flame. Thus, experimental work was conducted in the current study to elucidate the flammability behaviour (ignition, flame spread and extinction phenomena) of Polydimethylsiloxane under an array of environmental parameters (forced flows, oxygen concentration and ambient pressures).

The current experimental results indicate that Polydimethylsiloxane's flammability behaviour is far more complex than anticipated and depends on various environmental conditions. The thermal degradation study found that during pyrolysis, silica-ash is formed via gas-phase, and silica in the solid-phase is also formed. The amount of silica formed in the solid-phase is a function of the heating rate. This behaviour was confirmed when the PDMS samples of various thicknesses were exposed to a range of incident heat fluxes using the cone calorimeter. Under the stagnant conditions, the ignition delay times showed two distinctive behaviours, one at a low heating rate and the other at high heating rates. Thus, critical heat fluxes extrapolated at low heating rates are the consequence of PDMS pyrolysis and silica formation in the solid-phase. In other words, at low heating rates, the PDMS behaves like composite material. As a consequence, the computed critical heat flux and pyrolysis temperatures did not match the reference values from the literature. This behaviour has direct implications as it is determinant in the flammability behaviour of PDMS.

A summary of the experimental results obtained in the current investigation is listed in *Table 16*. These results concern the various aspects of flammability studied here, such as ignition, flame spread and near-limit phenomena, as a function of various environmental conditions and scenarios (forced flow, flow direction, oxygen concentration, ambient pressure and normoxic conditions).

Table 16 – Summary of the flammability experimental results obtained in the current investigation over the PDMS membranes as a function of a range of environmental conditions. The following acronyms were used: LD = linear dependency, AP = asymptotic dependency, NMD = non-monotonic dependency, ED = Exponential dependency, I = independent.

Phenomena			V_g	O_2	P	Normoxic
Ignition			LP ➔ mixing time AP ➔ SiO_2 formation in solid-phase	LP ➔ chemistry	LP ➔ chemistry	NMD (Unknown mechanism)
Flame spread behaviour	V_s	O	I (away from extinction)	LD ➔ chemistry & heat transfer.	LD ➔ heat transfer AD ➔ heat transfer & kinetics	O_2 >> P
		C	LP ➔ silica-ash transport and deposition	NS	NS	NS
	l_f	O	NS	ED ➔ fuel supply & local supply of oxidiser	(↑ l_f& ↑ P) regime ➔ fuel supply (thermal transfer) (↓ l_f& ↑ P) regime ➔ via oxidiser supply and enhanced mixing	O_2 >> P Largest l_f occurs at Normoxic
		C	NS	NS	NS	NS
Near-limit	e	O	High V_g ➔ kinetics Low V_g ➔ SiO_2 formation in solid-phase	NS	NS	NS
		C	➔ SiO_2 transport and deposition	NS	NS	NS
	O_2	O	High V_g & low O_2 ➔ kinetics Low V_g & low O_2(µg) ➔ SiO_2 transport and deposition		Low O_2 & low P ➔ heat transfer and kinetic	NS
		C	NS		NS	NS
SiO_2	Formation		NS	NS	NS	NS
	Transport & Deposition		1g or V_g ➔ buoyant or laminar forces µg ➔ thermophoresis		NS	NS

During piloted ignition in forced flow, it was shown that the ignition delay time over PDMS is directly proportional to the forced flow (via mixing time). As the forced flow increases the cooling down of the ignition wire (reducing the heating rate), the dominating mechanisms seem to shift to the formation of silica in the solid-phase. From these results, it is clear that ignition was successful during Saffire II tests. This means that the lack of flame spread in the Saffire II tests is indeed a flame spread problem rather than an ignition problem. The current ignition delay times exhibited linear dependency due to the oxygen concentration and ambient pressure. The mechanism that dominates both cases is chemistry. A special case was observed under normoxic conditions, where the ignition delay time showed a non-monotonic behaviour and reversed depending on the sample thickness. It is not clear the mechanism behind such behaviour, but it is suspected to be related to the gas-phase.

The flame spread behaviour in forced flows appears to be very distinct depending on the flame spread direction with respect to the imposed forced flow. In opposed forced flows, the flame spread rate is nearly independent of the forced flow, as predicted by de Ris [52]. It seems that the silica-ash produced does not affect the heat and mass transfer at the leading edge. However, for concurrent force flows, the flame spread showed to be affected predominantly by the transport and deposition of silica. The deposition of silica ash is dominated by thermophoretic forces and by convective forces. As forced flows increase, the momentum generated due to convection is much larger than those of thermophoresis, and the silica-ash deposition is reduced. In microgravity, thermophoretic forces are larger, and it is thus suspected that silica ash deposition also dominates flame spread in microgravity.

The effect of increasing the oxygen concentration on the opposed flame spread is via chemistry (flame temperature). The opposed flame length increases exponentially as a function of the oxygen concentration due to enhanced heat flux, increasing the fuel supply and soot oxidation. Changing the ambient pressure leads to two regimes for both the opposed flame spread rates and the corresponding flame lengths. Reducing the ambient pressure leads to an initial weak dependency (going from high to low pressures), where there is a reduction of heat flux from the gas-phase to the solid-phase at the flame leading edge. As the pressure is reduced further, flame spread becomes asymptotic due to a reduction in kinetics. For the flame length, the change in pressure affects the supply of fuel and oxygen entrainment into the combustion zone. For low pressures, flame lengths are dominated by fuel supply (increases with increasing pressure). For the reverse regime, where flame length decreases with increasing pressure, the flame is dominated by an oxidiser supply since there is an excess of fuel.

For normoxic conditions, where the oxygen concentration increases while the ambient pressure decreases, there is a competition of the leading mechanism explained above for flame spread and flame lengths. However, it was seen that the oxygen concentration (via chemistry) dominates over the reduction of heat due to lower ambient pressure. The change of regimes for the flame length as a function of the ambient pressure occurs near the normoxic conditions. Thus, normoxic conditions favour flame spread and flame length development. Near-limit phenomena for flame spread under concurrent forced flows are dominated by silica-ash transport and deposition. For opposed flame spread, kinetics dominate extinction at high forced flows. However, as the sample thickness is increased, and for low forced flows, the formation of silica via the solid-phase also affects extinction. Under low pressure, the extinction condition might occur under low pressure due to a combined effect of heat losses and kinetics.

Based on the experimental behaviour obtained for the PDMS, it can be concluded that the Saffire II extinction behaviour was mainly due to the silica-ash transport and deposition affecting the heat and mass transfer. That is, the accumulation of silica-ash produced in the gas-phase hindered the heat transfer from the flame and heating coil to the PDMS. At the same time, the protective layer of silica reduces the transport of pyrolysates from the PDMS. Another highlight of the current investigation is that the Saffire II tests with PDMS membranes provided valuable information, which along with the current investigation, can cast some light on the flammability behaviour of PDMS membranes in normal gravity and microgravity scenarios.

For PDMS, the LOI-MLOC method can only be applied for the kinetic regime where the effect of silica-ash deposition is not relevant. For low forced flows, for low oxygen concentrations, or microgravity conditions under very low-forced flows, the radiative regime is not representative as the transport and deposition of silica-ash dominate the extinction behaviour. Thus, the extinction dichotomy (radiative-kinetics) does not apply to PDMS materials. The LOI-MLOC's limitations have been exposed, and such a method, if it were to be used for flammability assessment, might need a limitation of usage on certain polymeric materials. Pressure modelling as a method to study ignition of extinction also has several limitations with PDMS as the formation of silica, via gas-phase and solid-phase, in microgravity might not be reproduced by reducing pressure. Again, such a method requires a defined scope of application. Thereby, no flammability assessment method alone can be a reasonable tool to evaluate the adequacy of solid materials (material selection) for spacecraft applications. Instead, a combination of methods can provide a robust material selection strategy.

Finally, are PDMS and silicone-based products safe enough for spacecraft applications? To answer that question will depend on the conditions encountered by the PDMS membranes on spacecraft. That is, in which environmental conditions are the PDMS membranes or similar materials will be used. For environmental conditions similar to those on Earth at sea level, current ISS spacecraft design, and low forced flows, thermally-thick PDMS are not likely to be flammable. However, under high forced flows or normoxic conditions, the thermally-thin PDMS might be readily flammable, and it is currently not possible to predict the flammability behaviour for those scenarios.

When compared to other thermoplastics used on spacecraft applications (e.g. PP or PE), PDMS shows to be less flammable due to the silica-ash formation and deposition and silica formation in the solid-phase. If further testing confirms the lower flammability of PDMS in other environmental conditions, siloxanes or other silicone-based products could be used, like fillers or additives, for other materials to reduce their flammability. Thus, there might be a window to improve the material selection strategy by improving the design of materials.

A series of properties could be extrapolated from all the experimental results on the PDMS membranes and are presented in the following table. The results for the LOI vary according to the sample thickness, which agrees with the literature due to the nature of the PDMS related to the thermal decomposition and formation of silica via solid-phase. The thicker the sample is, the more energy is required to decompose the silicone. Also, the pre-exponential factor found for the gas-phase varies on the sample thickness and should not be the case, but it is also a consequence of the thermal decomposition of this particular siloxane.

To finalise, all the empirically obtained or measured properties are listed in *Table 17*. This information can be deemed valuable for future investigations on the PDMS membranes.

Table 17 – Summary of the extrapolated properties for PDMS membranes studied in the current investigation.

Method	Property		Value	Units
Thermocouples measurements	Flame temperature		1180	℃
Cone Calorimeter	Critical heat flux		30	kW/m^2
TGA (ASTM E1641-16)	Activation energy (solid-phase)		148	kJ/mol
	Pre-exponential factor (solid-phase)		$3.4 \cdot 10^7$	min^{-1}
Improved FPA	LOI	e = 0.125 mm	19.3	%
		e = 0.25 mm	20	
		e = 0.36 mm	20.8	
MLOC method (empirical)	Activation energy (gas-phase)	e = 0.125 mm	224	kJ/mol
		e = 0.25 mm		
		e = 0.36 mm		
	Pre-exponential factor (gas-phase)	e = 0.125 mm	$2.59 \cdot 10^9$	$m^3/kg \cdot s$
		e = 0.25 mm	$2.19 \cdot 10^9$	
		e = 0.36 mm	$1.34 \cdot 10^9$	

8.1. Flame spread behaviour

Using the LOI-MLOC method does not seem to be applicable, or the assumptions established for the method break down for the PDMS samples. The method was only accurate in its quantitative prediction of the extinction limit for high forced flows (i.e. kinetic controlled regime). Therefore, the ultimate goal of predicting the MLOC was not feasible for the PDMS samples. Thus, the limitations of the method should be delimited. Consequently, other methods, or a combination of methods, should be used to assess flammability. Pressure modelling has many limitations as it relies on reducing the buoyancy effects, but ignition and near-limit conditions can also be affected by chemistry and kinetics. Thus, pressure modelling is not applicable for those particular flammability phenomena. As NASA is currently evaluating the LOI-MLOC method and pressure modelling, it is worth pointing out the limitations of those methods. Using an array of methods to predict the flammability behaviour and to provide fundamental properties to be used on classifications should provide a more robust and holistic framework to rate materials for spacecraft applications. If such a framework were to exist, the limitation of each method should be clearly defined and its range of applicability.

With respect to PDMS and other siloxane-based products for spacecraft applications – these materials are indeed very challenging to study. Because of their thermal stability and apparently improved flammability behaviour, they are widely used across various industries (including spacecraft). However, as shown in the experimental study, the flammability behaviour of PDMS is very complex and is strongly influenced by the environmental properties and heating rates. Nonetheless, a clear picture of its flammability behaviour requires further studies on various aspects. The first aspect is the formation of silica-ash in the gas-phase, its transport and deposition. In turn, if the silica-ash deposition can be predicted, then the flammability behaviour can be predicted more accurately (especially flame behaviour). The other aspect that requires further attention is the formation of silica in the solid-phase. These two aspects need to be understood in experiments carried out under more controlled conditions. Another relevant aspect is studying the effect of normoxic environments and microgravity especially.

REFERENCES

[1] Recapturing a Future for Space Exploration: Life and Physical Sciences Research for a New Era, The National Academies Press, Washington, D.C, 2012.

[2] R. Friedman, Fire Safety in the Shuttle and the Space Station Freedom, in: Second Int. Microgravity, 1991: pp. 213–225.

[3] D.L. Dietrich, H.D. Ross, Y. Shu, P. Chang, J.S. T'ien, Candle flames in non-buoyant atmospheres, Combust. Sci. Technol. 156 (2000) 1–24. doi:10.1080/00102200008947294.

[4] C. Payne, Candle Flame - 1g vs Microgravity, (2020). http://www.nasa.gov/image-feature/candle-flame-1g-vs-microgravity (accessed April 30, 2021).

[5] F.L. Thompson, F. Borman, M.A. Faget, E.B. Geer, C.F. Strang, R.W.V. Dolah, G.C. White, J.J. Williams, Report of Apollo 204 Review Board, Washington, D.C., 1967.

[6] D.L. Dietrich, Modeling and Analysis of Realistic Fire Scenarios in Spacecraft, in: 45th Int. Conf. Environ. Syst., Bellevue, Washington, 2015.

[7] P. Ferkul, K. Sacksteder, P. Greenberg, D. Dietrich, H. Ross, J. Tien, R. Altenkirch, L. Tang, M. Bundy, M. Delichatsios, Combustion experiments on the Mir Space Station, in: A.I. of A.& A. (AIAA) (Ed.), 37th Aerosp. Sci. Meet. Exhib., Reno, Nevada, 1999: pp. 1–14. doi:doi:10.2514/6.1999-439 10.2514/6.1999-439.

[8] The 5 Deadliest Disasters of the Space Race - HISTORY, (n.d.). https://www.history.com/news/the-5-deadliest-disasters-of-the-space-race (accessed April 30, 2021).

[9] C.K. Law, G.M. Faeth, Opportunities and challenges of combustion in microgravity, Prog. Energy Combust. Sci. 20 (1994) 65–113. doi:10.1016/0360-1285(94)90006-X.

[10] Space systems — Safety and compatibility of materials — Method to determine the flammability thresholds of materials (ISO/TS 16697:2012), International Organization for Standardization, Geneve, Switzerland, 2012.

[11] T.J. Ohlemiller, K.M. Villa, Material Flammability Test Assessment for Space Station Freedom, 1991.

[12] O. Fujita, Solid combustion research in microgravity as a basis of fire safety in space, Proc. Combust. Inst. 35 (2015) 2487–2502.

[13] J.H. Kimzey, Flammability during weightlessness, in: Twelfth Annu. Tech. Meet. Inst. Environ. Sci., Institute of Environmental Science, San Diego, California, 1966: pp. 433–437.

[14] J.H. Kimzey, W.R. Downs, C.H. Eldred, C.W. Norris, Flammability in zero-gravity environment, Washington, D.C., 1966.

[15] J.H. Kimzey, Skylab experiment M479 zero gravity flammability, in: Proc. Third Sp. Process. Symp. Skylab Results, National Aeronautics and Space Administration NASA, Alabama, 1974: pp. 115–130.

[16] H.D. Ross, P.D. Ronney, G.M. Faeth, M.Y. Choi, F.L. Dryer, J.S. T'ien, H.Y. Shih, C.B. Jiang, F.J. Miller, A.C. Fernandez-Pello, J.L. Torero, D. Walther, R.A. Yetter, R.L. Axelbaum, J.J. Moore, R. Friedman, Microgravity Combustion: Fire in Free

Fall, Academic Press, Beccles, Suffolk, UK, 2001.

[17] S.L. Olson, P. V. Ferkul, J.S. T'ien, Near-limit flame spread over a thin solid fuel in microgravity, Twenty-Second Symp. Combust. 22 (1988) 1213–1222. doi:10.1016/S0082-0784(89)80132-8.

[18] S.L. Olson, Mechanisms of Microgravity Flame Spread Over a Thin Solid Fuel: Oxygen and Opposed Flow Effects, Combust. Sci. Technol. 76 (1991) 233–249. doi:10.1080/00102209108951711.

[19] T. Vietoris, P. Joulain, J.L. Torero, Experimental Observations on the Geometry and Stability of a Laminar Diffusion Flame in Micro-Gravity, Fire Saf. Sci. 6 (2000) 373–384. doi:10.3801/IAFSS.FSS.6-373.

[20] P. Joulain, T. Vietoris, J. Torero, Gas-gas and gas-solid laminar flat plate diffusion flame in microgravity: Structure and stability, Microgravity Sci. Technol. 13 (2001) 3–6. doi:10.1007/bf02873324.

[21] S. Takahashi, H. Ito, Y. Nakamura, O. Fujita, Extinction limits of spreading flames over wires in microgravity, Combust. Flame. 160 (2013) 1900–1902. doi:10.2514/6.2013-3388.

[22] A.F. Osorio, K. Mizutani, C. Fernandez-Pello, O. Fujita, Microgravity flammability limits of ETFE insulated wires exposed to external radiation, Proc. Combust. Inst. 35 (2015) 2683–2689.

[23] D.W. Foutch, J.S. T'ien, Extinction of a stagnation-point diffusion flame at reduced gravity, AIAA J. 25 (1987) 972–976. doi:10.2514/3.9730.

[24] J.L. Rhatigan, H. Bedir, J.S. T'ien, Gas-phase radiative effects on the burning and extinction of a solid fuel, Combust. Flame. 112 (1998) 231–241. doi:10.1016/S0010-2180(97)81771-3.

[25] G. Jomaas, J.L. Torero, C. Eigenbrod, S.L. Olson, P. V. Ferkul, G. Legros, A.C. Fernandez-Pello, A.J. Cowlard, S. Rouvreau, N. Smirnov, O. Fujita, J.S. T'ien, G.A. Ruff, D.L. Urban, Fire Safety in Space – Beyond Flammability Testing of Small Samples, Acta Astronaut. 109 (2015) 208–216.

[26] P. Ferkul, S. Olson, D.L. Urban, G.A. Ruff, J. Easton, J.S. T'ien, Y.-T.T. Liao, A.C. Fernandez-Pello, J.L. Torero, C. Eigenbrod, G. Legros, N. Smirnov, F. Osamu, S. Rouvreau, B. Toth, G. Jomaas, Results of Large-Scale Spacecraft Flammability Tests, in: 47th Int. Conf. Environ. Syst. ICES, 2017.

[27] T. Ebisawa, S. Takahashi, Limiting oxygen concentration of a solid material in mild flow environment, Japan Soc. Mech. Eng. 10 (2013).

[28] S. Takahashi, M. Hotta, S. Bhattacharjee, T. Ihara, K. Wakai, Classification of Flame Spread Behavior over a Solid Material by Scale Analysis (In Japanese), 日本マイクログラビティ応用学会誌. 29 (2012) 23–31.

[29] R.A. Neustein, P.P. MAder, G. V. Colombo, D.E. Richardson, The effect of atmosphere selection and gravity on burning rate and ignition temperature, Santa Monica, 1968.

[30] T. Kashiwagi, K.B. McGrattan, S.L. Olson, O. Fujita, M. Kikuchi, K. Ito, Effects of slow wind on localized radiative ignition and transition to flame spread in microgravity, in: Symp. Combust., The Combustion Institute, 1996: pp. 1345–1352. doi:10.1016/S0082-0784(96)80353-5.

[31] M. Roslon, S. Olenick, Y.Y. Zhou, D.C. Walther, J.L. Torero, A.C. Fernandez-Pello, H.D. Ross, Microgravity Ignition Delay of Solid Fuels in Low-Velocity Flows, AIAA J. 39 (2001) 2336–2342. doi:10.2514/2.1239.

[32] Y. Nakamura, H. Yamashita, T. Takeno, G. Kushida, Effects of Gravity and Ambient Oxygen on a Gas-Phase Ignition Over a Heated Solid Fuel, Combust. Flame. 120 (2000) 34–48.

[33] M. Ikeda, Effects of Gravity on Ignition and Combustion Characteristics of Externally Heated Polyethylene Film, Microgravity Sci. Technol. 30 (2018) 331–338. doi:10.1007/s12217-018-9606-9.

[34] K. Wang, J. Fang, J.W. Wang, S.M. Zheng, J.F. Guan, H.R. Shah, J.J. Wang, Y.M. Zhang, Ignition Delay of Fluorinated Ethylene Propylene Wire Insulation in a Forced Flow Field in Microgravity, Combust. Explos. Shock Waves. 56 (2020) 412–420. doi:10.1134/S0010508220040048.

[35] S. Fereres, C. Fernandez-Pello, D. Urban, G. Ruff, Identifying the roles of reduced gravity and pressure on the piloted ignition of solid combustibles, Combust. Flame. 162 (2015). doi:10.1016/j.combustflame.2014.10.004.

[36] Y.T.T. Liao, J.S. T’ien, A numerical simulation of transient ignition and ignition limit of a composite solid by a localised radiant source, Combust. Theory Model. 17 (2013) 1096–1124. doi:10.1080/13647830.2013.831486.

[37] I.S. Wichman, Theory of opposed-flow flame spread, Prog. Energy Combust. Sci. 18 (1992) 553–593. doi:10.1016/0360-1285(92)90039-4.

[38] W.A. Sirignano, Theory of flame spread above solids, Acta Astronaut. 1 (1974) 1285–1299. doi:10.1016/0094-5765(74)90052-6.

[39] I.S. Wichman, F.A. Williams, A Simplified Model of Flame Spread in an Opposed Flow along a Flat Surface of a Semi-infinite Solid, Combust. Sci. Technol. 32 (1983) 91–123. doi:10.1080/00102208308923654.

[40] A.C. Fernandez-Pello, C.P. Mao, A unified analysis of concurrent modes of flame spread, Combust. Sci. Technol. 26 (1981) 147–155.

[41] A.C. Fernandez-Pello, Flame spread in a forward forced flow, Combust. Flame. 36 (1979) 63–78. doi:10.1016/0010-2180(79)90046-4.

[42] Y.T. Tseng, J.S. T’ien, A comparison of flame spread characteristics over solids in concurrent flow using two different pyrolysis models, J. Combust. 2011 (2011). doi:10.1155/2011/250391.

[43] S. Bhattacharjee, J. West, R.A. Altenkirch, Determination of the spread rate in opposed-flow flame spread over thick solid fuels in the thermal regime, Symp. Combust. 26 (1996) 1477–1485.

[44] A. Fernandez-Pello, F.A. Williams, A Theory of Laminar Flame Spread Over Flat Surfaces of Solid Combustibles, Combust. Flame. 28 (1977) 251–277.

[45] A.C. Fernandez-Pello, S.R. Ray, I. Glassman, Flame spread in an opposed forced flow: the effect of ambient oxygen concentration, Eighteenth Symp. Combust. 18 (1981) 579–589. doi:10.1016/S0082-0784(81)80063-X.

[46] M. Vedha-Nayagam, R.A. Altenkirch, Backward boundary layers in downward flame spread, in: Twent. Symp. Combust. Combust. Inst., 1984: pp. 1583–1590.

[47] N.N. Smirnov, V. V. Tyurenkova, M.N. Smirnova, Laminar diffusion flame propagation over thermally destructing material, Acta Astronaut. 109 (2015) 217–224. doi:10.1016/j.actaastro.2014.09.016.

[48] H. Emmons, The Film Combustion of Liquid Fuel, Zeitschrift Für Angew. Math. Und Mech. 36 (1956) 60–71.

[49] A.C. Fernandez-Pello, Flame Spread Modeling, Combust. Sci. Technol. 39 (1984) 119–134. http://dx.doi.org/10.1080/00102208408923786.

[50] C. Di Blasi, Modeling and simulation of combustion processes f charring and non-charring solid fuels, Prog. Energy Combust. Sci. 19 (1993) 71–104. doi:0360-1285/93.

[51] C.A. Fernandez-Pello, The Solid Phase, in: G. Cox (Ed.), Combust. Fundam. Fire, 1st ed., Academic Press, 1995: pp. 29–100.

[52] J.N. De Ris, Spread of a laminar diffusion flame, Symp. Combust. 12 (1969) 241–252. doi:10.1016/S0082-0784(69)80407-8.

[53] A.E. Frey, J.S. T'ien, A Theory of Flame Spread over a Solid Fuel Including Finite-Rate Chemical Kinetics, Combust. Flame. 9 (1979) 263–289.

[54] S. Bhattacharjee, J. West, S. Dockter, A simplified theory for de Ris flame over thick and thin fuel beds, Combust. Flame. 104 (1996) 66–80. doi:10.1016/0010-2180(95)00109-3.

[55] I.S. Wichman, F.A. Williams, I. Glassman, Theoretical aspects of flame spread in an opposed flow over flat surfaces of solid fuels, Symp. Combust. 19 (1982) 835–845. doi:10.1016/S0082-0784(82)80259-2.

[56] I.S. Wichman, Flame spread in an opposed flow with a linear velocity gradient, Combust. Flame. 50 (1983) 287–304.

[57] J. West, L. Tang, R.A. Altenkirch, S. Bhattacharjee, K. Sacksteder, M.A. Delichatsios, Quiescent flame spread over thick fuels in microgravity, in: Symp. Combust., The Combustion Institute, Pittsburgh, PA, 1996: pp. 1335–1343. doi:10.1016/S0082-0784(96)80352-3.

[58] J. West, P. Thomas, R. Chao, S. Bhattacharjee, L. Tang, R.A. Altenkirch, S.L. Olson, Low velocity opposed-flow flame spread in a transport-controlled environment DARTFire, in: Third Int. Microgravity Combust. Work., National Aeronautics and Space Administration NASA, Cleveland, Ohio, 1995: pp. 189–194.

[59] H.-Y. Shih, J. T'ien, A three-dimensional model of steady flame spread over a thin solid in low-speed concurrent flows, Combust. Theory Model. 7 (2003) 677–704. doi:10.1088/1364-7830/7/4/005.

[60] H.-Y. Shih, J.S. T'ien, Modeling concurrent flame spread over a thin solid in a low-speed flow tunnel, Proc. Combust. Inst. 28 (2000) 2777–2784.

[61] H.-Y. Shih, J.S. T'ien, Modeling wall influence on solid-fuel flame spread in a flow tunnel, in: 35th Aerosp. Sci. Meet. Exhib., American Institute of Aeronautics and Astronautics, Reno, NV, 1997: p. 0236. doi:10.2514/6.1997-236.

[62] X. Zhao, S.T. James, A three-dimensional transient model for flame growth and extinction in concurrent flows, Combust. Flame. 162 (2015) 1829–1839.

[63] Y.-T. Tseng, J.S. T’ien, Limiting Length, Steady Spread, and Nongrowing Flames in Concurrent Flow Over Solids, J. Heat Transfer. 132 (2010) 091201. doi:10.1115/1.4001645.

[64] A. Kumar, H.Y. Shih, J.S. T’ien, A comparison of extinction limits and spreading rates in opposed and concurrent spreading flames over thin solids, Combust. Flame. 132 (2003) 667–677. doi:10.1016/S0010-2180(02)00516-3.

[65] C. Lautenberger, S. McAllister, D. Rich, C. Fernandez-Pello, Effect of environmental variables on flame spread rates in microgravity, 45th AIAA Aerosp. Sci. Meet. Exhib. 7 (2007) 4662–4672. doi:10.2514/6.2007-383.

[66] P. Ferkul, J. Kleinhenz, H.Y. Shih, R. Pettegrew, K. Sacksteder, J. T’ien, Solid fuel combustion experiments in microgravity using a continuous fuel dispenser and related numerical simulations, Microgravity Sci. Technol. 15 (2004) 3–12. doi:10.1007/BF02870953.

[67] S. Bhattacharjee, R.A. Altenkirch, Radiation-controlled, opposed-flow flame spread in a microgravity environment, Twenty-Third Symp. Combust. Combust. Inst. 23 (1990) 1627–1633. doi:10.1016/S0082-0784(06)80435-2.

[68] S. Bhattacharjee, R. Nagarkar, Y. Nakamura, A correlation for an effective flow velocity for capturing the boundary layer effect in opposed-flow flame spread over thin fuels, Combust. Sci. Technol. 186 (2014) 975–987. doi:10.1080/00102202.2014.900056.

[69] L. Carmignani, G. Celniker, S. Bhattacharjee, The Effect of Boundary Layer on Blow-Off Extinction in Opposed-Flow Flame Spread over Thin Cellulose: Experiments and a Simplified Analysis, Fire Technol. (2016) 1–16. doi:10.1007/s10694-016-0613-3.

[70] L. Carmignani, S. Bhattacharjee, S.L. Olson, P. V. Ferkul, Boundary Layer Effect on Opposed-Flow Flame Spread and flame length over thin PMMA in microgravity, Combust. Sci. Technol. (2017). doi:10.1080/00102202.2017.1404587.

[71] J. Ching-Biau, A model of flame spread over a thin solid in concurrent flow with flame radiation, Case Western Reserve University, 1995. https://etd.ohiolink.edu/pg_10?0::NO:10:P10_ACCESSION_NUM:case1062696685#abstract-files.

[72] C.B. Jiang, J.S. T’ien, H.Y. Shih, Model calculation of steady upward flame spread over a thin solid in reduced gravity, Symp. Combust. 26 (1996) 1353–1360. doi:10.1016/S0082-0784(96)80354-7.

[73] P. V. Ferkul, J.S. T’ien, A Model of Low-Speed Concurrent Flow Flame Spread Over a Thin Fuel, Combust. Sci. Technol. 99 (1994) 345–370. doi:10.1080/00102209408935440.

[74] R.A. Altenkirch, S. Bhattacharjee, Opposed-flow flame spread with implications for combustion at microgravity, Low-Gravity Fluid Dyn. Transp. Phenom. 130 (1990) 723–741. doi:https://doi.org/10.2514/4.866036.

[75] J.N. De Ris, Spread of laminar diffusion flame, Symp. Combust. 12 (1969) 241–252.

[76] S. Bhattacharjee, W. Tran, M. Laue, C. Paolini, Y. Nakamura, Experimental validation of a correlation capturing the boundary layer effect on spread rate in the kinetic regime of opposed-flow flame spread, Proc. Combust. Inst. 35 (2015) 2631–

2638.

[77] C. Eigenbrod, J. Hauschildt, F. Meyer, D.L. Urban, G.A. Ruff, S.L. Olson, P. V. Ferkul, G. Jomaas, B. Toth, Experimental Results on the Effect of Surface Structures on the Flame Propagation Velocity of PMMA in Microgravity, in: 47th Int. Conf. Environ. Syst., Charleston, SC, 2017: p. 67.

[78] P. Ferkul, D.L. Urban, S. Olson, G.A. Ruff, J. Easton, S.T. James, Y.T. Liao, A.C. Fernandez-Pello, J.L. Torero, G. Legros, C. Eigenbrod, N. Smirnov, O. Fujita, S. Rouvreau, B. Toth, G. Jomaas, The Saffire Experiment: Large-Scale Combustion aboard Spacecraft, in: 10th U.S. Natl. Combust. Meet., Eastern States Section of the Combustion Institute, College Park, Maryland, 2017.

[79] D.L. Urban, P. Ferkul, S. Olson, G.A. Ruff, S.T. James, Y.T. Liao, A.C. Fernandez-Pello, J.L. Torero, G. Legros, C. Eigenbrod, N. Smirnov, O. Fujita, S. Rouvreau, B. Toth, G. Jomaas, Flame Spread: Effects of Microgravity and Scale, Combust. Flame. 199 (2018) 1–22. doi:10.1016/j.combustflame.2018.10.012.

[80] S. Bhattacharjee, A. Simsek, F. Miller, S. Olson, P. Ferkul, Radiative, thermal, and kinetic regimes of opposed-flow flame spread: A comparison between experiment and theory, Proc. Combust. Inst. 36 (2016) 2963–2969. doi:10.1016/j.proci.2016.06.025.

[81] T.J. Shah, F.J. Miller, Modeling and Analysis of Intermediate Thickness PMMA Sheets Burning in Microgravity Opposed Flow, in: West. States Sect. Combust. Inst. - Fall 2015 Meet., Provo, Utah, US, 2015.

[82] S.L. Olson, P. V. Ferkul, Microgravity flammability boundary for PMMA rods in axial stagnation flow: Experimental results and energy balance analyses, Combust. Flame. 180 (2017) 217–229. doi:10.1016/j.combustflame.2017.03.001.

[83] A. V Ivanov, V.F. Alymov, A.B. Smirnov, S.P. Shalayev, D.Y. Belov, Y.D. Balashov, T. V Andreeva, A. V Semenov, A.S. Melikhov, I.A. Bolodyan, V.I. Potyakin, Preliminary results of the third test series of nonmetal material flammability evaluation in SKOROST apparatus on the space station MIR, in: Fifth Int. Microgravity Combust. Work., National Aeronautics and Space Administration NASA, Cleveland, Ohio, 1999: pp. 47–50.

[84] A. V Ivanov, Y. V Balashov, A.S. Melikhov, Experimental Verification of Material Flammability in Space, Hannover, MD, 1999.

[85] S.L. Olson, D. Hirsch, Geometry Considerations in Evaluating 0g materials flammability limits for comparison with NASA upward flame propagation (test 1) limits, 41st Int. Conf. Environ. Syst. 2011, ICES 2011. (2011). doi:10.2514/6.2011-5068.

[86] C. Sanchez-Tarifa, M. Rodriguez, Combustion and flammability characteristics of solid at microgravity in very small velocity flows, in: Nat (Ed.), Fifth Int. Microgravity Combust. Work., National Aeronautics and Space Administration NASA, 1999: pp. 39–42.

[87] R.A. Altenkirch, S. Bhattacharjee, J. West, L. Tang, K. Sacksteder, M.A. Delichatsios, Solid Surface Combustion Experiment: Thick Fuel Results, in: Fourth Int. Microgravity Combust. Work., National Aeronautics and Space Administration NASA, Cleveland, Ohio, 1997: pp. 381–386.

[88] F. Meyer, T. Schwenteck, M. Ruhe, P. Bihn, A. Freier, C. Eigenbrod, UB-FIRE

Experiment Results on Upward Flame Propagation along Cylindrical PMMA Samples in Reduced Gravity, in: 47th Int. Conf. Environ. Syst. ICES, Charleston, South Caroline-US, 2017.

[89] S. Bhattacharjee, R.A. Altenkirch, A comparison of theoretical and experimental results in flame spread over thin condensed fuels in a quiescent, microgravity environment, in: Twenty-Fourth Symp. Combust., The Combustion Institute, Pittsburgh, PA, 1992: pp. 1669–1676.

[90] P.A. Ramachandra, R.A. Altenkirch, S. Bhattacharjee, L. Tang, K. Sacksteder, M. Katherine Wolverton, The behavior of flames spreading over thin solids in microgravity, in: Twenty-Fifth Symp. Combust., The Combustion Institute, Irvine, CA, 1995: pp. 71–84. doi:10.1016/0010-2180(94)00046-U.

[91] S. Bhattacharjee, R.A. Altenkirch, K. Sacksteder, The Effect of Ambient Pressure on Flame Spread Over Thin Cellulosic Fuel in a Quiescent, Microgravity Environment, J. Heat Transfer. 118 (1996) 181–190. http://dx.doi.org/10.1115/1.2824032.

[92] R.A. Altenkirch, L. Tang, K. Sacksteder, S. Bhattacharjee, M.A. Delichatsios, Inherently unsteady flame spread to extinction over thick fuels in microgravity, Twenty-Seventh Symp. Combust. 27 (1998) 2515–2524. doi:10.1016/S0082-0784(98)80103-3.

[93] S. Bhattacharjee, R.A. Altenkirch, The effect of surface radiation on flame spread in a quiescent, microgravity environment, Combust. Flame. 84 (1991) 160–169. doi:10.1016/0010-2180(91)90045-D.

[94] S.L. Olson, P. V. Ferkul, Microgravity Flammability of PMMA Rods in Concurrent Flow, in: 9th U. S. Natl. Combust. Meet., Cincinnati, Ohio, 2015.

[95] G. Grayson, K.R. Sacksteder, P.V. Ferkul, J.S. T'ien, Flame spreading over a thin solid in low-speed concurrent flow- Drop tower experimental results and comparison with theory, Microgravity Sci. Technol. VII (1994) 187–195.

[96] S.L. Olson, F.J. Miller, S. Jahangirian, I.S. Wichman, Flame spread over thin fuels in actual and simulated microgravity conditions, Combust. Flame. (2009) 1214–1226. doi:10.1016/j.combustflame.2009.01.015.

[97] S.L. Olson, The effect of microgravity on flame spread over a thin fuel, Cleveland, Ohio, 1987.

[98] K.R. Sacksteder, J.S. Tien, Buoyant downward diffusion flame spread and extinction in partial-gravity accelerations, in: Twenty-Fifth Symp. Combust., The Combustion Institute, Pittsburgh, PA, 1994: pp. 1685–1692. doi:10.1016/S0082-0784(06)80816-7.

[99] G.D. Grayson, An experimental study of low-speed concurrent-flow flame spread over a thin fuel, Case Western Reserve University, 1991.

[100] J.S. T'ien, Diffusion flame extinction at small stretch rates: The mechanism of radiative loss, Combust. Flame. 65 (1986) 31–34. doi:10.1016/0010-2180(86)90069-6.

[101] I.I. Feier, H.-Y. Shih, K.R. Sacksteder, J.S. Tien, Upward flame spread over thin solids in partial gravity, Proc. Combust. Inst. 29 (2002) 2569–2577. doi:http://dx.doi.org/10.1016/S1540-7489(02)80313-3.

[102] S.Y. Hsu, J.S. T'ien, Flame spread over solids in buoyant and forced concurrent flows: Model computations and comparison with experiments, Proc. Combust. Inst.

33 (2011) 2433–2440. doi:10.1016/j.proci.2010.05.093.

[103] S.L. Olson, F.J. Miller, Experimental comparison of opposed and concurrent flame spread in a forced convective microgravity environment, Proc. Combust. Inst. 32 II (2009) 2445–2452. doi:10.1016/j.proci.2008.05.081.

[104] S.L. Olson, G.A. Ruff, Microgravity Flame Spread over Non-Charring Materials in Exploration Atmospheres : Pressure , Oxygen , and Velocity Effects on Concurrent Flame spread., Soc. Automot. Eng. SAE. (2009). doi:10.4271/2009-01-2489.

[105] S. McAllister, C. Fernandez-Pello, D. Urban, G. Ruff, Piloted ignition delay of PMMA in space exploration atmospheres, Proc. Combust. Inst. 32 II (2009) 2453–2459. doi:10.1016/j.proci.2008.05.076.

[106] S. Fereres, C. Lautenberger, C. Fernandez-Pello, D. Urban, G. Ruff, Mass flux at ignition in reduced pressure environments, Combust. Flame. 158 (2011) 1301–1306. doi:10.1016/j.combustflame.2010.11.013.

[107] S. McAllister, C. Fernandez-Pello, D. Urban, G. Ruff, The combined effect of pressure and oxygen concentration on piloted ignition of a solid combustible, Combust. Flame. 157 (2010) 1753–1759. doi:10.1016/j.combustflame.2010.02.022.

[108] A.F. Osorio, D. Hsiao, D. Tran, C. Fernandez-Pello, Low-pressure flames spread limits of fire resistant fabrics, in: 43rd Int. Conf. Environ. Syst., Vail, CO, US, 2013: pp. 997–1004.

[109] S.L. Olson, G.A. Ruff, F.J. Miller, Microgravity Flame Spread in Exploration Atmospheres: Pressure, Oxygen and Velocity Effects on Opposed and Concurrent Flame Spread, in: 39th Int. Conf. Environ. Syst., San Francisco, California, 2008. doi:10.4271/2008-01-2055.

[110] S. Mcallister, C. Fernandez-Pello, G. Ruff, D. Urban, Ignition Delay of Combustible Materials in Normoxic Equivalent Environments, SAE. 4970 (2009). doi:10.4271/2009-01-2491.

[111] S.L. Olson, Piloted ignition delay times of opposed and concurrent flame spread over a thermally-thin fuel in a forced convective microgravity environment, Proceeding Combust. Inst. 33 (2011) 2633–2639. doi:10.1016/j.proci.2010.06.020.

[112] M. Coutin, A.S. Rangwala, J.L. Torero, S.G. Buckley, Material properties governing co-current flame spread: the effect of air entrainment, in: Seventh Int. Work. Microgravity Combust. Chem. React. Syst., National Aeronautics and Space Administration NASA, Cleveland, Ohio, 2003: pp. 205–208.

[113] L.K. Honda, P.D. Ronney, Mechanisms of concurrent-flow flame spread over solid fuel beds, Proc. Combust. Inst. 28 (2000) 2793–2801. doi:10.1016/S0082-0784(00)80701-8.

[114] X. Zhao, Y.T. Liao, M.C. Johnston, J.S. T'ien, P. V Ferkul, S.L. Olson, Concurrent flame growth , spread , and quenching over composite fabric samples in low speed purely forced flow in microgravity, Proc. Combust. Inst. 36 (2016) 2971–2978. http://dx.doi.org/10.1016/j.proci.2016.06.028.

[115] X. Zhao, J.S. T'ien, P. V. Ferkul, S.L. Olson, Concurrent flame growth , spread and extinction over composite fabric samples in low speed purely forced flow in microgravity, in: 9th U. S. Natl. Combust. Meet., 2015.

[116] T. Kashiwagi, W.E. Mell, Y. Nakamura, S.L. Olson, H.R. Baum, K.B. McGrattan,

Multidimensional Effects on Ignition , Transition , and Flame Spread in Microgravity, in: Sixth Int. Microgravity Combust. Work., 2001: pp. 81–84.

[117] I.I. Feier, A numerical study of three-dimensional flame propagation over thin solids in purely forced concurrent flow including gas-phase radiation, Case Western Reserve University, 2007. http://adsabs.harvard.edu/abs/2007PhDT........22F (accessed December 5, 2017).

[118] S. Bhattacharjee, S. Takahashi, K. Wakai, C.P. Paolini, Correlating flame geometry in opposed-flow flame spread over thin fuels, Proc. Combust. Inst. 33 (2011) 2465–2472. doi:10.1016/j.proci.2010.06.053.

[119] S. Takahashi, Y. Seki, T. Ihara, K. Wakai, S. Bhattacharjee, Effect of Sample Width on Flame Spread Rate over a Thin Material in Microgravity, Trans. Japan Soc. Aeronaut. Sp. Sci. Sp. Technol. Japan. 7 (2009) 61–66. doi:10.2322/tstj.7.Ph_61.

[120] S.L. Olson, U. Hegde, S. Bhattacharjee, J.L. Deering, L. Tang, R.A. Altenkirch, Sounding rocket microgravity experiments elucidating diffusive and radiative transport effects on flame spread over thermally thick solids, Combust. Sci. Technol. 176 (2004) 557–584. doi:10.1080/00102200490276773.

[121] S. Wang, J. Hu, Y. Xiao, T. Ren, F. Zhu, Opposed-flow Flame Spread Over Solid Fuels in Microgravity: the Effect of Confined Spaces, Microgravity Sci. Technol. 27 (2015) 329–336. doi:10.1007/s12217-015-9419-z.

[122] K.R. Sacksteder, I.I. Feier, P. V Ferkul, A. Kumar, J.S. T'ien, Upward And Downward Flame Spreading And Extinction In Partial Gravity Environments, in: Seventh Int. Work. Microgravity Combust. Chem. React. Syst., National Aeronautics and Space Administration NASA, Cleveland, Ohio, 2003: pp. 141–144. http://hdl.handle.net/2060/20040053567.

[123] R.A. Altenkirch, R. Eichhorn, P.C. Shang, Buoyancy Effects on Flames Spreading Down Thermally Thin Fuels, Combust. Flame. 37 (1980) 71–83.

[124] K.K. Wu, C.H. Chen, Radiation effects for downward flame spread over a thermally thin fuel in a partial-gravity environment, Combust. Sci. Technol. 176 (2004) 1909–1933. doi:10.1080/00102200490504553.

[125] C. Chen, M. Cheng, Gas-phase radiative effects on downwards flame spread in low gravity, Combust. Sci. Technol. 97 (1994) 63–83. doi:10.1080/00102209408935368.

[126] J. West, S. Bhattacharjee, R.A. Altenkirch, A Comparison of the Roles Played by Natural and Forced Convection in Opposed-Flow Flame Spreading, Combust. Sci. Technol. 83 (1992) 233–244. doi:10.1080/00102209208951834.

[127] J. Kleinhenz, I.I. Feier, S.Y. Hsu, J.S. T'ien, P. V. Ferkul, K.R. Sacksteder, Pressure modeling of upward flame spread and burning rates over solids in partial gravity, Combust. Flame. 154 (2008) 637–643. doi:10.1016/j.combustflame.2008.05.023.

[128] J.E. Kleinhenz, Flammability and flame spread of Nomex and cellulose in space habitat environments, Case Western Reserve University, 2006.

[129] J.L. Torero, Heat and mass transfer in fires: Scaling laws and their application, in: 12th Int. Meet. Heat Transf., Tangiers, Morocco, 2005.

[130] J.L. Torero, Material Properties that Control Ignition and Spread of a Fire in Micro-Gravity Environments, in: Proc. NHTC'00 34th Natl. Heat Transf. Conf., Pittsburgh, PA, 2000: pp. 1–13. doi:ASME-NHTC-2000-12314, 2000.

[131] J.S. T’ien, K.R. Sacksteder, P. V. Ferkul, G.D. Grayson, Combustion of solid fuel in very low speed oxygen streams, in: Second Int. Microgravity Combust. Work., National Aeronautics and Space Administration NASA, Cleveland, Ohio, 1992: pp. 245–250.

[132] K. Nakabe, K.B. McGrattan, T. Kashiwagi, H.R. Baum, H. Yamashita, G. Kushida, Ignition and transition to flame spread over a thermally thin cellulosic sheet in a microgravity environment, Combust. Flame. 98 (1994) 361–374. doi:10.1016/0010-2180(94)90175-9.

[133] S.L. Olson, H.R. Baum, T. Kashiwagi, Finger-like smoldering over thin cellulosic sheets in microgravity, Symp. Combust. 27 (1998) 2525–2533. doi:10.1016/S0082-0784(98)80104-5.

[134] W.E. Mell, T. Kashiwagi, Effects of finite sample width on transition and flame spread in microgravity, Proc. Combust. Inst. 28 (2000) 2785–2792. doi:10.1016/S0082-0784(00)80700-6.

[135] L. Carmignani, F. Lotti, S. Bhattacharjee, Comparison of flame spread and blow-off extinction over vertical and horizontal PMMA samples, Mech. Eng. J. (2016). doi:10.1299/mej.16-00277.

[136] S. Bhattacharjee, L. Carmignani, A. Simsek, Boundary Layer Effect on Opposed-Flow Flame Spread in the Microgravity Regime, in: 46th Int. Conf. Environ. Syst., Vienna, Austria, 2016.

[137] S. Takahashi, M. Kondou, K. Wakai, S. Bhattacharjee, Effect of radiation loss on flame spread over a thin PMMA sheet in microgravity, Proc. Combust. Inst. 29 (2002) 2579–2586. doi:10.1016/S1540-7489(02)80314-5.

[138] O. Zik, E. Moses, Fingering instability in solid fuel combustion: The characteristic scales of the developed state, Symp. Combust. 27 (1998) 2815–2820. doi:10.1016/S0082-0784(98)80139-2.

[139] S.L. Olson, Most Probable Fire Scenarios in Spacecraft and Extraterrestrial Habitats : Why NASA ’ s Current Test 1 Might Not Always be Conservative, NASA Glenn Research Center, 2014.

[140] S.L. Olson, F.J. Miller, I.S. Wichman, F.J. Miller, I.S.W. Characterizing, S.L. Olson, F.J. Miller, I.S. Wichman, Characterizing fingering flamelets using the logistic model, Combust. Theory Model. 10 (2007) 323–347. doi:10.1080/13647830600565446.

[141] T. Kashiwagi, S.L. Olson, Radiative ignition and transition to spread investigation (RITSI), in: Third United States Microgravity Payload One Year Rep., 1998: pp. 97–117.

[142] T. Kashiwagi, W.E. Mell, K.B. McGrattan, H.R. Baum, S.. Olson, O. Fujita, M. Kikuchi, K. Ito, Ignition, Transition, Flame Spread in Multidimensional Configurations in Microgravity, in: Fourth Int. Work. Microgravity Combust., National Aeronautics and Space Administration NASA, Cleveland, Ohio, 1997: pp. 411–416.

[143] T. Kashiwagi, W.E. Mell, K.B. McGrattan, H.R. Baum, S.. Olson, O. Fujita, M. Kikuchi, K. Ito, Ignition, Transition, Flame Spread in Multidimensional Configurations in Microgravity, in: Fifth Int. Microgravity Combust. Work., National Aeronautics and Space Administration NASA, Cleveland, Ohio, 1999: pp. 411–416.

[144] P.D. Ronney, Understanding combustion processes through microgravity research, Symp. Combust. 27 (1998) 2485–2506. doi:10.1016/S0082-0784(98)80101-X.

[145] F. Zhu, S. Wang, Z. Lu, A Comparative Study of Near-Limit Flame Spread Over a Thick Solid in Space- and Ground-Based Experiments, Microgravity Sci. Technol. 30 (2018) 943–949.

[146] S.L. Olson, D.L. Urban, G.A. Ruff, P. V. Ferkul, B. Toth, C. Eigenbrod, F. Meyer, Analysis of Saffire II two-sided concurrent flame spread over a thick PMMA slab, in: 48th Int. Conf. Environ. Syst., Alburquerque, NM, USA, 2018.

[147] X. Zhu, Y. Jiang, Z. Wang, C. Xiong, Y. Xia, W. Xu, The numerical and experimental analysis of upward flame spread over the flat surface and the wavy surface, J. Hazard. Mater. 368 (2019) 644–652. doi:10.1016/j.jhazmat.2019.01.056.

[148] H.D. Ross, S.A. Gokoglu, R. Friedman, Microgravity Combustion Science: A Program Overview, Cleveland, Ohio, 1989.

[149] S. Kumagai, H. Isoda, Combustion of fuel droplets in a falling chamber, Symp. Combust. 6 (1957) 726–731. doi:10.1016/S0082-0784(57)80100-3.

[150] H.D. Ross, S.A. Gokoglu, R. Friedman, Microgravity Combustion Science: 1995 Program Update, 1995. http://gltrs.grc.nasa.gov/reports/1995/TM-106858.pdf.

[151] T. Mori, K. Goto, R. Ohashi, A.B. Sawaoka, Capabilities and recent activities of Japan Microgravity Center (JAMIC), Microgravity Sci. Technol. 5 (1993) 238–242.

[152] Z. FABmbH, ZARM Drop Tower Bremen User Manual, (2011).

[153] Z. Xiaoqian, Y. Longgen, W.U. Wendong, T. Lanqiao, Some key technics of drop tower experiment device of National Microgravity Laboratory (China) (NMLC), Sci. China Ser. E Eng. Mater. Sci. 48 (2005) 305–316. doi:10.1360/102004-21.

[154] L.H. Hu, M.A. Delichatsios, J. Li, X.L. Zhang, S.F. Wang, R. Huo, Experimental study on diffusive solid combustion behavior during transition from normal- to reduced-gravity, Int. J. Heat Mass Transf. 55 (2012) 2035–2043. doi:10.1016/j.ijheatmasstransfer.2011.12.003.

[155] C.S. Tarifa, J. Salvá Monfort, Flame spreading over solid fuels at microgravity conditions results obtained in the minitexus rocket and future programmes, in: T.D. Guyenne (Ed.), Proc. Sp. Stn. Util. Symp., European Space Agency, Darmstadt, 1996: pp. 281–288.

[156] T. Vietoris, J.L. Ellzey, P. Joulain, S.N. Mehta, J.L. Torero, Laminar diffusion flame in microgravity: The results of the Minitexus 6 Sounding rocket experiment, Proc. Combust. Inst. 28 (2000) 2883–2889.

[157] C. Sanchez-Tarifa, B. Lazaro, Experiments conducted on combustion at microgravity in the Texus-38 sounding rocket. Results and conclusions, in: B. Schurmann (Ed.), First Int. Symp. Microgravity Res. Appl. Phys. Sci. Biotechnol., European Space Agency, Sorrento, Italy, 2000.

[158] R.A. Altenkirch, S.L. Olson, J.L. Deering, L. Tang, S. Bhattacharjee, U. Hedge, Diffusive and radiative transport in fires (DARTFire): Opposed-flow flame spread in low-velocity flows, in: Fifth Int. Microgravity Combust. Work., National Aeronautics and Space Administration NASA, Cleveland, Ohio, 1999: pp. 317–320.

[159] S.L. Olson, Sounding rocket microgravity experiments elucidating diffusive and

radiative transport effects on flame spread over thermally thick solids, Combust. Flame. (2004). doi:10.1080/00102200490276773.

[160] S.L. Olson, R.A. Altenkirch, S. Bhattacharjee, L. Tang, U. Hedge, Diffusive and Radiative Transport in Fires Experiment: DARTFire, in: Fourth Int. Microgravity Combust. Work., National Aeronautics and Space Administration NASA, Cleveland, Ohio, 1997: pp. 393–398.

[161] S.L. Olson, U. Hedge, R.A. Altenkirch, S. Bhatacharjee, DARTFire Sees Microgravity Fires in a New Light-Large Data Base of Images Obtained, 1999.

[162] W. Hu, Q. Kang, eds., Physical Science Under Microgravity: Experiments on Board the SJ-10 Recoverable Satellite, Springer, 2019. doi:10.1007/978-981-13-1340-0_8.

[163] W. Kong, B. Wang, W. Zhang, Y. Ai, S. Lao, Study on prefire phenomena of wire insulation at microgravity, Microgravity Sci. Technol. 20 (2008) 107–113. doi:10.1007/s12217-008-9041-4.

[164] W.R. Hu, J.F. Zhao, M. Long, X.W. Zhang, Q.S. Liu, M.Y. Hou, Q. Kang, Y.R. Wang, S.H. Xu, W.J. Kong, H. Zhang, S.F. Wang, Y.Q. Sun, H.Y. Hang, Y.P. Huang, W.M. Cai, Y. Zhao, J.W. Dai, H.Q. Zheng, E.K. Duan, J.F. Wang, Space Program SJ-10 of Microgravity Research, Microgravity Sci. Technol. 26 (2014) 159–169. doi:10.1007/s12217-014-9390-0.

[165] S. Bhattacharjee, R.A. Altenkirch, K. Sacksteder, Implications of Spread Rate and Temperature Measurements in Flame Spread Over a Thin Fuel in a Quiescent, Microgravity, Space-Based Environment, Combust. Sci. Technol. 91 (1993) 225–242. doi:10.1080/00102209308907646.

[166] W.E. Mell, S.L. Olson, T. Kashiwagi, Flame spread along free edges of thermally thin samples in microgravity, Proc. Combust. Inst. 28 (2000) 2843–2849. doi:10.1016/S0082-0784(00)80707-9.

[167] S.L. Olson, T. Kashiwagi, O. Fujita, M. Kikuchi, K. Ito, Experimental observations of spot radiative ignition and subsequent three-dimensional flame spread over thin cellulose fuels, Combust. Flame. 125 (2001) 852–864. doi:10.1016/S0010-2180(00)00249-2.

[168] R. Friedman, Fire Safety in Spacecraft, Fire Mater. 20 (1996) 235–243. doi:10.1002/(SICI)1099-1018(199609)20:5<235::AID-FAM580>3.0.CO;2-Y.

[169] J.S. T'ien, K.R. Sacksteder, P. V Ferkul, P.S. Greenberg, C. Jiang, R.D. Pettegrew, Flame spread over solid fuel in low-speed concurrent flow, in: Third Int. Microgravity Combust. Work., National Aeronautics and Space Administration NASA, Cleveland, Ohio, 1994.

[170] Y. Li, Y.T.T. Liao, P. V. Ferkul, M.C. Johnston, C. Bunnell, Experimental study of concurrent-flow flame spread over thin solids in confined space in microgravity, Combust. Flame. 227 (2021) 39–51. doi:10.1016/j.combustflame.2020.12.042.

[171] S. Link, X. Huang, C. Fernandez-Pello, S. Olson, P. Ferkul, The Effect of Gravity on Flame Spread over PMMA Cylinders in Opposed Flow with Variable Oxygen, Sci. Rep. 8 (2018). doi:10.1038/s41598-017-18398-4.

[172] K. Saito, A. Ito, Y. Nakamura, K. Kuwana, Effect of gravity on flame spread along a thin combustible solid for different sample orientations in opposed flow, Prog. Scale Model. Vol. II Sel. from Int. Symp. Scale Model. ISSM VI ISSM VII. II (2015) 1–

316. doi:10.1007/978-3-319-10308-2.

[173] S.L. Olson, P. V Ferkul, Evaluating Material Flammability in Microgravity and Martian Gravity Compared to the NASA Standard Normal Gravity Test, in: 42nd Int. Conf. Environ. Syst., American Institute of Aeronautics and Astronautics, San Diego, California, 2012: pp. 1–9. doi:DOI: 10.2514/6.2012-3492.

[174] P. V. Ferkul, S.L. Olson, Zero-Gravity Centrifuge Used for the Evaluation of Material Flammability in Lunar Gravity, J. Thermophys. Heat Transf. 25 (2011) 457–461. doi:10.2514/1.T3651.

[175] A. Guibaud, J.M. Citerne, J.L. Consalvi, O. Fujita, J. Torero, G. Legros, Experimental Evaluation of Flame Radiative Feedback: Methodology and Application to Opposed Flame Spread Over Coated Wires in Microgravity, Fire Technol. 56 (2020) 185–207. doi:10.1007/s10694-019-00853-5.

[176] A. Guibaud, J.M. Citerne, J.L. Consalvi, J.L. Torero, O. Fujita, M. Kikuchi, P. Ferkul, N. Smirnov, G. Jomaas, B. Toth, S. Rouvreau, G. Legros, Accessing the soot-related radiative heat feedback in a flame spreading in microgravity: Optical designs and associated limitations, Proc. Combust. Inst. 000 (2020) 1–10. doi:10.1016/j.proci.2020.06.036.

[177] A. Guibaud, J.L. Consalvi, J.M. Orlac'h, J.M. Citerne, G. Legros, Soot Production and Radiative Heat Transfer in Opposed Flame Spread over a Polyethylene Insulated Wire in Microgravity, Fire Technol. 56 (2020) 287–314. doi:10.1007/s10694-019-00850-8.

[178] A. Guibaud, J.L. Consalvi, J.M. Citerne, G. Legros, Pressure effects on the soot production and radiative heat transfer of non-buoyant laminar diffusion flames spreading in opposed flow over insulated wires, Combust. Flame. 222 (2020) 383–391. doi:10.1016/j.combustflame.2020.09.003.

[179] A. Guibaud, J.M. Citerne, J.L. Consalvi, G. Legros, Pressure effects on the soot production and radiative heat transfer of non-buoyant laminar diffusion flames spreading in opposed flow over insulated wires, Combust. Flame. 221 (2020) 530–543. doi:10.1016/j.combustflame.2020.07.044.

[180] A. Vetturini, W. Cui, Y.T. Liao, S. Olson, P. Ferkul, Flame Spread Over Ultra-thin Solids: Effect of Area Density and Concurrent-Opposed Spread Reversal Phenomenon, Fire Technol. 56 (2020) 91–111. doi:10.1007/s10694-019-00878-w.

[181] Y. Son, G. Zouein, S. Gokoglu, P. Ronney, Comparison of Carbon Dioxide and Helium as Fire Extinguishing Agents for Spacecraft, J. ASTM Int. 3 (2006). doi:10.1520/JAI13564.

[182] Y. Son, P.D. Ronney, Radiation-driven flame spread over thermally thick fuels in quiescent microgravity environments, Proc. Combust. Inst. 29 (2002) 2587–2594. doi:10.1016/S1540-7489(02)80315-7.

[183] J.C. Yang, A. Hamins, M.K. Donnelly, Reduced gravity combustion of thermoplastic spheres, Combust. Flame. 120 (2000) 61–74. doi:10.1016/S0010-2180(99)00084-X.

[184] P. Sun, C. Wu, F. Zhu, S. Wang, X. Huang, Microgravity combustion of polyethylene droplet in drop tower, Combust. Flame. 222 (2020) 18–26. doi:10.1016/j.combustflame.2020.08.032.

[185] A. Fuentes, G. Legros, P. Joulain, J.P. Vantelon, J.L. Torero, Evaluation of the

extinction factor in a laminar flame established over a PMMA plate in microgravity, Microgravity Sci. Technol. (2005). doi:10.1007/BF02872082.

[186] M. Summerfield, N. Messina, Smoldering combustion in porous fuels, in: T.H. Cochran (Ed.), Combust. Exp. a Zero-Gravity Lab., American Institute of Aeronautics and Astronautics, New York, 1981: pp. 129–194.

[187] S.A. Harper, A. Juarez, H. Perez III, D.B. Hirsch, H.D. Beeson, Oxygen Partial Pressure and Oxygen Concentration Flammability: Can They Be Correlated?, in: S.E. Davis, T.A. Steinberg (Eds.), Flammabl. Sensit. Mater. Oxyg. Atmos., ASTM, San Antonio, TX, 2016: pp. 413–427. doi:10.1520/STP159620150081.

[188] A. Ito, T. Kashiwagi, Characterization of Flame Spread over PMMA Using Holographic Interferometry Sample Orientation Effects, Combust. Flame. 204 (1988) 189–204.

[189] O. Fujita, J. Takahashi, K. Ito, Experimental study on radiative ignition of a paper sheet in microgravity, Proc. Combust. Inst. 28 (2000) 2761–2767.

[190] Y. Son, L. Honda, P. Ronney, S. Gokoglu, Radiation-driven flame spread experiments in the combustion integrated rack on ISS, 2001 Conf. Exhib. Int. Sp. Stn. Util. (2001). doi:10.2514/6.2001-5082.

[191] D.L. Urban, J.S. Goldmeer, Z.-G. Yuan, Interactions between flames on parallel solid surfaces, in: Fourth Int. Microgravity Combust. Work., National Aeronautics and Space Administration NASA, Cleveland, Ohio, 1997: pp. 429–434.

[192] S. Takahashi, S. Bhattacharjee, T. Ihara, K. WAKAI, Effect of Ambient Gas on Flame Spread over a Solid Material in Microgravity, JASMA J. Japan Soc. Microgravity Appl. = 日本マイクログラビティ応用学会誌. 24 (2007) 225–230. http://ci.nii.ac.jp/naid/10020006647/.

[193] S. Bhattacharjee, A. Simsek, S. Olson, P. Ferkul, The critical flow velocity for radiative extinction in opposed-flow flame spread in a microgravity environment: A comparison of experimental, computational, and theoretical results, Combust. Flame. 163 (2016) 472–477. doi:10.1016/j.combustflame.2015.10.023.

[194] C. Sanchez Tarifa, G. López Juste, A study of the combustion problems of solid materials at conditions existing in space stations, in: Second Eur. Symp. Util. Int. Sp. Stn., Noordwijk, The Netherlands, 1999.

[195] K. Maruta, K. Tsuboi, S. Takahashi, Limiting Oxygen Concentration of Flame Resistant Material in Microgravity, Microgravity Sci. Appl. 34 (2017) 1–6. doi:10.15011//jasma.34.340304.

[196] C.R. Andracchio, T.H. Cochran, Burning of solids in oxygen-rich environments in normal and reduced gravity, Washington, D.C., 1974.

[197] C.R. Andracchio, J.C. Aydelott, Comparison of flame spreading over thin flat surfaces in normal gravity and weightlessness in an oxygen environment, Washington, D.C., 1970.

[198] C.R. Andracchio, T.H. Cochran, Gravity effects on flame spreading over solid surfaces, Washington, D.C., 1976.

[199] S.L. Olson, R.G. Sotos, Combustion of Velcro in Low Gravity, 1987.

[200] P. V. Ferkul, An Experimental Study of Opposed Flow Diffusion Flame Extinction

Over a Thin Fuel in Microgravity, 1989.

[201] P. Cordeiro, G. Legros, S. Rouvreau, P. Joulain, J.L. Torero, Detailed description of the structure of a low velocity laminar diffusion flame in microgravity, in: Seventh Int. Work. Microgravity Combust. Chem. React. Syst., National Aeronautics and Space Administration NASA, Cleveland, Ohio, 2003: pp. 93–96.

[202] L. Brahmi, T. Vietoris, S. Rouvreau, P. Joulain, L. David, J.L. Torero, Microgravity laminar diffusion flame in a perpendicular fuel and oxidizer stream configuration, AIAA J. 43 (2005) 1725–1733. doi:10.2514/1.13442.

[203] P.B. Sunderland, S. Mortazavi, G.M. Faeth, D.L. Urban, Laminar smoke points of nonbuoyant jet diffusion flames, Combust. Flame. 96 (1994) 97–103. doi:10.1016/0010-2180(94)90161-9.

[204] D.L. Urban, Z.G. Yuan, P.B. Sunderland, K.C. Lin, Z. Dai, G.M. Faeth, Smoke-point properties of non-buoyant round laminar jet diffusion flames, Proc. Combust. Inst. 28 (2000) 1965–1972. doi:10.1016/s0082-0784(00)80602-5.

[205] H. Ito, O. Fujita, K. Ito, Agglomeration of soot particles in diffusion flames under microgravity, Combust. Flame. 99 (1994) 363–370. doi:10.1016/0010-2180(94)90142-2.

[206] D.F. Swinehart, The Beer-Lambert Law, J. Chem. Educ. 7 (1962) 333. https://pubs.acs.org/doi/pdf/10.1021/ed039p333?casa_token=kHi6f_7gbagAAAAA:G7FE4q5XXDhp8h85FVvAnnUd1fBCctJX-LE0HQN8h_dV3xxnMPm_M7F7gdJIQum5e1h2_qmdyp2-r5Q (accessed April 30, 2021).

[207] P.S. Greenberg, J.C. Ku, Soot volume fraction imaging, Appl. Opt. 36 (1997) 5514. doi:10.1364/ao.36.005514.

[208] C.M. Megaridis, D.W. Griffin, B. Konsur, Soot-field structure in laminar soot-emitting microgravity nonpremixed flames, Symp. Combust. 26 (1996) 1291–1299. doi:10.1016/S0082-0784(96)80347-X.

[209] P.S. Greenberg, J.C. Ku, Soot volume fraction maps for normal and reduced gravity laminar acetylene Jet diffusion flames, Combusit. Flame. 108 (1997) 227–230.

[210] B. Konsur, C.M. Megaridis, D.W. Griffin, Fuel preheat effects on soot-field structure in laminar gas jet diffusion flames burning in 0-g and 1-g, Combust. Flame. 116 (1999) 334–347. doi:10.1016/S0010-2180(97)00297-6.

[211] B. Konsur, C.M. Megaridis, D.W. Griffin, Soot aerosol properties in laminar soot-emitting microgravity nonpremixed flames, Combust. Flame. 118 (1999) 509–520. doi:10.1016/S0010-2180(99)00021-8.

[212] J.F. Guan, J. Fang, Y. Xue, J.W. Wang, J. jun Wang, Y.M. Zhang, Morphology and concentration of smoke from fluorinated ethylene propylene wire insulation in microgravity under forced airflow, J. Hazard. Mater. 320 (2016) 602–611. doi:10.1016/j.jhazmat.2016.07.056.

[213] W. Kong, K. Wang, W. Xia, S. Xue, Ignition and combustion characteristics of overloaded wire insulations under weakly buoyancy or microgravity environments, in: W. Hu, Q. Kang (Eds.), Phys. Sci. Under Microgravity Exp. Board SJ-10, Springer, 2019: pp. 191–236. doi:/10.1007/978-981-13-1340-0.

[214] R. Siegell, J.R. Howell, Thermal Radiation and Heat transfer, in: Therm. Radiat. Heat

Transf., 1981: pp. 450–595.

[215] G. Legros, P. Joulain, J. Vantelon, D. Bertheau, J.L. Torero, Soot volume fraction measurements in a three-dimensional laminar diffusion flame established in microgravity, Combust. Sci. Technol. 5 (2006) 813–835. doi:10.1080/00102200500271344.

[216] A. Fuentes, S. Rouvreau, P. Joulain, J.P. Vantelon, G. Legros, J.L. Torero, A.C. Fernandez-Pello, Sooting behavior dynamics of a non-buoyant laminar diffusion flame, Combust. Sci. Technol. 179 (2007) 3–19. doi:10.1080/00102200600805850.

[217] A. Fuentes, G. Legros, A. Claverie, P. Joulain, J.P. Vantelon, J.L. Torero, Interactions between soot and CH* in a laminar boundary layer type diffusion flame in microgravity, Proc. Combust. Inst. 31 II (2007) 2685–2692. doi:10.1016/j.proci.2006.08.031.

[218] A. Guibaud, J.M. Citerne, J.M. Orlac’H, O. Fujita, J.L. Consalvi, J.L. Torero, G. Legros, Broadband modulated absorption/emission technique to probe sooting flames: Implementation, validation, and limitations, Proc. Combust. Inst. 37 (2018) 3959–3966. doi:10.1016/j.proci.2018.06.199.

[219] G. Legros, Q. Wang, J. Bonnety, M. Kashif, C. Morin, J.L. Consalvi, F. Liu, Simultaneous soot temperature and volume fraction measurements in axis-symmetric flames by a two-dimensional modulated absorption/emission technique, Combust. Flame. 162 (2015) 2705–2719. doi:10.1016/j.combustflame.2015.04.006.

[220] B. Ma, S. Cao, D. Giassi, D.P. Stocker, F. Takahashi, B.A. V. Bennett, M.D. Smooke, M.B. Long, An experimental and computational study of soot formation in a coflow jet flame under microgravity and normal gravity, Proc. Combust. Inst. 35 (2015) 839–846. doi:10.1016/j.proci.2014.05.064.

[221] F. Zhu, Z. Lu, S. Wang, Y. Yin, Microgravity diffusion flame spread over a thick solid in step-changed low-velocity opposed flows, Combust. Flame. 205 (2019) 55–67. doi:10.1016/j.combustflame.2019.03.040.

[222] J.C. Ku, D.W. Griffin, P.S. Greenberg, Buoyancy-induced differences in soot morphology, Combust. Flame. 1 (1995) 216–218.

[223] A. Bar-Ilan, G. Rein, A.C. Fernandez-Pello, J.L. Torero, D.L. Urban, Forced forward smoldering experiments in microgravity, Exp. Therm. Fluid Sci. 28 (2004) 743–751. doi:10.1016/j.expthermflusci.2003.12.012.

[224] A. Bar-Ilan, G. Rein, D. C.walther, A.C. Fernandez-Pello, J.L. Torero, D.L. Urban, The effect of buoyancy on opposed smoldering, Combust. Sci. Technol. 176 (2004) 2027–2055. doi:10.1080/00102200490514822.

[225] J. Citerne, H. Dutilleul, K. Kizawa, M. Nagachi, O. Fujita, M. Kikuchi, G. Jomaas, S. Rouvreau, J.L. Torero, G. Legros, Fire safety in space – Investigating flame spread interaction over wires, Acta Astronaut. (2016). http://dx.doi.org/10.1016/j.actaastro.2015.12.021.

[226] L. Carmignani, K. Dong, S. Bhattacharjee, Radiation from Flames in a Microgravity Environment: Experimental and Numerical Investigations, Fire Technol. 56 (2020) 33–47. doi:10.1007/s10694-019-00884-y.

[227] A. Carney, Y. Li, Y.T. Liao, S. Olson, P. Ferkul, Concurrent-flow flame spread over thin discrete fuels in microgravity, Combust. Flame. 226 (2021) 211–221.

doi:10.1016/j.combustflame.2020.12.005.

[228] S.L. Olson, P. V. Ferkul, S. Bhattacharjee, J.M. Fletcher, A.C. Fernandez-Pello, S. Link, J.S. T'ien, I.S. Wichman, Results from on-board CSA-CP and CDM Sensor Readings during the Burning and Suppression of Solids – II (BASS-II) Experiment in the Microgravity Science Glovebox (MSG), in: 45th Int. Conf. Environ. Syst., Bellevue, Washington, 2015: pp. 12–16.

[229] K.D. Annen, J.A. Conant, K.J. Weiland, Retrieval of Temperature and Species Distributions from Multispectral Image Data of Surface Flame Spread in Microgravity, in: Sixth Int. Microgravity Combust. Work., Cleveland, Ohio, 2001: p. Paper No. 91.

[230] NASA, Flammability, offgassing, and compatibility requirements and test procedures. NASA-STD-6001B, (2016) 1–158.

[231] T. Steinhaus, S.M. Olenick, A. Sifuentes, R.T. Long, J.L. Torero, A method for assessing material flammability for micro-gravity environments, in: Proc. First Jt. Meet. U.S. Sect. Combust. Institute1, The Combustion Institute, Pittsburgh, PA, 1999: pp. 681–684.

[232] J.L. Torero, T. Vietoris, G. Legros, P. Joulain, Estimation of a total mass transfer number from the standoff distance of a spreading flame, Combust. Sci. Technol. 174 (2002) 187–203. doi:10.1080/713712953.

[233] A. Rangwala, Flame Spread Analysis Using a Variable B-Number, Fire Saf. Sci. 9 (2008) 243–254. doi:10.3801/IAFSS.FSS.9-243.

[234] A.S. Rangwala, S.G. Buckley, J.L. Torero, Upward flame spread on a vertically oriented fuel surface: The effect of finite width, Proc. Combust. Inst. 31 II (2007) 2607–2615. doi:10.1016/j.proci.2006.07.235.

[235] D. Hirsch, J. Williams, H. Beeson, Pressure effects on oxygen concentration flammability thresholds of polymeric materials for aerospace applications, J. Test. Eval. (2008) 3–8. doi:10.1520/jte100975.

[236] D.B. Hirsch, A. Juarez, G.J. Peyton, S.A. Harper, S.L. Olson, Selected Parametric Effects on Materials Flammability Limits, in: 41st Int. Conf. Environ. Syst., AIAA, Portland, Oregon, 2011: p. 5067. doi:doi:10.2514/6.2011-5067.

[237] S.L. Olson, G.A. Ruff, F.J. Miller, Microgravity Flame Spread in Exploration Atmospheres: Pressure, Oxygen, and Velocity Effects on Opposed and Concurrent Flame Spread, SAE Int. J. Aerosp. 1 (2008) 2008-01–2055. doi:10.4271/2008-01-2055.

[238] Plastics — Determination of burning behaviour by oxygen index - Part 2: Ambient-temperature test (ISO 4589-2:2017), European Committee for Standarization, Brussels, 2017.

[239] Standard Test Method for Measuring the Minimum Oxygen Concentration to Support Candle-Like Combustion of Plastics (Oxygen Index) - (D2863 − 17), (2015) 1–14. doi:10.1520/D2863-12.1.

[240] S. Takahashi, T. Ebisawa, S. Bhattacharjee, T. Ihara, Simplified model for predicting difference between flammability limits of a thin material in normal gravity and microgravity environments, Proc. Combust. Inst. 35 (2015) 2535–2543. doi:10.1016/j.proci.2014.07.017.

[241] K. Tsuboi, S. Takahashi, T. Ihara, S. Bhattacharjee, Effect of ambient gas on flammability limit of flat materials in microgravity, Trans. Japan Soc. Aeronaut. Sp. Sci. Aerosp. Technol. 14 (2016) Ph_1-Ph_6. doi:http://doi.org/10.2322/tastj.14.Ph_1.

[242] S. Takahashi, K. Maruta, Prediction of Limiting Oxygen Concentration of Thin Materials in Microgravity, Trans. Japan Soc. Aeronaut. Sp. Sci. Aerosp. Technol. Japan. 16 (2018) 28–34. doi:10.2322/tastj.16.28.

[243] S. Takahashi, A.F. Fahmi bin Borham, K. Terashima, A. Hosogai, Y. Kobayashi, Flammability limit of thin flame retardant materials in microgravity environments, Proc. Combust. Inst. 37 (2019) 4257–4265. doi:.1037//0033-2909.I26.1.78.

[244] S. Takahashi, K. Terashima, M.A.F. bin Borhan, Y. Kobayashi, Relationship Between Blow-Off Behavior and Limiting Oxygen Concentration in Microgravity Environments of Flame Retardant Materials, Fire Technol. 56 (2020) 169–183. doi:10.1007/s10694-019-00880-2.

[245] A. Kumar, J. T'Ien, Numerical modeling of limiting oxygen index apparatus for film type fuels, Int. J. Spray Combust. Dyn. 4 (2012) 299–322. doi:10.1260/1756-8277.4.4.299.

[246] J.L. Torero, T. Vietoris, P. Joulain, Material Flammability Studies for Micro-Gravity Environments, Eur. Rocket Balloon Programs Relat. Res. 437 (1999).

[247] R. Friedman, S.A. Gokoglu, L. Urban, David, Microgravity combustion research: 1999 Program and Results, Cleveland, Ohio, 1999.

[248] J.L. Cordova, Y. Zhou, C.C. Pfaff, A.C. Fernandez-Pello, Test Method for Ranking the Fire Properties of Materials in Space Based Facilities, Prev. Hazard. Fires Explos. (1999) 49–59. doi:10.1007/978-94-011-4712-5_5.

[249] G.A. Ruff, D.L. Urban, Technology Development for Fire Safety in Exploration Spacecraft and Habitats, in: 45th AIAA Aerosp. Sci. Meet. Exhib., Reno, Nevada, 2007: p. 350. doi:doi: 10.2514/6.2007-350.

[250] J.L. Córdova, a. C. Fernandez-Pello, Convection Effects on the Endothermic Gasification and Piloted Ignition of a Radiatively Heated Combustible Solid, Combust. Sci. Technol. 156 (2000) 271–289. doi:10.1080/00102200008947306.

[251] Y.Y. Zhou, D.C. Walther, A.C. Fernandez-Pello, J.L. Torero, H.D. Ross, Theoretical prediction of piloted ignition of polymeric fuels in microgravity at low velocity flows, Microgravity Sci. Technol. 14 (2003) 44–50. doi:10.1007/BF02873335.

[252] D. Rich, C. Lautenberger, J.L. Torero, J.G. Quintiere, C. Fernandez-Pello, Mass flux of combustible solids at piloted ignition, Proc. Combust. Inst. 31 (2007) 2653–2660. doi:10.1016/j.proci.2006.08.055.

[253] A.F. Osorio, C. Fernandez-Pello, D.L. Urban, G.A. Ruff, Limiting conditions for flame spread in fire resistant fabrics, Proc. Combust. Inst. 34 (2013) 2691–2697.

[254] S. McAllister, D. Rich, C. Lautenberger, C. Fernandez-Pello, Z.G. Yuan, Modeling microgravity and normal gravity opposed flame spread over polymer/glass composites, in: Collect. Tech. Pap. - 45th AIAA Aerosp. Sci. Meet., American Institute of Aeronautics and Astronautics Inc., 2007: pp. 9178–9187. doi:10.2514/6.2007-740.

[255] T. Vietoris, P. Joulain, J.L. Torero, Experimental characterization of a laminar diffusion flame in micro-gravity, J. Chim. Phys. Physico-Chimie Biol. 96 (1999)

1022–1030.

[256] H.C. Hottel, Certain laws governing diffusive burning of liquids, Fire Res. Abstr. Rev. 1 (1959) 41.

[257] F.A. Williams, Combustion Theory - The Fundamental Theory of Chemically Reacting Flow Systems, Second, Addison-Wesley, 2018.

[258] J. De Ris, A. Murty Kanury, M.C. Yuen, Pressure modeling of fires, Symp. Combust. 14 (1973) 1033–1044. https://doi.org/10.1016/S0082-0784(73)80093-1.

[259] M. Thomsen, C. Fernandez-Pello, D.L. Urban, G.A. Ruff, S.L. Olson, On simulating concurrent flame spread in reduced gravity by reducing ambient pressure, Proc. Combust. Inst. 37 (2018) 3793–3800. doi:10.1016/j.proci.2018.05.004.

[260] M. Thomsen, X. Huang, C. Fernandez-Pello, D.L. Urban, G.A. Ruff, Concurrent flame spread over externally heated Nomex under mixed convection flow, Proc. Combust. Inst. 37 (2019) 3801–3808. doi:10.1016/j.proci.2018.05.055.

[261] M. Thomsen, C. Fernandez-Pello, G.A. Ruff, D.L. Urban, Buoyancy effects on concurrent flame spread over thick PMMA, Combust. Flame. 199 (2019) 279–291. doi:10.1016/j.combustflame.2018.10.016.

[262] Y. Nakamura, N. Yoshimura, T. Matsumura, H. Ito, O. Fujita, Flame Spread over Polymer-Insulated Wire in Sub-Atmospheric Pressure: Similarity to Microgravity Phenomena, in: Prog. Scale Model., Springer Netherlands, Dordrecht, 2008: pp. 17–27. doi:10.1007/978-1-4020-8682-3_2.

[263] S. Dosanjh, J. Peterson, A.C. Fernandez-Pello, P.J. Pagni, Buoyancy effects on smoldering combustion, Acta Astronaut. 13 (1986) 689–696. doi:10.1016/0094-5765(86)90019-6.

[264] T. Yamazaki, T. Matsuoka, Y. Li, Y. Nakamura, Applicability of a Low-Pressure Environment to Investigate Smoldering Behavior Under Microgravity, Fire Technol. 56 (2020) 209–228. doi:10.1007/s10694-019-00911-y.

[265] J.M. Pepper, J.M. Fletcher, S.L. Olson, I.S. Wichman, A Study of the Effectiveness of a Narrow Channel Apparatus in Simulating Microgravity Flame Spread over Thin Fuels, in: 42nd Int. Conf. Environ. Syst., American Institute of Aeronautics and Astronautics, San Diego, California, 2012. doi:10.2514/6.2012-3493.

[266] G.R. Bornand, F.J. Miller, J.M. Pepper, S.L. Olson, I.S. Wichman, Opposed-Flow Flame Spread in a Narrow Channel Apparatus over Thin PMMA Sheets, in: 8th U. S. Natl. Combust. Meet., Utah, 2013: pp. 1–8.

[267] F. Zhu, Z. Lu, S. Wang, Flame spread and extinction over a thick solid fuel in low-velocity opposed and concurrent flows, Microgravity Sci. Technol. (2016). doi:10.1007/s12217-015-9475-4.

[268] T. Matsuoka, K. Nakashima, Y. Nakamura, S. Noda, Appearance of flamelets spreading over thermally thick fuel, Proc. Combust. Inst. 36 (2017) 3019–3026. doi:10.1016/j.proci.2016.07.112.

[269] K. Funashima, A. Masuyama, K. Kuwana, G. Kushida, Opposed-flow flame spread in a narrow channel: Prediction of flame spread velocity, Proc. Combust. Inst. 37 (2019) 3757–3765. doi:10.1016/j.proci.2018.08.017.

[270] K. Kuwana, K. Suzuki, Y. Tada, G. Kushida, Effective Lewis number of smoldering

spread over a thin solid in a narrow channel, Proc. Combust. Inst. 36 (2017) 3203–3210. doi:10.1016/j.proci.2016.06.159.

[271] H. Iizuka, K. Kuwana, G. Kushida, Numerical analysis of heat loss effects on the smoldering combustion of a thin solid in a narrow channel, J. Chem. Eng. Japan. 50 (2017) 535–541. doi:10.1252/jcej.16we035.

[272] K. Wang, W. Xia, B. Wang, Y. Ai, W. Kong, Study on Fire Initiation of Wire Insulation by a Narrow Channel at low Pressure, Microgravity Sci. Technol. 28 (2016) 155–163. doi:10.1007/s12217-016-9494-9.

[273] I.S. Wichman, S.L. Olson, F.J. Miller, S.A. Tanaya, Experimental evaluation of flame and flamelet spread over cellulosic materials using the narrow channel apparatus, Fire Mater. 37 (2013) 503–519. doi:10.1002/fam.2143.

[274] S. Hossain, I.S. Wichman, G.W. Sidebotham, S.L. Olson, F.J. Miller, Influence of gap height and flow field on global stoichiometry and heat losses during opposed flow flame spread over thin fuels in simulated microgravity, Combust. Flame. 193 (2018) 133–144. doi:10.1016/j.combustflame.2018.02.023.

[275] J.S. T'ien, The possibility of a reversal of material flammability ranking from normal gravity to microgravity, Combust. Flame. 80 (1990) 355–357. doi:10.1016/0010-2180(90)90111-4.

[276] S. Hossain, I.S. Wichman, F.J. Miller, S.L. Olson, Opposed flow flame spread over thermally thick solid fuels: buoyant flow suppression, stretch rate theory, and the regressive burning regime, Combust. Flame. 219 (2020) 57–69. doi:10.1016/j.combustflame.2020.05.001.

[277] J.W. Marcum, P. V. Ferkul, S.L. Olson, PMMA rod stagnation region flame blowoff limits at various radii, oxygen concentrations, and mixed stretch rates, Proc. Combust. Inst. 37 (2019) 4001–4008. doi:10.1016/j.proci.2018.05.081.

[278] J.W. Marcum, P. Rachow, P. V. Ferkul, S.L. Olson, Low pressure flame blowoff of the stagnation region of cast PMMA cylinders in axial mixed convective flow, Combust. Flame. 216 (2020) 385–397. doi:10.1016/j.combustflame.2020.02.031.

[279] S. Tao, J. Fang, L. Zhao, J. Wang, H.R. Shah, L. Hu, L. Yang, Flammability and critical parameters at low oxygen extinction limit of stagnation-point diffusion flames with varied stretch rates, Fire Saf. J. 116 (2020) 103203. doi:10.1016/j.firesaf.2020.103203.

[280] S. Tao, J. Fang, L. Zhao, J. Wang, H.R. Shah, L. Yang, Burning characteristics of PMMA with varied stretch rates under stagnation-point diffusion flames, Combust. Flame. 220 (2020) 63–72. doi:10.1016/j.combustflame.2020.06.022.

[281] S.L. Olson, J.S. T'Ien, Buoyant low-stretch diffusion flames beneath cylindrical PMMA samples, Combust. Flame. 121 (2000) 439–452. doi:10.1016/S0010-2180(99)00161-3.

[282] S.L. Olson, H.D. Beeson, J.P. Haas, J.S. Baas, An Earth-Based Equivalent Low Stretch Apparatus to Assess Material Flammability for Microgravity and Extraterrestrial Environments., Proc. Combust. Inst. 30 (2005) 2335–2343. doi:10.1016/j.proci.2004.08.044.

[283] S.L. Olson, Convective Heat Transfer Scaling of Ignition Delay and Burning Rate with Heat Flux and Stretch Rate in the Equivalent Low Stretch Apparatus., Fire Saf.

Sci. 10 (2011) 959–970. doi:10.3801/IAFSS.FSS.10-959.

[284] Y. Zhang, M. Kim, H. Guo, P.B. Sunderland, J.G. Quintiere, J. deRis, D.P. Stocker, Emulation of condensed fuel flames with gases in microgravity, Combust. Flame. 162 (2015) 3449–3455. doi:10.1016/j.combustflame.2015.05.005.

[285] F.V. Lundstrom, P.B. Sunderland, J.G. Quintiere, P. van Hees, J.L. de Ris, Study of ignition and extinction of small-scale fires in experiments with an emulating gas burner, Fire Saf. J. 87 (2017) 18–24.

[286] A. Markan, J.G. Quintiere, P.B. Sunderland, J.L. De Ris, D.P. Stocker, A Burning Rate Emulator (BRE) for study of condensed fuel burning in microgravity, Combust. Flame. 192 (2017) 1–6.

[287] A. Snegirev, E. Kuznetsov, E. Markus, P. Dehghani, P. Sunderland, Transient dynamics of radiative extinction in low-momentum microgravity diffusion flames, Proc. Combust. Inst. 000 (2020) 1–9. doi:10.1016/j.proci.2020.06.110.

[288] S.K. Srivastava, T. Kuila, Fire Retardancy of Elastomers and Elastomer Nanocomposites, Elsevier B.V., 2014. doi:10.1016/B978-0-444-53808-6.00018-4.

[289] A.F. Grand, C.A. Wilkie, Fire retardancy of polymeric materials, CRC Press, New York, 2000.

[290] R.R. Buch, Rates of heat release and related fire parameters for silicones, Fire Saf. J. 17 (1991) 1–12. doi:0379-7112/91.

[291] P.J. Austin, R.R. Buch, T. Kashiwagi, Gasification of silicone fluids under external thermal radiation Part I. Gasification rate and global heat of gasification, Fire Mater. 22 (1998) 239–252.

[292] F.-Y. Hshieh, Shielding effects of silica-ash layer on the combustion of silicones and their possible applications on the fire retardancy of organic polymers, Fire Mater. 22 (1998) 69–76.

[293] I. Hong, S. Lee, Cure kinetics and modeling the reaction of silicone rubber, J. Ind. Eng. Chem. 19 (2012) 42–47. doi:10.1016/j.jiec.2012.05.006.

[294] A. Bacher, Silicone rubber used for fire safety and fire retardant cables, Univ. Power Eng. Conf. (UPEC), 2010 45th Int. (2010) 1–4.

[295] J. Lipowitz, M.J. Ziemelis, Flammability of poly(dimethylsiloxanes). II. Flammability and fire hazards properties, Fire Flammabl. 7 (1976) 504–529.

[296] D. Laboureur, L. Aprin, A. Osmont, J.M. Buchlin, P. Rambaud, Small scale thin-layer boilover experiments: Physical understanding and modeling of the water sub-layer boiling and the flame enlargement, J. Loss Prev. Process Ind. 26 (2013) 1380–1389. doi:10.1016/j.jlp.2013.08.016.

[297] I.S. Wichman, S.L. Olson, F. Miller, A. Hariharan, Fire in Microgravity, Am. Sci. (2016). doi:10.1511/2016.118.44.

[298] A. Witkowski, A.A. Stec, T.R. Hull, Thermal Decomposition of Polymeric Materials, in: M.J. Hurley, D. Gottuk, J.R. Hall, K. Harada, E. Kuligowski, M. Puchovsky, J. Torero, J.M. Watts, C. Wieczorek (Eds.), SFPE Handb. Fire Prot. Eng., Fifth, Springer, 2016: pp. 167–254.

[299] A.C.M. Kuo, Poly(dimethylsiloxane), in: Polym. Data Handb., Oxford University

Press, 1999: pp. 411–435. doi:10.1007/978-1-4419-6247-8_9030.

[300] S. Hamdani, C. Longuet, D. Perrin, J.M. Lopez-cuesta, F. Ganachaud, Flame retardancy of silicone-based materials, Polym. Degrad. Stab. 94 (2009) 465–495. doi:10.1016/j.polymdegradstab.2008.11.019.

[301] T.H. Thomas, T.C. Kendrick, Thermal analysis of polydimethylsiloxanes. I. Thermal degradation in controlled atmospheres, J. Polym. Sci. Part A-2 Polym. Phys. 7 (1969) 537–549. doi:10.1002/pol.1969.160070308.

[302] G. Camino, S.M. Lomakin, M. Lageard, Thermal polydimethylsiloxane degradation. Part 2. The degradation mechanisms, Polymer (Guildf). 43 (2002) 2011–2015. doi:10.1016/S0032-3861(01)00785-6.

[303] N. Grassie, I.G. MacFarlane, The Thermal Degradation of Polysiloxanes - I, Eur. Polym. J. 14 (1978) 875–884.

[304] T.S. Radhakrishnan, New method for evaluation of kinetic parameters and mechanism of degradation from pyrolisis-GC studies: thermal degradation of PDMS, J. Appl. Polym. Sci. 73 (1999) 441–450.

[305] N. Grassie, K.F. Francey, I.G. MacFarlane, The thermal degradation of polysiloxanes - Part 4: poly(dimethyl/diphenyl siloxane), Polym. Degrad. Stab. 2 (1980) 67–83.

[306] G. Camino, S.M. Lomakin, M. Lazzari, Polydimethylsiloxane thermal degradation. Part 1. Kinetic aspects., Polymer (Guildf). 42 (2001) 2395–2402.

[307] R.R. Buch, P.J. Austin, T. Kashiwagi, Gasification of silicone fluids under external thermal radiation. Part 2. Gasification products - Characterization and quantitation, Fire Mater. 22 (1998) 239–252.

[308] J. Lipowitz, Flammability of poly(dimethylsiloxanes). I. A model for combustion, Fire Flammabl. 7 (1976) 482–503.

[309] G. Geiseler, J. D. Cox und G. Pilcher: Thermochemistry of Organic and Organometallic Compounds. Academic Press, London and New York 1970. 643 Seiten. Preis: 170s., Berichte Der Bunsengesellschaft Für Phys. Chemie. 74 (1970) 727–727. doi:10.1002/bbpc.19700740727.

[310] J.S.Q. Zeng, R. Greif, P. Stevens, M. Ayers, A. Hunt, Effective optical constants n and κ and extinction coefficient of silica aerogel, J. Mater. Res. 11 (2008) 687–693. doi:10.1557/jmr.1996.0083.

[311] W.D. Good, J.L. Lacina, B.L. Deprater, J.P. McCullough, A new approach to the combustion calorimetry of silicon and organosilicon compounds. Heats of formation of quartz, fluorosilicic acid, and hexamethyldisiloxane, J. Phys. Chem. 68 (1964) 579–586. doi:10.1021/j100785a024.

[312] W.H. Awad, Recent developments in silicon-based flame retardants, in: C.A. Wilkie, A.B. Morgan (Eds.), Fire Retard. Polym. Mater., 2nd ed., Taylor & Francis, Boca Raton, FL, 2010: pp. 187–206.

[313] M. Zeldin, D.W. Kang, G.P. Rajendran, B. Qian, S.J. Choi, Kinetics of thermal depolymerisation of trimethylsiloxy end-blocked polydimethylsiloxane and polydimethylsiloxane-n-phenylsilazane copolymer, Sci. Total Environ. 73 (1988) 71–85.

[314] F.Y. Hshieh, R.R. Buch, Controlled-atmosphere cone calorimeter studies of silicones,

Fire Mater. 21 (1997) 265–270. doi:10.1002/(SICI)1099-1018(199711/12)21:6<265::AID-FAM620>3.0.CO;2-U.

[315] R.N. Walters, S.M. Hackett, R.E. Lyon, Heats of combustion of high temperature polymers, Fire Mater. 24 (2000) 245–252. doi:10.1002/1099-1018(200009/10)24:5<245::AID-FAM744>3.0.CO;2-7.

[316] J. Lipowitz, J.E. Jones, M. Kanakia, Fire safety properties of some transformer dielectric liquids, Fire Flammabl. 15 (1982) 39—55. doi:10.1109/EIC.1979.7461124.

[317] J.E. Niehaus, P. V Ferkul, S.A. Gokoglu, G.A. Ruff, Buoyant Effects on the Flammability of Silicone Samples Planned for the Spacecraft Fire Experiment (Saffire), in: 45th Int. Conf. Environ. Syst. 12-16, Bellevue, Washington, 2015.

[318] D. Hirsch, S. Motto, A. Porter, H. Beeson, M.D. Pedley, Issues related to the flammability assessment of polymers for hazard analyses of oxygen systems, in: T.A. Steinberg, H.D. Beeson, B.E. Newton (Eds.), Flammabl. Sensit. Mater. Oxyg. Atmos. Tenth Vol., ASTM International, West Conshohocken, PA, 2003: pp. 21–26.

[319] R. Friendman, Principles of fire protection chemistry and physics, Thid, JOnes and Barlett Publishers, Sudbury< Massachusetts, 2009.

[320] SSP-M823 data sheet brochure, (n.d.). https://www.sspinc.com/img/spec_sheets/brochure_dankvcrrif.pdf (accessed April 30, 2021).

[321] A.C. Fernandez-Pello, A theoretical model for the upward laminar spread of flames over vertical fuel surfaces, Combust. Flame. 31 (1978) 135–148. doi:10.1016/0010-2180(78)90124-4.

[322] Radiant-interchange configuration factors between various selected plane surfaces, Proc. R. Soc. London. Ser. A. Math. Phys. Sci. 292 (1966) 51–60. doi:10.1098/rspa.1966.0118.

[323] G. Cox, Combustion fundamentals of fire, Academic, London, San Diego, 1995.

[324] S. Takahashi, T. Nagumo, K. Wakai, S. Bhattacharjee, Effects of ambient condition on flame spread over a thin PMMA sheet, JSME Int. J. 43 (2000) 556–562.

[325] S. Bhattacharjee, R. Ayala, K. Wakai, S. Takahashi, Opposed-flow flame spread in microgravity-theoretical prediction of spread rate and flammability map, Proc. Combust. Inst. 30 (2005) 2279–2286. doi:10.1016/j.proci.2004.08.020.

[326] M. Chaos, Spectral aspects of bench-scale flammability testing: Application to hardwood pyrolysis, Fire Saf. Sci. 11 (2014) 165–178. doi:10.3801/IAFSS.FSS.11-165.

[327] O. Rozenbaum, D. De Sousa Meneses, Y. Auger, S. Chermanne, P. Echegut, A spectroscopic method to measure the spectral emissivity of semi-transparent materials up to high temperature, Rev. Sci. Instrum. 70 (1999) 4020–4025. doi:10.1063/1.1150028.

[328] J.R. Hallman, J.R. Welker, C.M. Sliepcevich, Polymer surface reflectance-absorptance characteristics, Polym. Eng. Sci. 14 (1974) 717–723. doi:10.1002/pen.760141010.

[329] C.L. Tien, K.Y. Lee, A.J. Stretton, C. Lautenberger, Radiation heat transfer, in: SFPE Handb. Fire Prot. Eng. Fifth Ed., Springer New York, 2016: pp. 102–135.

doi:10.1007/978-1-4939-2565-0_4.

[330] R. GARDON, The Emissivity of Transparent Materials, J. Am. Ceram. Soc. 39 (1956) 278–285. doi:10.1111/j.1151-2916.1956.tb15833.x.

[331] J.H. Choi, O. Fujita, T. Tsuiki, J. Kim, S.H. Chung, In-situ observation of the soot deposition process on a solid wall with a diffusion flame along the wall, JSME Int. Journal, Ser. B Fluids Therm. Eng. 49 (2006) 167–175. doi:10.1299/jsmeb.49.167.

[332] C. Graf, Silica, amorphous, Kirk-Othmer Encycl. Chem. Technol. (2018) 1–43.

[333] H. Ono, R. Dobashi, T. Sakuraya, Thermophoretic velocity measurements of soot particles under a microgravity condition, Proc. Combust. Inst. 29 (2002) 2375–2382. doi:10.1016/s1540-7489(02)80289-9.

[334] M. Paul, F. Issacci, I. Catton, G.E. Apostolakis, Characterization of smoke particles generated in terrestrial and microgravity environments, Fire Saf. J. 28 (1997) 233–252. doi:10.1016/S0379-7112(96)00078-1.

[335] J.H. Choi, O. Fujita, T. Tsuiki, J. Kim, S.H. Chung, A study of the effect of oxygen concentration on the soot deposition process in a diffusion flame along a solid wall by in-situ observations in microgravity, JSME Int. Journal, Ser. B Fluids Therm. Eng. 48 (2006) 839–848. doi:10.1299/jsmeb.48.839.

[336] J.H. Choi, J. Kim, S.K. Choi, B.H. Jeon, O. Fujita, S.H. Chung, Numerical simulation on soot deposition process in laminar ethylene diffusion flames under a microgravity condition, J. Mech. Sci. Technol. 23 (2009) 707–716. doi:10.1007/s12206-009-0203-0.

[337] O. Fujita, K. Ito, H. Ito, Y. Takeshita, Effect of thermophoretic force on soot agglomeration process in diffusion flames under microgravity, in: NASA Conf. Publ., 1997: pp. 217–222.

[338] A. Toda, Y. Ohi, R. Dobashi, T. Hirano, T. Sakuraya, Accurate measurement of thermophoretic effect in microgravity, J. Chem. Phys. 105 (1996) 7083–7087. doi:10.1063/1.472510.

[339] R.R. Retamal Marín, F. Babick, G.G. Lindner, M. Wiemann, M. Stintz, Effects of sample preparation on particle size distributions of different types of silica in suspensions, Nanomaterials. 8 (2018). doi:10.3390/nano8070454.

[340] J.H. Choi, O. Fujita, T. Tsuiki, J. Kim, S.H. Chung, Experimental study on thermophoretic deposition of soot particles in laminar diffusion flames along a solid wall in microgravity, Exp. Therm. Fluid Sci. 32 (2008) 1484–1491. doi:10.1016/j.expthermflusci.2008.03.008.

[341] A.S. Kuz'minskii, Y.A. Goldovskii, Investigation of the oxidation of polydimethylsiloxane rubbers, Polym. Sci. U.S.S.R. 3 (1962) 823–832. doi:10.1016/0032-3950(62)90158-2.

[342] N. Panek, M.R.J. Charest, Ö.L. Gülder, Simulation of Microgravity Diffusion Flames Using Sub-Atmospheric Pressures, (2011). doi:10.2514/1.J051306.

[343] S. Fereres, C. Lautenberger, A.C. Fernandez-Pello, D.L. Urban, G.A. Ruff, Understanding ambient pressure effects on piloted ignition through numerical modeling, Combust. Flame. 159 (2012) 3544–3553. doi:10.1016/j.combustflame.2012.08.006.

[344] D. Zhuo, A. Gu, G. Liang, J.T. Hu, L. Cao, L. Yuan, Flame retardancy and flame retarding mechanism of high performance hyperbranched polysiloxane modified bismaleimide/cyanate ester resin, Polym. Degrad. Stab. 96 (2011) 505–514. doi:10.1016/j.polymdegradstab.2011.01.006.

[345] M.J. Scudamore, P.J. Briggs, F.H. Prager, Cone calorimetry—a review of tests carried out on plastics for the association of plastic manufacturers in Europe, Fire Mater. 15 (1991) 65–84. doi:10.1002/fam.810150205.

[346] M.A. Delichatsios, Ignition times for thermally thick and intermediate conditions in flat and cylindrical geometries, in: Fire Saf. Sci., International Association for Fire Safety Science, 2000: pp. 233–244. doi:10.3801/IAFSS.FSS.6-233.

[347] J.G. Quintiere, Fundamentals of Fire Phenomena, 1st ed., John Wiley & Sons Ltd, Chichester, West Sussex, England, 2006. www.wiley.com.

[348] A. Bejan, A.D. Kraus, eds., Heat Transfer Handbook , Wiley, 2003.

[349] K.K. Wu, C.H. Chen, A numerical analysis of ignition to steady downward flame spread over a thin solid fuel, Combust. Sci. Technol. 175 (2003) 933–964. doi:10.1080/00102200302408.

[350] T. Lin, Effects of ambient oxygen on ignition over a vertical thin solid fuel, Combust. Sci. Technol. 175 (2010) 83–102. doi:10.1080/00102200302365.

[351] K. Agata, O. Fujita, Y. Ichimura, T. Fujii, H. Ito, Y. Nakamura, Wire Insulation Ignition with Excess Electric Current in Microgravity, Japan Soc. Microgravity Appl. 25 (2008) 11–16.

[352] S. Bhattacharjee, M. Laue, L. Carmignani, P. Ferkul, S. Olson, Opposed-flow flame spread: A comparison of microgravity and normal gravity experiments to establish the thermal regime, Fire Saf. J. 79 (2016) 111–118. doi:10.1016/j.firesaf.2015.11.011.

[353] M. Endo, J.S. T'ien, P. V. Ferkul, S.L. Olson, M.C. Johnston, Flame Growth Around a Spherical Solid Fuel in Low Speed Forced Flow in Microgravity, Fire Technol. 56 (2020) 5–32. doi:10.1007/s10694-019-00848-2.

[354] C.T. Yang, J.S. T'ien, Numerical simulation of combustion and extinction of a solid cylinder in low-speed cross flow, J. Heat Transfer. 120 (1998) 1055–1063. doi:10.1115/1.2825890.

[355] A. Atreya, S. Agrawal, Effect of radiative heat loss on diffusion flames in quiescent microgravity atmosphere, Combust. Flame. 115 (1998) 372–382. doi:10.1016/S0010-2180(97)00364-7.

[356] P. Kumar B, A. Kumar, Effects of fuel Lewis number on self-propagating flame spread over thin solid fuels in microgravity, Combust. Flame. 219 (2020) 293–311. doi:10.1016/j.combustflame.2020.05.021.

[357] Y. Zhang, P.D. Ronney, E. V. Roegner, J.B. Greenberg, Lewis number effects on flame spreading over thin solid fuels, Combust. Flame. 90 (1992) 71–83. doi:10.1016/0010-2180(92)90136-D.

[358] I. Glassman, Sooting laminar diffusion flames: Effect of dilution, additives, pressure, and microgravity, Symp. Combust. 27 (1998) 1589–1596. doi:10.1016/S0082-0784(98)80568-7.

[359] M. Kikuchi, O. Fujita, K. Ito, A. Sato, T. Sakuraya, Experimental study on flame spread over wire insulation in microgravity, Symp. Combust. 27 (1998) 2507–2514. doi:10.1016/S0082-0784(98)80102-1.

[360] J. Fang, X. ze He, K. yuan Li, J. wu Wang, Y. ming Zhang, Transition condition and control mechanism of subatmospheric flame spread rate over horizontal thin paper sample, Combust. Flame. 188 (2018) 90–93. doi:10.1016/j.combustflame.2017.09.010.

[361] L. Gagnon, C. Fernandez-Pello, J.L. Urban, V.P. Carey, Y. Konno, O. Fujita, Effect of reduced ambient pressures and opposed airflows on the flame spread and dripping of LDPE insulated copper wires, Fire Saf. J. (2020) 103171. doi:10.1016/j.firesaf.2020.103171.

[362] A.E. Frey, J.S. T'ien, Near-limit flame spread over paper samples, Combust. Flame. 26 (1976) 257–267. doi:10.1016/0010-2180(76)90076-6.

[363] S. Bhattacharjee, L. Carmignani, Radiation-kinetics interactions: A comparison of opposed-flow flame spread in a low-velocity microgravity and low-pressure downward environments, Proc. Combust. Inst. (2020) 1–9. doi:10.1016/j.proci.2020.05.014.

[364] Q. Wang, L. Hu, A. Palacios, S.H. Chung, Burning characteristics of candle flames in sub-atmospheric pressures: An experimental study and scaling analysis, Proc. Combust. Inst. 37 (2019) 2065–2072. doi:10.1016/j.proci.2018.06.113.

[365] J. Fang, Y. Xue, J. Wang, X. He, Y. Zhang, S. Zhao, Y. Zhang, PE and ETFE wire insulation flame morphologies and spread rates under subatmospheric pressures, J. Thermoplast. Compos. Mater. (2020) 1–14. doi:10.1177/0892705720904090.

[366] K. Annamalai, M. Sibulkin, Flame Spread Over Combustible Surfaces for Laminar Flow Systems Part II: Flame Heights and Fire Spread Rates, Combust. Sci. Technol. 19 (1979) 185–193.

[367] S. Bang, B.J. Lee, S.H. Chung, Effect of pressure on the characteristics of lifted flames, Proc. Combust. Inst. 37 (2019) 2013–2020. doi:10.1016/j.proci.2018.06.094.

[368] S.Y. Hsua, J.S. T'ien, Pressure extinction limits of non-premixed flames, Combust. Theory Model. 13 (2009) 885–900. doi:10.1080/13647830903225284.

[369] L.K. Honda, P.D. Ronney, Effect of Ambient Atmosphere on Flame Spread at Microgravity, Combust. Sci. Technol. 133 (1998) 267–291. doi:10.1080/00102209808952037.

[370] G.W. Sidebotham, S.L. Olson, Microgravity opposed-flow flame spread in polyvinyl chloride tubes, Combust. Flame. 154 (2008) 789–801. doi:10.1016/j.combustflame.2008.05.014.

[371] D.L. Urban, Interactions Between Flames on Parallel Solid Surfaces, in: Third Int. Microgravity Combust. Work., National Aeronautics and Space Administration NASA, Cleveland, Ohio, 1995: pp. 233–238.

[372] K.B. McGrattan, T. Kashiwagi, H.R. Baum, S.L. Olson, Effects of ignition and wind on the transition to flame spread in a microgravity environment, Combust. Flame. 106 (1996) 377–391. doi:10.1016/0010-2180(96)00184-8.

[373] Y. Kobayashi, Y. Konno, X. Huang, S. Nakaya, M. Tsue, N. Hashimoto, O. Fujita, C. Fernandez-Pello, Laser piloted ignition of electrical wire in microgravity, Proc.

Combust. Inst. 37 (2019) 4211–4219. doi:.1037//0033-2909.I26.1.78.

[374] S. Bhattacharjee, R.A. Altenkirch, S.L. Olson, R.G. Sotos, Heat Transfer to a Thin Solid Combustible in Flame Spreading at Microgravity, J. Heat Transfer. 113 (1991) 670–676. http://dx.doi.org/10.1115/1.2910617.

[375] O. Fujita, M. Kikuchi, K. Ito, K. Nishizawa, Effective mechanisms to determine flame spread rate over ethylene-tetrafluoroethylene wire insulation: Discussion on dilution gas effect based on temperature measurements, Proc. Combust. Inst. 28 (2000) 2905–2911. doi:10.1016/S0082-0784(00)80715-8.

[376] K. Prasad, Y. Nakamura, S.L. Olson, O. Fujita, K. Nishizawa, K. Ito, T. Kashiwagi, Effect of wind velocity on flame spread in microgravity, Proceeding Combust. Inst. 29 (2002) 2553–2560.

[377] O. Fujita, K. Nishizawa, K. Ito, Effect of low external flow on flame spread over polyethylene-insulated wire in microgravity, Proc. Combust. Inst. 29 (2002) 2545–2552. doi:10.4045/tidsskr.18.0669.

[378] J. Takahashi, O. Fujita, K. Ito, The effect of irradiation angle on laser ignition of cellulose sheet in microgravity, Proc. Combust. Inst. 30 II (2005) 2311–2317. doi:10.1016/j.proci.2004.08.097.

[379] Y. Takano, O. Fujita, N. Shigeta, Y. Nakamura, H. Ito, Ignition limits of short-term overloaded electric wires in microgravity, Proc. Combust. Inst. 34 (2013) 2665–2673. doi:10.1016/j.proci.2012.06.064.

[380] K. Shimizu, M. Kikuchi, N. Hashimoto, O. Fujita, A numerical and experimental study of the ignition of insulated electric wire with long-term excess current supply under microgravity, Proc. Combust. Inst. 36 (2017) 3063–3071. doi:10.1016/j.proci.2016.06.134.

[381] O. Fujita, T. Kyono, Y. Kido, H. Ito, Y. Nakamura, Ignition of electrical wire insulation with short-term excess electric current in microgravity, Proc. Combust. Inst. 33 (2011) 2617–2623. doi:10.1016/j.proci.2010.06.123.

[382] S. Takahashi, H. Takeuchi, H. Ito, Y. Nakamura, O. Fujita, Study on unsteady molten insulation volume change during flame spreading over wire insulation in microgravity, Proc. Combust. Inst. 34 (2013) 2657–2664. doi:10.1016/j.proci.2012.06.158.

[383] R.A. Neustein, P.P. Mader, G. V. Colombo, D.E. Richardson, Effect of atmosphere selection and gravity upon flammability, SAE Tech. Pap. 78 (1969) 2156–2163. doi:10.4271/690639.

[384] C.S. Tarifa, G. Corchero, G.L. Juste, An Experimental Programme on Flame Spreading at Reduced Gravity Conditions, Appl. Micrograv. Technol. I (1988) 165–169.

[385] C. Sanchez Tarifa, A. Liñan, J.J. Salva, G. Corchero, G.L. Juste, F. Esteban, Heterogeneous Combustión Processes Under Microgravity Conditions, in: B. Kaldeich (Ed.), Combust. Exp. Dur. KC-135 Parabol. Flight, European Space Agency, Paris, 1989: pp. 53–64.

[386] J.M. Cavanagh, D.A. Torvi, K.S. Gabriel, G.A. Ruff, Test method for evaluating fabric flammability and predicted skin burn injury in microgravity, Microgravity Sci. Technol. 18 (2006) 14–26. doi:10.1007/BF02870979.

[387] K.J. Weiland, Intensified Array Camera Imaging of Solid Surface Combustion Aboard the NASA Learjet, AIAA J. 31 (1993) 786–788. doi:10.2514/3.49023.

[388] Y. Kobayashi, K. Terashima, M.A.F. bin Borhan, S. Takahashi, Opposed Flame Spread over Polyethylene Under Variable Flow Velocity and Oxygen Concentration in Microgravity, Fire Technol. 56 (2020) 113–130. doi:10.1007/s10694-019-00862-4.

[389] Y. Konno, Y. Kobayashi, C. Fernandez-Pello, N. Hashimoto, S. Nakaya, M. Tsue, O. Fujita, Opposed-Flow Flame Spread and Extinction in Electric Wires: The Effects of Gravity, External Radiant Heat Flux, and Wire Characteristics on Wire Flammability, Fire Technol. 56 (2020) 131–148. doi:10.1007/s10694-019-00935-4.

[390] M. Nagachi, F. Mitsui, J.M. Citerne, H. Dutilleul, A. Guibaud, G. Jomaas, G. Legros, N. Hashimoto, O. Fujita, Effect of Ignition Condition on the Extinction Limit for Opposed Flame Spread Over Electrical Wires in Microgravity, Fire Technol. 56 (2020) 149–168. doi:10.1007/s10694-019-00860-6.

[391] M. Nagachi, J.M. Citerne, H. Dutilleul, A. Guibaud, G. Jomaas, G. Legros, N. Hashimoto, O. Fujita, Effect of ambient pressure on the extinction limit for opposed flame spread over an electrical wire in microgravity, Proc. Combust. Inst. 000 (2020) 1–8. doi:10.1016/j.proci.2020.05.005.

[392] M. Nagachi, F. Mitsui, J.M. Citerne, H. Dutilleul, A. Guibaud, G. Jomaas, G. Legros, N. Hashimoto, O. Fujita, Can a spreading flame over electric wire insulation in concurrent flow achieve steady propagation in microgravity?, Proc. Combust. Inst. 000 (2018) 1–8. doi:10.1016/j.proci.2018.05.007.

[393] S. Wang, X. Zhang, Microgravity smoldering combustion of flexible polyurethane foam with central ignition, Microgravity Sci. Technol. 20 (2008) 99–105. doi:10.1007/s12217-008-9014-7.

[394] C. Wu, X. Huang, S. Wang, F. Zhu, Y. Yin, Opposed Flame Spread over Cylindrical PMMA Under Oxygen-Enriched Microgravity Environment, Fire Technol. 56 (2020) 71–89. doi:10.1007/s10694-019-00896-8.

[395] S.L. Olson, P. V. Ferkul, J.W. Marcum, High-speed video analysis of flame oscillations along a PMMA rod after stagnation region blowoff, Proc. Combust. Inst. 37 (2019) 1555–1562. doi:10.1016/j.proci.2018.05.080.

[396] K.R. Sacksteder, P.S. Greenberg, R.D. Pettegrew, J.S. T'ien, P. V. Ferkul, H.-Y. Shih, Forced flow flame spreading test: Preliminary findings from the USMP-3 Shuttle mission, in: Third United States Microgravity Payload One Year Rep., 1998: pp. 83–96.

[397] P.S. Greenberg, K.R. Sacksteder, T. Kashiwagi, Wire Insulation Flammability Experiment: USML-1 One Year Post Mission Summary, NASA CP3272. 2 (1994) 631–655.

[398] D.P. Stocker, S.L. Olson, D.L. Urban, J.L. Torero, D.C. Walther, A. Carlos Fernandez-Pello, Small-scale smoldering combustion experiments in microgravity, Symp. Combust. 26 (1996) 1361–1368. doi:10.1016/S0082-0784(96)80355-9.

[399] D.C. Walther, A.C. Fernandez-Pello, D.L. Urban, Space shuttle based microgravity smoldering combustion experiments, Combust. Flame. 116 (1999) 398–414. doi:10.1016/S0010-2180(98)00095-9.

[400] C. Li, Y.T.T. Liao, Effects of ambient conditions on concurrent-flow flame spread

over a wide thin solid in microgravity, Proc. Combust. Inst. 000 (2020) 1–10. doi:10.1016/j.proci.2020.05.011.

[401] C. Li, Y.-T.T. Liao, J.S. T'ien, D.L. Urban, P. Ferkul, S. Olson, G.A. Ruff, J. Easton, Transient flame growth and spread processes over a large solid fabric in concurrent low-speed flows in microgravity - Model versus experiment, Proc. Combust. Inst. 37 (2018) 4163–4171. doi:10.1016/j.proci.2018.05.168.

[402] S.L. Olson, D.L. Urban, G.A. Ruff, P. V. Ferkul, B. Toth, C. Eigenbrod, F. Meyer, G. Jomaas, Concurrent Flame Spread Over Two-Sided Thick PMMA Slabs in Microgravity, Fire Technol. 56 (2020) 49–69. doi:10.1007/s10694-019-00863-3.

[403] Y. Nakamura, T. Kashiwagi, S.L. Olson, K. Nishizawa, O. Fujita, K. Ito, Two-sided ignition of a thin PMMA sheet in microgravity, Proc. Combust. Inst. ·. 30 (2005) 2319–2325. doi:10.1016/j.proci.2004.07.037.

[404] S. Bhattacharjee, R.A. Altenkirch, N. Srikantaiah, M. Vedha-Nayagam, A theoretical description of flame spreading over solid combustibles in a quiescent environment at zero gravity, Combust. Sci. Technol. 69 (1990) 1–15. doi:10.1080/00102209008951599.

[405] D.B. Bullard, L. Tang, R.A. Altenkirch, S. Bhattacharjee, Unsteady flame spread over solid fuels in microgravity, Adv. Sp. Res. 13 (1993) 171–184. doi:10.1016/0273-1177(93)90369-M.

[406] P. V. Ferkul, J.S. T'ien, A model of low-speed concurrent flow flame spread over a thin fuel, Combust. Sci. Technol. 99 (1994) 345–370. doi:10.1080/00102209408935440.

[407] J. West, S. Bhattacharjee, R.A. Altenkirch, Surface Radiation Effects on Flame Spread Over Thermally Thick Fuels in an Opposing Flow, J. Heat Transfer. 116 (1994) 646–651. http://dx.doi.org/10.1115/1.2910918.

[408] W. Fan, J. Xi, Numerical Simulation of Microgravity Flame Spread Over Solid Combustibles, J. Therm. Sci. 4 (1994) 141–149.

[409] M.A. Delichatsios, R.A. Altenkirch, M.F. Bundy, S. Bhattacharjee, L. Tang, K. Sacksteder, Creeping flame spread along fuel cylinders in forced and natural flows and microgravity, Proc. Combust. Inst. 28 (2000) 2835–2842. doi:10.1016/S0082-0784(00)80706-7.

[410] W. Du, W. Hu, Effect of ambient pressure and radiation reabsorption of atmosphere on the flame spreading over thermally thin combustibles in microgravity, Sci. China, Ser. E Technol. Sci. 46 (2003) 381–390. doi:10.1360/02ye0366.

[411] S. Bhattacharjee, K. Dong, A numerical investigation of radiation feedback in different regimes of opposed flow flame spread, Int. J. Heat Mass Transf. 150 (2020) 119358. doi:10.1016/j.ijheatmasstransfer.2020.119358.

[412] S. Olson, O. Fujita, M. Kikuchi, T. Kashiwagi, Quantitative infrared image analysis of simultaneous upstream and downstream microgravity flame spread over thermally thin cellulose fuel in low speed forced flow, Combust. Flame. 227 (2021) 402–420. doi:10.1016/j.combustflame.2021.01.011.

[413] J.M. Tizón, J.J. Salvá, A. Liñán, Wind-aided flame spread under oblique forced flow, Combust. Flame. 119 (1999) 41–55. doi:10.1016/S0010-2180(99)00038-3.

[414] C. Kumar, A. Kumar, On the role of radiation and dimensionality in predicting flow

opposed flame spread over thin fuels, Combust. Theory Model. 16 (2012) 537–569. doi:10.1080/13647830.2011.642003.

[415] S.Y. Hsu, J.S. T'ien, Effect of chemical kinetics on concurrent-flow flame spread over solids: A comparison between buoyant flow and forced flow cases, Combust. Sci. Technol. 183 (2011) 390–407. doi:10.1080/00102202.2010.516288.

[416] F.C. Duh, C.H. Chen, A Theory for Downward Flame Spread Over a Thermally-Thin Fuel, Combust. Sci. Technol. 77 (1991) 291–305. doi:10.1080/00102209108951732.

[417] J. West, S. Bhattacharjee, R.A. Altenkirch, A comparison of the roles played by natural and forced convection in opposed-flow flame spreading, Combust. Sci. Technol. 83 (1992) 233–244. doi:10.1080/00102209208951834.

[418] Y. Nakamura, T. Kashiwagi, K.B. McGrattan, H.R. Baum, Enclosure effects on flame spread over solid fuels in microgravity, Combust. Flame. 130 (2002) 307–321. doi:10.1016/S0010-2180(02)00381-4.

[419] J.H. Park, J. Brucker, R. Seballos, B. Kwon, Y.T.T. Liao, Concurrent flame spread over discrete thin fuels, Combust. Flame. 191 (2018) 116–125. doi:10.1016/j.combustflame.2018.01.008.

[420] J.S. Goldmeer, J.S. T'ien, D.L. Urban, Combustion and extinction of PMMA cylinders during depressurization in low-gravity, Fire Saf. J. 32 (1999) 61–88. doi:10.1016/S0379-7112(98)00017-4.

[421] K. Kumar MN, A. Kumar, The dynamics of near limit self-propagating flame over thin solid fuels in microgravity, Proc. Combust. Inst. 36 (2017) 3081–3087. doi:10.1016/j.proci.2016.06.154.

[422] P. Kumar B., A. Kumar, A. Karpov, Near limit flame spread over thin solid fuels in a low convective microgravity environment, Proc. Combust. Inst. 37 (2019) 3825–3832. doi:.1037//0033-2909.I26.1.78.

[423] S.S. Dosanjh, P.J. Pagni, A.C. Fernandez-Pello, Forced cocurrent smoldering combustion, Combust. Flame. 68 (1987) 131–142. doi:10.1016/0010-2180(87)90052-6.

[424] G. Rein, A. Bar-Ilan, A.C. Fernandez-Pello, J.L. Ellzey, J.L. Torero, D.L. Urban, Modeling of one-dimensional smoldering of polyurethane in microgravity conditions, Proc. Combust. Inst. 30 (2005) 2327–2334. doi:10.1016/j.proci.2004.08.150.

[425] G. Rein, A.C. Fernandez-Pello, D.L. Urban, Computational model of forward and opposed smoldering combustion in microgravity, Proc. Combust. Inst. 31 II (2007) 2677–2684. doi:10.1016/j.proci.2006.08.047.

[426] Z. Lu, Y. Dong, Fingering instability in forward smolder combustion, Combust. Theory Model. 15 (2011) 795–815. doi:10.1080/13647830.2011.564658.

[427] C.R. Kaplan, E.S. Oran, K. Kailasanath, H.D. Ross, Gravitational effects on sooting diffusion flames, Symp. Combust. 26 (1996) 1301–1309. doi:10.1016/S0082-0784(96)80348-1.

[428] G. Legros, A. Fuentes, S. Rouvreau, P. Joulain, B. Porterie, J.L. Torero, Transport mechanisms controlling soot production inside a non-buoyant laminar diffusion flame, Proc. Combust. Inst. 32 (2009) 2461–2470. doi:10.1016/j.proci.2008.06.179.

[429] G. Legros, J.L. Torero, Phenomenological model of soot production inside a non-

buoyant laminar diffusion flame, Proc. Combust. Inst. 35 (2015) 2545–2553. doi:10.1016/j.proci.2014.05.038.

[430] A. Guibaud, J.M. Citerne, J.L. Consalvi, G. Legros, On the effects of opposed flow conditions on non-buoyant flames spreading over polyethylene-coated wires – Part II: Soot oxidation quenching and smoke release, Combust. Flame. 221 (2020) 544–551. doi:10.1016/j.combustflame.2020.08.038.

[431] D.P. Stocker, S.L. Olson, D.L. Urban, J.L. Torero, D.C. Walther, A.C. Fernandez-Pello, Small-scale smoldering combustion experiments in microgravity, in: Twenty-Sixth Symp. Combust. Combust. Inst., The Combustion Institute, Pittsburgh, PA, 1997: pp. 1361–1368.

[432] S.L. Olson, P. V. Ferkul, S. Bhattacharjee, C. Fernandez-Pello, S. Link, J.S. T'ien, I. Wichman, Results from on-board CSA-CP and CDM sensor readings during the burning and suppression of solids - II (BASS-II) experiment in the Microgravity Science Glovebox (MSG), in: 45th Int. Conf. Environ. Syst., Bellevue, Washington, 2015.

[433] X. Huang, S. Link, A. Rodriguez, M. Thomsen, S. Olson, P. Ferkul, C. Fernandez-Pello, Transition from opposed flame spread to fuel regression and blow off: Effect of flow, atmosphere, and microgravity, Proc. Combust. Inst. 37 (2019) 4117–4126. doi:10.1016/j.proci.2018.06.022.

APPENDIX A

Platform	Name	Rig	Test time [s]	Specimen size	Sample area [cm^2]	Vol [L]	Ref
Droptower	NASA 2.2		2.2	10x11.5 cm	115	20	[182]
			2.2	5x15cm	75	20	[369]
			2.2	10 x 11.5 cm	115	20	[181]
			2.2	Outer ⌀ 0.953 cm, Inner ⌀ 0.635 cm x 14.5 cm e=.16 cm	13.81	25.5	[370]
			2.2		30.2	44.5	[196] [198]
			2.2	3 x 15 cm	45	44.5	[17] [197]
			2.2	5 cm x7.5cm	37.5	45	[371]
			2.2	5x15 cm	75	113	[18] [372]
	NASA 5.18		5.18		30.2	1.2	[196] [198]
			5.18	3 x 15 cm	45	1.2	[17]
			5.18	5x10 cm	50	1.5	[373]
			5.18	5x15 cm	75	20	[369]
			5.18	5.08x5.08 cm	25.8	100	[199]
			5.18	10 x 3 cm	30	113	[374] [278]
			5.18	30 x 5 cm	150	113	[180]
			5.18	5 x 0.5 or 1 cm	5	113	[227]
	NASA 5.18 + DROP Bus		5.18	5x15 cm	75	299	[174] [173]
	JAMIC		10	e = 0.15 mm 200 mm	0.9	1	[359] [375]
			10	10x8.7cm	87	1.38	[30] [167]
			10	14x7.5 cm	105	3.5	[167] [376]
			10	9.5 x 5.6 cm	53.2	5.9	[189]
			10	100 mm x Core, e = 0.5 mm, PE, e = 0.075 & 0.15 mm	7.5	19.63	[377]
	MGLAB		4.5	140 x 50 mm	70	1.47	[172]
			4.5	9.5 x 5.6 cm	53.2	5.45	[189] [378]
			4.5	70 mm x e=0.15mm	0.32	5.47	[351,379–381]
			4.5	60x10 mm	6	6	[324]
			4.5	60xW=5, 10, 20 mm	12	7	[119]
			4.5	80x10 mm	8	10.6	[192]
			4.5	6x1cm	6	10.65	[28]
			4.5	200 mm x Core ⌀ 0.5 mm PE e = 1.5mm	21.2	33.8	[382]
			4.5	30x10 mm	3	175	[324]
	HASTIC		3	70 mm x e=0.15mm	0.32	5.47	[351]
	COSMOTORRE		2.7	70 mm x e=0.15 mm, 0.75 mm	0.32	1.38	[379] [380]
			2.7	6 x 6mm	0.36	1.38	[33]
	ZARM		4.7	50x50 mm	25	28	[19,20,255]
	Key Laboratory of Microgravity China		3.6	5x14 cm	70	2.25	[121]
			3.6	50 x e = 0.075 mm	2.87	3.15	[212]

				Core ⌀ =1 mm			
			3.5	50 mm x e=0.075 mm	0.11	5.62	[34]
			3.6	⌀ 3mm sphere	0.07	27	[184]
	Drop system		2.3	⌀ 5, 8 & 10 mm	0.01	98	[154]
Parabolic flight	KC-135	FIST	25	30x30x10 mm	9	6.5	[65] [254]
		Chamber	8	5x20 cm	100	22	[29] [383]
			20	60 x ⌀ 6 or 4 mm	3.6	25	[86,194,384,385]
			20	60 x ⌀ 4mm Flat: 60x12 mm	2.4 & 7.2	25	[384]
			20	20x8 cm	160	25.8	[386]
			20	8 x 7 cm	54	26	[98]
		GIFFT	20	12 cm x 1 or 2cm	24	27	[102] [101]
		Small FIST	25	40x40mm	160	36	[31]
			12	5x20 cm	100	65	[29]
			20	⌀ 2 – 6.4 mm	0.32	24.5	[183]
	DC.9		20	⌀ 2 – 6.4 mm	0.32	24.5	[183]
	Learjet	SSCE Chamber	15	100x30 mm	30	39	[387]
	DAS		22	20 cm x Cu wire ⌀ 0.5 mm	3	0.7	[22]
			22	9x2 cm 100 mm x NiCr e= 0.8 mm	18	2.54	[21,27]
			22	40x20 mm	8	3.62	[388]
			20	9.5 x 5.6 cm	53.2	5.9	[189]
			22	130 mm x e = 0.75 & 1.65 mm	6.44	7.84	[389]
			22	6x1cm	6	10.65	[28]
		FIRE WIRE	20	13 cm, e=0.3mm	1.17	33.8	[390]
			22	80x20 mm	16	35	[195,241,243,244]
	Carevelle		22	60 x ⌀ 6 mm	3.6	25	[86,194]
	CNES	DIAMONDS	20	13 cm, e=0.3mm	1.17	26	[390,391]
			20	12 cm x Core ⌀ 0.5 mm PE e = 0.3 mm	1.32	26	[175,177,178,225,392]
			20	50x50x10mm	25	28	[19,20,255]
Rockets	REXUS		2017	Ø 15 mm		0.36	[88]
	DARTFire		360	50x50x10 mm	25	1.5	[120]
	Minitexus 6		180	60x50x10 mm	30	5.6	[20,156]
	MiniTexus 3		180	140 x ⌀ 6mm	25.2	6	[86,155]
	TEXUS-38		2000	80 x ⌀ 6mm,	14.4	7.53	[157]
Satellite	SJ-8		3000	100 mm x e=0.1mm	0.3	5.79	[163,213]
			3000	⌀150 x170 mm	255	7.95	[393]
	SJ-10			40 mm x e=0.2 to 0.5 mm	0.6	1L tunnel x8 in 39 L chamber	[213]
			120	61.6 x 50 x 10 mm L = 69 mm x ⌀ 10 mm	30.8	8 flow tunnels (95 x95x 120 mm or 1L) in a 39 L chamber	[145,221,394]
Spacecraft	BASS-II			90x20mm 57.2 mm x ⌀ 6.4, 9.5 &12.7 mm	18	0.98	[70,80,114,170,171,226,395]

	BASS-II		250	⌀ 6.35 x 59 mm	3.7	0.98	[82]
	BASS			⌀ 2 cm	3.14	0.98	[353]
	USMP-3			10x4cm	40	1.2	[396]
	MIR			10x4cm 100 x ⌀ 7 mm	40	1.2	[7]
	USMP-3			10 x 8.7 cm	87	1.4	[133]
	STS-75 USMP-3 Space shuttle			10x4 cm	40	1.4	[166,167]
	USMP			10x8.7cm	87	1.4	[167]
	STS			12 x ⌀ 5 mm	0.6	1.52	[3]
	MIR			60 x ⌀ 4-5 mm	3	3.8	[83]
	USML-1			110 mm x e = 0.375 mm	1.23	3.9	[397]
	USML-1 glovebox		2400	80 mm x ⌀ 50 mm	40	4.5	[398]
	USML-1		2400	80 mm x ⌀ 50 mm	40	4.5	[398]
	USML		3000	140 mm x ⌀ 132 mm	184.8	21.7	[223,224,399]
	CYGNUS		1000	5 x 29 cm, 41 x 94 cm	3894	121	[79,400–402]
	MIR		300	12 x ⌀ 5 mm	0.6	8	[3,7]
	SKYLAB			6.67x9.2 cm	61.4	22	[15]
	SSCE		70	10 x 3 cm	30	39	[165] [90] [91]
	SSCE		510	25.4 x 6.35 mm	1.61	39	[57,92]
	MWT				400	16	
	SCEM (FLARE)				48	30	
	SOFIE				150	6	

APPENDIX B

PILOTED IGNITION

ref.	year	Goal	Parameters	thermal behaviour	sample type	material type	Specimen size cm2, or cm	Scale time [s]	Rig/facility	Chamber vol. size	Diagnostics,	Comments
[14]	1966	**Experimental** Time to ignition, species	μG &1G			Paraffin (paraffin-asbestos),neoprene, Teflon, polyester, black foam rubber, epon 828, ERB ph film, silicone O-ring, nylon cord, match, tygon, phenol, paper bleached (cellulosic)			KC-135	22 L		Ni-Cr wire
[29]	1968	**Experimental** Flame spread, time to ignition, heat transfer (solid-phase temperature)	Gravity level, forced flow, quiescent, oxygen concentration, pressure, diluent	thin	flat	Cotton cloth strips (MIL-C-5646C)	5x20 cm		KC-135 & Centrifuge	65 L	Camera	
[383]	1969	**Experimental** Ignition temperature	Gravity (>1G), ambient pressure, diluent gas	thin	Rod	Cotton cloth strips	5x20 cm		KC-135 & Centrifuge	65 L	Video imaging	Hot wire
[398]	1997	**Piloted ignition smouldering** Temperature, gas analysis	Gravity, forced flow, ignition type (axial, plate)		cylinder	Open-cell Flexible polyurethane	80 mm x ⌀ 50 mm	2400	on the USML-1	Spacelab Glovebox, 0.15 x 0.15 x 0.2 m 4.5 L	thermocouples	Ni-Cr igniter
[31]	**2001**	**Ignition delay time over thick fuels** Ignition delay time, heat transfer (temp.), critical pyrolysate mass flux	Opposed flow, radiative heat, normal gravity and microgravity	Thick	Flat slab	PMMA and PP/GL	40x40x12.7 mm	20	Parabolic KC-135	Small FIST (36 L)	Video imaging	Pilot flame
[251]	**2003**	**Theoretical prediction** Ignition delay time, critical heat flux, heat and mass transfer	Opposed flow, radiative heat, normal gravity and microgravity	Thick	Flat	PMMA and PP/GL	40x40x12.7 mm		Parabolic KC-135	Small FIST (36 L)		Pilot flame, only solid phase

[403]	**2005**	**Two-sided ignition of thin fuel** Piloted ignition, fuel mass fraction, gas-phase temperature, oxygen mass flux, fuel mass fraction	Sample thickness			PMMA	12 x 16 cm e = 0.2 mm & 0.4 mm		JAMIC	3.46 L	Video imaging	CO_2 laser
[35]	**2015**	**Role of pressure and gravity** Ignition delay time, pyrolysis fuel mass flux, heat transfer, mass transfer	Gravity, pressure, radiative heat, flow	thick		PMMA	30x30x10 mm					Pilot flame
[82]	**2017**	**Experimental over rods** Ignition delay time	Oxygen concentration, forced flow		Rod	PMMA	(⌀ 6.35 to 12.7 mm)	250	BASS-II	Microgravity Science Glovebox (MSG) on ISS (7.6x7.6x17cm). 0.98 L	Video camera	Hot wire pyrolysis
[111]	**2019**	**Experimental, effect of forced flow direction** Ignition delay time	Oxygen Concentration, forced flow, oppose, concurrent, ambient pressure	Thin	Flat slab	Kimwipe	5x10 cm	2	5.18 NASA, droptower		Color video Imag.	Kanthal wire
[373]	**2019**	**Experimental laser piloted ignition** Ignition delay time, ignitability limit	Heat flux, forced flow, sample thickness, wire core (cupper and stainless steel), oxygen concertation, normal gravity and microgravity		Wire jacket	Black Polyethylene PE	13 cm x e 1.62, 0.75 mm	20	DAS	300mm x ⌀ 80 mm 1.5 L	Camera	Laser-induced spark ignition
[390]	**2020**	**Experimental ignition over wires** heat transfer , pre-heat lengths	Sample core (NiCr, Cu), applied heat, oxygen concentration		Wire jacket	Low density PE	13 cm, e=0.3mm	20	Parabolic flight CNES DAS	DIAMONDS 26 L FIRE WIRE 26 x 26 x 50 cm 33.8L	CCD Camera Video camera	How wire

SPONTANEOUS IGNITION

Surface

Problem	ref.	year	Goal	Parameters	thermal behaviour	sample type	material type	Specimen size cm2, or cm	Scale time [s]	Rig/facility	Chamber vol. size	Diagnostics,	Comments
Transient	[30]	1996	**Effect of forced flow on localised ignition and transition to flaming** Ignition delay time	Forced flow, oxygen concentration	0.00385 g/cm2	Flat sample	Ashless filter paper	10x8.7cm	4	Droptower	10 s droptower JAMIC (3 tests), 8.5 x 9.5 x 17.1 cm 1.38 L	Camera	Tungsten-halogen lamps
Transient	[189]	2000	**Experimental radiative ignition** Ignition delay time, heat transfer	Oxygen concentration, ambient pressure	0.2 mm	Flat sample	Filter paper (advantec), 93 g/mm^2	9.5 x 5.6 cm	3	JAMIC drop tower (10s), MGLAB drop tower (5s), Parabolic flight DAS	5.9 L	IR camera, interferometry	CO$_2$ laser ignition
Transient	[167]	2001	**Spot radiative ignition** Ignition delay time	Forced flow, oxygen concentration	0.00385 g/cm2	Flat sample	Ashless filter paper	10x8.7cm	4	USMP / Droptower	Glovebox (85x95x171mm or 1.4 L) USMP-3 STS-75 Space Shuttle mission. And 10 s droptower JAMIC (3 tests) 1.38 L	Camera	Tungsten-halogen lamps
Transient	[378]	2005	**Laser ignition: effect of incident angle** Ignition delay time	ignition system, applied heat, Incident angle,	0.2 mm	Flat sample	Filter paper (advantec), 93 g/mm^2 coated with carbon black	9.5 x 5.6 cm	4	MGLAB	230 x 140 x 170 mm 5.45 L	Video imaging	CO$_2$ laser, near-infrared laser
Transient	[36]	**2013**	**Numerical localised ignition** Time to ignition, minimum ignition energy, heat and mass transfer, reaction rates	Applied heat, sample thickness, gravity, forced flow	9 mg/cm2	Flat	1:1 (cellulose and inert						

Conduction (solid-phase)

Sub-topic	ref.	year	Goal	Parameters	thermal behaviour	sample type	material type	Specimen size cm2, or cm	Scale time [s]	Rig/facility	Chamber vol. size	Diagnostics,	Comments
Conductive (solid surface)	[32]	2000	**Effect of oxygen and gravity** Heat transfer , mass transfer, time to ignition,	Gravity, oxygen Concentration		Flat			0.4				
	[351]	2008	**Experimental ignition due to excess current** Ignition delay time, ignitability limit	Electric current oxygen concentration, ambient pressure, nickel-chrome, normal gravity and microgravity		Wire Jacket	Polyethylene,	70 mm x e=0.15mm	4	Droptower 3s HASTIC & MGLAB 4.5	23 x 14 x17 cm 5.47 L	Video imaging	Current
	[163]	2008	**Pyrolysis temperature** Heat transfer	Current overload, Current, silver-gilt copper wire		Wire jacket	Polytetrafluoroethylene (PTFE)	100 mm x e=0.1mm	3000	Satellite SJ-8	45 x ⌀ 32 cm 5.79 L	Video, thermocouple	Pre-pyrolysis
	[379]	2013	**Overloaded wire: ignitability limits** Ignitability limits, ignition delay time, heat transfer , mass transfer	Excess current, oxygen concentration, sample thickness		Wire jacket	Polyethylene nickel–chrome core wire	70 mm x e=0.15 mm, 0.75 mm		Droptowers: MGLAB, COSMOTORRE in Hokkaido (2.7 s)	23 x 14 x17 cm 5.47 L 1.38 L (COSMOTORRE)	Video camera	Current
	[381]	2011	**Ignition under short excess electric current** Ignition delay time, minimum ignition energy, ignitability map	Electric current, oxygen concentration, nickel-chrome, normal gravity and microgravity		Wire Jacket	Polyethylene	70 mm x e=0.15mm	4	MGLAB	23 x 14 x17 cm 5.47 L	Video imaging	Current
	[380]	2017	**Numerical and experimental ignition due excess electric current** Ignitability limits, ignition delay time, heat transfer , mass transfer, minimum energy	Excess current, oxygen concentration, sample thickness		Wire jacket	Polyethylene nickel–chrome core wire	70 mm x e= 0.15 mm, 0.75 mm		Droptowers: MGLAB, COSMOTORRE	23 x 14 x17 cm 5.47 L 1.38 L (COSMOTORRE)	Video camera	Current
	[33]	2018	**Ignition due to hot surrounding environment** Heat transfer, ignition delay time,	Heated air, normal gravity and microgravity	thin	Flat plate	Polyethylene e = 0.03 mm	6 x 6, 5 x 5, 4 x4 mm		COSMOTORRE Drop tower, 3 s	44 x ⌀ 20 cm 1.38 L	CCD, thermocouple.	Hot environment

			ignitability										
	[213]	2019	**Ignition of overloaded wires** Heat transfer, bubbling jet behaviour	Current, silver-gilt copper wire,		Wire jacket	Polytetrafluoroethylene (PTFE)	100 mm x e=0.1 mm		Satellite SJ-8	45 x ⌀ 32 cm 5.79 L	CCD, laser extinction imaging (smoke), thermocouples	Current
				material type, current, pressure, Crome-Niquel		Wire jacket	PE, PTFE, PVC	40 mm x e=0.2 to 0.5 mm		Satellite SJ-10	8 flow tunnels (95 x95x120 mm or 1L) in a 39 L chamber		
	[34]	2020	**Effect of forced flow on ignition** Ignition delay time, heat transfer	Forced flow, current 1g-microg, Ni-chrome core, normal and microgravity		Wire jacket	Fluorinated Ethylene Propylene	50 mm x e=0.075 mm	2.2	NML Beijing droptower , 3.5 s	15 x 15 x 25 cm 5.62 L	Video, laser extinction imaging (smoke), thermocouples	Current
solid (smoulde													

Transition to flaming

Sub-topic	**ref.**	**year**	**Goal**	**Parameters**	**thermal behaviour**	**sample type**	**material type**	**Specimen size cm2, or cm**	**Scale time [s]**	**Rig/facility**	**Chamber vol. size**	**Diagnostics,**	**Comments**
Flaming	[132]	1994	**Ignition and transition to flaming over a thin fuel** Velocity vector, gas-phase temperature, reaction rate, solid-phase temperature, flame structure, heat flux (energy balance), transition limit	Quiescent, oxygen concentration,	Thin, 0.0046 m, 0.6 g/cm^3	Flat	Cellulosic						External radiation (spontaneous)
	[372]	1996	**Ignition and transition to flaming: effect of forced flow** Reaction rate, flame spread, flame structure, heat flux, transition time	Forced flow, quiescent, simultaneous flame spread	1.998 x 10_3 g/cm^2	Flat	Kimwipe	5 x 15 cm	2	2.2 s droptower NASA		Video	External radiation (spontaneous)

			to steady flame										
	[30]	1996	**Effect of forced flow on localised ignition and transition to flaming** Ignition delay time, transition, char front histories	Forced flow, oxygen concentration	0.00385 g/cm^2	Flat sample	Ashless filter paper	10x8.7cm	4	10 s droptower JAMIC (3 tests)	,8.5 x 9.5 x 17.1 cm 1.38 L	Camera	Tungsten-halogen lamps (spontaneous)
	[349]	2003	**Numerical ignition and transition to opposed forced flow** Ignition delay time, opposed Flame spread, mass transfer, heat transfer, near-limit	Fuel thickness, , gravity level, incident heat flux, oxygen concentration	Thin 0.0196cm	Vertical flat sample							Spontaneous
Smouldering													

APPENDIX C

FLAME SPREAD

NO FORCED FLOW

Sub-topic	ref.	year	Goal	Parameters	thermal behaviour	sample type	material type	Specimen size	Scale time [s]	Rig/facility	Chamber vol. size	Diagnostics	Comments
Quiescent	[13]	1966	**Experimental** Flame spread	µG &1G, oxygen concentration, ambient pressure	?	Cylindrical, threaded over steel or ceramic mandrel	Styrene, foam rubber, paraffin, neoprene, silicone rubber, teflon, polyurethane, dracon-wrapped polyurethane			KC-135 (12 s)	22 L	Camera	
	[29]	1968	**Experimental** Flame spread horizontal	Gravity level, forced flow, quiescent, oxygen concentration, pressure, diluent	thin	Flat	Cotton cloth strips (MIL-C-5646C)	5x20 cm		KC-135 & Centrifuge	65 L	Camera	
	[196]	1974	**Experimental** Flame spread	Oxygen concentration, pressure, sample thickness	thin	Flat	Cellulose acetate	30.2 cm^2 x e=0.025, 0.051, 0.0122		2.2 & 5.18 drop tower	44. 5 L & 1.2 L	Camera	
	[15]	1974	**Experimental** Flame spread	65% Oxygen concentration, 5.2 psia pressure, sample distance (discrete)	Thin/thick	Cylindrical, threaded over steel or ceramic mandrel	Aluminized mylar	6.67x9.2 cm, e=0.0076 mm		SKYLAB	22 L	Camera	
							nylon sheet	2.54x2.54 cm, e=3.175 mm					
							neoprene coated nylon fabric	6.67x9.2 cm					
							polyurethane foam	0.635x0.635cm e=50.8 mm					
							bleached cellulose paper	6.67x9.2 cm e=0.23mm					
							Teflon fabric	6.67x9.2 cm					
							parallel pieces of paper	6.67x9.2 cm e=0.23mm					

							(cellulosic)						
						Cylindrical, threaded over steel or ceramic mandrel	Dacron thread, neoprene rubber foamed, neoprene rubber tubing, paraffin, polyurethane rubber, silicone rubber, styrene plastic, Teflon tubing.			KC-135	22 L		
	[198]	1976	**Experimental** Flame spread	Oxygen concentration, pressure, diluent gas, sample thickness		Flat	Cellulose acetate	30.2 cm^2 x e=0.025, 0.051, 0.0122		2.2 s & 5.18 s droptower	44. 5 L & 1.2 L	Camera	
	[199]	1987	**Experimental** Flame spread	Oxygen concentration, pressure		Flat	Velcro: Nomex pile, Nomex hook, , Nylon pile, Nylon hook	5.08x5.08 cm		5.18 s droptower	100 L	Camera	
	[384,385]	1988 1989	**Experimental flame spread** Flame spread	Oxygen concentration, ambient pressure	Thick	Cylinder, flat	PMMA	60 x ⌀ 4 mm (⌀ 2 hole) & 60 x 12 mm x e = 2 mm		KC-135	Combustion chamber 25 L	Camera, IR camera	
	[86,194]	1999	**Experimental flame spread** Flame spread	Gravity level, oxygen concentration	Thick	Cylinder	PMMA	60 x ⌀ 6 mm x e =2 to 0.2 mm		KC-135 and ESA Caravelle	Combustion chamber 25 L	Camera, IR camera	
	[7]	1999	**Experimental and numerical results from MIR tests** Flame spread, flame geometry (height, diameter), gas-phase temperature, flame structure, consumption rate	Wick diameter, candle diameter, wick length, oxygen concentration		Cylinder	Candle (80% n-paraffin wax and 20% stearic acid)	⌀ 2 and 10 mm x 20 mm	300	MIR	CFM 8 L	Camera, thermocouples, radiometer	
	[404]	1990	**Theoretical model** Solid-phase temperature, gas-phase	Oxygen concentration, finite-rate or infinite-rate chemistry,	Thin	Flat	Cellulosic						No radiation

			temperature, velocity profile, flame spread, flame structure	atmospheres									into account
	[374]	1991	**Heat transfer from flame to solid** Flame spread, solid-phase temperature, density profiles, heat flux	Oxygen concentration	Thin	Flat	Ashless filter paper, 4.28 x 10~2 kg/m2 were	10 x 3 cm x 0.1632 mm		5.18 droptower	113 L	Camera, thermocouples	
	[93]	1991	**Effect of surface radiation** flame spread, flame structure, gas-phase temperature, fuel consumption rate, heat flux	Surface emittance, oxygen concentration, ambient pressure, oxygen concentration	Thin	Flat	cellulosic						Includes radiation
	[89]	1992	**Comparison theoretical & experimental** Solid-phase temperature, density profile, fuel consumption, heat flux, oxygen mass fraction, gas-phase temperature	Oxygen and pressure	Thin	Flat	Ashless filter paper	10 x 3 x 0.165 mm				Camera, thermocouples	
	[405]	1993	**Unsteady model for thick sample** Flame spread, gas-phase temperature, solid-phase temperature, density profile	Surface radiation, pressure	thick	Flat	PMMA					Camera, thermocouples	
	[387]	1994	**Flame experiments** Flame spread rate	Oxygen concentration	Thin	Flat	Ashless filter paper, laboratory wipers (cellulosic)	100x30 mm e=0.19mm, e=0.076mm	10-15	SSCE Combustion chamber on Learjet	39 L	Intensified array camera Xybion ISG-207, it is a charge injection device (CID)	
	[165]	1993	**Flame experimental results** Solid-phase & gas-phase temperature, heat flux	Oxygen concentration, pressure	Thin	Flat	Ashless filter paper	10 x 3 cm x 0.165 mm	70	SSCE apparatus	39 L	Camera, thermocouples	
	[90]	1995	**Experimental and numerical flame spread over thin solid** (solid-phase & gas-phase temperature, heat flux, flame structure	Oxygen concentration, pressure,	Thin	Flat	Ashless filter paper, 7 x 10-2 kg/m^2	3 x 11 x 0.01645 cm		SSCE apparatus	39 L	Camera, thermocouples	No soot model included
	[91]	1996	**Experimental and numerical Effect of**	Oxygen concentration,	Thin	Flat	Ashless filter paper	3 x 10 x		SSCE	39 L	Camera,	No

			ambient pressure Flame geometry, gas-phase temperature, solid-phase temperature, heat flux	pressure, radiation			, 7 x 10-2 kg/m^2	0.01645 cm		apparatus		thermocouples	radiation from soot,
	[57]	1996	**Experimental & Flame spread over thick fuel** flame spread, flame geometry	Oxygen concentration, pressure, radiation	Thick	Flat	PMMA	25.4 x 6.35 x 3.18 mm		SSCE apparatus	39 L	Camera, thermocouples	Radiation included
	[92]	1998	**Experiment flame spread over thick fuel** flame spread , gas-phase temperature, flame geometry	Oxygen concentration, pressure	Thick	Flat	PMMA	25.4 x 6.35 x 3.18 mm	510	SSCE apparatus	39 L	Camera, thermocouples	
	[359]	1998	**Experimental study on flame spread over wire** Flame spread	Wire diameters, oxygen concentration, wire temperature, wire diameter, ambient pressure, dilution gas,1G & µG		Wire	Ethylene-tetrafluoroethylene ETFE insulated wire. Wire ⌀ = 0.61, 0.7, 0.81 mm	e = 0.15 mm 200 mm		Chamber at JAMIC	157 L (set up) 1 L (Chamber)	Hi-8 video camera, still camera, thermocouple	
	[375]	2000	**Experimental study on flame spread over wire: effect of dilution gas on temperature.** Flame spread, gas-phase temperature, solid-phase temperature	Oxygen concentration, dilution gas,1G & µG		Wire	Ethylene-tetrafluoroethylene ETFE insulated wire. Wire ⌀ = 0.62	e = 0.15 mm 200 mm		Chamber at JAMIC	157 L (set up) 1 L (Chamber)	Hi-8 video camera, still camera, thermocouple	
	[3]	2000	**Experimental & numerical candle flames** Heat & mass transfer (temperature, oxygen and mass fraction, fuel vapour reaction rates) , flame geometry	Oxygen concentration, pressure, wick diameter, candle diameter	-	Candle	Candle (80% n-paraffin wax and 20% stearic acid)	⌀ 2 and 10 mm x 20 mm	300	STS & MIR	STS: 11.5x11.5x 11.5 cm (1.52 L) MIR: 20x20x 20 cm (8 L)	Video camera	
	[182]	2002	**Flame spread over thick fuel** Flame spread, heat transfer	Oxygen concentration, pressure, fuel thickness, diluents gases, 1 or 2 sided.	Thick	Flat	Polyphenolic foams	10x11.5 cm, e= 10 and variable mm	2.2	2.2 drop Tower	20 L	CCD camera, radiometer	

	[386]	2006	**<u>Fabric flammability and predicted skin burn</u>** Flame spread rate, flame heat flux, time to 2nd degree burn	1G and µG, gap between fabric and sensor, fabric type, oxygen concentration	thin	Flat	Lightweight cotton (144 g/m^2)	20x8 cm, e = 0.43 mm		KC-135	25.8 L	Video camera, infrared camera, heat flux gauge	
							heavy weight cotton (176 g/m^2)	20x8 cm, e = 0.74 mm					
							lightweight blend (129 g/m^2)	20x8 cm, e = 0.52 mm					
Droplet	[184]	2020	**<u>Droplet combustion</u>** Flame geometry (standoff), droplet diameter (mass loss), flame burning flux			Sphere	Polyethylene	⌀ 3mm		3.6s drop tower at NMLC	1 L	High speed camera	Could be used for m and HRR

FORCED FLOW

Parallel flow

Concurrent

Dim.	**ref.**	**year**	**Goal**	**Parameters**	**thermal behaviour**	**sample type**	**material type**	**Specimen size cm2, or cm**	**Scale time [s]**	**Rig/facility**	**Chamber vol. size**	**Diagnostics,**	**Comments**
2D	[95]	1994	**<u>Experimental, numerical and theoretical flame spread over a thin fuel</u>** Flame spread, flame geometry, consumption rate	Oxygen concentration and forced flow	Thin	Flat	Kimwipe (1mg/cm^2) (cellulosic)	4.9x10cm	5.2	5.18 drop tower	113 L	Camera	
2D	[406]	1994	**<u>Modelling flame spread over a thin fuel</u>** Gas-phase temperature, solid-phase temperature, heat flux, flame structure, flame geometry (stand-off, thickness) , solid-phase characteristic lengths (pyrolysis, pre-heat), fuel consumption rate	Oxygen concentration, forced flow	Thin	Flat	Cellulosic						
	[396]	1998	**<u>Preliminary findings from FFFT</u>**	Forced flow		Flat &	Cellulose flat sheets,	10x4cm		USMP-3	FFFT	Camera,	

			aboard USMP-2 Flame spread, solid-phase& gas-phase temperature, flame geometry (length)			cylinder	cast cylinders of cellulose			mission	1.2 L	thermocouple	
2D	[7]	1999	**Experimental and numerical results from MIR tests** Flame spread, flame geometry (height, diameter), gas-phase temperature, flame structure, consumption rate	Fuel density, oxygen concentration, 2 cm/s forced flow	Thin	Flat	Paper sheets.	10x4cm		MIR	FFFT 1.2 L		
2D	[83]	1999	**Preliminary results in SKOROST on MIR** Flame spread	Oxygen concentration, forced flow		Cylindrical	PMMA, PE, Delrin	60 x ⌀ 4-5 mm		SKOROST on MIR	150x80x320 mm or 3.8 L	Camera	
2D	[63]	2010	**Modelling for thin and thick fuels: steady, limiting length and transient growth** Flame structure, flame growth, solid-phase characteristic lengths (pyrolysis), heat flux	Sample thickness	Thick/thin	Flat	90% combustible 10% inert						
3D	[62]	2015	**Modelling for flame growth and near-limit** Solid-phase characteristic lengths (pyrolysis), gas-phase temperatures, reaction rate, flame structure	1G & μG	Thin	Flat	Fabric, 75% fabric 13.4 mg/cm2, 25% inert	e = 0.3175 mm					
3D	[114]	2016	**Experimental and numerical study for growth, spread and quenching** Flame spread, flame geometry (length), heat flux, HRR, radiative loss	Oxygen concentration, forced flows, sample width	thin	Flat	SIBAL	1.2x10 cm or 2.2x10 cm e=0.32 mm		ISS. BASS & BASS II	MSG (7.6x7.6x17cm) 0.98 L	Camera	
2D	[392]	2018	**Experimental Flame over wire insulation** Flame spread, flame geometry (length), heat flux, molten spread	Forced flow, oxygen concentration, core wire (Ni-Cr and Cu), 1G and G		Wire	Polyethylene	12 cm x Core ⌀ 0.5 mm PE e = 0.3 mm	22	CNES parabolic flight	DIAMONDS rig 26 L	Tri-CCD camera	
2-3 D	[400]	2020	**Numerical flame spread over thin fuel: effect of environment**	Forced flow, oxygen concentration and	Thin	Flat	SIBAL (18.02 mg/cm^2)	94 x 41 cm	460	Saffire I & II CYGNUS	6.6 L (Rig)	Video camera, Thermocouple,	Validation of model and

			conditions Flame spread, characteristic solid-heat length (pyrolysis), heat flux, mass burning rate, remaining mass fraction, gas-phase temperature, flame structure, flow profiles	pressure								radiometer	parametric study

Opposed

Dim.	ref.	year	Goal	Parameters	thermal behaviour	sample type	material type	Specimen size cm2, or cm	Scale time [s]	Rig/facility	Chamber vol. size	Diagnostics,	Comments
2D	[17]	1988	**Experimental near-limit flame spread over a thin fuels** Flame spread, sample thickness	Oxygen concentration , forced flows, sample thickness	Thin	flat	Kimwipe (1. 998 X 10^{-3} g/cm^2)	3 x 15 x 0.0076 cm		2.2 & 5.18 droptowers	44.5 L & 1.2 L	Camera, thermocouples	
2D	[384]	1988	**Experimental Flame spreading** Flame spread	Oxygen concentration, pressure	Thick	Flat & cylindrical	PMMA cylindrical and flat	60 x ⌀ 4mm & hole ⌀2mm. Flat: 60x12x2mm		KC-135	25 L	Camera	
2D	[67]	1990	**Numerical flame spread: effect of radiation (surface and gas-phase)** flame spread, heat flux, gas-phase temperatures	Forced flow, incident radiation	Thin	flat							No soot radiation
2D	[18]	1991	**Flame spread over a thin fuel: effect of oxygen and forced flow** Flame spread, solid-phase temperatures (surface), characteristic solid-phase length (pre-heat, pyrolysis)	Oxygen concentration, forced flow, thickness	Thin	flat	Kimwipe	5x15 cm e=0.0076 cm	2.2	2.2 drop tower	113 L	Camera, Thermocouples	
2D	[407]	1994	**Numerical flame spread over thick fuel: surface radiation effect** Flame spread, gas-phase	Oxygen concentration, ambient pressure, sample thickness,	thick	flat	PMMA						Evaluates radiation (no soot)

			temperature	surface radiation									
3D	[408]	1994	**Numerical flame spread over thin fuel** spread rate, gas-phase temperature, gas-phase velocity	Opposed forced flow, oxygen concentration, pressure	Thin	Flat	Cellulosic						
2D	[155]	1996	**Experimental flame spread** Flame spread	Forced flow		Cylinder	Hollow cylinder	Two cylinders: 140 x ⌀ 6mm, e= 2mm		MiniTexus 3	MiniTexus 6 L		
2D	[7]	1999	**Experimental and numerical results from MIR tests** Flame spread, flame geometry (height, diameter), gas-phase temperature, flame structure, consumption rate	Forced flow		Cylinder	Paper cylinder	100 x ⌀ 7 mm x ID=3mm, ⌀ 12 x ID=8 mm (half is solid)		MIR	OFFS 1.2 L		
2D	[86]	1999	**Experimental flame spread** Flame spread	Oxygen concentration, forced flow, Sample thickness		Cylinder	PMMA	Cylinder	60 x ⌀ 4 mm e= 2 & 0.2 mm,	NASA KC-135 and ESA Caravelle.	25 L	CCD camera	
									140 x ⌀ 6mm, e= 2 mm	MiniTexus 3	6 L		
2D	[157]	2000	**Experimental flame spread** Flame spread, heat transfer (gas & solid)	Forced flow		Cylinder	PMMA hollow cylinder	80 x ⌀ 6mm, e=2mm, ⌀ 6mm, e= 0.5mm		TEXUS-38	7.53 L	IR camera, Thermocouple	
2D	[409]	2000	**Semi-analytical expressions** Flame spread	Sample thickness, 1g & µG		Cylinder	PMMA						
2D	[324]	2000	**Experimental flame over thin fuel: effect of ambient** Flame spread	Forced flow, oxygen concentration, sample thickness, 1g & µG,	thin	Flat	PMMA	30x10mm (combustion chamber) &		MGLAB drop-tower	Combustion Chamber for quiescent (175	CCD camera	

				pressure				60x10mm (tunnel) e=0.015, 0.05, 0.125 mm			L.) Wind tunnel (6L)		
2D	[377]	2002	**Experimental flame spread over wire: effect of flow** Flame spread, characteristic solid-phase length (pre-heat), flame geometry (standoff), gas-phase temperature, heat flux	Sample thickness, forced flow, oxygen concentration		Wire	Polyethylene	100 mm x Core, e = 0.5 mm, PE, e = 0.075 & 0.15 mm		JAMIC	19.63 L	Camera, thermocouple	
2D	[410]	2004	**Numerical flame spread over thin fuel: effect of pressure and atmosphere (radiation reabsorption)** Flame spread, flame structure, gas-phase temperature, heat flux	Diluent gas, ambient pressure	thin								No soot
3D	[120]	2004	**Experimental flame spread over thick fuel:** Flame spread, mass loss, burning rate, flame geometry (stand-off, flame length), gas-phase temperature, heat flux	Oxygen concentration, forced flow, incident heat flux	Thick	Flat	Black cast PMMA	50x50x10mm	120	DARTFire,	two mirror-image flow tunnels (each 10x10x15cm or 1.5L)	UV video camera, radiometer	
2D	[325]	2005	**Semi-empirical prediction of flame spread and near-limit** Flame spread	Sample thickness, oxygen concentration, forced flow	thin	Flat	PMMA, cellulose						
3D	[65]	2007	**Modelling and experimental Flame spread over thick fuel: effect of forced flow and incident heat** Flame spread	Forced flow, incident heat flux, 1G µG	Thick	Flat	PMMA	30x30x10 mm		KC-135	Small FIST (28.5x19x12cm or 6.5 L)	IR camera	
3D	[254]	2007	**Modelling and experimental Flame spread over thick fuel: effect of forced flow and incident heat**	Forced flow, incident heat flux, 1G µG	Thick	Flat	PMMA, PPGL (Polypropylene glass fiber)	30x30x10 mm		KC-135	Small FIST (28.5x19x12cm or 6.5 L)	IR camera	

			Flame spread										
2D	[370]	2008	**Experimental Flame spread over tubes** Flame spread rate, flame geometry (length), characteristic, flame structure,	Pressure, forced flow		Cylindrical	PVC tubes	Outer ⌀ 0.953 cm, Inner ⌀ 0.635 cm x 14.5 cm e=.16 cm	2.2	2.2 s droptower	25.5 L	video camera	
2D	[118]	2011	**Correlations for flame geometry** Flame geometry (length, height), characteristic solid-phase length (pyrolysis)	Forced flow			PMMA						Close analytical correlations
2D	[193]	2016	**Determination of a critical flow velocity for radiative extinction** Flame spread, critical velocity	Forced flow, sample thickness	Thin	Flat	PMMA	e =0.1, 0.2, 0.3 & 0.4 mm	5	BASS-II	7.6 x 7.6 x 17 cm 0.98 L	CCD camera, radiometer	Critical velocity for radiative regime
2D	[80]	2016	**Comparison between theory and experiments: regimes of flame spread** Flame spread, flame structure	Oxygen concentration, forced flow, flame geometry	Thin	Flat	PMMA	90x20mm e=0.1 & 0.2 mm	5	BASS-II	7.6 x 7.6 x 17 cm 0.98 L	Camera, radiometer	
	[241]	2016	**Flammability limits (LOC): effect of ambient** Flame spread, characteristic solid-phase lengths (pre-heat), LOC & MLOC	Oxygen concentration, forced flow, gas diluent	Thin	Flat	PMMA	80x20x0.125mm	8	DAS	Rolling chamber 35 L	CCD, infrared camera	Similar to fuel dispenser
2D	[70]	2017	**Effect of boundary layer on flame behaviour** Flame spread, flame geometry (flame length)	Forced flow, sample thickness, entrance length (boundary layer)	thin	Flat	PMMA	100 mm x(10,20mm), e=0.1 , 0.2 & 0.3 µm	7	BASS-II	7.6 x 7.6 x 17 cm 0.98 L	Colour video camera, Radiometer	Boundary layer effect
2D	[171]	2018	**Experimental flame spread over cylinder** Flame spread	Oxygen concentration, forced flow		cylindrical	Black PMMA	57.2 mm x ⌀ 6.4, 9.5 &12.7 mm	100 - 500	BASS-II	MSG Glovebox 7.6 x 7.6 x 17 cm 0.98 L	Camera, radiometer	
2D	[221]	2019	**Experimental flame spread over**	Oxygen concentration,	Thick	Flat	PMMA	61.6 x 50 x 10	55	SJ-10	4 tunnels (12	CCD camera, RGB	

			thick samples Flame spread, flame geometry (stand-off distance, inclination angle), gas-phase temperature, flamelet, heat flux	forced flow				mm			cm x 9.5 x 9.5 or 1L) in chamber 39 L	pyrometry	
2D	[226]	2020	**Experimental and numerical: radiation from flame** flame geometry (flame area), heat transfer (flame radiation), burning rate, flame structure	Forced flow, oxygen concentration, sample width, sample thickness	Thin	Flat	PMMA	100 mm x e = 0.1, 0.2, 0.3 & 0.4 mm width = 1, 2 cm		BASS	7.6 x 7.6 x 17 cm 0.98 L	Camera, radiometer	FIAT Matlab code to analyse flames. No soot radiation
2D	[180]	2020	**Experimental flame spread over ultra-thin fuels** Flame spread, flame geometry (length), flame structure, burning rate	Sample density, forced flow, sample type	Ultra-thin	flat	Cellulosic paper (TENGU) , density = 0.2 to 13 mg/cm2 Cheesecloth	30 x 5 cm	1	5.18 Drop tower	113 L	Camera	Concurrent-opposed reversed phenomena
2D	[394]	2020	**Experimental flame spread over cylinder** Flame spread	Oxygen concentration, forced flow		Cylinder	PMMA	L = 69 mm x ⌀ 10 mm	2	SJ-10	4 tunnels (12 cm x 9.5 x 9.5 or 1 L) in chamber 39 L	Camera, thermocouples	
2D	[388]	2020	**Flame spread over wires** Dripping, flame spread, flame geometry (length), characteristic solid-phase length (pre-heat), heat transfer analysis	Forced flow, oxygen concentration, sample type	thick	flat	LDPE and HDPE	40 x 20 mm LDPE e= 1.5mm HDPE e= 2.5 mm	20	DAS	3.62 L	Camera, IR camera	
2D	[389]	2020	**Flame spread and near-limit over electric wires** Flame spread	1G & µG, incident heat flux, core diameter, sample colour (radiation absorption effect), 10 cm/s forced flow, 100 kPa		wire	Standard & black LDPE with Cu wire (⌀ 2.5 & 0.7 mm),	130 mm x e = 0.75 & 1.65 mm	20	DAS	39 x ⌀ 8 cm 7.84 L	Camera, IR camera	Oscillatory flames were observed
2D	[363]	2020	Radiation-kinetics interaction, flame geometry, flame spread,	Gravity, pressure, radiation, kinetics	Thin	Flat	PMMA						

2D	[411]	2020	**Numerical flame spread: radiation feedback (gas- and solid-phase)** Gas-phase temperature, flame structure, flame structure, vaporisation temperature, heat flux	Radiation effect (gas-phase, solid-phase)	thin	Flat	PMMA						No soot radiation
2D	[175]	2020	**Experimental evaluation of flame radiative feedback** Soot volume fraction, gas-phase temperature, soot radiative loss, radiative feedback from soot to solid	19% Oxygen concentration and 20 cm/s opposed forced flow		wire	LDPE coated Ni-Cr wire			Parabolic flight	DIAMONDS 26 L	Broadband Modulated Absorption/Emission technique	
2D	[176]	2020	**Method to assess Soot radiative feedback** Soot volume fraction, gas-phase temperature, radiative balance.	Opposed forced flow, pressure		Wire	LDPE coated Ni-Cr wire			Parabolic flight	DIAMONDS 26 L	Broadband Modulated Absorption Emission (BMAE) technique	
2D	[177]	2020	**Soot production and radiative heat transfer** Soot volume fraction, gas-phase temperature, flame geometry (stand-off distance, incident radiative heat flux, radiative neat flux	Opposed forced flow		wire	LDPE coated Ni-Cr wire			Parabolic flight	DIAMONDS 26 L	Broadband Modulated Absorption Emission (BMAE) technique	
2D	[178]	2020	**Soot production and radiative heat transfer: pressure effect** Soot volume fraction, spread rate, pyrolysis mass flow rate, radiation fraction, incident radiative flux.	Opposed Forced flow, ambient pressure		wire	LDPE coated Ni-Cr wire			Parabolic flight	DIAMONDS 26 L	Broadband Modulated Absorption Emission (BMAE) technique	
2D	[179]	2020	**Opposed flame spread rate and soot production** Flame spread rate, soot formation length, soot volume fraction, gas-phase temperature, formation rate	Opposed forced flow, oxygen concentration, ambient pressure		wire	LDPE coated Ni-Cr wire			Parabolic flight	DIAMONDS 26 L	Broadband Modulated Absorption Emission (BMAE) technique	

Flat plate case

Sub-topic	ref.	year	Goal	Parameters	thermal behaviour	sample type	material type	Specimen size cm2, or cm	Scale time [s]	Rig/facility	Chamber vol. size	Diagnostics,	Comments
Flat plate	[255]	1999	**Experimental characterisation of flame** Heat flux, flame geometry (length, stand-off)	Oxygen concentration, forced flow	thick	Flat	PMMA	50x50x10mm		ZARM droptower, CNES airbus	0.4x ⌀ 0.3m (28 L) in ZARM Droptower and CNES airbus A300	2 CCD cameras, 1 intensified high speed camera, Planar laser induced fluorescence system (Trace OH radicals) thermocouple	
	[156]	2000	**Experimental results** flame geometry (length, stand-off), flow dynamics, gas-phase & solid-phase temperatures	Forced flow	Thick	Flat	PMMA	60x50x10 mm	160	Minitexus 6	Combustion chamber 5.6 L	2 CCD camera, IR camera, thermocouple	
	[19]	2000	**Experimental results: flame geometry and stability of flame** Solid-phase temperature (surface), heat flux estimation, flame geometry (stand-off distance, flame length), extinction limits	Oxygen concentration, forced flow	Thick	Flat	PMMA	50x50x10mm		ZARM droptower, CNES airbus	0.4x ⌀ 0.3m (28 L) in ZARM Droptower and CNES airbus A300	2 CCD cameras, 1 intensified high speed camera, Planar laser induced fluorescence system (Trace OH radicals) thermocouple	
	[20]	2001	**Experimental results: flame geometry and stability of flame** Stability limits, extinction limits	Oxygen concentration, forced flow	Thick	Flat	PMMA	50x50x10mm		ZARM droptower, CNES airbus, & Minitexus 6	0.4x ⌀ 0.3m (28 L) in ZARM Droptower and CNES airbus A30 & Combustion chamber Minitexus 6 5.6 L		

Opposed and concurrent

Dim.	ref.	year	Goal	Parameters	thermal behaviour	sample type	material type	Specimen size cm2, or cm	Scale time [s]	Rig/facility	Chamber vol. size	Diagnostics,	Comments
2D	[397]	1994	**Wire insulation flammability experiment: USML-1 One year post mission summary** Flame spread, flame structure, gas-phase temperature, gas-phase characteristic length (flame length)	10 cm/s forced flow, flow direction (opposed and concurrent), 1G & µG, electrical power (1.27 to 1.75 W)			Polyethylene	110 mm x e = 0.375 mm, onto Ni-Cr wire (⌀ 0.75 mm)		USML-1 mission on the STS-50 mission	WIF GBX 3.9 L	Video, and still camera, thermocouple	
2D	[7]	1999	**Experimental and numerical results from MIR tests** Flame spread, flame geometry (height, diameter), gas-phase temperature, flame structure, consumption rate	Forced flow	Thin	Cylinder	PE	⌀ 1.5 mm		MIR	FFFT 1.2 L		
2D	[137]	2002	**Experimental flame spread: effect of radiation loss**	Forced flow, oxygen concentration, sample thickness	Thin	Flat	PMMA	60x10mm		MGLAB	6.5 L (forced flow) 4.2 L (quiescent)	Thermal camera, interferometry	
2D	[64]	2003	**Numerical flame spread and near-limit: comparison of opposed and concurrent over thin fuels** flame spread, solid-phase temperature, heat flux, flame geometry	Entrance length, forced flow, oxygen concentration,	Thin	flat	Kimwipe						No soot radiation
2D	[192]	2007	**Experimental flame spread: effect of ambient** Flame spread, heat loss	Oxygen concentration, diluent gas, forced flow	Thin	Flat	PMMA	8 0 x 10 x 0.125 mm	4.5	MGLAB	37 x 12 x 24 cm 10.6 L	CCD cameras, interferometer	
2D	[237]	2008	**Flame spread experiments: effect of environmental conditions** Flammability index (Ultem, Nomex and Mylar G), flame spread	Oxygen concentration, ambient pressure, forced flow (30 cm/s for Ultem, Nomex and Mylar G)	Thin	Flat	Ultem 1000	100x50x0.25 mm		5.13 Droptower	12.56 L	Camera	
							Nomex HT90-40	100x50x0.3 mm					
							Mylar G	100x50x0.13					

								mm					
							Kimwipes	100x50					
2D	[26]	2017	**Overview of results from Saffire II** Flame spread	Forced flow	Thin/thick	Flat	PMMA, PMMA-Nomex, PDMS, SIBAL	30 x 5 cm		Saffire II		Camera	

Simultaneous

ref.	year	Goal	Parameters	thermal behaviour	sample type	material type	Specimen size cm2, or cm	Scale time [s]	Rig/facility	Chamber vol. size	Diagnostics,	Comments
[197]	1970	**Experimental flame spread over thin fuels** Flame spread	Pressure, oxygen concentration, sample orientation, 1g &µG	Thin	Flat	Plastic (Cellulose acetate)	e=0.025 & e=0.051 mm		2.2 s droptower	44.5 L	High speed camera	
						Japanese tissue	e=0.05 mm					
						Silkspan paper	e=0.03mm					
						bond paper type III	e= 0.1mm					
[372]	1996	**Effect of ignition and forced flow on the transition to flame** Flame spread, flame structure, oxygen mass fraction, gas-phase reaction	Oxygen concentration, forced flows	Thin	Flat	Tissue paper (area* density 1.998x10^{-3} g/cm^2)	5x15cm		2.2 s drop tower	113 L		No radiation included in the model
[166]	2000	**Flame spread along free edges** Flame spread, flame structure, fuel mass fraction, heat flux, oxygen mass flux, gas-phase temperature, gas-phase reaction	Forced flow, 33% Oxygen concentration	Thin	Flat	Ashless filter paper (area* density 0.0077 g/cm^2)	10x4cm, e=0.017 cm		STS-75 USMP-3 Space shuttle	RITSI Glovebox 8.5x9.5x17.1mm 1.4 L		
[167]	2001	**Experimental of spot ignition and 3D flame spread** Flame spread, flame geometry (limiting angle), heat flux	Forced flow, oxygen concentration	Thin	Flat	Ashless filter paper	10x8.7cm		Glovebox) USMP-3 STS-75. And droptower JAMIC (3 tests)	8.5x9.5x17.1mm or 1.4 L JAMIC 3.5 L		
[376]	2002	**Numerical ignition and subsequent flame spread: effect of forced flow** Flame spread, flame structure, heat flux, oxygen mass fraction, fuel mass	Forced flow	Thin	Flat	Cellulosic sheet	14x7.5 cm		droptower JAMIC	12x16x18 cm or 3.5 L	Camera	

		fraction										
[412]	2021	**Experimental simultaneous flame spread: analysis of infrared imaging** flame spread, characteristic solid-phase temperatures (pre-heating, pyrolysis), heat flux balance	Force flow, oxygen concentration	Thin	Flat	Cellulose (area density 60 g/m^2)	75 x 140 mm		JAMIC	12x16x18 cm or 3.5 L	Camera, IR camera, thermocouples	

Non-parallel flow

Sub-topic	ref.	year	Goal	Parameters	thermal behaviour	sample type	material type	Specimen size cm2, or cm	Scale time [s]	Rig/facility	Chamber vol. size	Diagnostics,	Comments
Oblique	[155]	1996	**Experimental flame spread** Flame spread	Forced flow		Cylinder	Hollow cylinder	Two cylinders: 140 x ⌀ 6mm, e= 2mm		MiniTexus 3	MiniTexus 6 L		
	[413]	1999	**Flame spread under oblique force** Flame spread, flow structure, flame structure, spread limit , gas-phase temperature, oxygen mass fraction, fuel mass fraction, heat flux	Forced flow, oxygen concentration, radiation parameter, infinite/finite reaction rates	thick	Cylinder	PMMA						
Perpendicular	[354]	1998	**Flame spread and near-limit around a cylinder fuel** Flame geometry, gas-phase temperature, velocity profile, fuel reaction rate, surface temperature, burning rate, heat flux (gas-phase and radiative), flame geometry (stand-off distance)	Forced flow, heat flux into solid		cylinder	PMMA						No gas-phase radiation
	[353]	2020	**Flame growth and extinction around a spherical solid: effect of thickness** Heat transfer, flame geometry, Effect of solid in-depth	Forced flow	Thick	sphere	PMMA	⌀ 2 cm		BASS GEL (prep)	0.98 L	Camera	Limiting thickness

TANGENT ASPECTS

Sample size

Sub-topic		ref.	year	Goal	Parameters	thermal behaviour	sample type	material type	Specimen size cm2, or cm	Scale time [s]	Rig/facility	Chamber vol. size	Diagnostics,	Comments
Sample size	Quiescent	[356]	2020	**Numerical: effect of Le number on flame spread (width effect)** Flame structure, flame spread, instabilities, reaction rate, gas-phase temperature	Le number, sample width, oxygen concentration	Thin	Flat	Cellulosic						
	Concurrent	[134]	2000	**Ignition and transition to flame: effect of sample width** Flame spread, flame structure, gas-phase temperature, flow field, heat release rate (gas-phase reaction)	Sample width	Thin	Flat	cellulosic						
		[59]	2003	**Numerical flame spread over thin fuel: wall heat loss and oxygen side diffusion** Gas-phase temperature, flow profiles, flame spread, flame geometry, oxygen mass flux, solid-phase profiles	Forced flow, sample width, oxygen concentration, forced flow, tunnel insulation	Thin	flat	Cellulosic						
		[102]	2011	**Experimental and numerical upwards flame spread in 1g and µG** Flame spread, solid-phase profiles, solid-phase temperature, surface emittance	Gravity, forced flow, pressure, oxygen concentration, sample width	Thin	Flat	Cellulosic sample	12 cm x 1 or 2cm		5.3 droptower Parabolic flight KC-135	GIFFT 27 L	Video	
		[401]	2018	**Transient and steady flame spread over a large sample** Flow profile, characteristic solid-phase length (pyrolysis), solid-phase temperature, flow profile, oxygen mass flux, heat flux, mass fraction, burning rate	Sample width	Thin	Flat	SIBAL	5 x 29 cm, 41 x 94 cm		Saffire I & II	6.6 L (Rig)	Camera, thermocouple	Effect of flow profile
	Opposed	[119]	2009	**Flame spread over a thin fuel: effect of sample width** Flame spread, flame geometry, characteristic	Forced flow, sample width, dilution gas, 30% Oxygen, and 100	Thin	Flat	PMMA	6xWx0.125cm W=5, 10, 20 mm		MGLAB drop tower	7 L	CCD camera, interferometer, radiometer	

				gas-phase lengths, heat flux (heat losses)	kPa									
		[245]	2012	**Modeling of LOI apparatus** Opposed Flame spread rate, LOI, extinction limits	Sample width, 1G &µG, opposed forced flow	Thin	flat	Cellulosic						
		[414]	2012	**Flame spread over thin fuels: effect of radiation and sample width** Heat flux, flame spread, flame geometry (length), flame structure , gas-phase temperature, reaction rate	Radiation effect (gas, solid), 1G and µG, oxygen concentration, sample thickness, sample width	Thin	Flat	Cellulosic						
		[226]	2020	**Experimental and numerical: radiation from flame** flame geometry (flame area), heat transfer (flame radiation), burning rate, flame structure	Forced flow, oxygen concentration, sample width, sample thickness	Thin	Flat	PMMA	100 mm x e = 0.1, 0.2, 0.3 & 0.4 mm width = 1, 2 cm		BASS	7.6 x 7.6 x 17 cm 0.98 L	Camera, radiometer	FIAT Matlab code to analyse flames. No soot radiation
	Conc/opp	[79]	2018	**Flame spread over thin fuel: effect of microgravity and scale** Flame spread, heat flux , gas-phase and solid-phase temperature, heat flux, characteristic solid-phase length (pyrolysis), gas-phase reaction rate, solid mass pyrolysis rate, flow profile, burning rate, heat flux	Sample width, forced flow, boundary layer effect	Thin, thick	Flat	Sibal & PMMA	Saffire I&III: 94x40.6 cm Saffire II:29x5cm PMMA: 10x50x290mm	1000	CYGNUS, Saffire	6.6 L (Rig)	CCD camera, radiometer, thermocouple	

Gravity level

Sub-topic	ref.	year	Goal	Goal	thermal behaviour	sample type	material type	Specimen size cm2, or cm	Scale time [s]	Rig/facility	Chamber vol. size	Diagnostics,	Comments
Concurrent or upwards	[72]	1996	**Upward flame spread over a thin fuel** Flame spread, radiation flux, solid-phase temperature, velocity profile, heat flux, flame structure, fuel consumption rate, characteristic solid-phase length (pyrolysis)	gravity	Thin	Flat	Kimwipe						
	[102]	2011	**Experimental and numerical upwards flame**	Gravity, forced flow,	Thin	Flat	Cellulosic sample	12 cm x 1 or		5.3	GIFFT 27 L	Video	

			spread in 1g and µG Flame spread, solid-phase profiles, solid-phase temperature, surface emittance	pressure, oxygen concentration, sample width				2cm		droptower Parabolic flight KC-135			
	[415]	2011	**Numerical, effect of kinetics on concurrent flame spread in 1g and µG** Flame structure, gas-phase temperature, solid-phase temperature, mass flux, flame geometry (length), characteristic solid-phase length (pyrolysis), escaped fuel vapour	gravity, chemical kinetics	Thin	Flat	Kimwipe						
Opposed	[29]	1968	**Experimental** Flame spread horizontal	Gravity level, forced flow, quiescent, oxygen concentration, pressure, diluent			Cotton cloth strips (MIL-C-5646C)	5x20 cm		KC-135 & Centrifuge	65 L	Camera	
	[123]	1980	**Experimental downwards flame spread over thin fuel** Flame spread	Oxygen concentration, pressure, gravity level	Thin	Flat	Index cards (thickness 0.019 cm & 0.75 g/cm3) machine tape (0.0086 cm & 0.64 g/cm3)	Card e=0.098 mm Tape e=0.043 mm		Centrifuge	Chamber 37 L	Camera	
	[416]	1991	**Theoretical downwards flame spread over a thin fuel** Flame spread, flame structure, heat flux, gas-phase temperature, velocity profile, fuel pyrolysis		Thin	Flat	Cellulosic						
	[417]	1992	**Opposed flame spread: effect of natural and forced convection** Flame spread, velocity profiles	Surface emittance	Thin	flat	Cellulosic						
	[98]	1994	**Downward flame spread and extinction** Flame spread	Oxygen concentration, forced flow, gravity level	Thin	flat	Kimwipe	8 x 7 cm		Parabolic KC-135	26 L	Simultaneous Schlieren camera	
	[125]	1994	**Downwards flame spread: radiative effects** Flame spread, flame structure, gas-phase temperature, velocity profile, heat flux, optical thickness, flame geometry	gravity level, oxygen concentration, radiation effect (gas, solid)	Thin	Flat	Cellulosic						Gas-phase radiation included

	[349]	2003	**Numerical of ignition to steady downwards flame spread** Flame spread, flame structure, solid-phase temperature, solid-phase density, gas-phase temperature, velocity profile, fuel mass fraction, oxygen mass fraction, solid-phase characteristic length (pyrolysis)	Fuel thickness, , gravity level, oxygen concentration	thin	Flat	cellulosic						
Conc/opp	[101]	2002	**Upward flame spread over thin fuel** Flame spread, flame structure , solid-phase thickness, solid-surface temperatures, velocity profile, oxygen mass fraction, fuel reaction rate, gas-phase temperature	Oxygen concentration, gravity level, pressure, sample width	Thin	Flat	Kimwipe	Width= 1 or 2 cm Length= 12 cm		KC-135	GIFFTS (26 L)	IR camera	
	[172]	2015	**Flame spread over thin fuel: effect of sample orientation and forced flow** Flame spread	Sample orientation, oxygen concentration, gravity level, 0.1 m/s forced flow, upwards/downwards.	Thin	Flat	Filter paper (density 140 g/m^2)	140 x 50 x 0.25 mm		MGLAB & Centrifuge (Rotating arm at JAXA)	7x7x30 cm 1.47 L	Camera, UV camera	
1g-µg	[154]	2016	**Experimental diffusion solid combustion during transition 1g-µg** Flame geometry, gas-phase temperature			Sphere	Methenamine	⌀ 5, 8 & 10 mm		Drop system (2.3 s)	98 L	CCD camera, image pyrometry	

Confined space

Sub-topic	ref.	year	Goal	Parameters	thermal behaviour	sample type	material type	Specimen size cm2, or cm	Scale time [s]	Rig/facility	Rig vol. size	Diagnostics,	Comments
Concurrent	[418]	2002	**Modelling Flame spread over thin fuel: effect of enclosure** Flame structure, flame spread, flow field, char front spread, angle of char pattern, total heat release	Forced flow	Thin	Flat	Cellulosic paper						
	[60]	2000	**Modelling flame spread over a thin fuel: effect of tunnel and sample width**	Forced flow, oxygen concentration, tunnel	Thin	flat	80% non-charring & 20% inert (Kimwipe)						Surface radiation

			Flame spread , solid-phase thickness profile, velocity profile, gas-phase temperature	height, fuel width									included, but no gas radiation
	[170]	2021	**<u>Experimental flame spread over thin fuel: effect of confined space</u>** Flame spread, flame geometry (length), flame structure	Enclosure distance, enclosure type (transparent, black, metal), Forced flow	Thin	Flat	SIBAL	10 x 2.2 cm		BASS	0.98 L	Camera	
Opposed	[121]	2015	**<u>Flame spread over thin fuel: effect of confined space</u>** Flame spread, flame geometry (length), flow velocity pattern, heat release rate, gas-phase temperature	Tunnel height	Thin	Flat	Laboratory wipe	5x14 cm and e = 0.062 mm	3.6	droptower at Key Lab. Of MicroG., China	30x15x(1.5-5cm) 2.25 L	Digital camera	

Surface features

Sub-topic	ref.	year	Goal	Parameters	thermal behaviour	sample type	material type	Specimen size cm2, or cm	Scale time [s]	Rig/facility	Rig vol. size	Diagnostics,	Comments
Concurrent	[88]	2017	**<u>Experimental upward flame spread over cylinder</u>** Pyrolysis spread, solid-phase characteristic length (pyrolysis)	Corrugation effect, 1 cm/s Forced flow		Cylinder	Grooved PMMA	Ø 15 mm		REXUS	0.36 L (3 chambers)	IR camera	
	[402]	2020	**<u>Flame spread over thick fuel</u>** Flame spread, regression rate, CO_2 readings	Sample feature (groove)	Thick	Flat	PMMA & grooved PMMA	50 x 290 x 10 mm	1000	Saffire II	6.6 L (Rig)	Camera, radiometer	Smoke detector test

Discrete position

Sub-topic	ref.	year	Goal	Parameters	thermal behaviour	sample type	material type	Specimen size cm2, or cm	Scale time [s]	Rig/facility	Rig vol. size	Diagnostics,	Comments
Concurrent	[225]	2016	**<u>Flame spread interaction of wires</u>** Mass burning rate	Forced flow		Wire	PE, core Ni-Cr D 1.1 mm	10 cm		CNES parabolic	DIAMONDS 26 L	CCD + backlighting	

										flight		technique	
	[419]	2018	**Flame spread over thin discrete fuels** Flame spread, gas-phase temperature, burning rate, heat flux	1G & µG	Thin	Flat	Paper						
	[227]	2021	**Experimental flame spread over discrete fuels** Flame spread, burning rate, flame geometry (length)	Gap size, fuel ratio, 30 cm/s forced flow, segment length	Thin	Flat	Cellulose (TENGU)	5 x 0.5 or 1 cm		5.18s droptower	113 L		
Quiescent	[15]	1974	**Experimental** Flame spread	65% Oxygen concentration, pressure, sample distance (discrete)		Flat, cylindrical, thread	parallel pieces of paper (cellulosic)			SKYLAB	22 L	Camera	
	[371]	1995	**Interaction between flames on parallels thin fuels** Flame spread	Pressure, sample separation, diluent gases		Flat	Parallel sheets of Kimwipe (1.9 mg/cm^2)	5 cm x7.5cm		2.2 s droptower	45 L	Camera	

Fire extinguishment

Sub-topic	ref.	year	Goal	Parameters	thermal behaviour	sample type	material type	Specimen size	Scale time [s]	Rig/facility	Rig vol. size	Diagnostics,	Comments
quiescent	[369]	1998	**Flame spread over thick fuels: effect of ambient atmosphere** Flame spread	Diluent gases, oxygen concentration, pressure, sample thickness, 1g & µG	Thin	Flat	Kimwipe	5x15cm		2.2 & 5.18 droptowers	20 L	CCD cameras	
	[181]	2006	**Flame spread over thick fuels: CO_2 and He comparison as flame extinguishment** Flame spread	Oxygen concentration, diluent gas, pressure	Thick	Flat	Polyurethane foam (0.03 g/cm^3)	10 x 11.5 cm		2.2 droptower	20 L	CCD cameras	
	[29]	1968	**Experimental** Flame spread horizontal	Gravity level, forced flow, quiescent, oxygen concentration, pressure, diluent			Cotton cloth strips (MIL-C-5646C)	5x20 cm		KC-135 & Centrifuge	65 L	Camera	
Opposed	[192]	2007	**Experimental flame spread: effect of ambient** Flame spread	Oxygen concentration, diluent gas, forced	Thin	Flat	PMMA	80 x 10 x 0.125 mm		MGLAB 4.5 s	37 x 12 x 24 cm	CCD cameras, interferometer	

				flow							10.65 L		
Depress.	[15]	1974	**<u>Experimental</u>** Flame spread	65% Oxygen concentration, 5.2 psia pressure, sample distance (discrete)	Thin, thick		Aluminised mylar, nylon sheet, neoprene coated nylon fabric, polyurethane foam, bleached cellulose paper, Teflon fabric, parallel piece of paper			SKYLAB	22 L		
						Cylindrical, threaded over steel or ceramic mandrel	(Dacron thread, neoprene rubber foamed, neoprene rubber tubing, paraffin, polyurethane rubber, silicone rubber, styrene plastic, Teflon tubing.			KC-135	65 L		
	[420]	1999	**<u>Burning and extinction of thick fuel during depressurisation</u>** Flame geometry, heat transfer, burning rate (heat from gas to solid)	10 cm/s forced flow, ambient pressure	Thick	cylinder	PMMA	2.54 x ⌀1.9 cm		Parabolic flight DC	25 L	Video camera	

NEAR-LIMIT

POINT DIFFUSION STAGNATION FLAME

Sub-topic	ref.	year	Goal	Parameters	thermal behaviour	sample type	material type	Specimen size cm2, or cm	Scale time [s]	Rig/facility	Chamber vol. size	Diagnostics,	Comments

Cylindrical surface	[100]	1986	**Radiative extinction** Gas-phase temperature, burning rate, characteristic gas-phase length (stand-off distance), flammability map	Stretch rate, surface radiation			PMMA						Surface radiative loss
	[23]	1987	**Near-limit of a stagnation-point diffusion flame: effect of radiation and** Extinction limits (oxygen concentration and mixed-convection stretch rate), effect of radiation, effect of convection type (forced and natural convection) on limits, heat flux (energy balance), surface regression rate	Mixed-convection stretch rate, densimetric Fr number, emissivity			PMMA						
	[24]	1998	**Gas-phase radiative effects on burning and flame extinction** Gas-phase temperature, burning rate, extinction boundary, heat flux	Stretch rate, radiation treatment									Gas and surface radiative loss
Concurrent	[82]	2017	**Flammability boundary for rods in axial stagnation flow** Boundary limits (oxygen concentration & stretch rate) , flame geometry (length), heat transfer (balance), regression rate, CO, CO$_2$ & O$_2$ readings, global equivalence ratio	Forced flow, oxygen concentration, pressure, gravity		Cylinder	Black PMMA	⌀ 0.318, 0.476 & 0.635 mm		BASS-II	7.6x7.6x17 cm 0.98 L	Video camera, radiometer	
	[278]	2020	**Flammability boundary for rods in axial stagnation convective flow: comparison between 1G low pressure and μG** Boundary limit (pressure and stretch rate, pressure and force flow, oxygen partial pressure & pressure), flame geometry (stand-off), heat loss (surface re-radiation + heat sink), flame spread	Pressure, 1G & μG, forced flow		Cylinder	PMMA	⌀ 0.318		5.18s drop tower	113 L		

PARALLEL FLOW: quiescent, concurrent, opposed, opposed & concurrent

Quiescent

ref.	year	Goal	Parameters	thermal behaviour	sample type	material type	Specimen size cm2, or cm	Scale time [s]	Rig/facility	Chamber vol. size	Diagnostics,	Comments
[92]	1998	**Experiment flame spread over thick fuel**	Oxygen concentration, pressure	Thick	Flat	PMMA	25.4 x 6.35 x 3.18 mm	510	SSCE apparatus	39 L	Camera, thermocouples	

Forced flow

Concurrent

ref.	year	Goal	Parameters	thermal behaviour	sample type	material type	Specimen size cm2, or cm	Scale time [s]	Rig/facility	Chamber vol. size	Diagnostics,	Comments
[95]	1994	**Experimental, numerical and theoretical flame spread over a thin fuel** Flammability limit (oxygen concentration and forced flow)	Oxygen concentration and forced flow	Thin	Flat	Kimwipe (1mg/cm^2) (cellulosic)	4.9x10cm	5.2	5.18 drop tower	113 L	Camera	
[406]	1994	**Modelling flame spread over a thin fuel** Flammability limits (oxygen concentration and forced flow)	Oxygen concentration, forced flow	Thin	Flat	Cellulosic						
[59]	2003	**Numerical flame spread over thin fuel: wall heat loss and oxygen side diffusion**	Forced flow, sample width, oxygen concentration, forced flow, tunnel insulation	Thin	flat	Cellulosic						
[62]	2015	**Modelling for flame growth and near-limit** Radiative extinction	1G/µG	Thin	Flat	Fabric, 75% fabric 13.4 mg/cm2, 25% inert	e = 0.3175 mm					

[114]	2016	**Experimental and numerical study for growth, spread and quenching** Extinction limits (oxygen concentration and forced flow)	Oxygen concentration, forced flows, sample width	thin	Flat	SIBAL	1.2x10 cm or 2.2x10 cm e=0.32 mm		(MSG) on ISS. BASS & BASS II	(7.6x7.6x17cm) 0.98 L	Camera	

Opposed

ref.	year	Goal	Parameters	thermal behaviour	sample type	material type	Specimen size cm2, or cm	Scale time [s]	Rig/facility	Chamber vol. size	Diagnostics,	Comments
[17]	1988	**Experimental near-limit flame spread over a thin fuels** Extinction limits (oxygen concentration and forced flow)	Oxygen concentration , forced flows	Thin	flat	Kimwipe (1. 998 X 10^{-3} g/cm^2)	3 x 15 x 0.0076 cm	5.18	2.2 & 5.18 droptowers	113 L	Camera, thermocouples	
[18]	1991	**Flame spread over a thin fuel: effect of oxygen and forced flow** Extinction limits (oxygen concentration and forced flow)	Oxygen concentration, forced flow, thickness	Thin	flat	Kimwipe	5x15 cm e=0.0076 cm	2.2	2.2 drop tower	113 L	Camera, Thermocouples	
[19]	2000	**Experimental results: flame geometry and stability of flame** extinction limits	Oxygen concentration, forced flow	Thick	Flat	PMMA	50x50x10mm		ZARM droptower, CNES airbus	0.4x ⌀ 0.3m (28 L) in ZARM Droptower and CNES airbus A300	2 CCD cameras, 1 intensified high speed camera, Planar laser induced fluorescence system (Trace OH radicals) thermocouple	

[20]	2001	**Experimental results: flame geometry and stability of flame** extinction limits	Oxygen concentration, forced flow	Thick	Flat	PMMA	50x50x10mm		ZARM droptower, CNES airbus, & Minitexus 6	0.4x ⌀ 0.3m (28 L) in ZARM Droptower and CNES airbus A30 & Combustion chamber Minitexus 6 5.6 L		
[325]	2005	**Semi-empirical prediction of flame spread and near-limit** Extinction limits (oxygen concentration and forced flow)	Sample thickness, oxygen concentration, forced flow	thin	Flat	PMMA, cellulose						
[28]	2012	**Scale analysis: flame spread over thin fuel and LOC** Extinction limits (oxygen concentration and forced flow)	Oxygen concentration, forced flow, diluent gas	Thin	Flat	PMMA	6x1cm, e=0.125	1	MGLAB (4.5 s), DAS (20 s)	Chamber, 37x12x24 cm 10.65 L	CCD camera, IR camera, interferometer	Scale analysis
[27]	2013	**LOI of thin fuel in microgravity** Extinction limits (forced flow and oxygen concentration)	Forced flow, oxygen concentration	Thin	Flat	PMMA	9x2 cm x 0.125 mm		DAS	13x14x14 cm 2.54 L (rig)		
[21]	2013	**Near-limit over wires** Extinction limits (forced flow and oxygen concentration)	Core (NiCr & Cu), 1G & µG, oxygen concentration, forced flow		wire	PE	100 mm x NiCr e= 0.8 mm Cu e = 0.5 mm		DAS	13x14x14 cm 2.54 L (rig)		
[240]	2015	**Scale analysis: flame near-limit over thin fuel and LOC** Extinction limits (forced flow and oxygen concentration)	Oxygen concentration, forced flow, diluent gas	Thin	Flat	PMMA	6x2cm, e=0.125	2.6	DAS	Chamber 35 L	CCD camera, IR camera	Chamber similar to fuel dispenser

[22]	2015	**Flammability limits of wires** Extinction limits (oxygen concentration and external radiant flux)	Oxygen concentration, incident heat flux, 12 cm/s air flow		Wire	EFTE	20 cm x Cu wire ⌀ 0.5 mm, EFTE e = 0.3 mm		DAS	25 x ⌀ 6 cm 0.7 L		
[241]	2016	**Flammability limits (LOC): effect of ambient** boundary limits (Oxygen concentration and forced flow)	Oxygen concentration, forced flow, gas diluent	Thin	Flat	PMMA	80x20x0.125mm	8	DAS	Rolling chamber 35 L	CCD, infrared camera	Similar to fuel dispenser
[195]	2017	**LOI for thin fuel** LOC & MLOC, boundary limits (Oxygen concentration and forced flow)	Oxygen concentration, forced flow, diluent	thin		PMMA, Nomex HT-90	8x2cm, e=0.125 mm		DAS	ASTM D2863 chamber (35 L)	CCD camera	
[145]	2018	**Comparison near-limit between µG & NCA** Flammability limits (oxygen concentration and forced flow), flamelets	Oxygen concentration, forced flow, 1G & µG, comparison with NCA	thick	flat	PMMA	61.6 x 50 x 10mm		SJ-10	8 flow tunnels (95 x95x 120 mm or 1L) in a 39 L chamber	CCD camera	
[171]	2018	**Experimental flame spread over cylinder** Limits (oxygen concentration and forced flow)	Oxygen concentration, forced flow		cylindrical	Black PMMA	57.2 mm x ⌀ 6.4, 9.5 &12.7 mm	100 - 500	MSG Glovebox (BASS-II) the ISS	7.6x7.6x17 cm 0.98 L	Camera, radiometer	
[242]	2018	**LOI of thin fuels** Flammability limit (oxygen concentration and forced flow)	Oxygen concentration, forced flow		Flat	PMMA & Nomex HT90-40	e = 0.125		DAS			
[221]	2019	**Experimental flame spread over thick samples** Flammability limits (oxygen concentration and forced flow)	Oxygen concentration, forced flow	Thick	Flat	PMMA	61.6 x 50 x 10 mm	55	SJ-10	4 tunnels (12 cm x 9.5 x 9.5) in chamber 39 L	CCD camera, RGB pyrometry	
[243]	2019	**LOI of retardant fuels** Flammability limit (oxygen concentration and forced flow)	Oxygen concentration	Thin	Flat	Meta-aramid fabric: NOMEX HT90-40	8x2 cm x e=0.3 mm		DAS	35 L		

						Para-amid fabric: Kevlar KE5847	8x2 cm x e=0.35 mm					
						polyimide film (Kapton)	8x2 cm x e=0.125 mm					
						Polycarbonate CARBOGLASS C110C	8x2 cm x e=0.25 mm					
[388]	2020	**Flame spread over flat samples** Flammability limit (oxygen concentration and forced flow)	Forced flow, oxygen concentration, sample type	thick	flat	LDPE and HDPE	40x20 mm LDPE = 1.5mm HDPE = 2.5 mm	20	DAS	62 x 18 x 32 cm or 36 L (effective chamber)	Camera, IR camera	
[244]	2020	**LOI of retardant fuels** Flammability limit (oxygen concentration and forced flow)	Forced flow, oxygen concentration	Thin	flat	Polycarbonate: CARBOGLASS C110C	8x2 cm x e=0.25 mm		DAS	62 x 18 x 32 cm or 36 L (effective chamber)	CCD camera	
						Polyether ether ketone: PEEK4000	8x2 cm x e=0.2 mm					
						Poly-phenylsulfone: PPSU U1-1	8x2 cm x e=0.03 mm					
						Polyimide: Kapton 500H	8x2 cm x e=0.125 mm					
						Silicone resine: SR-50	8x2 cm x e=0.5 mm					
						Meta-aramid fiber: NOMEX HT90-40	8x2 cm x e=0.3 mm					
						Meta-aramid fiber: CONEX	8x2 cm x e=0.3 mm					
						Para-aramid fiber: KEvlar KE5847	8x2 cm x e=0.3 mm					

						silicone rubber: SH144YA	8x2 cm x e=1 mm					
[391]	2020	**Near-limit: effect of pressure for a wire** Flammability limit (oxygen concentration and ambient pressure, oxygen partial pressure and total ambient pressure)	Pressure, oxygen concentration, 10 cm/s opposed forced flow		Ni-Cr Wire D 0.5 mm	LDPE	e = 0.3 mm		A310 CNES	DIAMONDS rig 26 L		
[389]	2020	**Flame spread and near-limit over electric wires** Flammability limits (oxygen concentration and external radiation)	1G & µG, incident heat flux, core diameter, sample colour (radiation absorption effect), 10 cm/s forced flow, 100 kPa		wire	Standard & black LDPE with Cu wire (⌀2.5 & 0.7 mm),	130 mm x e = 0.75 & 1.65 mm	5-10	DAS	390 x ⌀ 80 mm 7.84 L	Camera, IR camera	Oscillatory flames were observed

Opposed/Concurrent

ref.	year	Goal	Parameters	thermal behaviour	sample type	material type	Specimen size cm2, or cm	Scale time [s]	Rig/facility	Chamber vol. size	Diagnostics,	Comments
[64]	2003	**Numerical flame spread and near-limit: comparison of opposed and concurrent over thin fuels** Flammability limits (oxygen concentration and forced flow)	Entrance length (boundary layer), forced flow, oxygen concentration,	Thin	flat	Kimwipe						No soot radiation

NON-PARALLEL FORCED FLOW

ref.	year	Goal	Parameters	thermal behaviour	sample type	material type	Specimen size cm2, or cm	Scale time [s]	Rig/facility	Chamber vol. size	Diagnostics,	Comments
[354]	1998	**Flame spread and near-limit around a cylinder fuel** Flammability limits (forced flow/ Da, Surface loss parameters and heat flux into the solid)	Forced flow, heat flux into solid		cylinder	PMMA						No gas-phase radiation

[420]	1999	**Burning and extinction of thick fuel during depressurisation** Flammability limit (heat transfer from gas to solid & pressure)	10 cm/s forced flow, ambient pressure	Thick	cylinder	PMMA	2.54 x ⌀1.9 cm		Parabolic flight DC	25 L	Video camera	
[353]	2020	**Flame growth and extinction around a spherical solid: effect of thickness** Heat transfer, flame geometry, Effect of solid in-depth	Forced flow	Thick	sphere	PMMA	⌀ 2 cm		BASS GEL (prep)	0.98 L	Camera	Limiting thickness

TANGENT ASPECTS:

Sample width

Sub-topic	ref.	year	Goal	Parameters	thermal behaviour	sample type	material type	Specimen size cm2, or cm	Scale time [s]	Rig/facility	Chamber vol. size	Diagnostics,	Comments
opposed	[245]	2012	**Modeling of LOI apparatus** Opposed Flame spread rate, LOI, extinction limits	Sample width, 1G &µG, opposed forced flow	Thin	flat	Cellulosic						
Concurrent	[60]	2000	**Modelling flame spread over a thin fuel: effect of tunnel and sample width** Quenching extinction	Forced flow, oxygen concentration, sample width	Thin	flat	80% non-charring & 20% inert (Kimwipe)						Surface radiation included, but no gas radiation
	[114]	2016	**Experimental and numerical study for growth, spread and quenching** Extinction limits (oxygen concentration and forced flow)	Oxygen concentration, forced flows, sample width	thin	Flat	SIBAL	1.2x10 cm or 2.2x10 cm e=0.32 mm		(MSG) on ISS. BASS & BASS II	(7.6x7.6x17cm) 0.98 L	Camera	
Conc. /op	[101]	2002	**Upward flame spread over thin fuel** Flammability boundary (pressure and gravity level)	Oxygen concentration, gravity level, pressure, sample width	Thin	Flat	Kimwipe	Width= 1 or 2 cm Length= 12 cm		KC-135	GIFFTS (26 L)	IR camera	

Gravity level

Sub-topic	ref.	year	Goal	Parameters	thermal behaviour	sample type	material type	Specimen size cm2, or cm	Scale time [s]	Rig/facility	Chamber vol. size	Diagnostics,	Comments
opposed	[98]	1994	**Downward flame spread and extinction** Boundary limits (oxygen concentration and gravity)	Oxygen concentration, forced flow, gravity level	Thin	flat	Kimwipe	8 x 7 cm		Parabolic KC-135, centrifuge	26 L	Simultaneous Schlieren camera	
	[125]	1994	**Downwards flame spread: radiative effects** Boundary limits (oxygen concentration and gravity)	gravity level, oxygen concentration	Thin	Flat	Cellulosic						Gas-phase radiation included
	[363]	2020	Radiation-kinetics interaction, flame geometry, flame spread,	Gravity, pressure, radiation, kinetics	Thin	Flat	PMMA						
Conc.	[72]	1996	**Upward flame spread over a thin fuel** Quenching limit (gravity level)	Gravity, radiative effect	Thin	Flat	Kimwipe						
Conc. /op	[101]	2002	**Upward flame spread over thin fuel** Flammability boundary (pressure and gravity level)	Oxygen concentration, gravity level, pressure, sample width	Thin	Flat	Kimwipe	Width= 1 or 2 cm Length= 12 cm		KC-135	GIFFTS (26 L)	IR camera	

Oscillations & flamelets

Sub-topic	ref.	year	Goal	Parameters	thermal behaviour	sample type	material type	Specimen size cm2, or cm	Scale time [s]	Rig/facility	Chamber vol. size	Diagnostics,	Comments
Quiescent	[3]	2000	**Experimental & numerical candle flames** Extinction behaviour (oscillations)	Oxygen concentration, pressure, wick diameter, candle diameter	-	Candle	Candle (80% n-paraffin wax and 20% stearic acid)	⌀ 2 and 10 mm x 20 mm	300	STS & MIR	STS: 11.5x11.5 x 11.5 cm or 1.52 L MIR: 20 x 20 x 20 cm or 8 L	Video camera	

	[421]	2017	**Dynamic behaviour of near-limit flame (oscillatory)** Spread rate, flame structure, flamelet structure	Sample width, oxygen concentration	Thin								
Concurrent	[395]	2019	**Flame oscillation along a rod in a stagnation flame** Flame spread, number of oscillations, frequency	Oxygen concentration, forced flow		Cylinder	PMMA			BASS-II	7.6x7.6x17 cm 0.98 L		
Opposed	[145]	2018	**Comparison near-limit between µG & NCA** Flammability limits (oxygen concentration and forced flow), flamelets	Oxygen concentration, forced flow, 1G & µG, comparison with NCA	thick	flat	PMMA	61.6 x 50 x 10mm		SJ-10	8 flow tunnels (95 x95x 120 mm or 1L) in a 39 L chamber	CCD camera	
	[422]	2019	**Near-limit spread behaviour: flamelets** Flamelets, flame spread, flame geometry	Sample width, oxygen concentration, forced flow	thin	Flat							No soot radiation

Confined spaces

Sub-topic	**ref.**	**year**	**Goal**	**Parameters**	**thermal behaviour**	**sample type**	**material type**	**Specimen size cm2, or cm**	**Scale time [s]**	**Rig/facility**	**Chamber vol. size**	**Diagnostics,**	**Comments**
Concurrent	[60]	2000	**Modelling flame spread over a thin fuel: effect of tunnel and sample width** Quenching extinction	Forced flow, oxygen concentration, sample width	Thin	flat	80% non-charring & 20% inert (Kimwipe)						Surface radiation included, but no gas radiation

Limiting thickness	[352]	2016	**Establishing the thermal regime (thickness limit)** Transition thickness				PMMA						

APPENDIX D

Topic	ref.	year	Goal	variables	thermal behaviour	sample type	material type	Specimen size cm2, or cm	Scale time [s]	Rig/facility	Chamber vol. size	Diagnostics,	Comments
Smouldering combustion	[423]	1987	**Modeling concurrent smoldering** Influence of buoyancy	Opposed		Cylinder							
	[263]	1986	**Buoyancy effect on smouldering** Theoretical and low pressure experiments										
	[398]	1997	**Experimental: transition from piloted ignition to smouldering** Temperature, gas analysis	Gravity, forced flow, ignition type (axial, plate)		cylinder	Open-cell Flexible	80 mm x ⌀ 50 mm	2400	on the USML-1	Spacelab Glovebox, 0.15 x 0.15 x 0.2 m 4.5 L	thermocouples	Ni-Cr igniter
	[399]	1999	**Experimental smouldering** temperature, smolder velocity, gas analysis	Quiescent, forced, opposed forced flow, gravity		cylinder	flexible polyurethane foam	140 mm x ⌀ 132 mm	3000	(STS-69 and STS-77 missions	MSC (microg. Smold. Combustion) 21.77 litre	Thermocouple, TGA	
	[223]	2004	**Experimental smouldering** Reaction temperature , smolder velocity	Gravity, concurrent forced flow		Cylinder	polyurethane foam	140 mm x ⌀ 132 mm	2000	STS-105 and STS-108	MSC 21.7 litres	Thermocouple, ultrasonic imaging	Cylindrical disc igniter
	[224]	2004	**Experimental smouldering** Opposed smolder flow, reaction temperature , char permeability, O_2 mass flux, heat loss, gas mass flux	Opposed forced flow, gravity, pressure		cylinder	Unretarded polyurethane foam	140 mm ⌀ 120 mm	2000	STS-69, STS-77, STS-105	MSC 21.7 litres	Thermocouple, ultrasound imaging data	Cylindrical disc igniter
	[424]	2005	**Modelling forward smouldering** temperature, smolder propagation velocity	Concurrent forced flow			Polyurethane foam		1200				
	[425]	2007	**Modelling forward and opposed smouldering** reaction temperatures, smoulder propagation velocity, heat release rate	Opposed and concurrent forced flow			Polyurethane foam		1200				
	[393]	2008	**Experimental smouldering** reaction temperatures, opposed	Opposed and concurrent forced flows, smoulder		cylinder	White flexible polyurethane	⌀150 x170 mm	3000	SJ-8	45 mm x ⌀ 15 cm	thermocouples	Cylindrical disc igniter

			smoulder velocity	velocity							7.95 L		
Instability	[133]	1998	**Finger-like smouldering** downstream and upstream smolder propagation velocity, population studies, heat transfer, oxygen fraction	Forced flow		Flat	Cellulosic sheet (Whatman ashless filter paper) + potassium acetate	10 x 8.7x0.017 cm		RITSI Glovebox on STS-75 USMP-3	(85x95x171mm) 1.38 L	Thermocouple, video camera	Non-piloted (external radiation)
	[426]	2011	**Finger instability** Heat transfer, growth rate	Concurrent forced flow	Thin		Porous solid (cellulosic fuel)						
	[424]	2005	**Modelling forward smouldering** Extinction limit	Concurrent forced flow			Polyurethane foam		1200				
	[425]	2007	**Modelling forward opposed smouldering** Extinction limit	Opposed and concurrent forced flow			Polyurethane foam		1200				

APPENDIX E

SOOT

Sub-topic	**ref.**	**year**	**goal**	**Parameters**	**thermal behaviour**	**sample type**	**material type**	**Specimen size cm2, or cm**	**Scale time [s]**	**Rig/facility**	**Chamber vol. size**	**Diagnostics**	Comments
Jet flame	[203]	1994	**Smoke-point properties of jet diffusion flames in microgravity** Luminous flame length, residence time, fuel flow rate	1g to μg, burner diameter, ambient pressure, fuel		Jet	Ethylene-air, propane-air			KC-135	87 L	Colour video camera	
	[222]		**Soot morphology: effect of microgravity** Soot morphology (diameter)	1g to μg		Jet	Propane, ethylene			2.2 s drop tower		Transmission electron microscope (TEM) + CCD for post-processing	
	[208]	1996	**Soot-field structure** Soot volume fraction	1g to μg		Jet	Acetylene-air			2.2 s drop tower		full-field laser extinction	
	[209]	1997	**Quantification of Soot volume fraction** Volume fraction	1g to μg		Jet	Acetylene-air			2.2 s drop tower		Full-field laser extinction technique	
	[358]	1998	**Soot laminar flames: effect of environmental parameters (literature review)** Soot volume fraction	Dilution gas, additives, pressure		Jet	Ethylene						Review
	[355]	1998	**Diffusion flame in quiescent environment: effect of radiative heat loss (Counterflow flame)** Maximum reaction rate, soot volume fraction, , radiative heat loss, soot radiation										Model includes gas and soot radiation
	[210]	1999	**Soot-field structure: effect of fuel preheat** Soot volume fraction	1g to μg		Jet	Acetylene-Nitrogen			2.2 s drop tower		Full-field laser extinction technique	
	[211]	1999	**Soot aerosol properties** Soot volume fraction, soot	1g to μg		Jet	Acetylene - Nitrogen			2.2 s drop tower		Soot distribution: Full-field laser-light	

			morphology									extinction Soot morphology (thermophoretic soot sampling and transmission electron microscopy)	
	[427]	1996	**Effect of gravity on sooting** Fuel fraction, oxygen fraction, gas-phase temperature, soot volume fraction, velocity vectors,	gravity		Jet	Ethylene-air						
	[204]	2000	**Smoke-point properties of jet diffusion flames** flame residence time, luminous flame length, smoke point	Ambient pressure, burner diameter, jet velocity,			Ethylene, propane in air		100-230	STS		Colour CCD camera	
Flat plate	[185]	2005	**Evaluation of extinction factor** Extinction factor	Forced flow, oxygen concentration	Thick	Flat plate	PMMA			ZARM drop tower		CCD Camera + green LEDs emitter	
	[215]	2006	**Methodology to measure soot volume** CH* intensity and local spectral absorption coefficient, soot volume fraction	Forced flow		Flat plate burner	Ethylene			Parabolic flight		Chemiluminescence (Laser Extinction measurement) with a tri-CCD camera and line-of-sight light attenuation technique Soot morphology: SEM	
	[217]	2007	**Interactions between soot & chemiluminescence (CH*)** Soot volume fraction, CH* spontaneous emission	Forced flow		Flat plate burner	Ethylene			Parabolic flight	50L	Laser-induced incandescence LII (soot vol. fraction) + Chemiluminescence	
	[216]	2007	**Sooting behaviour dynamics: soot trajectory** Soot volume fraction	Forced flow		Flat plate burner	Ethylene		22	Parabolic flights		Full-field laser-light extinction same as [215]	
	[336]	2009	**Numerical Soot deposition process**	Forced		Flat plate burner	Ethylene						

			Reaction temperature, soot deposition length, soot volume fraction										
	[428]	2009	**Transport mechanisms controlling soot production over a flame length** Soot volume fraction, velocity gradients, temperature, soot oxidation characteristic velocities	Forced flow		Flat plate burner	Ethylene					Full-field laser-light extinction	
	[429]	2015	**Modelling of soot production** Flame structure, soot volume fraction	Forced flow		Flat plate burner	Ethylene					laser-induced incandescence signal trapping	Not for blow-off regime
	[220]	2015	**Soot formation in a coflow flame**			Santoro coflow flame	Methane-Nitrogen			Microgravity Science glovebox on ISS	SLICE experiment	Color-ratio pyrometry	
	[218]	2018	**Validation of new method to study soot**			Santoro coflow flame	Ethylene/air						
Solid fuel	[205]	1994	**Soot particles agglomeration** Soot morphology and soot distribution (characterisation)			Flat & jet flame	Paper sheet and butane		10	JAMIC	51 L	Soot distribution: Videocamera Soot morphology: TEM & SEM	
	[212]	2016	**Morphology and concentration of smoke: Jet bursting flame wire** Particle size distribution, particle size diameter, smoke particle concentration, extinction coefficient	Forced flow		Wire	Fluorinated ethylene propylene wire			3.5 s drop tower National Microgravity Lab.	Chamber 3.15 L	SEM	
	[213]	2019	**Ignition and combustion of overloaded wire insulation** Smoke emission, smoke distribution	Pressure		wire	PE, PTFE, PVC			SJ-10		Laser extinction method	Compares with the low pressure narrow channel method

	[175]	2020	**Experimental evaluation of flame radiative feedback** Soot volume fraction, gas-phase temperature, soot radiative loss, radiative feedback from soot to solid	19% Oxygen concentration and 20 cm/s opposed forced flow		wire	LDPE coated Ni-Cr wire			Parabolic flight	DIAMONDS 26 L	Broadband Modulated Absorption/Emission technique	
	[176]	2020	**Method to assess Soot radiative feedback** Soot volume fraction, gas-phase temperature, radiative balance.	Opposed forced flow, pressure		Wire	LDPE coated Ni-Cr wire			Parabolic flight	DIAMONDS 26 L	Broadband Modulated Absorption Emission (BMAE) technique	
	[177]	2020	**Soot production and radiative heat transfer** Soot volume fraction, gas-phase temperature, flame geometry (stand-off distance, incident radiative heat flux, radiative neat flux	Opposed forced flow		wire	LDPE coated Ni-Cr wire			Parabolic flight	DIAMONDS 26 L	Broadband Modulated Absorption Emission (BMAE) technique	
	[178]	2020	**Soot production and radiative heat transfer: pressure effect** Soot volume fraction, spread rate, pyrolysis mass flow rate, radiation fraction, incident radiative flux.	Opposed Forced flow, ambient pressure		wire	LDPE coated Ni-Cr wire			Parabolic flight	DIAMONDS 26 L	Broadband Modulated Absorption Emission (BMAE) technique	Novel radiative model
	[179]	2020	**Opposed flame spread rate and soot production** Flame spread rate, soot formation length, soot volume fraction, gas-phase temperature, formation rate	Opposed forced flow, oxygen concentration, ambient pressure		wire	LDPE coated Ni-Cr wire			Parabolic flight	DIAMONDS 26 L	Broadband Modulated Absorption Emission (BMAE) technique	
	[430]	2020	**Opposed flame spread: soot oxidation quenching and smoke release** Quenching temperature, transitional limit between open tip and close tip flame (smoke point curve)	Opposed Forced flow, oxygen concentration, ambient pressure		wire	LDPE coated Ni-Cr wire			Parabolic flight	DIAMONDS 26 L	Broadband Modulated Absorption Emission (BMAE) technique	Finds the smoke-point transition

SMOKE AND GAS ANALYSIS

Topic	**ref.**	**year**	**goal**	**Parameters**	**thermal behaviour**	**sample type**	**material type**	**Specimen size cm2, or cm**	**Scale time [s]**	**Rig/facility**	**Chamber vol. size**	**Diagnostics**	Comments
Gas analysis	[431]	1997	**Experimental smoldering combustion** Gas-sample gases (post-flight)			Thick	Flexible polyurethane			USLM		Gas chromatography / mass spectrometry	
	[399]	1999	**Experimental smoldering combustion** Gas-sample gas analysis (post-flight)			Thick	Flexible polyurethane			STS		Gas chromatography / mass spectrometry	
	[432]	2015	**Oxygen and CO readings during BASS II** CO & CO_2 readings, Stoichiometric ratio, heat release rate, global equivalence ratio	Opposed, concurrent	Thin/thick	Rod, flat, sphere	PMMA, SIBAL			BASS II		MSG working volume dilution used. CSA-CP= Compound specific analyser-combustion products MCA= Major Constituents analyser	
	[82]	2017	**Flammability boundary for rods in axial stagnation flow** Boundary limits (oxygen concentration & stretch rate) , flame geometry (length), heat transfer (balance), regression rate, CO, CO_2 & O_2 readings, global equivalence ratio	Forced flow, oxygen concentration, pressure, gravity		Cylinder	Black PMMA	⌀ 0.318, 0.476 & 0.635 mm		BASS-II	7.6x7.6x17 cm 0.98 L	MSG working volume dilution used. CSA-CP= Compound specific analyser-combustion products MCA= Major Constituents analyser	
Smoke particles	[334]	1997	**Characterisation of smoke particles: pyrolysis products** Particle diameter, particle size distribution			Wire	Fluorinated wire insulation, TEFLON, TEFZEL			2.2 drop tower		Transmission electron microscope (TEM) and Energy dispersion spectroscopy (EDS)	

BURNING RATE

Subtopic	ref.	year	goal	Parameters	thermal behaviour	sample type	material type	Specimen size cm2, or cm	Scale time [s]	Rig/facility	Chamber vol. size	Diagnostics	Comments
Sphere droplet	[183]	2000	**Combustion of thermoplastic spheres** Burning rate	Sphere diameter, ambient pressure, oxygen concertation		Sphere	PMMA, PP, PS (polystyrene)	⌀ 2 – 6.4 mm		DC-9 and KC-135	24.5 L	CCD camera	bubble bursting phenomena
	[184]	2020	**Combustion of PE droplet** Burning rate, flame geometry (stand-off ratio), flame burning flux	Droplet diameter			PE			3.6 drop tower at NMLC	27 L	High-speed camera	Method to estimate mass loss rate & HRR
Side objective in these studies	[420]	1999	**Burning and extinction of thick fuel during depressurisation** Flame geometry, heat transfer, burning rate (heat from gas to solid)	forced flow, ambient pressure	Thick	cylinder	PMMA	2.54 x ⌀1.9 cm		Parabolic flight DC	25 L	Video camera	
	[120]	2004	**Experimental flame spread over thick fuel:** Flame spread, mass loss, burning rate, flame geometry (stand-off, flame length), gas-phase temperature, heat flux	Oxygen concentration, opposed forced flow, incident heat flux	Thick	Flat	Black cast PMMA	50x50x10mm	120	DARTFire, two mirror-image flow tunnels	(each 10x10x15cm or 1.5L)	UV video camera, radiometer	
	[225]	2016	**Flame spread interaction of wires** Mass burning rate	Concurrent forced flow		Wire	PE, core Ni-Cr D 1.1 mm	10 cm		CNES parabolic flight	DIAMONDS 26 L	CCD + backlighting technique	
	[79]	2018	**Flame spread over thin fuel: effect of microgravity and scale** Flame spread, heat flux , gas-phase and solid-phase temperature, heat flux, characteristic solid-phase length (pyrolysis), gas-phase reaction rate, solid mass pyrolysis rate,	Sample width, forced flow	Thin, thick	Flat	Sibal & PMMA	Saffire I&III: 94x40.6 cm Saffire II:29x5cm PMMA: 10x50x290mm	1000	CYGNUS, Saffire	6.6 L (Rig)	CCD camera, radiometer, thermocouple	

			flow profile, burning rate, heat flux										
	[400]	2020	**Numerical flame spread over thin fuel: effect of environment conditions** Flame spread, characteristic solid-heat length (pyrolysis), heat flux, mass burning rate, remaining mass fraction, gas-phase temperature, flame structure, flow profiles	Forced flow, oxygen concentration and pressure	Thin	Flat	SIBAL (18.02 mg/cm^2)	94 x 41 cm	460	Saffire I & II CYGNUS	6.6 L (Rig)	Video camera, Thermocouple, radiometer	Validation of model and parametric study
	[226]	2020	**Experimental and numerical: radiation from flame** flame geometry (flame area), heat transfer (flame radiation), burning rate, flame structure	Opposed forced flow, oxygen concentration, sample width, sample thickness	Thin	Flat	PMMA	100 mm x e = 0.1, 0.2, 0.3 & 0.4 mm width = 1, 2 cm		BASS	7.6 x 7.6 x 17 cm 0.98 L	Camera, radiometer	FIAT Matlab code to analyse flames. No soot radiation
	[180]	2020	**Experimental flame spread over ultra-thin fuels** Flame spread, flame geometry (length), flame structure, burning rate	Sample density, opposed forced flow, sample type	Ultra-thin	flat	Cellulosic paper (TENGU) , density = 0.2 to 13 mg/cm^2 Cheesecloth	30 x 5 cm	1	5.18 Drop tower	113 L	Camera	Concurrent-opposed reversed phenomena
	[227]	2021	**Experimental flame spread over discrete fuels** Flame spread, burning rate, flame geometry (length)	Gap size, fuel ratio, 30 cm/s concurrent forced flow, segment length	Thin	Flat	Cellulose (TENGU)	5 x 0.5 0r 1 cm		5.18s droptower	113 L		

HRR & OTHER

Subtopic	ref.	year	goal	Parameters	thermal behaviour	sample type	material type	Specimen size cm2, or cm	Scale time [s]	Rig/facility	Chamber vol. size	Diagnostics	Comments
HRR	[418]	2002	**Modelling Flame spread over thin fuel: effect of enclosure** Flame structure, flame spread, flow field, char front spread, angle of char pattern, total heat release	Force flow	Thin	Flat	Cellulosic paper						
	[121]	2015	**Flame spread over thin fuel: effect of confined space** Flame spread, flame geometry (length), flow velocity pattern, heat release rate, gas-phase temperature	Opposed forced flow, Tunnel height	Thin	Flat	Laboratory wipe	5x14 cm and e = 0.062 mm	3.6	droptower at Key Lab. Of MicroG., China	30x15x(1.5-5cm) 2.25 L	Digital camera	
	[432]	2015	**Oxygen and CO readings during BASS II** CO & CO_2 readings, Stoichiometric ratio, heat release rate, global equivalence ratio	Opposed, concurrent	Thin/thick	Rod, flat, sphere	PMMA, SIBAL			BASS II		MSG working volume dilution used. CSA-CP= Compound specific analyser-combustion products MCA= Major Constituents analyser	
Molten formation	[382]	2012	**Molten insulation volume change during flame spreading** Volumetric change rate	Opposed Forced flow		Wire	LDPE Ni-Cr wire	Core ⌀ 0.5 mm PE e = 1.5mm		MGLAB	33.8 L	Digital camera, high speed camera	
	[392]	2018	**Experimental Flame over wire insulation**	Concurrent Forced flow, oxygen		Wire	Polyethylene	Core ⌀ 0.5 mm	22	CNES parabolic	DIAMONDS rig	Tri-CCD camera	

			Flame spread, flame geometry (length), heat flux, molten spread	concentration, core wire (Ni-Cr and Cu), 1G and μG				PE e = 0.3 mm		flight	26 L		
Pool burning behaviour	[433]	2019	**Transition from opposed to fuel regression and blowoff** Flame spread, fuel regression angle	Forced flow, oxygen concentration, 1G &μG, pressure, incident heat flux		rod	PMMA			BASS-II	0.98 L		

FLAMMABILITY INDEX

Subtopic	ref.	year	goal	Parameters	thermal behaviour	sample type	material type	Specimen size	Scale time [s]	Rig/facility	Chamber vol. size	Diagnostics	Comments
Skin burn	[386]	2006	**Fabric flammability and predicted skin burn** Flame spread rate, flame heat flux, time to 2nd degree burn	1G and μG, gap between fabric and sensor, fabric type, oxygen concentration	thin	Flat	Lightweight cotton (144 g/m^2)	20x8 cm, e = 0.43 mm		KC-135	25.8 L	Video camera, infrared camera, heat flux gauge	Canadian General Standards Board (CGSB) Vertical Flammability Test
							heavy weight cotton (176 g/m^2)	20x8 cm, e = 0.74 mm					
							lightweight blend (129 g/m^2)	20x8 cm, e = 0.52 mm					
ULOI & MOC	[237]	2008	**Material flammability index: effect of gravity** ULOI & MOC	Martian, lunar gravity, gravity, 30 cm/s concurrent forced flow	Thin	Flat	Polyetherimide (PEI) ULTEM 1000, retarded aromatic nylon (NOMEX HT90-40), Polyethylene terephthalate (Mylar G)	5x15 cm		5.18 droptower DROP Bus Droptower + centrifuge	299 L	Video camera	
	[174]	2011	**Material flammability index: Lunar gravity** ULOI & MOC	1G and lunar gravity, 30 cm/s concurrent forced flow	thin	Flat	Ultem 1000, Nomex HT90-40, Mylar G	5x15 cm		5.18 droptower DROP Bus Droptower + centrifuge	299 L	Video camera	

	[173]	2012	**Material flammability index: effect of gravity** ULOI & MOC	Martian, lunar gravity, gravity, 30 cm/s concurrent forced flow	Thin	Flat	Polyetherimide (PEI) ULTEM 1000, retarded aromatic nylon (NOMEX HT90-40), Polyethylene terephthalate (Mylar G)	5x15 cm		5.18 droptower DROP Bus Droptower + centrifuge	299 L	Video camera	
LOI/LOC & MLOC	[245]	2012	**Modeling of LOI apparatus** Opposed Flame spread rate, LOI	Sample width, 1G &µG, opposed forced flow	Thin	flat	Cellulosic						
	[28]	2012	**Scale analysis: flame spread over thin fuel and LOC** Extinction limits (oxygen concentration and forced flow)	Oxygen concentration, forced flow, diluent gas	Thin	Flat	PMMA	6x1cm, e=0.125	1	MGLAB (4.5 s), DAS (20 s)	Chamber, 37x12x24 cm 10.65 L	CCD camera, IR camera, interferometer	Scale analysis
	[27]	2013	**LOI of thin fuel in microgravity** Extinction limits (forced flow and oxygen concentration)	Forced flow, oxygen concentration	Thin	Flat	PMMA	9x2 cm x 0.125 mm		DAS	13x14x14 cm 2.54 L (rig)		
	[240]	2015	**Scale analysis: flame near-limit over thin fuel and LOC** Extinction limits (forced flow and oxygen concentration)	Oxygen concentration, forced flow, diluent gas	Thin	Flat	PMMA	6x2cm, e=0.125	2.6	DAS	Chamber 35 L	CCD camera, IR camera	Chamber similar to fuel dispenser
	[241]	2016	**Flammability limits (LOC): effect of ambient** Flame spread, characteristic solid-phase lengths (pre-heat), LOC & MLOC	Oxygen concentration, forced flow, gas diluent	Thin	Flat	PMMA	80x20x0.125mm	8	DAS	Rolling chamber 35 L	CCD, infrared camera	Similar to fuel dispenser
	[241]	2016	**Flammability limits (LOC): effect of ambient** boundary limits (Oxygen concentration and forced flow)	Oxygen concentration, forced flow, gas diluent	Thin	Flat	PMMA	80x20x0.125mm	8	DAS	Rolling chamber 35 L	CCD, infrared camera	Similar to fuel dispenser
	[195]	2017	**LOI for thin fuel** LOC & MLOC, boundary limits (Oxygen concentration and forced flow)	Oxygen concentration, forced flow, diluent	thin	Flat	PMMA, Nomex HT-90	8x2cm, e=0.125 mm		DAS	ASTM D2863 chamber (35 L)	CCD camera	

	[242]	2018	**LOI of thin fuels** Flammability limit (oxygen concentration and forced flow)	Oxygen concentration, forced flow	Thin	Flat	PMMA & Nomex HT90-40	e = 0.125		DAS			
	[243]	2019	**LOI of retardant fuels** Flammability limit (oxygen concentration and forced flow)	Oxygen concentration	Thin	Flat	Meta-aramid fabric: NOMEX HT90-40 Para-amid fabric: Kevlar KE5847 polyimide film (Kapton) Polycarbonate CARBOGLASS C110C			DAS	35 L		
	[244]	2020	**LOI of retardant fuels** Flammability limit (oxygen concentration and forced flow)	Forced flow, oxygen concentration	Thin	flat	Polycarbonate: CARBOGLASS C110C Polyether ether ketone: PEEK4000 Poly-phenylsulfone: PPSU U1-1 Polyimide: Kapton 500H Silicone resine: SR-50 Meta-aramid fiber: NOMEX HT90-40 Meta-aramid fiber: CONEX Para-amid fabric: Kevlar KE5847 Silicone rubber: SH144YA			DAS	62 x 18 x 32 cm or 36 L (effective chamber)	CCD camera	